

# Conception and design of a mirror alignment and control system for the Ring Imaging Cherenkov detector of the CBM experiment

Inaugural-Dissertation zur Erlangung des  
Doktorgrades der Naturwissenschaften (Dr. rer. nat.)

vorgelegt von

**Jordan Bendarouach**

in der Justus-Liebig-Universität Gießen  
Fachbereich 07 (Mathematik und Informatik, Physik,  
Geographie)



Mai 2019



*To my family*



Dekan: Prof. Dr. Kai-Thomas Brinkmann  
1. Gutachter: Prof. Dr. Claudia Höhne  
2. Gutachter: Prof. Dr. Kai-Thomas Brinkmann



# Erklärung der Urheberschaft

Ich erkläre: Ich habe die vorgelegte Dissertation selbständig und ohne unerlaubte fremde Hilfe und nur mit den Hilfen angefertigt, die ich in der Dissertation angegeben habe. Alle Textstellen, die wörtlich oder sinngemäß aus veröffentlichten Schriften entnommen sind, und alle Angaben, die auf mündlichen Auskünften beruhen, sind als solche kenntlich gemacht. Bei den von mir durchgeführten und in der Dissertation erwähnten Untersuchungen habe ich die Grundsätze guter wissenschaftlicher Praxis, wie sie in der “Satzung der Justus-Liebig-Universität Gießen zur Sicherung guter wissenschaftlicher Praxis” niedergelegt sind, eingehalten.

---

Datum

---

Unterschrift



# Abstract

The Compressed Baryonic Matter (CBM) experiment at the future Facility for Antiproton and Ion Research (FAIR) complex will investigate the phase diagram of strongly interacting matter at high baryon density and moderate temperatures in A+A collisions. The beam energy will range from 2 up to 11 AGeV for the heaviest nuclei at the SIS 100 accelerator set-up. Due to their penetrating nature, electromagnetic probes are particularly interesting, as they deliver undistorted information from the fireball, unveiling properties of the created hot and dense matter.

To cope with the CBM physics program, an efficient and clean electron identification and pion suppression (for momenta up to 8 GeV/c) will be provided by the CBM-RICH (Ring Imaging Cherenkov) detector. In the SIS 100 set-up, the RICH detector together with four layers of Transition Radiation Detector, should reach a combined pion suppression factor of 1000 to 5000 in a wide acceptance. The RICH detector will be made of a CO<sub>2</sub> gaseous radiator, Multi-Anode Photo-Multipliers (H12700 MAPMTs from Hamamatsu) for photon detection and 80 trapezoidal glass mirror tiles, equally distributed in two half-spheres and used as focusing elements with spectral reflectivity down to the UV range.

One of the technical challenges emerging, while interchanging the RICH with the MuCh (Muon Chambers) presumably on a yearly basis, is a rigid and stable mechanical design along with a mirror alignment monitoring system. The latter combines two methods used in the COMPASS and HERA-B experiments and was adapted to the CBM-RICH detector geometry. In addition, a correction cycle was designed, which guarantees a proper operation of the detector even though mirrors are misaligned. These developments are the subject of the presented thesis.

The first method to determine mirror rotations is the Continuous Line Alignment Monitoring (CLAM) method. It uses a dedicated equipment: cameras with good pixel resolution, LEDs as light source and a grid made of retroreflective material. The principle relies on the fact that the reflected grid on the mirrors will appear broken at mirror edges, if the neighbouring mirrors are misaligned with one another. This is the fast qualitative variant of the method.

Furthermore, it can be used as a quantitative method to determine mirror rotations. In this case a previous laboratory calibration is prerequisite, which consists in measuring the pixel shift generated by given mirror rotations for a single mirror tile. This calibration has to be conducted on all mirrors to allow a complete measurement of mirror rotations.

The second technique adapted for the CBM-RICH detector uses data in software. The principle is to measure, for a high enough number of cumulated rings reflected on a single mirror tile, two quantities referred to as the ‘Cherenkov distance’ and ‘Cherenkov angle’. In case of mirror misalignment, plotting the ‘Cherenkov distance’ as a function of the ‘Cherenkov angle’, reveals a sinusoidal behaviour. After a fitting procedure, the extracted parameters can be related to the mirror rotations, allowing an accurate quantification of mirror rotations.

The performances of this technique were investigated. For a horizontal rotation of the mirror tile, the technique works for misalignments ranging between 0.3 and 14 mrad. For a vertical rotation of the tile, the technique yields accurate results for misalignments ranging from 0.4 mrad up to 15 mrad. It is more reliable for tiles located in the centre of the mirror wall than for tiles in the outer region.

A mirror correction cycle specifically designed for the CBM-RICH detector is introduced. It uses the mirror rotation information from the two presented methods to correct the track extrapolation on the MAPMT planes. Thus the distance between the extrapolated track and the reconstructed ring centre is reduced. It was added inside the CbmRoot framework and can run automatically in the reconstruction procedure.

The correction cycle was tested in simulations. The mirror tiles were artificially misaligned on both their axes following a Gaussian distribution with a standard deviation of 1 mrad. The mean ring-track distance then amounts to 0.47 cm, while being 0.14 cm in the aligned case. Applying the correction cycle reduces this number to 0.17 cm, which is close to the ideal case. In addition, it corrects the matching efficiency of the CBM-RICH and the electron identification efficiency with respect to the misaligned case. Even with a standard deviation of 3 mrad, the results obtained remain within the specifications required by the technical design report of the CBM-RICH detector.

# Zusammenfassung

Das ‘Compressed Baryonic Matter’ (CBM) Experiment an der zukünftigen ‘Facility for Antiproton and Ion Research’ (FAIR) Anlage hat zum Ziel, das Phasendiagramm von stark wechselwirkender Materie in A+A Kollisionen bei hoher baryonischer Dichte und moderater Temperatur zu untersuchen. Die Strahlenergie wird von 2 bis 11 AGeV für die schwersten Kerne an der SIS 100 Beschleunigeranlage reichen. Aufgrund ihrer durchdringenden Natur sind elektromagnetische Sonden wie Photonen oder  $e^-/e^+$  Paare besonders interessant um die erzeugte Materie zu untersuchen, da sie nicht mit dem erzeugten Feuerball stark wechselwirken. Durch ihr Studium sollten die Eigenschaften der erzeugten heißen und dichten Materie besser verstanden werden.

Eine der Voraussetzungen zur Durchführung des Physikprogramms von CBM ist eine effiziente und saubere Elektron Identifizierung zusammen mit einer Pionen Unterdrückung für Impulse bis zu 8 GeV/c. Diese werden durch einen ‘Ring Imaging Cherenkov’ (RICH) Detektor erreicht. Zusammen mit vier Schichten eines ‘Transition Radiation Detectors’ soll der RICH Detektor einen kombinierten Pion Suppression Faktor von 1000 bis 5000 in einer breiten Akzeptanz an der SIS 100 Anlage erreichen. Der Detektor wird aus einem gasförmigen CO<sub>2</sub> Radiator, ‘Multi-Anode Photo-Multipliers’ (H12700 MAPMTs von Hamamatsu) und 80 trapezförmigen Spiegelkacheln aus Glas bestehen. Die Kacheln werden in zwei Halbkugeln gleichmäßig verteilt und als Fokussierelemente mit einem spektralen Reflektionsvermögen bis hinunter in den UV Bereich genutzt.

Eine der technischen Herausforderungen stammt von dem angestrebten jährlichen Austausch des RICH Detektors und des MuCh Detektors (Muon Chambers). Dafür sind eine starre und stabile mechanische Konstruktion zusammen mit einem Überwachungssystem für die Spiegelausrichtung notwendig. Das Spiegelüberwachungssystem kombiniert zwei Methoden, die bereits in den COMPASS und HERA-B Experimenten genutzt werden und an die Geometrie des CBM-RICH Detektors angepasst wurden. Darüber hinaus wurde ein Korrekturzyklus entwickelt, der einen vorgabengemäßen Betrieb des Detektors sicherstellt, selbst bei falscher Ausrichtung der Spiegel. Diese Entwicklungen sind das Thema der vorliegenden Dissertation.

Die erste Methode ist die ‘Continuous Line Alignment Monitoring’ (CLAM) Methode. Sie kommt aus dem COMPASS Experiment und wird genutzt, um die Spiegelorientierung zu bestimmen. Sie benötigt eine spezifische Ausrüstung: Kameras mit guter Pixelauflösung, LEDs als Lichtquellen und ein Gitter aus retroreflektierendem Material. Das Prinzip der schnellen qualitativen Variante der Methode ist Folgendes. Falls angrenzende Spiegel zueinander verstellt sind, wird das reflektierte Gitter an den Spiegelkanten gebrochen

aussehen.

Außerdem kann die CLAM Methode genutzt werden, um Spiegeldrehungen quantitativ zu bestimmen. In diesem Fall ist eine vorherige Laborkalibration Voraussetzung. Durch die Kalibrierung werden Pixelverschiebungen mit gegebenen Spiegeldrehungen für jede einzelne Kachel verbunden. Diese Kalibrierung muss an allen Spiegelkacheln durchgeführt werden, damit eine vollständige Messung ermöglicht wird.

Die zweite Methode, die an den CBM-RICH Detektor angepasst wurde, benötigt Daten in der CbmRoot Software. Das Prinzip besteht darin, zwei Größen bezeichnet als ‘Cherenkov Abstand’ und ‘Cherenkov Winkel’ zu bestimmen. Dazu braucht man eine genügend große Anzahl von kumulierten Ringen, die auf einer einzelnen Spiegelkachel reflektiert wurden. Falls die Spiegelkachel nicht ausgerichtet ist, wird die Darstellung des ‘Cherenkov Abstandes’ als Funktion des ‘Cherenkov Winkels’ sinusförmig sein. Die Parameter der sinusförmigen Funktion können gefitted werden und stehen in direktem Verhältnis zu der Spiegeldrehung, was eine präzise Quantifizierung der Spiegeldrehung ermöglicht.

Die Leistungsfähigkeit dieser Methode wurde in Simulationen untersucht. Die Methode funktioniert für Drehungen einer Spiegelkachel um ihre horizontale Achse zwischen 0,3 und 14 mrad. Für eine vertikale Drehung des Spiegels, ergibt die Methode genaue Ergebnisse für falsche Spiegeljustierungen zwischen 0,4 und 15 mrad. Die Methode ist genauer für Spiegelkacheln, die sich im Zentrum der Spiegelwand befinden, als für Kacheln, die in dem äußeren Bereich der Spiegelwand liegen.

Als dritter Schritt wurde ein Korrekturzyklus für die Spiegeljustierung in der CbmRoot Software eingeführt, der gezielt für den CBM-RICH Detektor gestaltet wurde. Der Korrekturzyklus verwendet die Spiegeldrehungswerte aus den zwei vorgelegten Methoden, um die Extrapolation der Spuren auf die MAPMT Ebene zu korrigieren. So wird der Abstand zwischen der extrapolierten Spur und dem rekonstruierten Ring Zentrum verringert. Der Korrekturzyklus kann automatisch in der Rekonstruktion der Ereignisse in CbmRoot mitlaufen.

Der Korrekturzyklus wurde in Simulationen getestet. Die Spiegelkacheln wurden künstlich um beide Drehachsen mit einer Gaußschen Verteilung mit einer Standardabweichung von 1 mrad verstellt. Der typische Ring-Spur Abstand beträgt damit 0.47 cm, mit dem Korrekturzyklus läßt er sich auf 0.17 cm reduzieren, was nahe an dem idealen Fall von 0.14 cm liegt. Der Zyklus korrigiert damit auch die Matching Effizienz und die Elektronenidentifizierungseffizienz. Auch wenn die Standardabweichung der Gaußschen Verteilung auf 3 mrad erhöht wird, bleiben die Ergebnisse innerhalb der Spezifikationen, die in dem CBM-RICH Technical Design Report gefordert wurden.

# Contents

<b>1</b>	<b>State of the art physics of strong interactions</b>	<b>1</b>
1.1	Major achievements in particle physics . . . . .	1
1.1.1	From nuclear to particle physics . . . . .	1
1.1.2	Quark model . . . . .	2
1.1.3	Lepton family . . . . .	3
1.1.4	Four fundamental forces and their mediators . . . . .	4
1.1.5	Standard Model . . . . .	5
1.2	Investigation of the QCD phase diagram . . . . .	7
1.3	Heavy ion collisions . . . . .	11
1.3.1	Evolution of a Heavy Ion collision . . . . .	11
1.3.2	Lepton pairs . . . . .	13
1.4	Other probes to study the QGP . . . . .	17
1.4.1	Collective flow . . . . .	17
1.4.2	Fluctuations and correlations . . . . .	18
1.4.3	Charm production . . . . .	19
1.4.4	Strangeness . . . . .	20
1.4.5	Hypernuclei and strange objects . . . . .	21
<b>2</b>	<b>The FAIR facility and the CBM experiment</b>	<b>23</b>
2.1	FAIR Motivations . . . . .	23
2.2	Four pillars . . . . .	26
2.3	Compressed Baryonic Matter . . . . .	27
2.3.1	Dipole magnet . . . . .	30
2.3.2	Micro Vertex Detector . . . . .	30
2.3.3	Silicon Tracking System . . . . .	31
2.3.4	Ring Imaging Cherenkov . . . . .	32
2.3.5	Muon Chamber . . . . .	33
2.3.6	Transition Radiation Detector . . . . .	34
2.3.7	Time Of Flight . . . . .	36
2.3.8	Calorimeters . . . . .	37
2.3.9	Data Acquisition System . . . . .	39
<b>3</b>	<b>The RICH detector of CBM</b>	<b>41</b>
3.1	Principle of RICH detectors . . . . .	41
3.1.1	The Cherenkov effect . . . . .	41

3.1.2	Evolution of detectors relying on the Cherenkov effect . . . . .	44
3.1.3	Functioning principle of the CBM RICH detector . . . . .	46
3.2	Physics objectives and detector requirements of the CBM RICH detector .	48
3.2.1	Physics objectives . . . . .	48
3.2.2	Environmental conditions . . . . .	50
3.3	Detector design . . . . .	52
3.3.1	Detector geometry and mechanics . . . . .	53
3.3.2	Mirror wall . . . . .	55
3.3.3	Photon detector plane . . . . .	56
3.3.4	Readout chain and electronics . . . . .	59
3.3.5	RICH Software . . . . .	62
3.3.6	Real-size projects . . . . .	67
3.4	The importance of mirror alignment - Scope of this work . . . . .	70
<b>4</b>	<b>Determination of mirror rotations with hardware</b>	<b>73</b>
4.1	Principle of the method . . . . .	73
4.2	CBM RICH prototype in 2014 beam time at CERN . . . . .	75
4.2.1	Real size RICH prototype . . . . .	75
4.2.2	2014 beam time set-up at CERN PS/T9 beamline . . . . .	75
4.3	Results from beam time at CERN . . . . .	79
4.4	Mirror calibration for the CLAM method . . . . .	86
4.5	Application of the CLAM calibration on pictures taken at CERN . . . . .	91
<b>5</b>	<b>Quantification of mirror rotations with software</b>	<b>97</b>
5.1	Principle of the technique . . . . .	97
5.2	Implementation of misalignments in the RICH geometry . . . . .	99
5.3	Quantification of mirror rotation . . . . .	102
5.4	Performances of the technique . . . . .	104
5.4.1	Detection limits . . . . .	104
5.4.2	Performances in the inner and outer regions of the mirror wall . . .	106
<b>6</b>	<b>Correction cycle developed for the RICH software</b>	<b>111</b>
6.1	Correction cycle with the former RICH geometry . . . . .	111
6.1.1	Principle of the correction cycle . . . . .	111
6.1.2	Correction cycle for a single mirror tile . . . . .	114
6.2	Results with the RICH geometry v17a_1e . . . . .	119
6.2.1	Identical rotation of each mirror tile in the upper half of the mirror wall . . . . .	119
6.2.2	1 mrad Gaussian misalignment . . . . .	124
6.2.3	3 mrad Gaussian misalignment . . . . .	127
6.3	Improvements from the correction cycle on reconstruction efficiencies . . .	131
<b>7</b>	<b>Summary and outlook</b>	<b>135</b>
7.1	Summary . . . . .	135
7.2	Future developments to optimise the correction procedure . . . . .	137

<b>A</b>	<b>EPICS based control systems for the CBM RICH prototype</b>	<b>139</b>
A.1	Hardware installation . . . . .	139
A.2	Run TwinCAT on the windows machine . . . . .	141
A.2.1	Numerical control (local without PLC program and without EPICS)	141
A.2.2	TwinCAT with PLC program but without EPICS . . . . .	144
A.3	Linux with EPICS to run TwinCAT remotely . . . . .	147
A.3.1	In the case EPICS is not installed . . . . .	147
A.3.2	Run TwinCAT via EPICS . . . . .	147
A.4	Run high voltage via EPICS . . . . .	150
<b>B</b>	<b>Complements to Chapter 5</b>	<b>153</b>
B.1	Reconstruction of mirror rotation for a 0.1 mrad misalignment . . . . .	153
B.2	Calculation of mirror rotations with the software for mirror tile 0_8 . . . . .	154



# List of Figures

1.1	Meson and baryon octets . . . . .	3
1.2	Standard model of elementary particles . . . . .	6
1.3	QCD phase diagram . . . . .	7
1.4	Measurements of vector and axial-vector spectral functions in $\tau$ -decays and predicted consequences from chiral symmetry restoration . . . . .	9
1.5	Sketched heavy ion collision and definition of the reaction plane . . . . .	12
1.6	Sketched evolution of a heavy ion collision . . . . .	13
1.7	$e^-/e^+$ invariant-mass spectrum of Au+Au collisions at 25 AGeV . . . . .	14
1.8	Invariant mass spectra of dielectrons with selection cuts, before and after an additional cut on the transverse momentum was applied . . . . .	15
1.9	Energy dependence of the volume independent cumulant ratio of the net proton distribution . . . . .	19
1.10	Measured over expected $J/\Psi$ ratio versus number of participants in A+A collisions at various energies and experiments and $R_{AA}$ factor versus $N_{part}$ for different rapidity . . . . .	20
2.1	Current GSI and future FAIR facilities in Darmstadt . . . . .	24
2.2	Scheme of the GSI and future FAIR facilities . . . . .	25
2.3	3D view of the CBM building and scientific diversity among the CBM experiment . . . . .	27
2.4	Interaction rate at CBM and multiplicity times branching ratios for several probes of interest for the experiment . . . . .	28
2.5	Experimental set-up of the CBM experiment . . . . .	29
2.6	Latest CBM magnet design and cooling strategy . . . . .	30
2.7	The Micro-Vertex Detector of CBM. . . . .	31
2.8	Engineering view of the STS detector and reconstructed charges pions, kaons and protons in the $p_t$ - $y_{cm}$ plane . . . . .	32
2.9	MUCH detector and invariant mass spectra from muon pairs . . . . .	33
2.10	TRD detector and its performances with the RICH and ToF detectors . . . . .	35
2.11	ToF detector and particle identification histogram . . . . .	36
2.12	ECAL detector and invariant mass spectra of reconstructed photon pairs after background subtraction . . . . .	37
2.13	PSD detector and energy deposition distributions . . . . .	39
2.14	DAQ chain of the CBM experiment at SIS100 . . . . .	40
3.1	Cherenkov experimental set-up . . . . .	41

3.2	Illustration of the Cherenkov effect . . . . .	42
3.3	Different types of focusing RICH detectors . . . . .	45
3.4	Schematic baseline design and mechanical design of the PANDA barrel DIRC . . . . .	46
3.5	Combinatorial background for different pion suppression factors and invariant mass spectrum . . . . .	49
3.6	Momentum distributions for $\rho$ and $J/\Psi$ and transverse momentum distribution in dependence on rapidity for $J/\Psi$ . . . . .	49
3.7	Ring density on the photon detector planes . . . . .	50
3.8	Material budget of the RICH detector . . . . .	51
3.9	RICH detector structure . . . . .	52
3.10	Radius versus particle momentum distribution . . . . .	54
3.11	RICH mirror supporting structures . . . . .	54
3.12	Dimensions of the RICH mirror tiles . . . . .	55
3.13	Inner structure and pictures of the H12700 MAPMT . . . . .	57
3.15	Mounted DiRICH readout modules on a backplane connected to a photomultiplier . . . . .	60
3.16	DiRICH family . . . . .	60
3.17	Set-up used in a beam time at COSY . . . . .	61
3.18	Shielding box engineering drawings and magnetic field map inside the box . . . . .	62
3.19	RICH detector in the CATIA software . . . . .	63
3.20	RICH detector in the CbmRoot framework . . . . .	63
3.21	RICH old two-wing geometry . . . . .	64
3.22	Reconstruction process of the RICH software . . . . .	64
3.23	Simulated ring reconstruction and STS-RICH matching efficiencies . . . . .	65
3.24	Simulated electron identification efficiency and pion suppression factor . . . . .	66
3.25	Front view of the HADES RICH and close-up view of the mounted MAPMTs . . . . .	67
3.26	Rear view of the HADES RICH detector with electronics and cooling cables. . . . .	68
3.27	Detector test area and mCBM test set-up . . . . .	69
3.28	Simulated mRICH stations and radius versus momentum histogram . . . . .	69
3.29	Integrated rings in the case of mirror misalignment . . . . .	70
3.30	Ring reconstruction and STS-RICH matching efficiencies for a 5 mrad Gaussian misalignment . . . . .	71
4.1	Apparatus and principle of the CLAM method in the old two-wing geometry of the CBM RICH detector . . . . .	74
4.2	Technical drawing of the CBM-RICH prototype vessel . . . . .	75
4.3	Mounted mirror system inside the CBM-RICH prototype . . . . .	76
4.4	Mirror frame and readout system. . . . .	77
4.5	Definition of the rotation axes of one mirror tile to induce artificial misalignment . . . . .	77
4.6	CLAM equipment and reference picture. . . . .	79
4.7	Distributions of main ring parameters for an aligned mirror system . . . . .	80
4.8	Impact of mirror rotation seen by the CLAM method . . . . .	81
4.9	Distribution of main ring parameters for a 4 mrad rotation . . . . .	82

4.10	Event selection strategy obtained from a cut on the B axis histogram . . .	83
4.11	Event selection enhancement obtained from a cut on the A axis histogram	84
4.12	Integrated rings for different configuration of the mirror wall . . . . .	85
4.13	Reference and rotated CLAM pictures . . . . .	87
4.14	Subtracted and threshold CLAM pictures . . . . .	87
4.15	Measurement bands on the threshold picture . . . . .	88
4.16	Relation between band widths in pixel and vertical rotations in mrad on one measurement row . . . . .	88
4.17	Relation between the band widths and the horizontal and vertical rotations on all measurements rows and columns . . . . .	89
4.18	Relation between band widths in pixel and mirror rotations on all mea- surements rows and columns for the lower right mirror . . . . .	90
4.19	CERN pictures obtained after the initial mirror alignment, after a 4 mrad rotation around the vertical axis of the lower left mirror tile and after subtraction of the two pictures and application of a threshold . . . . .	91
4.20	Pictures obtained after the initial mirror alignment, after a 4 mrad rotation around the diagonal axis of the lower left mirror tile and after subtraction of the two upper pictures and application of a threshold . . . . .	94
4.21	Mirror wall after a diagonal rotation of the lower left tile, seen at CERN and in the laboratory . . . . .	95
5.1	Principle of the quantification technique developed by the HERA-B exper- iment. . . . .	97
5.2	Definitions of the horizontal and vertical mirror rotations in simulation . .	99
5.3	Illustration of the shift induced by mirror rotations appearing between the fitted ring centre and the extrapolated track hit . . . . .	100
5.4	Sinusoidal distributions obtained with the quantification technique . . . . .	102
5.5	Quantification technique for a rotation on both axes of one mirror tile simultaneously . . . . .	104
5.6	Minimal and maximal detected misalignments for a horizontal rotation of the mirror tile 5_3 . . . . .	105
5.7	Minimal and maximal detected misalignments for a vertical rotation of the mirror tile 5_3 . . . . .	105
5.8	Performances of the quantification technique for inner and outer mirrors and their locations on the photon sensor plane . . . . .	108
5.9	Difference between the applied and reconstructed mirror rotations obtained by the software technique for different types of mirror rotations . . . . .	109
6.1	Sketch of the correction method . . . . .	112
6.2	Correction cycle . . . . .	113
6.3	Influence of mirror rotations on the ring-track distance projected horizon- tally and vertically . . . . .	115
6.4	Corrections for central mirror tiles . . . . .	116
6.5	Performances of the correction cycle for an outer mirror tile . . . . .	118

6.6	Histograms of the mean distances between fitted ring centres and extrapolated track hits for the aligned mirror wall . . . . .	120
6.7	Histograms of the mean distances between fitted ring centres and extrapolated track hits for a rotation of all tiles of the upper mirror wall around the horizontal axis by -3 mrad and before the correction cycle was applied.	121
6.8	Histograms of the mean distances between fitted ring centres and extrapolated track hits for a rotation of all tiles of the upper mirror wall around the vertical axis by +3 mrad and before the correction cycle was applied. .	121
6.9	Histograms of the mean distances between fitted ring centres and extrapolated track hits for a rotation around the horizontal axis of all tiles of the upper mirror wall by -3 mrad, once the correction cycle has been applied. .	122
6.10	Histograms of the mean distances between fitted ring centres and extrapolated track hits for a rotation around the vertical axis of all tiles of the upper mirror wall by +3 mrad, once the correction cycle has been applied.	123
6.11	Impact of the ‘1 mrad Gaussian misalignment’ in the average ring-track distance distribution . . . . .	125
6.12	Results from the correction cycle for the ‘1 mrad Gaussian misalignment’ .	126
6.13	Comparison of the ring-track distance distribution over the complete photon sensor plane between the aligned case, before and after corrections are applied with a ‘1 mrad Gaussian misalignment’ geometry . . . . .	127
6.14	Impact of the ‘3 mrad Gaussian misalignment’ in the average ring-track distance distribution . . . . .	128
6.15	Results from the correction cycle for the ‘3 mrad Gaussian misalignment’ .	129
6.16	Comparison of the ring-track distance distribution over the complete photon sensor plane between the aligned case, before and after corrections are applied with a ‘3 mrad Gaussian misalignment’ geometry . . . . .	130
6.17	STS-RICH matching efficiency combined with ring finding efficiency, RICH electron identification efficiency and pion suppression factor for a ‘1 mrad Gaussian misalignment’ . . . . .	132
6.18	STS-RICH matching efficiency combined with the ring finding efficiency, RICH electron identification efficiency and pion suppression factor for a ‘3 mrad Gaussian misalignment’ . . . . .	133
A.1	Cabling of the IPC system. . . . .	139
A.2	Cabling of the Motors to the Beckhoff system. . . . .	140
A.3	Switch and High voltage connections . . . . .	140
A.4	TwinCAT software interface. . . . .	141
A.5	TwinCAT status in runtime mode and config mode . . . . .	141
A.6	Different modes in TwinCAT. . . . .	142
A.7	Searching for the IPC on the network in TwinCAT. . . . .	142
A.8	Reset the router connection on TwinCAT. . . . .	143
A.9	TwinCAT PLC graphical user interface. . . . .	144
A.10	Detailed view of the PLC program. . . . .	145
A.11	EPICS default set-up and switching to the edit mode . . . . .	148

A.12 EPICS editor view. . . . .	148
A.13 EPICS high voltage GUI. . . . .	151
B.1 Reconstructed misalignments for a 0.1 mrad rotation of the mirror tile around its horizontal and vertical axes . . . . .	153
B.2 Applied and reconstructed misalignments for horizontal and vertical rota- tions of the mirror tile 0_8 and the corresponding calculation errors . . . .	155



# List of Tables

1.1	The four fundamental forces . . . . .	5
1.2	Reconstruction efficiencies of $\omega$ and $\phi$ mesons and their respective signal to background ratios . . . . .	16
2.1	Predicted hyperon yields per week of operation in CBM . . . . .	28
3.1	Summary of the CBM-RICH detector main components . . . . .	53
3.2	Hamamatsu H12700 main specifications . . . . .	58
3.3	Comparison of efficiencies for different simulation inputs . . . . .	67
3.4	Comparison of efficiencies for different geometries . . . . .	72
4.1	Reference actuator values of different mirrors given in volts and applied for the initial alignment during the mirror calibration study . . . . .	86
4.2	Retrieved mirror rotations in the case of a vertical rotation of the lower left mirror . . . . .	92
4.3	Equations obtained from the pictures taken at CERN, once the image processing operations have been applied and the resulting threshold pictures have been fitted with a linear fit . . . . .	93
4.4	Retrieved mirror rotations in the case of a diagonal rotation of the lower left mirror . . . . .	94
A.1	Address ruling of the TwinCAT PLC system. . . . .	146



# Chapter 1

## State of the art physics of strong interactions

### 1.1 Major achievements in particle physics

#### 1.1.1 From nuclear to particle physics

Mankind has always been eager to understand its surrounding world. What are the predominant processes in nature, how do they function, what is matter made of, what lies behind the beauty of the universe ... ? To be able to give an objective interpretation to those questions, the introduction of standard fields of study as well as the establishment of basic rules had to be performed.

This triggered the emergence of several research activities such as philosophy, biology, chemistry, mathematics and also physics. The latter aims at the comprehension and explanation of nature and natural phenomena, incorporating and synthesizing them in models. One of its fields, called nuclear physics, focuses in particular on the structure of matter.

This field has allegedly started in ancient Greece during the 5th century BCE, with Leucippe, and later carried on by his disciple Democrite. Matter was defined as an aggregation of tiny grains, the atoms. Over two millennia later this assumption was taken over by Dalton, who published an essay in 1805 summarizing his experiments and laying the grounds of his atomic theory [1]. Chemists have thereafter tried to enumerate each existing atom. Their answers was summed up in a table in 1869, whose name comes from its creator: Mendeleïev.

The first real proof of the existence of atoms was given in 1895 by Crookes, who used an experiment with cold cathode tubes. Two years later its composition was completed by Thomson, who used Crookes' tubes and showed that the rays emitted by the cathode could be deflected when applying a magnetic field. He introduced the Thomson model, which considered atoms as a neutrally-charged entity, where the negative electrons revolve in a uniform positively-charged sphere [2]. A few years later followed a new model, postulated by Rutherford, who compared the nucleus to a solar system, where electrons are supposed to circle around the positively charged nucleus [3]. He used a scattering

experiment to show that most of the mass was concentrated in the core of the atom, the nucleus. However according to this model, the electrons must eventually crash on the surface of the nucleus. In 1913 Bohr completed this model, using his results from hydrogen atom experiments, claiming that electrons revolve on stable orbitals, with given energy level, on which electrons can transfer [4, 5, 6]. With the discovery of the neutron in 1932, Chadwick refined the nucleus structure, finalizing the classical atomic model [7, 8].

Nevertheless this classical vision does not account for all observed phenomena and a more abstract description has been later given by Heisenberg and Schrödinger, using a quantum-based definition and introducing occupation probabilities of electrons in the atom.

With the improvements of the detection technology, new particles were discovered afterwards. First the muon (member of the lepton family, the light-weight particles) in 1936 and later the pi-mesons (middle-weight particles) in 1947 were discovered with experiments conducted on cosmic rays.

In Dirac's study to establish a relativistic quantum mechanics theory, he formulated the Dirac equation [9]:

$$(i\gamma^\mu \delta_\mu - m) \cdot \Psi(x) = 0 \quad (1.1)$$

Where  $\mu$  is the implied summation parameter,  $\gamma^\mu$  is the corresponding gamma matrix,  $\delta_\mu$  is the covariant derivative and  $\Psi$  is the wave function.

Strikingly, not only did this equation have positive energy solutions, it also had negative ones.

$$E = \pm \sqrt{p^2 \cdot c^2 + m^2 \cdot c^4} \quad (1.2)$$

This opened the door to a new kind of particles, the antiparticles and it proved right in 1932, with the discovery of the positron by Anderson, using a cloud chamber. In accordance with these new notations, the constituents of the nucleus were declared members of the hadrons (strongly interacting particles).

From around 1950 on, an increasing number of new hadron particles were found by several experiments, such as the neutral and positive kaons in 1947 and 1949, respectively, and later the  $\rho$ ,  $\eta$ ,  $\omega$  and  $\phi$  mesons as well. At the same time, new baryons (heavy-weight particles) like the  $\Lambda$ ,  $\Sigma$  and  $\Xi$  were discovered.

This huge number of new particles puzzled the physics community, who had no tools to arrange all the discovered particles in a logical way. Until Gell-Mann addressed this problem.

### 1.1.2 Quark model

In 1961, Gell-Mann established the Eightfold Way, a new theory organizing the hadrons into mathematical shapes, on which particles are placed based on their charge and strangeness number. Particles were organised in so called hadron multiplets, such as the octets

sketched in Figure 1.1. Just like the periodic table in chemistry, these multiplets classify all known particles in physics. This theory was confirmed, when the baryon decuplet predicted the existence of the Omega minus particle ( $\Omega^-$ ), as well as its main characteristics, which was discovered in 1964. The Eightfold Way was a major milestone in particle physics, even though some physicists remained sceptical at that time [10].

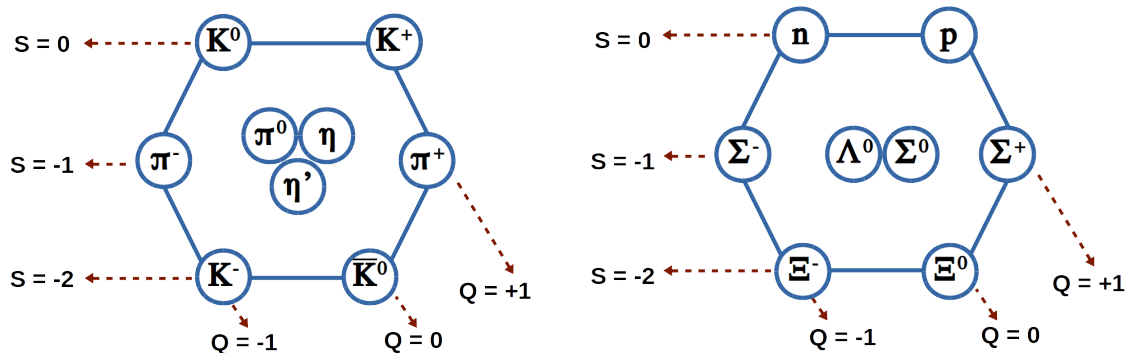


Figure 1.1: Meson (left) and baryon (right) octets. They gather the lightest mesons and baryons on a hexagonal shape. The hadrons are classified according to their strangeness number in the horizontal direction and their charge in the diagonal direction (brown arrows).

Gell-Mann and Zweig went furthermore deeper in the understanding of the hadrons constitution and postulated independently in 1964 the existence of quarks, elementary fermionic constituents [11, 12]. They theorised the existence of three entities: the ‘*up*’, ‘*down*’ and ‘*strange*’ quarks. Moreover, these particles have particular behaviours. They cannot be observed in a free form, a phenomenon called confinement, and they carry an additional degree of freedom, referred to as *colour* [13]. Each quark carries a single colour, ‘*red*’, ‘*green*’, or ‘*blue*’. This property introduces a restriction in hadron composition, as any hadron has to either display a combination of colour and anti-colour or a combination of all three colours or anti-colours. According to colour theory these combinations are considered as ‘*white*’ and seem to be prerequisite to form a stable hadron.

In 1974, the  $J/\Psi$  ( $c\bar{c}$ ) particle was discovered by Ting’s and Richter’s groups independently at Brookhaven [14] and SLAC [15], followed in 1977 by the  $\Upsilon$  ( $b\bar{b}$ ) at Fermilab [16]. They are bound state of ‘*charm*’ and ‘*bottom*’ quarks. The last bound state made of the ‘*top*’ quark is not generated in the laboratory, due to the high top mass. Before forming a bound state, the  $t$  quarks decay via the electroweak interaction.

Quarks are nowadays considered as the smallest existing and so far discovered constituents of matter.

### 1.1.3 Lepton family

First hints for the existence of neutrinos appeared in the year 1930, while studying the radioactive beta decay.

$${}^A_Z X \rightarrow {}^A_{Z+1} X' + e^- \quad (1.3)$$

It was found, that the energy of the outgoing electron varies when the experiment is

repeated, although when considering the conservation of energy it should not be the case. While some physicists argued at that time the veracity of the conservation of energy, others (including Pauli) suggested that the emission of a third particle was the reason of this phenomenon.



Experiments for instance on pion and muon decays also suggested the existence of a neutral and very low mass particle [17, 18]. The existence of the neutrino and its anti-particle, the antineutrino, was finally experimentally confirmed in 1953 by Reines and Cowan with the reversed beta decay reaction [19].

Following this experiment a new quantum number, called lepton number, was introduced to explain whether a decay involving leptons is allowed or not. To each known leptons, the electron, muon and tau, a corresponding neutrino was introduced.

#### 1.1.4 Four fundamental forces and their mediators

The four known fundamental forces in nature are the gravitational, the electromagnetic, the weak and the strong forces. They are summarised in Table 1.1. To act on matter, these forces require force carriers, called mediators, which are defined in each physical theory, where the forces were introduced.

The mediator of the electromagnetic interaction, the photon, was the first to be discovered and extensively studied. In 1900 Planck proposed at first that the electromagnetic radiation was quantified, which would solve the ultraviolet catastrophe [20]. He argued that light is emitted in small quanta of energies, illustrated in the following equation:

$$E = h\nu \quad (1.5)$$

$E$  stands for the energy of the photon,  $h$  is the Planck constant and  $\nu$  the frequency of the photon.

In 1905 Einstein adapted this idea to explain the photoelectric effect, which accounts for the pull-off of electrons in a metal at precise energy quanta [21]. Although his theory met quite a hostile opinion, it always proved to be right in the various experiments, which were subsequently realised. In 1923, Compton and Debye yielded independently a nuanced picture of light, as we know it today [22]. From their experiments, light can be seen as an electromagnetic radiation and as a particle of zero rest mass. The Compton effect gave birth to the concept of wave-particle duality.

In order to explain the stability of the nucleus, the strong interaction force was introduced. The exchange particle of this force is named gluon. It binds quarks together in nuclei and more generally speaking in hadrons. The underlying theory characterizing the interaction between quarks and gluons is called quantum chromodynamics (QCD). First traces of gluons were revealed by the PLUTO detector in three-jet events resulting from the  $\Upsilon(9.46)$  resonance in 1978 at DORIS in the DESY accelerator facility [23]. It was confirmed in 1979 by the PLUTO, MARK-J and TASSO experiments at PETRA in

Interaction	Theory	Mediator	Particles coupling to the interaction	Range (m)	Relative strength
<b>Electromagnetism</b>	Quantum electrodynamics	Photon	All electromagnetically charged particles	$\infty$	$\sim 10^{36}$
<b>Strong</b>	Quantum chromodynamics	Gluon	Quarks and gluons	$10^{-15}$	$\sim 10^{38}$
<b>Weak</b>	Electroweak theory	$W^+$ , $W^-$ , $Z^0$	Quarks and leptons	$10^{-18}$	$\sim 10^{25}$
<b>Gravitation</b>	General relativity	Graviton	All massive particles	$\infty$	1

Table 1.1: The four known fundamental forces and their main properties.

three-jet events due to gluon bremsstrahlung in  $e^-/e^+$  collisions [24, 25, 26].

The weak force has multiple force carriers, namely the  $W^+$ ,  $W^-$  and  $Z^0$  bosons, also called intermediate vector bosons. They mediate the weak interaction and are described by the electroweak theory, developed by Weinberg, Glashow and Salam. First hints of weak neutral currents were shown in the Gargamelle bubble chamber at CERN in 1973. The particles were finally confirmed in 1983 in the SPS at CERN by the UA1 and UA2 experiments [27, 28, 29].

In Einstein's general theory of relativity, the gravitational force is introduced. This force is not included in the standard model of elementary particles, as it cannot be formulated as quantum field theory. The mediator of gravity is named graviton. So far its existence is still controversial, although first observation of gravitational waves have been realised and made public in 2016 by the LIGO and Virgo collaborations [30].

### 1.1.5 Standard Model

To finalise the classical picture of particle physics, a last particle has to be included, the Higgs scalar boson. This particle was discovered in 2012 at CERN by the CMS and ATLAS experiments [31, 32]. The Higgs boson is responsible for the mechanism giving mass to particles.

The theory classifying all known elementary particles, while incorporating three of the four known fundamental forces, gravitation being left aside, is the Standard Model. It is summarised in Figure 1.2.

This model describes elementary components of matter and stands as the reference for particle physicists. It is though not considered as complete, as it does not incorporate all phenomena, such as the theory of gravitation or dark matter particle candidates. Figure 1.2 shows in total 18 particles. To complete this picture of particle physics, it can

be added, that all quarks come in three different colours, that there are six antileptons and six antiquarks, each carrying one of three anticolours and that gluons come in eight different colour combinations. Thus 61 particles are in total counted and supposedly held as elementary particles. Some have argued, that at least some of those particles must be composite of more elementary particles [10].

Nevertheless, the standard model remains a solid ground, on which more exotic theories can be built.

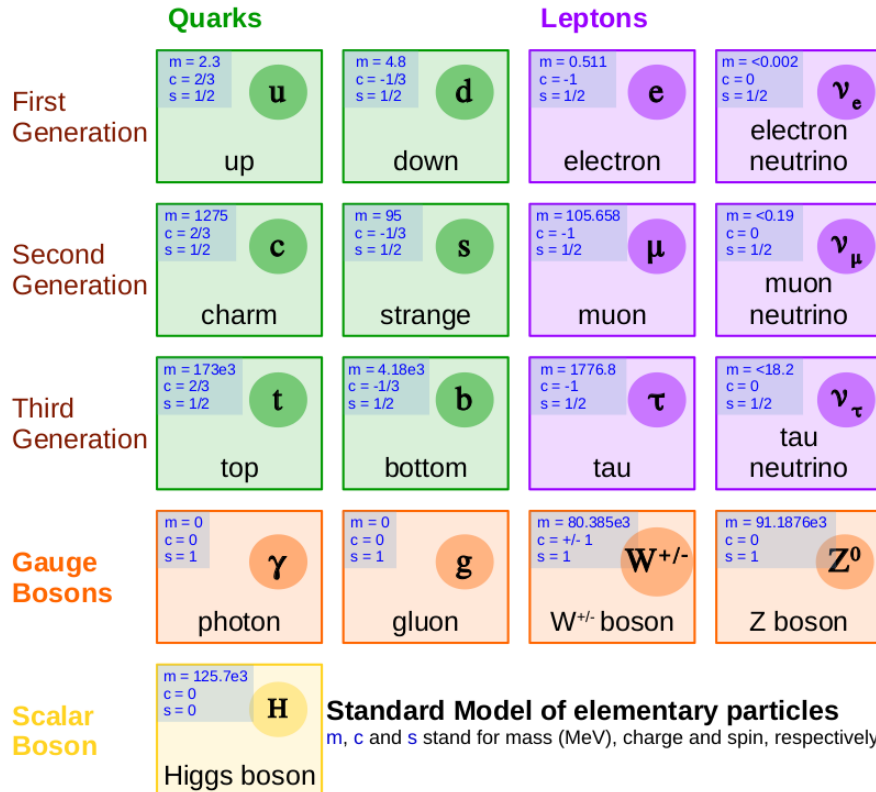


Figure 1.2: Standard model of elementary particles. It includes three generations of quarks (in green) and leptons (in purple), the gauge bosons (in orange) and the scalar Higgs boson (yellow). Masses (m) are indicated in MeV/c<sup>2</sup>, charges in units of the absolute value of the electron charge. In total 61 particles can be counted, when considering colour combinations and antiparticles.

## 1.2 Investigation of the QCD phase diagram

The Compressed Baryonic Matter experiment (CBM), presented in Section 2.3, aims at the exploration of the QCD phase diagram. This section will describe the phase diagram, as well as its importance for the physics of the strong interaction.

A tool used to characterise matter and its possible phases is a phase diagram. The different regions in the diagram correspond to different external conditions applied to the studied system. In the particular case of QCD, the system is made of quarks and gluons. The first phase diagram of QCD was proposed in 1975 [33]. Cabibbo and Parisi proposed in their paper a plot summing up the phases of quark matter, in a diagram of temperature versus baryon density. At that time, hadronic matter was thought to be either confined, or unconfined, with a transition boundary in between.

Figure 1.3 represents the current conjectured QCD phase diagram of strongly interacting matter, showing temperature  $T$  versus baryon chemical potential  $\mu_B$  [34]. Compared to the early version, it exhibits a more complex structure of the possible phases of matter, with the expected boundaries between them. However it is still a rather theoretical picture with little experimental information.

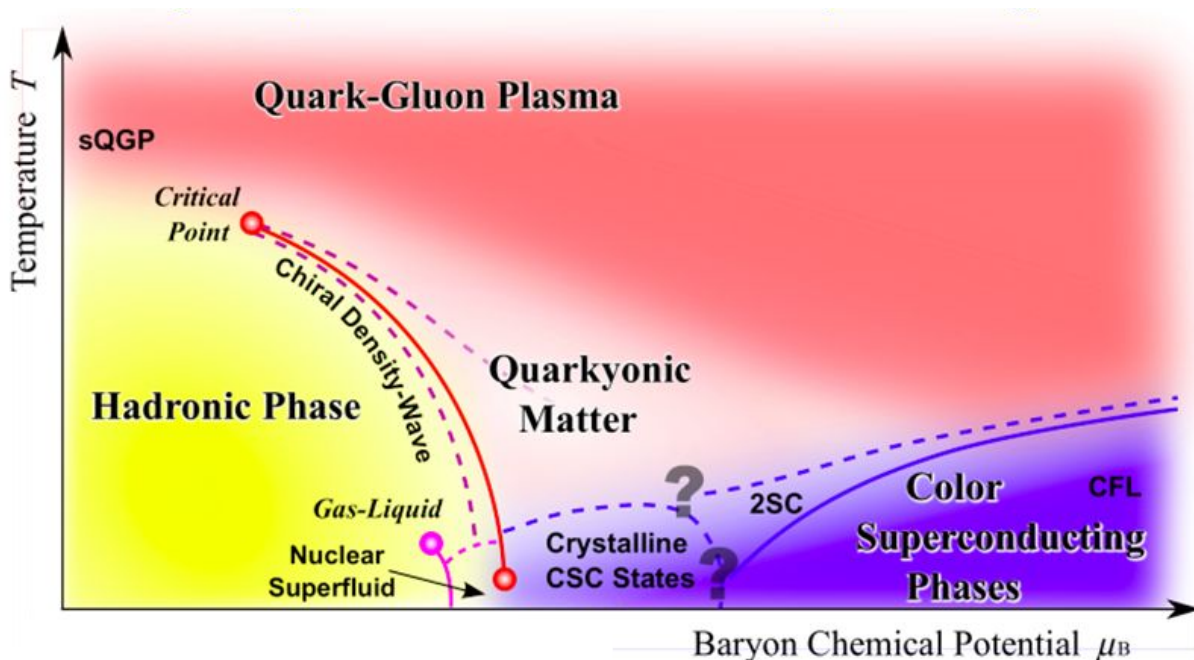


Figure 1.3: Sketch of the conjectured QCD phase diagram of strongly interacting matter. Figure taken from [34].

Many regions can be identified in this diagram. First, in the region of low baryon densities and low temperatures, cold nuclear matter is in a hadronised state, which consists of quarks and gluons bound together and forming hadrons. In these conditions, the quarks are confined in the hadrons and the number of particles and antiparticles is supposed to be almost the same.

Through an increase in the temperature, hadrons start melting and quarks and gluons behave quasi-freely in a quark-gluon plasma (QGP) phase, forming a deconfined state.

Intuitively, hadrons can be seen as bags containing quarks and gluons. Deconfinement is the point at which the external conditions of temperature and baryon density reach values, such that the ‘hadron bags’ start overlapping and become permeable. In terms of the partition function of the system, when the temperature reaches a threshold value, also called Hagedorn temperature, thermodynamic parameters of the system like the pressure and the energy density start diverging [35].

Experiments at the Large Hadron Collider (LHC) and the Relativistic Heavy Ion Collider (RHIC) are exploring the low baryon density and high temperature region in the QCD phase diagram, using high energy heavy-ion collisions (see Section 1.3.1) [36, 37, 38]. The QGP and its final hadronic state can be observed, via the measurement of the produced hadrons, leptons and photons, along with their phase space distributions. The transition from QGP to hadrons is what happened a few microseconds after the big bang. At low density, calculations show that the phase transition should be a crossover from hadronic to partonic matter [39].

The hadronisation temperature, also called freeze-out temperature, was determined at LHC energies to be  $T = 156 \text{ MeV}/c$  at  $\mu_B = 0 \text{ MeV}/c$  [40]. Alternatively, using a thermal model from fluctuation observables, a freeze-out temperature of  $T = 161 \pm 4 \text{ MeV}/c$  at  $\mu_B = 0.8_{-0.6}^{+1.2} \text{ MeV}/c$  was extracted [41, 42]. These values coincide with the predictions from Lattice QCD calculations, for which the critical temperature is calculated to be  $T = 165 \pm 8 \text{ MeV}/c$  at  $\mu_B = 0 \text{ MeV}/c$  [43, 44].

A critical point is expected to appear at a slightly lower freeze out temperature, but at higher baryon chemical potential. This is under investigation by the STAR experiment at RHIC [45] as well as the NA61 collaboration at CERN-SPS [46].

In a region of even larger baryon chemical potential, the nature of the transition between the hadronic and hadronic gas phase is supposed to be first order [44, 47, 48].

Along with the deconfinement phase transition, chiral symmetry breaking is taking place. A famous example of spontaneous symmetry breaking is the Mexican hat potential, where the potential  $V$  is plotted versus  $\Phi$ . This potential is symmetric with respect to its vacuum state at  $\Phi = 0$ , however the ground state is not at  $\Phi = 0$ . A system exhibiting this potential, is unstable at  $\Phi = 0$  and reaches a stable position for  $\Phi > 0$ . However, if referring to this new ground state at  $\Phi > 0$ , the potential becomes asymmetric. A similar process of spontaneous symmetry breaking happens in QCD with the chiral symmetry, when matter hadronises.

An evidence of chiral symmetry breaking can be seen in the generation of hadron masses. In the example of the proton, present in each atomic nucleus, the sum of its bare valence quarks equals to:  $2 * m_u + m_d = 9.4 \text{ MeV}/c$ , although the proton mass has been measured to be  $938 \text{ MeV}/c$ . This excess mass comes from the chiral symmetry breaking, related to the binding energy of QCD. Another illustration of chiral symmetry breaking is given in Figure 1.4. The spectral functions of the chiral partners, the  $\rho$  and  $a_1$  mesons, are depicted in the  $\tau$ -lepton decay [49]. Those are results obtained from the ALEPH [50]

and OPAL experiments. When chiral symmetry is restored, the spectral functions of  $\rho$  and  $a_1$  should be the same. On the right side, potential scenarios are illustrated for chiral symmetry restoration. The two extreme scenarios are the dropping mass and the melting resonances [51]. In both cases the spectral functions are the same in a system where chiral symmetry is restored.

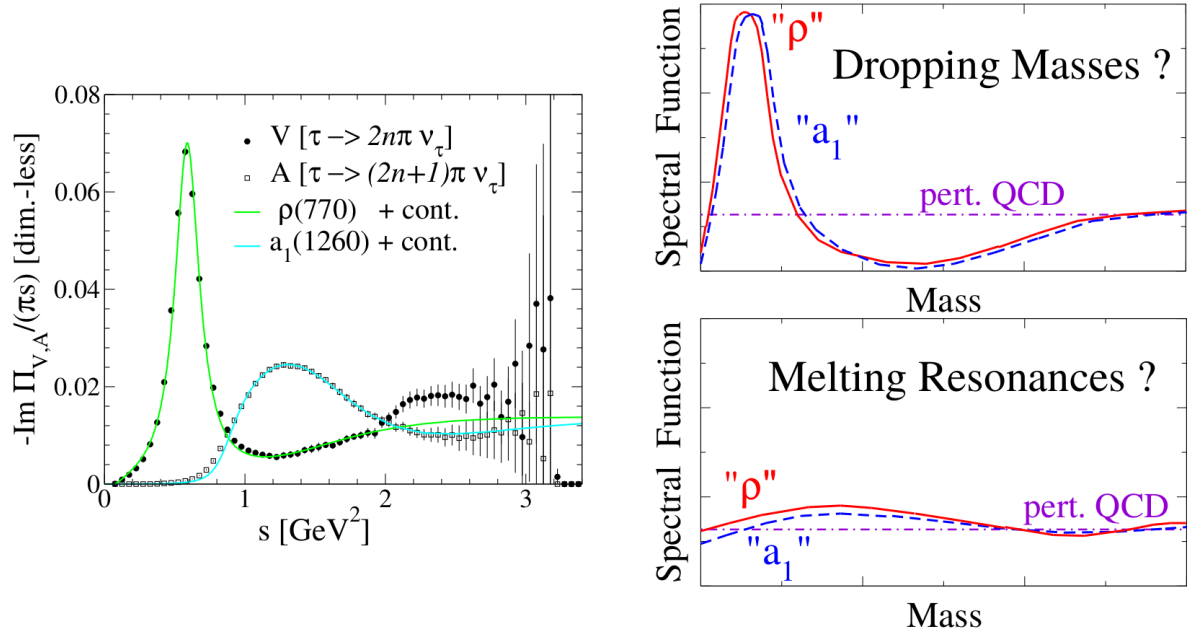


Figure 1.4: Left: measurements of vector and axial-vector spectral functions in  $\tau$ -decays. The coloured lines represent model fits from the spectral functions of  $\rho$  and  $a_1$ . Right: predicted consequences from chiral symmetry restoration. Figures taken from [49].

In addition to the phases described before, a new phase, the so called quarkyonic phase might exist. This phase would consist of baryonic matter with the properties of deconfined and chirally symmetric matter [52, 53]. If quarkyonic matter were to be discovered the critical endpoint would be considered as a triple point [54].

To explore in detail the phase transition in the region of moderate temperature and high baryon chemical potential of the QCD phase diagram, new projects are planned. The NICA project at JINR, as well as the CBM experiment at FAIR are being designed [55, 56].

At very high densities and low temperatures the Colour Flavor Lock (CFL) phase is expected, which corresponds to a colour superconducting phase. Those conditions could be met in the core of neutron stars [57].

Many questions can be raised concerning the QCD phase diagram, especially in the region of the phase transition at moderate temperature and high baryon chemical potential, which are of particular interest to the CBM experiment (see Section 2.3). Some of them can be addressed experimentally by the SIS100 accelerator set-up, which will be built at the Facility for Antiproton and Ion Research facility (FAIR) (see Section 2.1). The main themes tackled are [49, 56]:

- In the region of high net-baryon densities
  - What is the equation of state of QCD matter at high net-baryon densities?
  - What are the relevant degrees of freedom near the deconfinement phase and at high net-baryon densities?
- In the phase transition region
  - Is there a phase transition from quark-gluon plasma to hadronic matter, or a region of phase coexistence?
  - How are the properties of hadrons affected in dense baryonic matter?
  - Are there indications of chiral symmetry restoration and is it possible to detect evidence of this process?
- In producing heavier particles or states
  - Do exotic QCD phases exist?
  - Does strange matter exist in the form of multi-strange objects?
  - How is charm produced at threshold beam energies and how does it propagate in QCD matter?

The two following sections will present major probes on which the CBM experiment will focus to obtain a better understanding of the properties of matter in the high net-baryon density region of the QCD phase diagram.

## 1.3 Heavy ion collisions

### 1.3.1 Evolution of a Heavy Ion collision

To study elementary constituents of matter and explore the QCD phase diagram, particle accelerators are used. They accelerate charged particles using electromagnetic fields. These particle beams are directed towards another and collide, hence producing new particles, which are measured and analysed in experiment to characterise the created matter. Depending on how particles interact, two types of collisions are distinguished:

- Fixed target experiment: An accelerated beam interacts with a fixed target, which consists in a fixed thin foil of matter suited for the experiment. The target is placed at the end of an extraction line or also inside the accelerator.
- Collider experiment: Two beams of particles or nuclei collide with each other. Mostly these experiments take place at ring colliders, such that the beams go in opposite directions using the same, or two different beam pipes. This process greatly increases the collision energy, for example up to 13 TeV in the second run of LHC.

Whereas the first generation of accelerators used static high voltage cavities to accelerate the charged ions inside the beam-line, the development of dynamic fields in the acceleration cavities allowed the use of electrodynamic particle accelerators [58]. They are employing oscillating radio frequency fields to bring the acceleration cavities to resonance. This system can be used for linear as well as circular accelerators, requiring magnetic fields in between cavities to bend particles in the case of circular accelerator.

Once accelerated, particles can be guided towards multiple lines of experiments with the use of magnets. This allows multiple experiments to share the same beam produced in an accelerator facility and work alternately with it.

Figure 1.5 sketches the collision of two nuclei (labelled 1 and 2 in the figure) moving along the beam axis. It either illustrates the case of a collider, or of a fixed target in the centre of mass frame. In the interaction region each nucleus gets stripped of nucleons, called participants, while the nucleons carrying on their paths are called spectators.

To characterise the centrality of the collisions, an impact parameter has been introduced, being defined as the vector between the nuclei centres and perpendicular to the beam axis. If the nuclei completely overlap, the collision is called head-on and the impact parameter is zero. In the other cases the impact parameter represents how central (or peripheral) the studied collision is.

Calculating the impact parameter, as well as reconstructing the reaction plane are two essential tasks in heavy ion collisions, in order to characterise the overall collision geometry. In the case of the CBM experiment, these tasks are done by the PSD detector (see Section 2.3.8).

After a nuclei collision has happened, one needs to analyse, whether a state of matter was produced and if so, to be able to characterise it. In particular one looks for signs of a system-like behaviour, which would be a first hint to support that a QGP has been created.

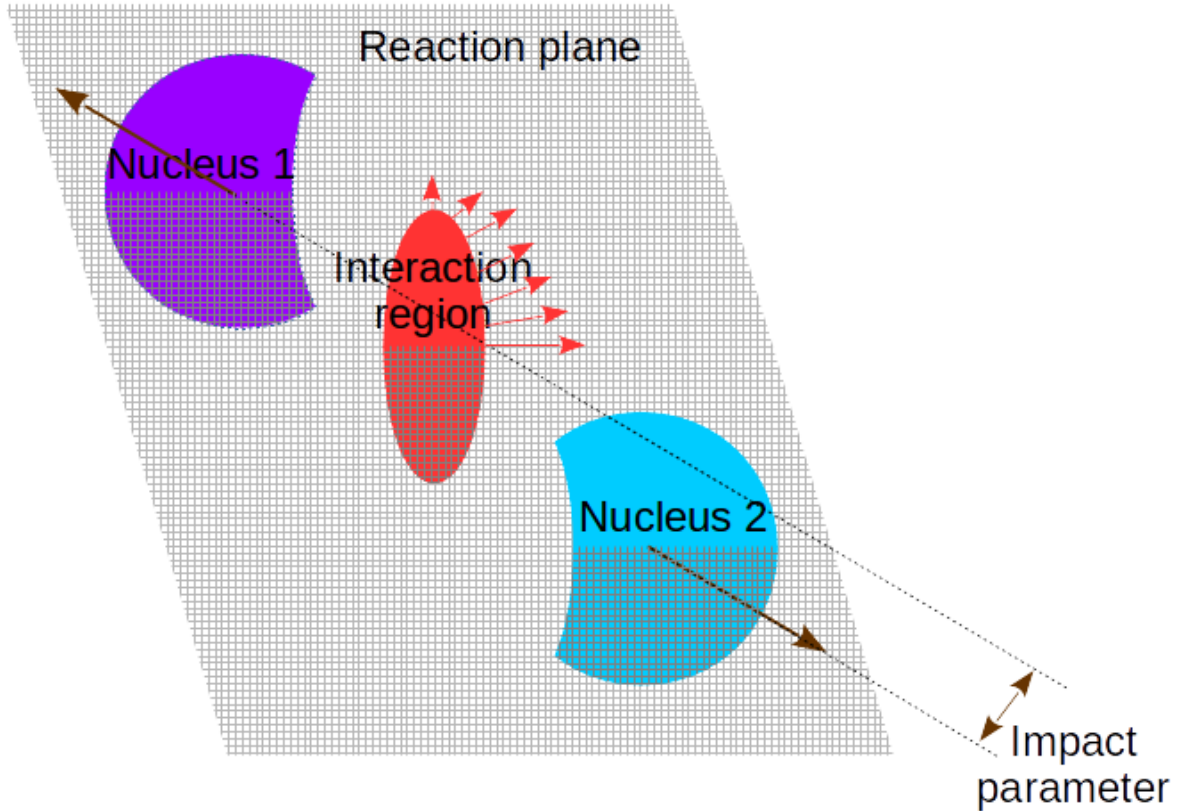


Figure 1.5: Sketch of a heavy ion collision. Two nuclei (labelled 1 and 2) collide after acceleration and leave each participant in the interaction region. In each collisions an impact parameter and a reaction plane can be reconstructed. The red arrows around the interaction region illustrate the elliptic flow generated in the collision and were only represented in the upper right corner, for better clarity.

To address this question, an observable called collectivity (see Section 1.4.1) was introduced, which serves for the analysis and investigation of the pressure or equation of state in the created matter. The asymmetry in the interaction region translates to an anisotropy in space-momentum, due to the pressure difference in the system (illustrated as red arrows on Figure 1.5). The underlying effects of the anisotropy in pressure come from two geometrical factors [59]. The velocity of the emitted particles in-plane should be greater than the one from particles created outside of the reaction plane. And the number of created particles should be bigger in-plane than out of plane. The collective phenomenon at the source of these space-momentum correlations, is called elliptic flow (see Section 1.4.1). Furthermore, the magnitude of the elliptic flow depends on the centrality and can be used to measure the pressures which were created during the collision.

In addition to the elliptic flow, one can look at the size, shape and homogeneity regions of the created system [59].

Figure 1.6 illustrates the different collision stages from a heavy ion collision. Two nuclei are in a first step approaching and look like flat objects, due to the velocities at which the nuclei are moving and thus the length contraction. During the collision phase,

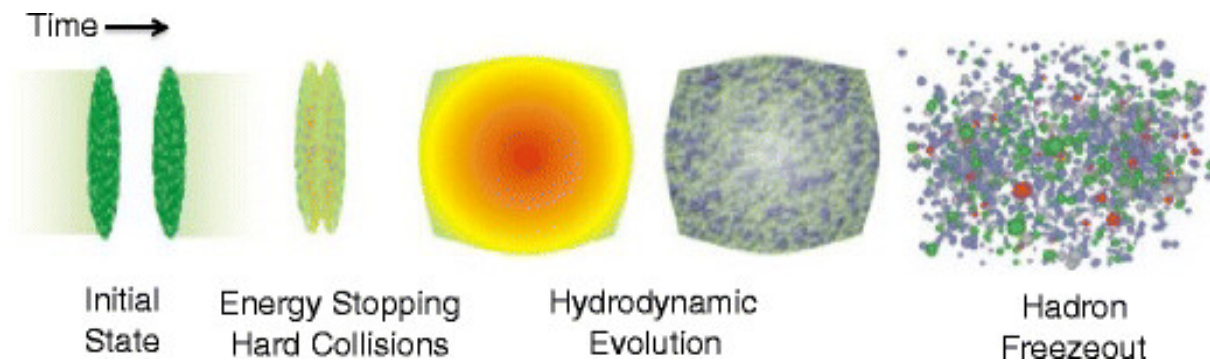


Figure 1.6: Evolution in a heavy ion collision sketched for high energy collisions. After the initial collision, a hydrodynamical expansion of the system takes place. This process is followed by hadronisation at freeze-out temperature. Figure taken from [59].

participants from each nucleus start colliding with each other with an energy coming from the accelerated nuclei.

In case a thermalised system has been formed, quarks and gluons generated by these first interactions keep colliding, potentially forming a thermalised system. In this so called fireball, deconfinement is thought to happen. Hydrodynamical models can reproduce the evolution of the system.

After further expansion and cooling down, hadronisation will occur at the so called freeze-out temperature. At this stage hadrons and mesons are created and emitted into the detectors. The chemical composition of the hadron gas is fixed but elastic collisions might still happen on the hadrons way to the detectors.

### 1.3.2 Lepton pairs

The CBM Ring Imaging CHerenkov (RICH) detector (see Section 3.3) is built in order to measure dielectrons. They are of particular interest to characterise the matter created in heavy ion collisions.

Real and virtual photons are emitted throughout the full evolution process of heavy ion collisions (Figure 1.6). Due to their penetrating nature, photons and dielectrons or dimuons leave the created fireball undistorted. The information carried by the lepton pairs is not altered by the strong interaction, thus the leptons reach the detector with negligible final-state interactions.

That is why a dilepton invariant-mass spectrum is a useful observable, revealing in-medium spectral functions of hadrons in the dense and hot matter, as well as measuring the temperature of the fireball [60].

The identification of these probes is however complicated. First, they are produced at a quite low multiplicity, due to the relatively low temperature of the plasma produced in ultrarelativistic nuclear collisions ( $T$  ranges from  $\sim 200$ - $300$  MeV/c, up to  $\sim 500$ - $800$  MeV/c [61]). Thus dileptons from the created plasma are often buried under a large background.

Considering the case of dielectrons, the relevant electrons stemming from the hot and dense matter are overwhelmed by electron pairs coming from gamma conversions in the

target and from Dalitz decays of  $\pi^0$  and  $\eta$  [56].

Another factor limiting the identification of electron pairs is the misidentification of  $\pi$ , due to the performances of the detectors involved with the task.

Figure 1.7 shows a simulated invariant mass spectrum of dielectrons, with the different sources and no background. It displays three main mass regions, which will be probed via dilepton conversions. The first two regions will be reached with the SIS100 accelerator set-up at FAIR, while the high-mass region will be achieved at the SIS300 energies.

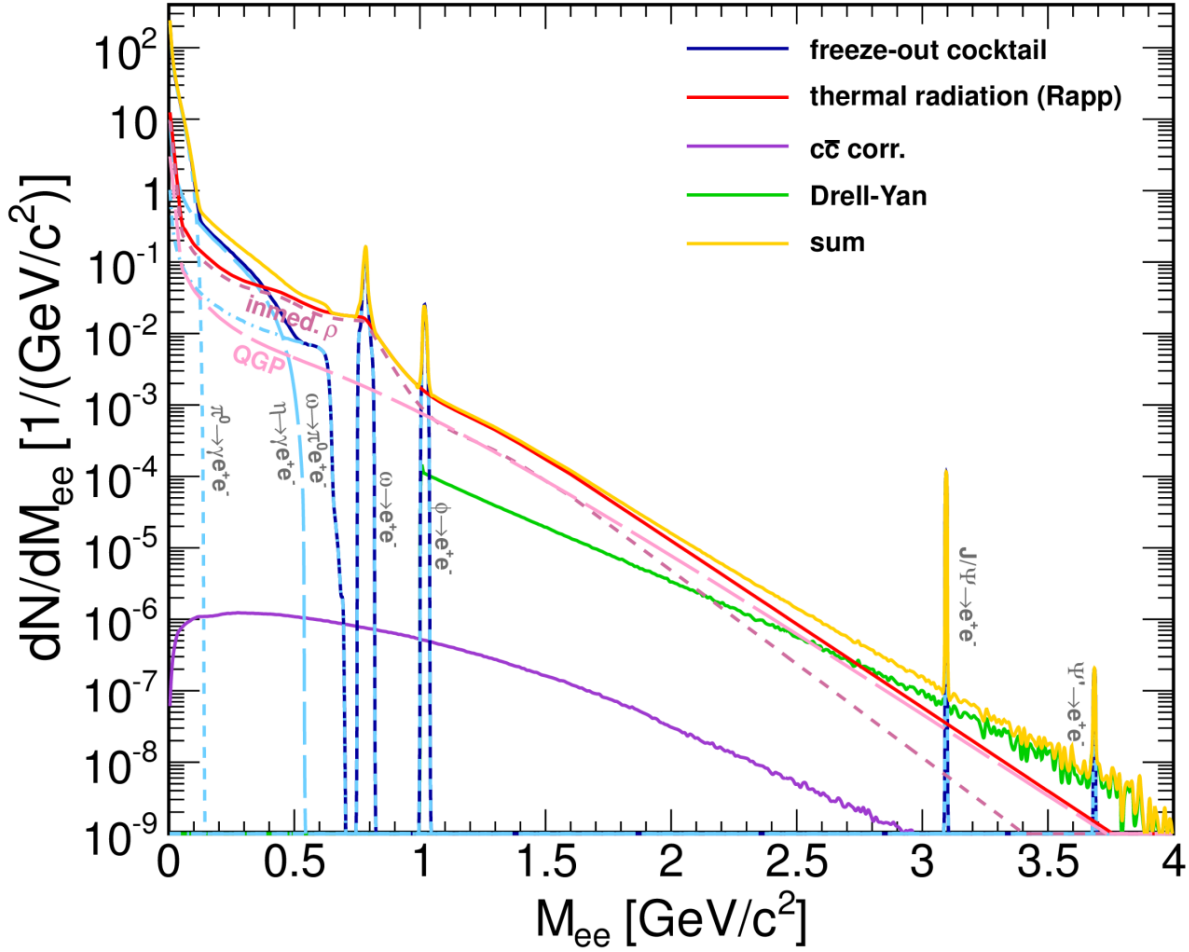


Figure 1.7:  $e^-/e^+$  invariant-mass spectrum of Au+Au collisions at 25 AGeV, where no background but only sources are simulated. Several mass regions can be identified on the plot, corresponding to different hadronic contributions (see text for details). Results are obtained from theoretical model calculations [62]. Figure taken from [63].

In the low-mass region ( $m_{e^-e^+} \leq 1 \text{ GeV}/c^2$ ), the main contributions come from  $\pi^0$ ,  $\eta$ ,  $\rho$ ,  $\omega$  and  $\phi$ . In particular, this region will be used to probe the  $\rho$  spectral function [56]. The  $\rho$  spectral function might give hints to chiral symmetry restoration via the  $\rho$ - $a_1$  chiral mixing (Figure 1.4).

The intermediate-mass region ( $1 \text{ GeV}/c^2 \leq m_{e^-e^+} \leq 3 \text{ GeV}/c^2$ ) is expected to give access to the fireball temperature, which is directly correlated with the slope of the spectrum. The intermediate-mass region measurement might also provide some insights to the landmarks of the QCD phase diagram, such as the measurement of a critical endpoint, a

quarkyonic phase, or the onset of deconfinement, as additional radiation is expected to show at these landmarks [64].

The high-mass region ( $m_{e^-e^+} \geq 3 \text{ GeV}/c^2$ ) can be used to investigate the charm quark propagation among hadrons, using for example the  $J/\Psi$  dielectron decay-channel.

For a high quality dielectron measurement, the aim is to reach a signal to background (S/B) ratio of about 1/100 in the  $\rho$  mass region. Thus, to hope measuring these signals with accuracy, it is necessary to overcome the low cross-sections, the small decay probabilities as well as the high background.

Figure 1.8 shows simulated invariant mass spectra for dielectrons using the CbmRoot framework. The simulation was done with 1 million central Au+Au collisions at 8 AGeV energy, with a 25  $\mu\text{m}$  target and background from UrQMD.  $\omega$ ,  $\phi$  and in medium  $\rho$  signals were added with the PLUTO generator.

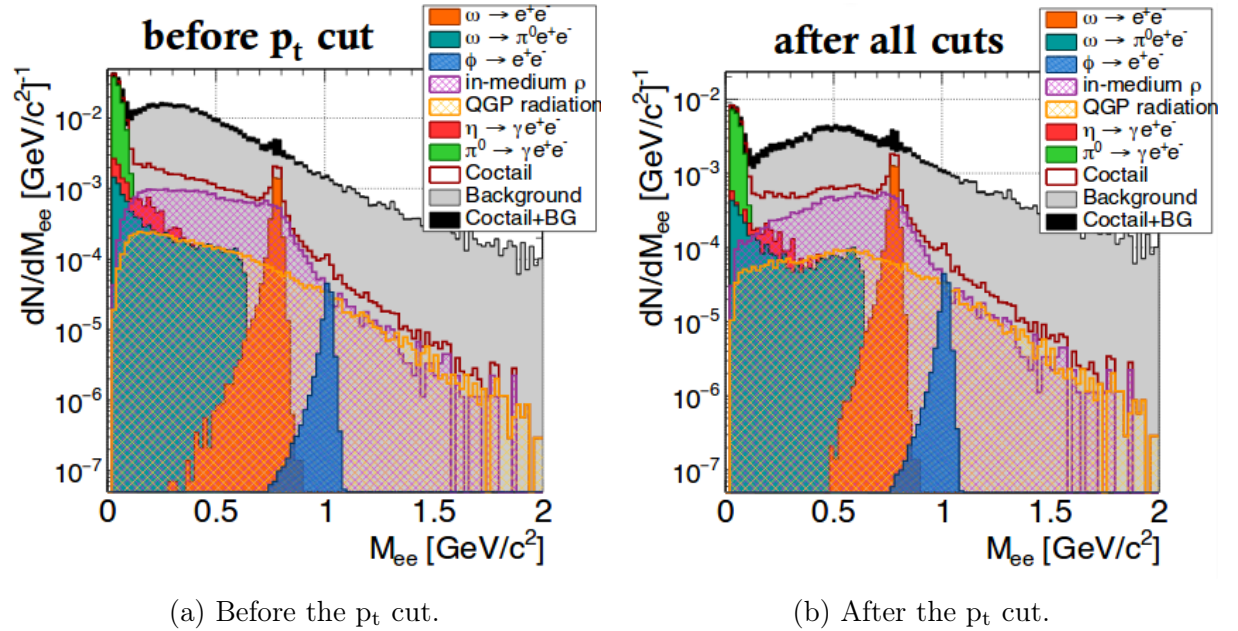


Figure 1.8: Invariant mass spectra of dielectrons after all cuts, left still excluding the transverse momentum cut and right also including the later. Contributions are shown in different colours. The spectra are shown for 1 million central Au+Au collisions at 8 AGeV beam energy. Figures taken from [65].

The analysis was done using the RICH, TRD and ToF detectors of the CBM experiment. Several cuts were applied to remove the background and get a cleaner signal. On the figure, all contributions are represented with different colours. The main contributions are coming from  $e^-/e^+$  from  $\pi^0$  Dalitz decays,  $\gamma$  conversions and misidentified electrons from  $\pi^+$ .

Table 1.2 shows the reconstruction efficiencies and signal to background ratios obtained at the end of the analysis.

---

	$\omega$	$\varphi$
efficiency (%)	4.63	5.93
Signal/Background	0.445	0.030

Table 1.2: Reconstruction efficiencies of  $\omega$  and  $\varphi$  mesons and their respective signal to background ratios after all cuts have been applied.

## 1.4 Other probes to study the QGP

In addition to the dileptons and especially dielectrons, which are particularly important for the CBM RICH detector (see Section 3.2.1), other important probes essential to the understanding of the QGP will be investigated in CBM. The following sections will briefly present some of them.

### 1.4.1 Collective flow

To study the collective flow in a nuclear collision, two observables were formulated in [66], the ‘in-plane’ or ‘directed flow’,  $v_1$ , and the ‘elliptic flow’,  $v_2$ . These coefficients correspond to the Fourier decomposition of the azimuthal distribution of the emitted particles:

$$dN/d\Phi \simeq 1 + 2 \cdot \sum_{n=1}^{\infty} v_n \cdot \cos(n \cdot (\Phi - \Psi_n)) \quad (1.6)$$

Where  $\Psi_n$  represents the collision symmetry plane. The directed flow is a measure of the bounce-off, while the elliptic flow is a measure of the squeeze-out. They are defined as [49]:

$$v_1 = \left\langle \frac{p_x}{p_t} \right\rangle, \quad v_2 = \left\langle \frac{p_x^2 - p_y^2}{p_x^2 + p_y^2} \right\rangle \quad (1.7)$$

Where  $p_x$  and  $p_y$  correspond to the transverse momentum in the reaction plane and out of reaction plane, respectively.  $p_t$  is the total transverse momentum defined as:

$$p_t = \sqrt{p_x^2 + p_y^2} \quad (1.8)$$

Given that these observables are created in the very early phase of a collision, this makes them very promising to comprehend the properties of the hot and dense created matter. It has been shown, that the elliptic flow takes negative values (for example in proton collisions at energies below 5 AGeV beam energy [49]), confirming the squeeze-out prediction from hydrodynamics.

The flow might also give hint to the nature of the phase transition to the QGP, as the disappearance of flow and the prediction by hydrodynamical calculations of a third flow component, called ‘antiflow’, are considered as signatures for a first order phase transition. In particular, a clear indication of strongly reduced proton flow has been seen by NA49 [67].

In addition, the collective flow is influenced by the pressure in the created fireball. Thus understanding it might help understanding the equation of state of QCD. Hints of hot and dense matter might also be shown indirectly by flow. This was revealed by measurements conducted at the RHIC in high energy Au+Au and Cu+Cu collisions and at the LHC in high energy p+p and Pb+Pb collisions. There a ‘ridge’-like structure was observed in  $\Delta\eta$ - $\Delta\Phi$  angular correlations [68, 69]. The ‘ridges’ appear at  $\Delta\Phi \sim 0$  and at  $\Delta\Phi \sim \pi$  and were both seen with and without a  $p_t$  trigger.

### 1.4.2 Fluctuations and correlations

Consider a system in thermal equilibrium characterised by a partition function,  $Z$ , defined as:

$$Z = Tr \left[ \exp \left( -\frac{H - \sum_i Q_i \mu_i}{T} \right) \right] \quad (1.9)$$

Here  $Q_i$  and  $\mu_i$  stand for the conserved charges and the corresponding chemical potentials,  $H$  is the Hamiltonian of the system.

By deriving the mean and covariances, as derivatives of the partition function, one can introduce the susceptibilities  $\chi_{i,j}$  [49]:

$$\chi_{i,j} = \frac{T}{V} \cdot \frac{\partial^2}{\partial \mu_i \partial \mu_j} \log(Z) \quad (1.10)$$

The diagonal susceptibilities  $\chi_{i,i}$  are used to determine the fluctuations of the system, while the non-diagonal susceptibilities  $\chi_{i,j}$ , ( $i \neq j$ ) are used to correlate between the conserved charges  $Q_i$  and  $Q_j$ .

The measured quantities are conserved for the entire system, however they might fluctuate if measured in a reduced phase space either by applying cuts or limiting the acceptance [49].

Different fluctuations can then be investigated, such as fluctuations of the particle multiplicity, the mean transverse momentum, the electric charge, the baryon number or strangeness (the last three correspond to the conserved charges in the case of three flavour QCD) [56]. The measurements of kinematic and chemical observables might provide hints for a first order phase transition and a critical end point [49].

The measurement in STAR of the energy dependence of the product  $\kappa\sigma^2$  (excess kurtosis times squared standard deviation) of the net-proton multiplicity distribution in Au+Au collision is an example of the search for the critical end point [70] (see Figure 1.9). In the absence of an end point, this quantity should remain constant, which was not observed by the experiment at lower energies. CBM will allow in this case a more precise study of this region.

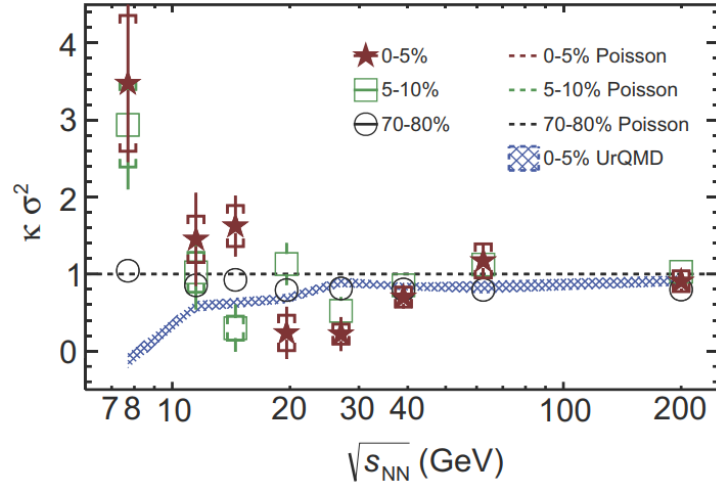


Figure 1.9: Energy dependence of the volume independent cumulant ratio of the net proton distribution. 0-5% central (red stars), 5-10% (green squares) and 70-80% peripheral (black circles) collisions are displayed. Poisson expectations and UrQMD calculations are represented in dotted lines and blue bands, respectively. Figure taken from [70].

### 1.4.3 Charm production

Particles containing charm quarks are produced during the early stage of the fireball from hard processes only. This makes it an interesting probe, as it allows to determine the degrees of freedom of heavy ion collisions over its entire evolution. Once created, the charm (and anti-charm) quarks will hadronise in D mesons, charmed baryons or charmonium.

The latter presents an attractive characteristic, as it is suppressed ( $J/\Psi$  and  $\Psi'$  are dissociated) in the deconfined phase. This suppression is sensitive to the created fireball. Separating charm absorption in hadronic matter from colour screening of the heavy quark in the deconfined phase is the key to study the created system with charmonium. Indeed the charmonium suppression due to colour screening has been predicted as a signature for the formation of a QGP [56].

In addition to the degrees of freedom of the hot and dense matter, its transportation properties can be investigated via the propagation of open charm and elliptic flow of charm.

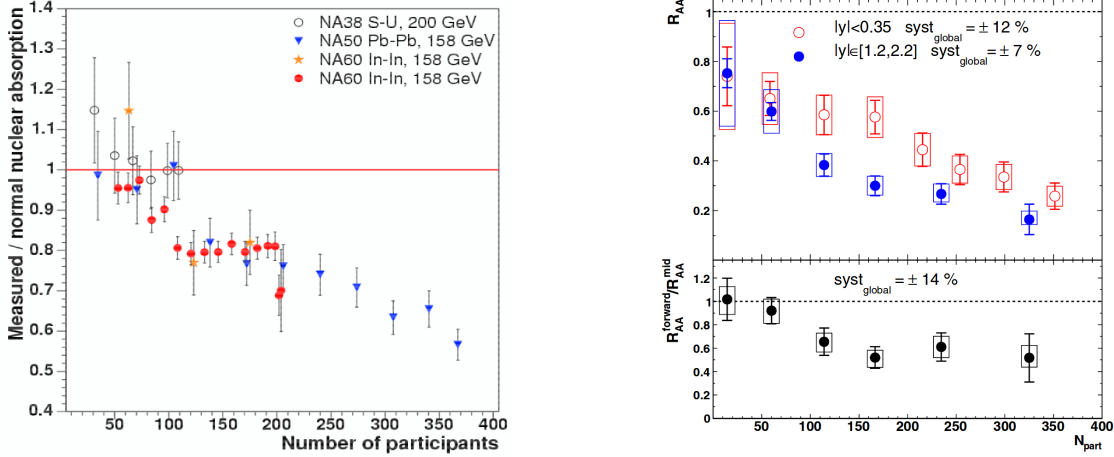
At FAIR energies charm measurements close to threshold energies will be possible, which is particularly sensitive to the condition in the fireball, as the  $c\bar{c}$  pair production threshold is lower than the energy required for the production of a pair of charmed hadrons.

Understanding the effects of absorption mechanisms in proton-nucleus collisions on  $J/\Psi$  and comparing them to data obtained in A+A collisions, could hint effects from colour screening. In NA38, NA50 and later confirmed by the NA60 experiment,  $J/\Psi$  suppression was observed (Figure 1.10a) for semi-central and central collisions by looking at the ratio of measured over expected  $J/\Psi$  mesons [49].

The nuclear modification factor,  $R_{AA}$ , was also introduced to visualise absorption

effects of the hot and dense created matter. This factor is defined as the ratio between the charmonium yield in A+A collisions and that of p+p collisions, scaled by the number of participants.

$$R_{AA} = \frac{N_{AA}^{J/\Psi}}{N_{pp}^{J/\Psi} \cdot N_{part}} \quad (1.11)$$



(a) Measured over expected  $J/\Psi$  ratio versus number of participants in A+A collisions at various energies and experiments. Figure taken from [49].

(b) Upper panel:  $R_{AA}$  versus  $N_{part}$  for central Au+Au collisions at  $\sqrt{s} = 200$  GeV. Lower panel:  $R_{AA}$  ratio of forward over mid rapidity versus  $N_{part}$ . Figure taken from [71].

Figure 1.10

The upper part of Figure 1.10b shows the nuclear modification factor in Au+Au collisions as a function of the number of participants for mid and forward rapidity. Here  $R_{AA}$  decreases with an increasing number of participants. The lower part of Figure 1.10b displays the ratio of  $R_{AA}$  at forward rapidity over  $R_{AA}$  at mid rapidity. A plateau is reached for  $N_{part} > 100$  with a value of around 0.6. Thus  $J/\Psi$  suppression is revealed in both cases.

At the foreseen energies of CBM, measurements on the excitation function of the ratio  $\Psi'$  over  $J/\Psi$  will help understand the absorption processes in dense matter. However, detailed charm measurements would require the SIS300 accelerator set-up.

#### 1.4.4 Strangeness

Another probe of interest for CBM is particles containing strange quarks. First through the measurements of the yield of the  $\Omega$  and  $\bar{\Omega}$  and then with the measurements in the yield of  $\Xi^-$ . In the HADES experiment it was shown that the yields exceeded that of the chemical equilibrium [56]. For higher energies however the yields correspond to that of equilibrium. Thus measurements of excitation functions of multi-strange hyperons in A+A collisions will be undertaken at SIS100 energies to study the equilibration degree of the hot and dense matter and look for the onset of deconfinement.

### 1.4.5 Hypernuclei and strange objects

The relatively high energy regime offered by the SIS100 accelerator of FAIR (see Section 2.1) will yield high baryon densities, where strange composite hypernuclei are expected to be produced. Thermal model calculations indeed show that the excitation function of hypernucleus production peaks in the energy range of SIS100 [56]. Understanding their formation will be carried out in CBM via the measurements of the light double- $\Lambda$  hypernuclei:  ${}^5_{\Lambda\Lambda}H$  and  ${}^6_{\Lambda\Lambda}He$ . According to the used thermal model [72], a yield of about 5 and 0.1 of each of these particles is expected for one million events with a beam energy of about 10 AGeV. Thus 3,000  ${}^5_{\Lambda\Lambda}H$  and 60  ${}^6_{\Lambda\Lambda}He$  should be produced per week of operation in CBM.

Furthermore, other exotic forms might be measured such as dibaryon states with strangeness, giving insights to, for example, the equation of state of nuclear matter at high densities.



# Chapter 2

## The FAIR facility and the CBM experiment

### 2.1 FAIR Motivations

The Gesellschaft für Schwerionenforschung (GSI) and nowadays referred to as GSI Helmholtzzentrum für Schwerionenforschung is located in Darmstadt and was founded in 1969. It was created as a research centre for the Hessian universities and became with the FAIR project a worldwide association, coping with increasing technical challenges emerging in physics [73]. The GSI research program is strongly oriented towards nuclear physics, but meanwhile extended to the heavy-ion and hadron physics, through several upgrades of the accelerator facilities.

It is supported by the Bundesrepublik Deutschland, the Bundesländer Hessen and Rheinland-Pfalz and the Freistaat Thüringen. In 2018, GSI counts about 1,400 employees, 1,200 visiting scientists and worldwide cooperation with approximately 400 institutes from over 50 countries.

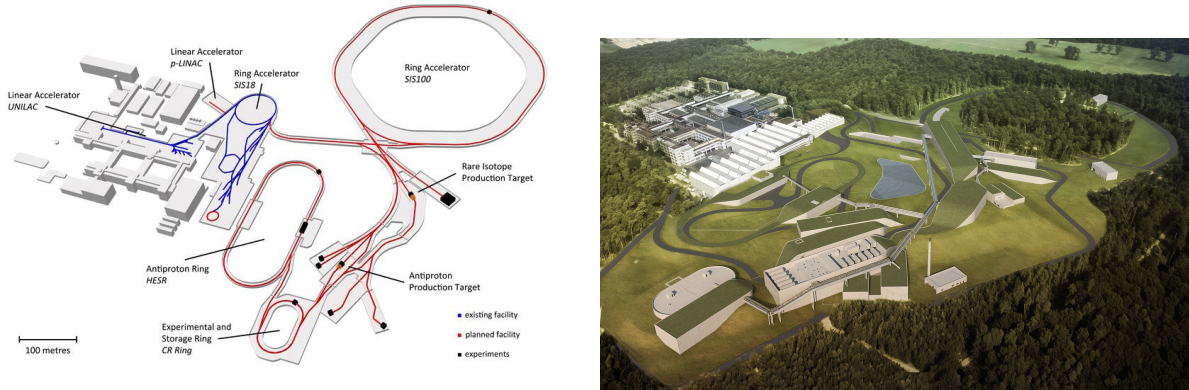
The Facility for Antiproton and Ion Research (FAIR) complex will be built as an extension of the GSI research center. The official start of the project was November 7th 2007. The project was at the time ratified by nine countries (in alphabetical order: Finland, France, Germany, India, Poland, Romania, Russia, Slovenia and Sweden) and was later joined by the United Kingdom. In 2018, FAIR counts about 3,000 scientists from over 50 countries. Its physics objectives are divided into four pillars, corresponding to four grouped experiments. Each will focus on particular physics cases, requiring dedicated detectors (see Section 2.2).

Due to long lead times for civil construction planning and a reorganisation of the FAIR management board, the project is, at the time of writing of this thesis, expected to deliver its first beams by 2025. Moreover, the Modularized Start Version (MSV [74]) is estimated to be fully operational by 2025, too [75, 76].

The layout of the GSI and FAIR projects is shown in Figure 2.1a. In addition, a satellite view from both complexes is modelled in Figure 2.1b.

The existing GSI installations are represented in blue on the left side of Figure 2.1a.

The linear accelerator (UNILAC) and synchrotron SIS18 will be used as injectors for the ring accelerator of FAIR. The new FAIR installations are shown in red on the right side of Figure 2.1a. The incoming particles will be further accelerated in the SIS100 synchrotron. This accelerator will have a circumference of 1,100 meters and will be provided with 100 Tm rigidity magnets. It will be the crucial centre piece of equipment of FAIR. Particles will then be distributed to the different experiment lines, detailed on Figure 2.2.



(a) Sketched GSI and FAIR complexes. The left side in blue corresponds to the currently existing GSI facility. The right side in red shows the new accelerator layout. The future experiments involved with FAIR are represented in black.

(b) Modelling of a satellite view of the current GSI and future FAIR complexes.

Figure 2.1: Different views of the current GSI and future FAIR facilities in Darmstadt. Figures taken from [77].

Figure 2.2 illustrates the construction plan of the FAIR complex. It will be built in several coloured steps corresponding to different operation phases. The SIS100 synchrotron is shown in green and the CBM/HADES, NuSTAR and PANDA experiments are represented in red, yellow and orange, respectively. APPA, the fourth pillar of FAIR is not highlighted on this plan.

One of the major enhancement provided by FAIR is an increase in the beam intensities, by a factor of 100 for primary beams and 10,000 for secondary beams, with respect to the current state in GSI [76]. Furthermore an improvement in the beam luminosity by a factor of 10,000 will allow to observe extremely rare physics processes and explore unique physics cases [73]. The energies reached at SIS100 will range from 2 to 11 AGeV/c for the heaviest nuclei. A future synchrotron SIS300 will allow to access even larger energies up to 35 AGeV/c.

Using the UNILAC and the SIS18 synchrotron, along with already available instrumentations, such as the Cryring, R3B magnet, or the HADES experiment, a so called FAIR phase 0 will take place. This will allow the different experiments to test their hardware set-up and readout systems in the best case already in running experiments delivering physics outputs.



Figure 2.2: Scheme of the GSI and future FAIR facilities. On the left side in white, GSI. On the right side, the different modules included in the Modularized Start Version of FAIR. The SIS100 synchrotron is shown in green (module 0). The CBM and HADES caves are sketched in red (module 1). The NuSTAR area is represented in yellow (module 2). The PANDA and antiproton region is in orange (module 3). Additional domain for the APPA experiment is not indicated (module 1). Figure taken from [73]

## 2.2 Four pillars

This section will not give an extended survey on the different experiments taking place at FAIR and their tackled physics cases, but a global overview. For a deep insight on the physics programs, the reader is recommended to the given references.

Experiments taking place at FAIR are grouped into four scientific pillars, listed in alphabetical order:

- Atomic Plasma Physics and Applications (APPA), grouping several experiments, such as BIOMAT, FLAIR, HED@FAIR and SPARC. It will study atomic and material physics, as well as biophysics [78]. APPA will try to bring an answer to questions like: Which fundamental symmetries define our universe? What are the properties of high density plasmas, present inside large planets? How can particles be used to cure illnesses? How can astronauts be protected against cosmic radiations? Can ion beams be used to change specific properties of materials?
- Nuclear Matter Physics, grouping the High Acceptance DiElectron Spectrometer (HADES) and the Compressed Baryonic Matter (CBM). The project will look at the properties of hadrons in the region of high temperature and pressure [49, 79]. Here questions like what is the landscape of the QCD phase diagram in the region of high baryon density and moderate temperatures and in what form does matter exist in neutron stars will be tackled.
- Nuclear STructure, Astrophysics and Reactions (NuSTAR), grouping several experiments, such as DESPEC/HISPEC, ELISe, EXL, ILIMA, LaSpec, MATS and R3B. It will focus on nuclear physics and astrophysics [80, 81]. At NuSTAR questions like how are heavy elements created in stars and stellar explosions are addressed.
- antiProton ANnihilation at DArmstadt (PANDA). This experiment will aim at understanding the structure of hadrons and their properties in vacuum and matter and searching for exotic phases of matter in the form of for instance glueballs or hyper-nuclei [82]. PANDA will investigate how can antimatter help understand massive matter and the strong force.

## 2.3 Compressed Baryonic Matter

In 2018, the CBM experiment consists of more than 460 scientists from 54 institutes and 11 countries (see Figure 2.3). Left of Figure 2.3 shows a 3D schematic view of the CBM building. Right of Figure 2.3 shows a pie chart showing the scientific diversity among the CBM experiment in 2017.

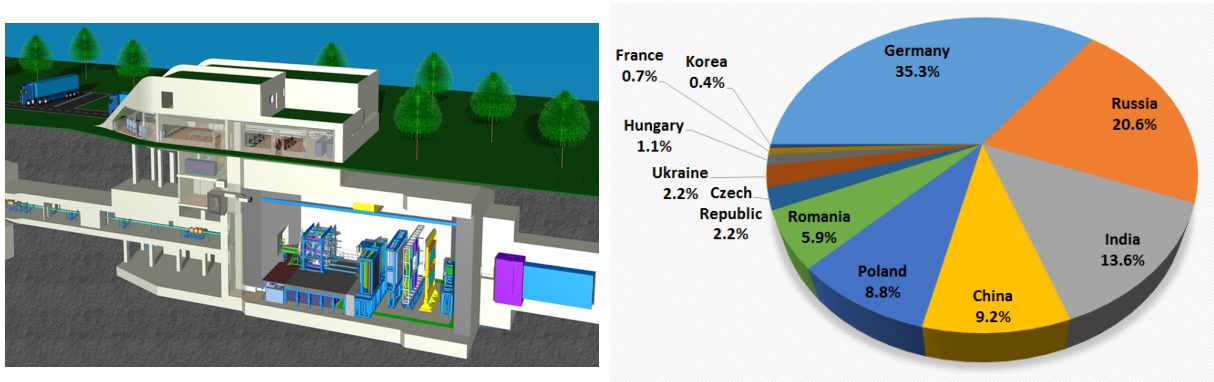
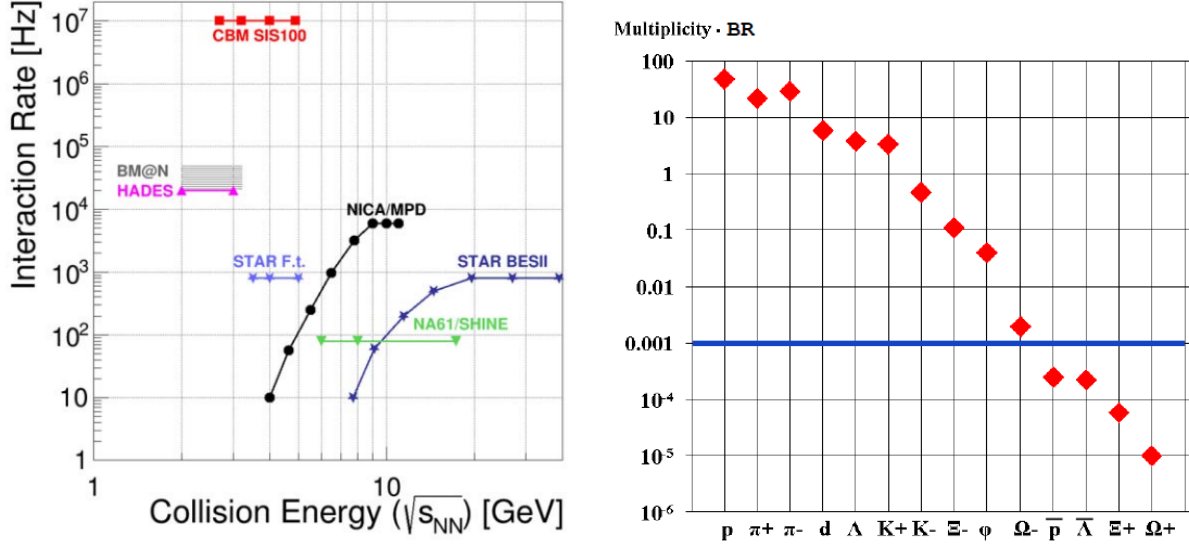


Figure 2.3: Left: 3D schematic view of the CBM building. At the lowest level, the HADES and CBM experiments will run. Figure taken from [83]. Right: Pie chart showing the scientific diversity among the CBM experiment in 2017. Figure inspired from [84].

The physics objectives of the CBM experiment have been explained in detail in Sections 1.3.2 and 1.4. The list below sums up the most promising observables, which will be investigated in CBM at SIS100 and, hopefully, later at SIS300 energies:

- Photons, giving information on the early stages in the fireball
- Low mass vector mesons,  $\rho$ ,  $\omega$  and  $\varphi$ , via their dilepton decay pairs, investigating in-medium spectral functions
- Collective hadron flow, yielding equation of state information
- Strange and multi-strange hyperons,  $\Lambda$ ,  $\Xi$  and  $\Omega$ , for the understanding of the fireball evolution and possible thermal equilibrium
- D-mesons and charmonium, as probes of compressed matter on a large mass/energy scale and below production threshold
- Dynamical fluctuations, possibly hinting towards a phase transition or a critical point
- Two-particle correlations, carrying information on the time evolution and size of the fireball

In order to answer the questions raised above and investigate the addressed probes, CBM needs to measure rare probes and perform systematic studies. The resulting quest for high rates puts a technical challenge: reaction rates from 0.1 up to 10 MHz with charged particle multiplicities of up to 1,000 per event [49] have to be reached, which would be the highest achieved in the world of heavy ion collision (see Figure 2.4a). Figure 2.4b



(a) Interaction rate of CBM in dependence on the collision energy and compared to other heavy ion experiments. The foreseen interaction rate is about two orders of magnitude higher than the second highest interaction rate reached in a heavy ion experiment. This rate will allow the search for new physics observables.

(b) Multiplicity times branching ratio for rare probes of interest for CBM in central Au+Au collisions at 4 AGeV/c. The calculations were done according to the HSD transport code and the statistical model from [49]. All particles above the horizontal line have already been measured.

Figure 2.4: Left figure taken from [56]. Right figure taken from [49].

illustrates how ‘rare’ the probes investigated in CBM are, by calculating the product of their multiplicity by the branching ratio. Particles above the horizontal line have already been detected by other experiments at energies of 4 AGeV [85]. To measure the missing particles, high rates combined with a dedicated high precision and fast timing of the instrumentation are required.

Beam energy (AGeV)	Anti- $\Lambda$	$\Xi^+$	$\Xi^-$	$\Omega^+$	$\Omega^-$
4.0	$9.8 \times 10^4$	$8.9 \times 10^4$	$1.7 \times 10^7$	$1.2 \times 10^3$	$2.3 \times 10^5$
6.0	$2.5 \times 10^5$	$2.3 \times 10^5$	$4.3 \times 10^7$	$3.6 \times 10^3$	$6.8 \times 10^5$
8.0	$3.5 \times 10^6$	$3.7 \times 10^6$	$6.9 \times 10^7$	$8.0 \times 10^4$	$1.9 \times 10^6$
10.7	$6.8 \times 10^6$	$7.1 \times 10^6$	$9.2 \times 10^7$	$1.6 \times 10^5$	$3.0 \times 10^6$

Table 2.1: Predicted hyperon yields obtained per week in CBM, with a reaction rate of  $10^4$ /s in central Au+Au collisions. Table inspired from [49].

An example emphasising the need for such high reaction rates is the measurement of multi-strange hyperons. For Au+Au collisions at 6 AGeV/c, corresponding to SIS100 energies, reconstruction efficiencies of multi-strange hyperons have been calculated. They include geometrical acceptance, track reconstruction efficiency and background cuts. The simulations yielded detection efficiencies of  $\epsilon(\Lambda) = 7.4\%$ ,  $\epsilon(\Xi) = 2.6\%$  and  $\epsilon(\Omega) = 2.0\%$ . The measurements of these probes at these energies would require a beam intensity of

$10^7$  ions/s and a 1% interaction target, corresponding to a rate of  $10^4$ /s for the 10% most central events [49]. Table 2.1 summarises the hyperon yields for central Au+Au collisions at energies between 4 and 10.7 AGeV. The discussed detection efficiencies and the multiplicities per event calculated with a statistical model have been used. Aiming at systematic measurements and multi-differential analysis, such rates are indispensable.

For those reasons, fast and radiation hard detectors and electronics are demanded to ensure a proper functioning during data recording. The high speed data taking has to be backed up by fast online data processing and trigger decisions. Subsequently the detectors involved in CBM will be briefly introduced. The full set-up of the experiment is represented in Figure 2.5 in the SIS100 configuration and for the case of electron identification. The most recent advancements are summarised in [86].

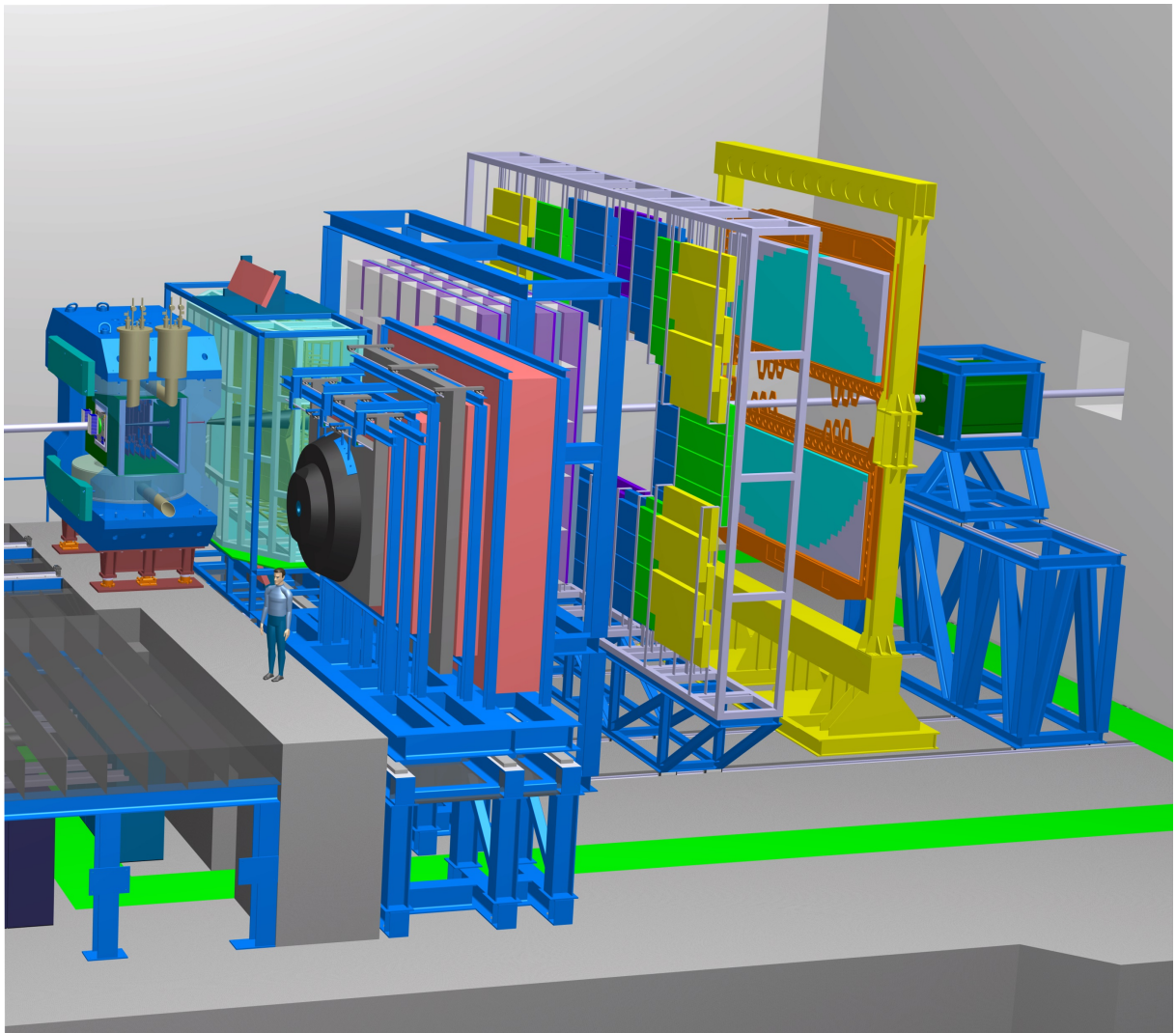


Figure 2.5: Experimental set-up of the CBM experiment in the electron detection configuration. From left to right, Magnet, MVD, STS, RICH, MUCH, TRD, TOF, ECAL, PSD. The MUCH is placed at a parking position next to the beamline and at the side of the RICH detector. Figure taken from [87].

### 2.3.1 Dipole magnet

A superconducting dipole magnet, surrounding the interaction region, will induce a bending power of 1 Tm. A magnetic field of 3.9 T is reached on the coils [88]. The left-hand side of Figure 2.6 presents a design of the dipole magnet realised in 2018 by BINP. The poles and coils have a cylindrical shape and the field clamps are modified, so that they fit with the shielding box of the RICH detector. The right-hand side of Figure 2.6 illustrates the chosen cooling strategy for the coils. The design of the magnet is still subject to optimisations in 2019.

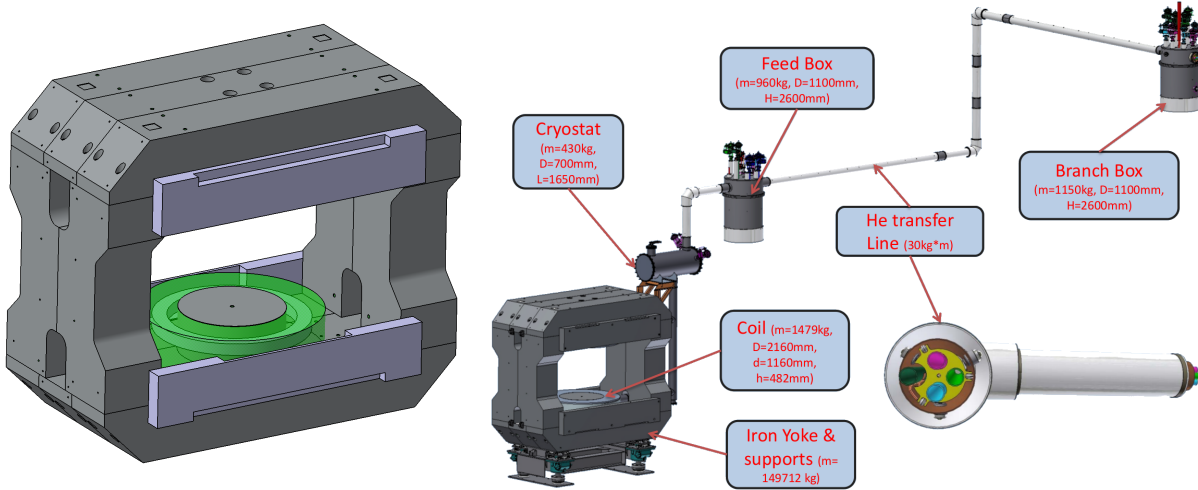


Figure 2.6: Left: Engineering design of the CBM magnet. The poles (central part) and coils (in green) are cylindrical and the field clamps (in blue-grey) shape fits with the shielding box of the RICH detector. Right: 3D model of the magnet mounted on a support structure and connected to a cooling system. Figures taken from [89].

### 2.3.2 Micro Vertex Detector

The Micro Vertex Detector (MVD) will be placed inside the dipole magnet aperture. It will consist of four stations placed at 5, 10, 15 and 20 cm from the interaction point (see Figure 2.7). Main tasks of the MVD detector will be the highest precision tracking and excellent secondary vertex finding closest to the main vertex.

This capability will then be used for the reconstruction of conversion and Dalitz-pair suppression in light vector meson analysis, low momentum particle tracking multi-strange particles and hyperons detection and open charm decays.

In addition and due to the high rates of the CBM experiment, the MVD detector should achieve a relatively high rate capability.

To evacuate a heat of about  $350 \text{ mW/cm}^2/\text{sensor}$  and keep an operation temperature at  $-20^\circ\text{C}$ , the sensors will be mounted on high heat-conductive carriers, clamped into liquid cooled heat sinks, located outside the detector acceptance [90]. To validate the MVD concept, a PRESTO (PREcursor of the Second sTatiOn) board was designed, made of 15 thin ( $50 \text{ }\mu\text{m}$ ) MIMOSA-26 sensors, nine of which are glued on the front and six on the

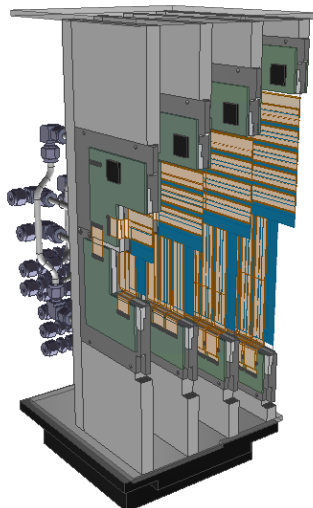


Figure 2.7: The Micro-Vertex Detector of CBM.

back side of the PRESTO. The readout is done with 10 FPCs (Flex Print Cables) per PRESTO.

The MIMOSA-26 sensors are fabricated in a CMOS 0.35  $\mu\text{m}$  technology, with a pixel size of  $18.4 \times 18.4 \mu\text{m}^2$  and a sensitive surface of  $10.6 \times 21.2 \text{ mm}^2$  [91]. They will provide a hit resolution from 3.5  $\mu\text{m}$  to 6  $\mu\text{m}$ , yielding a secondary vertex resolution of  $50 \mu\text{m}^2$  up to  $100 \mu\text{m}^2$  in the beam axis direction [92].

Each PRESTO requires a material budget of  $X/X_0 \geq 0.5\%$ , the sensor tolerance to non-ionizing radiation has to be kept below  $10^{13}$  neutron equivalent per  $\text{cm}^2$  ( $n_{\text{eq}}/\text{cm}^2$ ), while the tolerance to ionizing radiation amounts to  $\sim 3 \text{ Mrad}$ .

### 2.3.3 Silicon Tracking System

The Silicon Tracking System (STS) will be placed behind the MVD detector and also inside the aperture of the magnet. It is represented in Figure 2.8a.

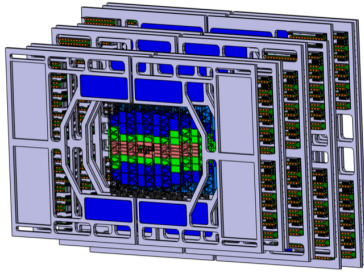
Two of the most important requirements imposed by the CBM conditions are excellent track reconstruction efficiency and momentum resolution. They have to be maintained at 95% and  $\Delta p/p = 1\%$ , respectively, for tracks with momenta greater than 1 GeV. The principle of momentum reconstruction via only tracking in magnetic fields is based on the combination of the Lorentz force and circular movement:

$$\vec{F} = \frac{m \cdot v^2}{R} = q \vec{v} \times \vec{B} \implies p = q \cdot B \cdot R \quad (2.1)$$

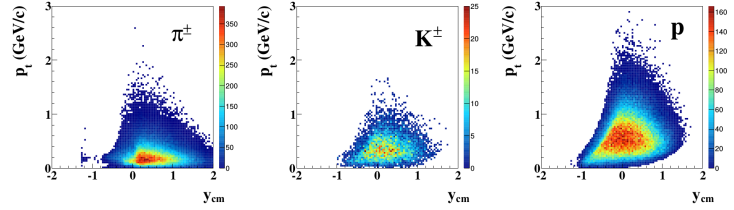
Where  $p$  is the particle momentum,  $q$  the particle charge,  $B$  the magnetic field and  $R$  the radius of the particle trajectory. To meet with these requirements, a spatial resolution of 25  $\mu\text{m}$  is foreseen to be used, which can be achieved with a 58  $\mu\text{m}$  read-out strip pitch [92, 93].

Moreover a full coverage from centre of mass rapidity, to close to beam rapidity is required over a wide center-of-mass energy range. To fulfil this constraint, a polar angular coverage of  $2.5^\circ \leq \theta \leq 25^\circ$  was chosen. Figure 2.8b shows reconstructed charged  $\pi^\pm$ ,  $K^\pm$

and protons in the  $p_t$  versus  $y_{cm}$  plane. Those were reconstructed with the STS detector for simulated Au+Au collisions at 6 AGeV.



(a) Engineering view of the STS detector.



(b) From left to right: distribution of reconstructed charged pions, kaons and protons in the  $p_t$ - $y_{cm}$  plane. The histograms are shown for Au+Au collisions at 6 AGeV with a beam rapidity of 1.28.

Figure 2.8: Figures taken from [93].

Single hit detection efficiency should remain close to 100% and the equipment should be fast to cope with the hit rates, while withstanding high levels of radiation up to  $10^{14}$   $n_{eq}/cm^2$ .

To meet the requirements, a STS detector with 8 planar tracking stations was chosen and will be placed from 30 cm to 1 m, in 10 cm steps, downstream of the target.

To fulfill the very low material budget constraint, micro-strip sensors have been selected. They will be double-sided with a stereo angle of  $7.5^\circ$ , a strip pitch of  $58 \mu m$  and strip lengths ranging from 20 to 60 mm. The front-end electronics will be placed outside the active area of the detector and low mass cables will transport the information to a readout chip placed outside of the acceptance. A  $CO_2$  cooling system, will be placed outside the acceptance as well, to keep the temperature to  $-5^\circ C$  and a maximum non-ionizing dose for the sensors closest to the beam line should not exceed  $10^{14}$   $n_{eq}/cm^2$  [93].

The number of read-out channels was also optimised, while minimizing the read-out pitch size and the read-out strips length. A total of 1,835k channels will be required to ensure a proper detector operation (the first station has 156k channels and the last 279k). With this configuration a material budget ranging from 0.3 %  $X_0$  to 1.2 %  $X_0$  is achieved [93].

### 2.3.4 Ring Imaging Cherenkov

Following the STS downstream of the beamline the RICH detector will be placed. The main properties of the detector are summarised here, but a more extensive description is given in Section 3.3.

The RICH detector will be used in the electron configuration of CBM to reconstruct dileptons radiating off the created fireball, yielding information for example on low mass vector mesons. It will use  $CO_2$  as a gaseous radiator, with a radiator length of 1.7 m, yielding in simulation a mean of 28 hits per electron ring on the photon detector plane.

The latter is made of Multi-Anode Photo-Multiplier Tubes (MAPMT). About 80 spherical mirror tiles, with an Al+MgF<sub>2</sub> coating and a radius of curvature of 3 m, will be used to reflect and focus photons onto the PMT plane. A magnetic shield will also be used to protect the MAPMTs from the residual magnetic fields emanating from the dipole magnet, thus ensuring a proper operation of the detector [94].

Under these conditions the detector will be able to clearly identify electrons up to 7-8 GeV/c.

### 2.3.5 Muon Chamber

The counterpart to the RICH detector is the MUon CHamber (MUCH), employed for muon detection. This detector will be positioned after the STS detector and interchanged with the RICH. While interchanging the two detectors, RICH will be transported by crane and MUCH will slide on a railway system.

Analogous to the RICH, the MUCH will aim at detecting dimuons to provide a complete picture of emanating dileptons. To do so, GEM (Gas Electron Multipliers) chambers placed between absorber layers will be used to facilitate continuous tracking through the absorber. This conception of the detector allows also for low momentum muon detection. Optimisations on the absorber length have been conducted with simulations of Au+Au collisions from 4 to 25 AGeV/c. The muons coming from  $\omega$  mesons get suppressed by a factor of 10 after 250 cm of absorber, whereas the ones from J/ $\Psi$  are merely affected [95].

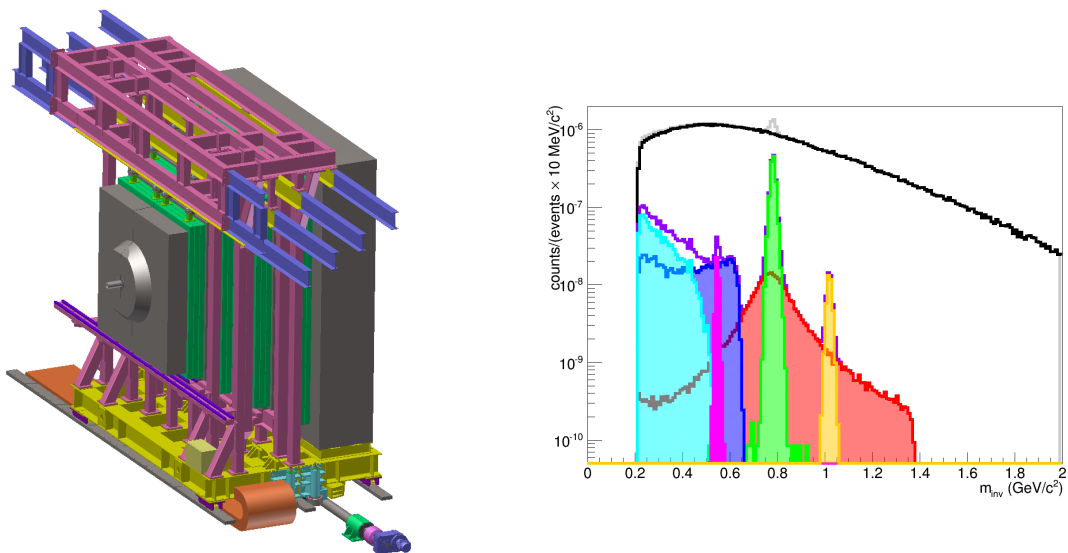


Figure 2.9: Left: cut view of the MUCH detector, with the screw and captive nut option for the drive unit. Right: Di-muon simulation for central Au+Au collisions at 8 AGeV, with the SIS100-B set-up [95]. Combinatorial background (black histogram) along with the invariant mass spectrum of reconstructed muon pairs from decays of low mass vector mesons. Each signal spectrum is colour coded: in light blue  $\eta$ -Dalitz, in magenta  $\rho$ , in dark blue  $\omega$ -Dalitz, in green  $\omega$ , in yellow  $\phi$  and in red  $\eta$ . Figures taken from [95].

Figure 2.9 shows the MUCH detector, where the first and last absorption layers are visible. They will be made of carbon and iron with different thicknesses. 4 detection layers

are represented, which are gaseous tracking chamber triplets, either made of GEM or straw tubes, depending on the track density. For the last station the first Transition Radiation Detector layer may be used. For  $J/\Psi$  measurements, only the last 3 chamber triplets would be sufficient at SIS100 energies. The drive unit variant shown is using screw and captive nut, but another option with rack and pinion is also being studied. Additionally, Figure 2.9 shows the invariant mass spectrum obtained from simulated Au+Au collisions at 8 AGeV/c energy.

### 2.3.6 Transition Radiation Detector

The next detector placed downstream of the target will be the Transition Radiation Detector (TRD). An engineering rear view is shown on the top left of Figure 2.10. It will also serve for electron identification, to complete the RICH information for momenta in particular larger than 7 GeV/c.

The detector has been designed to help giving insights to the dense quark and nuclear matter generated. Identifying high momentum electrons gives in particular access to intermediate mass dileptons (in the range between the  $\Phi$  and  $J/\Psi$ ). The dilepton spectrum in this range allows to directly access the fireball temperature [96]. The overall improved electron purity will allow for an improved signal to background ratio in the dielectron measurement also at low masses.

Moreover the detector allows to measure nuclear fragments together with the Time of Flight detector information, in order to study hyper-nuclei and anti-nuclei.

To answer the challenges raised by electron identification at high momenta, the TRD will consist of four to five detector layers grouped into one station in the SIS100 configuration and 10 detector layers grouped into three stations in the SIS300 configuration [97]. Every second layer is rotated by  $90^\circ$ .

The bottom left of Figure 2.10 illustrates how the TRD completes the ToF information for particle identification.

The detector readout will be constructed with rectangular pads, providing a resolution of 3 to 30 mm along the pad and  $\sim 300 \mu\text{m}$  across it. Gas mixtures of either Xe (85%) and  $\text{CO}_2$  (15%), or Ar (80%) and  $\text{CO}_2$  (20%) will be employed.

The achieved pion suppression factor at 90% electron efficiency and for a momentum higher than 8 GeV/c is at around 15. This value increases to 50 with an electron efficiency of 80%. In this momentum region and for an electron efficiency of 80%, additional information from the RICH and ToF detectors increases this value to about 80. The energy resolution for momenta above 1 GeV/c will be around 25%.

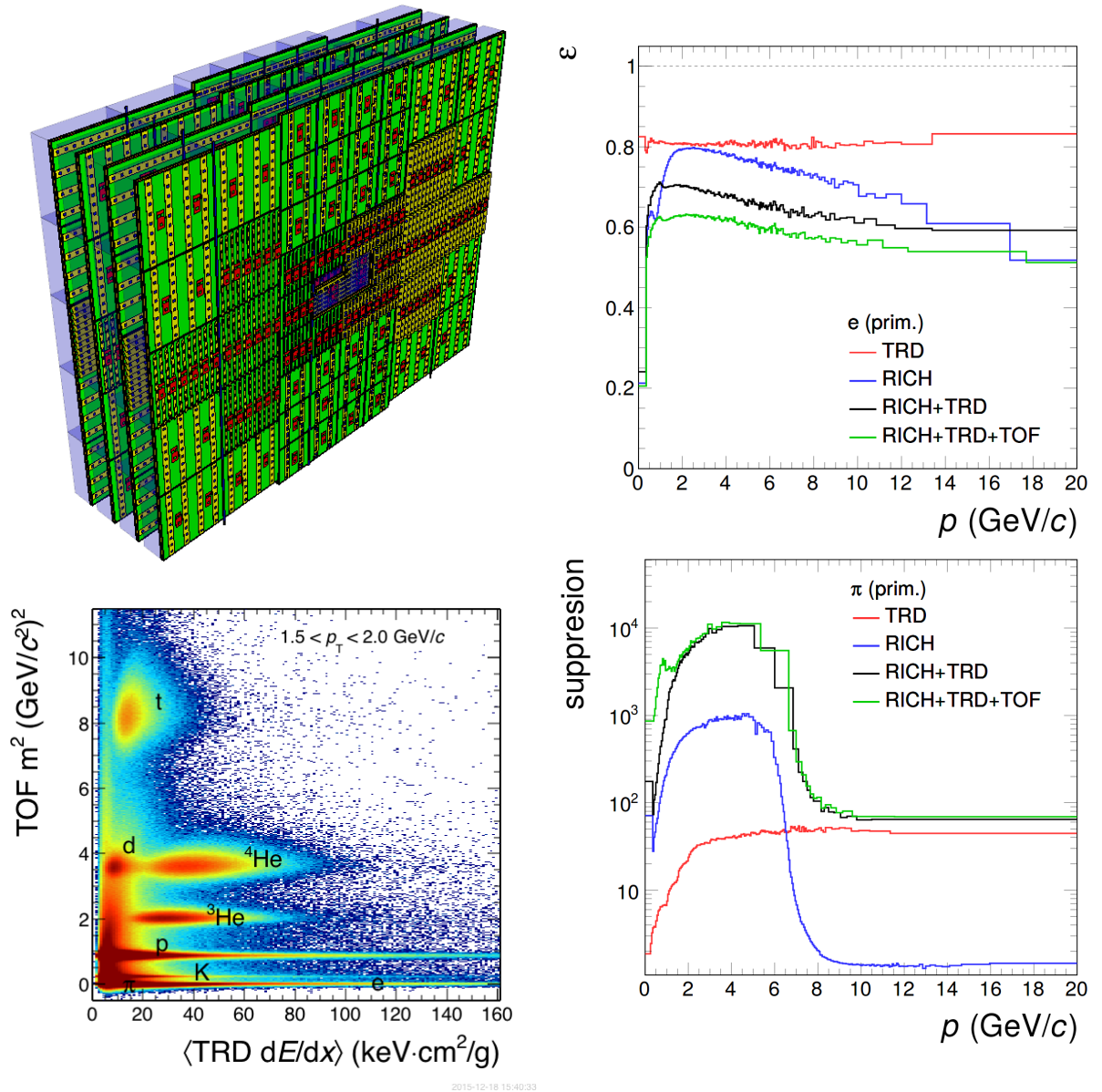


Figure 2.10: Top left: Engineering rear view of the transition radiation detector for the CBM experiment. Bottom left: Mass squared measured by the ToF detector in dependence of the TRD signal for central Au+Au collisions at 8 AGeV. Top right: Electron identification efficiency. Bottom right: Pion suppression factor versus momentum. Results of the two right histograms were obtained for the 10% most central Au+Au collisions at 8 AGeV beam energy. The colour code is similar: TRD and RICH performances are shown separately (red and blue curves, respectively) and together (black curves). In green, the Time of Flight detector information is added to the TRD and RICH. Figures taken from [97].

### 2.3.7 Time Of Flight

Behind the TRD, a Time of Flight (ToF) detector will be employed. The detection principle relies on the accurate measurement of a particle's momentum and velocity, that is its time of flight, assuming a track trajectory has been reconstructed. The two parameters give access to the mass of the particle, calculated as:

$$m^2 = p^2 \left( \frac{1}{\beta^2} - 1 \right) \quad (2.2)$$

The right-hand side of Figure 2.11 shows the distribution of  $m^2$  in dependence of momentum for an ideal detector and positively charged particles. The resolution in  $m^2$  measurement has a quadratic dependence on the momentum. This translates into a quick decrease in the particle identification capability with increasing momentum.  $\pi^+$ ,  $K^+$  and protons can be separated up to roughly 3 GeV/c momentum.

An array of Multi-Gap Resistive-Plate Chambers will be employed to identify hadrons via the time of flight information (see left-hand side of Figure 2.11). To cover polar angles of  $2.5 \leq \theta \leq 25$ , an active area of around 120 m<sup>2</sup> will be built. A total number of 226 modules separated into six different types will be operated.

To keep a time resolution of about 80 ps and sustain rates up to 25 kHz/cm<sup>2</sup>, low-resistive glass has been designed, still delivering time resolution on the order of 60 ps. The size of the pad is, for small deflection angles, around 5 cm<sup>2</sup>, corresponding to an occupancy below 5% for central Au+Au collisions [98].

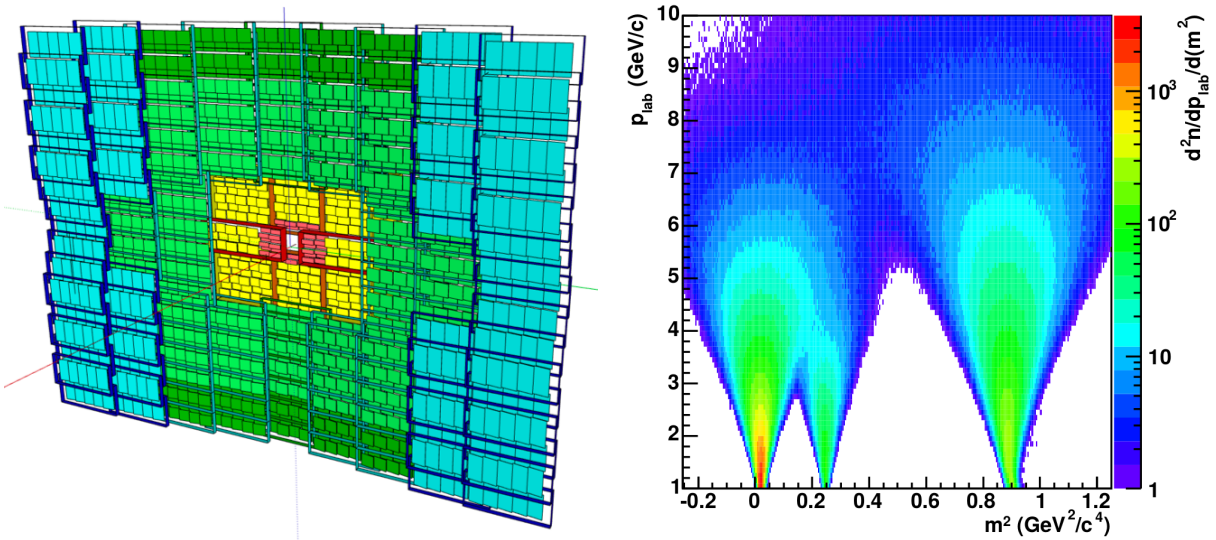
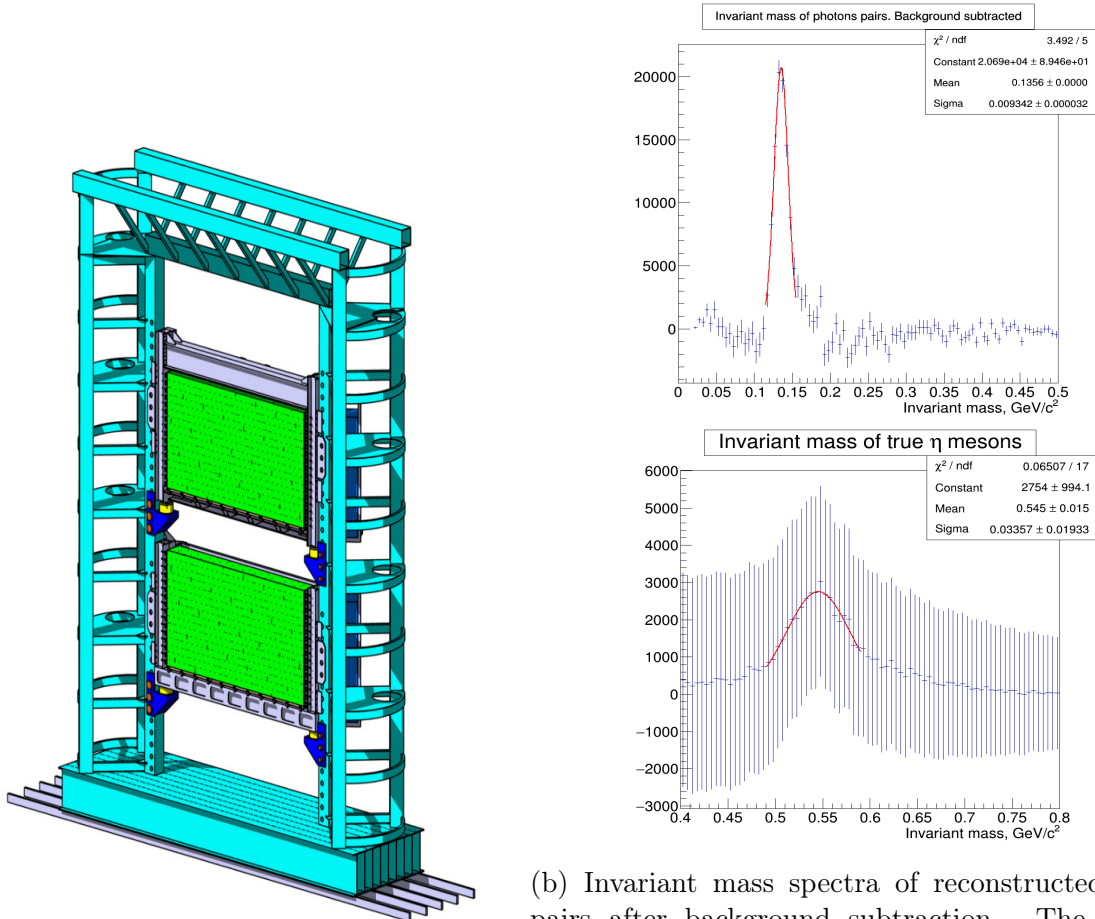


Figure 2.11: Left: time of flight detector and its different modules. Right: distribution of  $m^2$  versus momentum for positively charged hadrons, for an ideal detector. The distance to the target is 10 m and the time resolution 80 ps. Figures taken from [98].

### 2.3.8 Calorimeters

Two calorimeters will be used in the CBM experiment, an Electromagnetic CALorimeter (ECAL) and a Projectile Spectator Detector (PSD), placed subsequently behind the ToF detector.

The aim of the ECAL is to identify photons and electrons and measure their energy and position. The direct measurement of photons allows to access additional hadrons decaying electromagnetically [99].



(a) Optimised ECAL for SIS100 energies.

(b) Invariant mass spectra of reconstructed photon pairs after background subtraction. The top histogram shows results in the  $\pi^0$  mass region. The bottom histogram shows reconstructed photon pairs from MC-truth  $\eta$ -mesons. 1.5 million UrQMD events were simulated for central Au+Au collisions at 10 AGeV beam energy.

Figure 2.12: Electromagnetic calorimeter of the CBM experiment. Figures taken from [99].

The ECAL will be made of 140 layers of lead absorbers, separated by scintillator sheets used as active material. The plates will be assembled together in a ‘*shashlik*’ structure Figure 2.12a. For SIS100 1,088 modules made of  $60 \times 60 \text{ mm}^2$  cells will however not cover the full angular acceptance, due to financial reasons.

Figure 2.12b shows invariant mass distributions of reconstructed photon pairs using the ECAL detector in simulation of 1.5 million UrQMD events in central Au+Au collisions

at 10 AGeV beam energy. The mass peak of the  $\pi^0$  is well pronounced, while the used statistics is insufficient for a proper  $\eta$ -meson reconstruction. Here, the significance of the  $\eta$ -meson peak is 2.7 and increasing the statistics to about  $10^7$  central Au+Au collisions at 10 AGeV beam energy should yield a satisfying reconstruction of the  $\eta$ -meson [99].

The PSD is designed to reconstruct the centrality and the reaction plane, along with its orientation for each events, which makes it decisive for event-by-event observable analysis, flow and centrality selection. It will determine the energy distribution of the projectile spectators and the forward going particles produced close to the beam rapidity during a collision.

Some of the main constraints, which needs to be fulfilled by the PSD are the following. First the detection of spectators in the range of 2-35 AGeV/c has to be achieved. Then the reaction plane should be reconstruct with an accuracy better than 40 degrees. In addition, the determination of the collision centrality should be given with an accuracy better than 10%.

To meet with these requirements, the PSD will use, like the ECAL, layers of lead and scintillator materials in a ‘*shashlik*’ structure, providing a very good and uniform energy resolution. 44 individual modules will be mounted together, each consisting of 60 lead/scintillator layers. A transverse area of around  $1.5 \times 1.5 \text{ m}^2$ , with a transverse granularity of  $20 \times 20 \text{ cm}^2$ , will allow to measure the collision spectators down to beam energies of a few AGeV/c. The performances of the detector [100] show that an energy resolution of  $\sigma_E/E < 60\% \sqrt{E(\text{GeV})}$  is achieved. In addition, high-rate capabilities and radiation hard photon detectors will be employed.

The left-hand side of Figure 2.13 represents the mechanical design of the PSD. The right-hand side illustrates the energy deposition from hadrons and positrons inside the PSD module at 30 GeV beam energy.

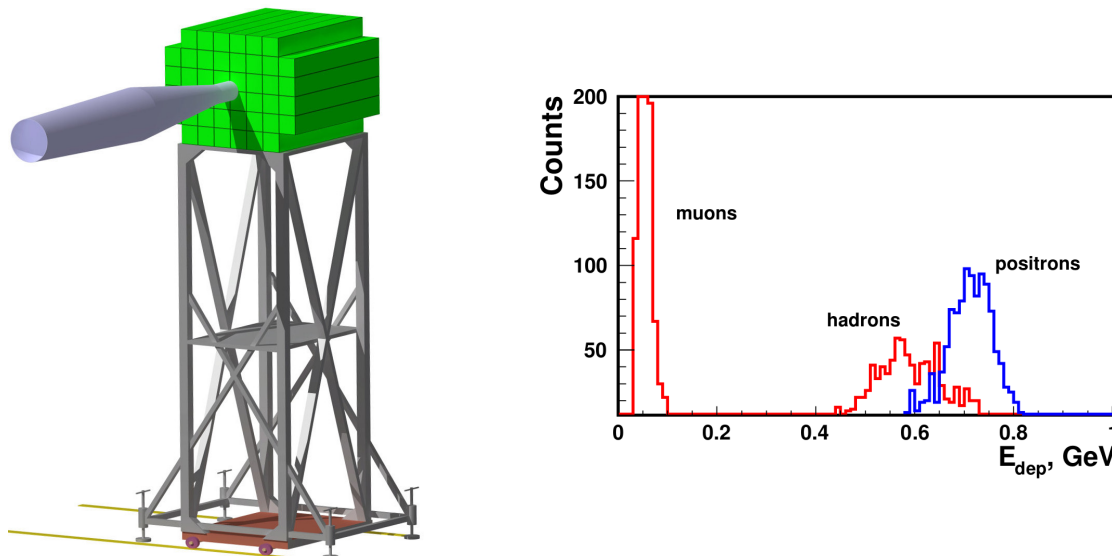


Figure 2.13: Left: Engineering view of the projectile spectator detector of CBM. Right: energy deposition in the full PSD module from hadrons and positrons at 30 GeV/c energy. Figures taken from [100].

### 2.3.9 Data Acquisition System

To hope observing rare probes of interest for CBM, such as dileptons, or multi-strange particles ( $\Xi$ ,  $\Omega$ ) at SIS100 energies and ultimately D-mesons or  $J/\Psi$  at the SIS300 energy regime, interaction rates up to 10 MHz are required, due to the small branching ratios and cross sections of the mentioned particles. At this interaction rate, a raw data rate of up to 1 TB/s is expected from the detector front end electronics. The limiting factor comes from the storage capacity, which requires an archival rate not exceeding about 3 GB/s. The raw data rate online thus have to be reduced by a factor of more than 300 [101].

The experimental challenge of CBM is the selection for archival of complex event topologies and signal signatures, using specific online triggers. For this purpose a dedicated data acquisition (DAQ) system has been designed. It is based on a self-triggered and free-streaming front-end electronics, delivering all signals above a pre-defined threshold to the DAQ. Together with the detector signals, a precise time stamp is added, which allows the grouping of the individual hits to separate events. Event selection and reconstruction will then be performed in software on a high performance computer farm (FLES), equipped with many-core CPUs and GPUs in the GSI Green-IT Cube.

The planned DAQ chain for the CBM experiment at SIS100 is illustrated in Figure 2.14. A prototype version will be tested during phase II of mCBM (see Section 3.3.6).

For this concept to work, partial event reconstruction in real time is required. Highly efficient reconstruction algorithms need to be developed, too. For example, track reconstruction, one of the most time consuming operation of the event reconstruction, will be performed with parallel algorithms for track finding and fitting.

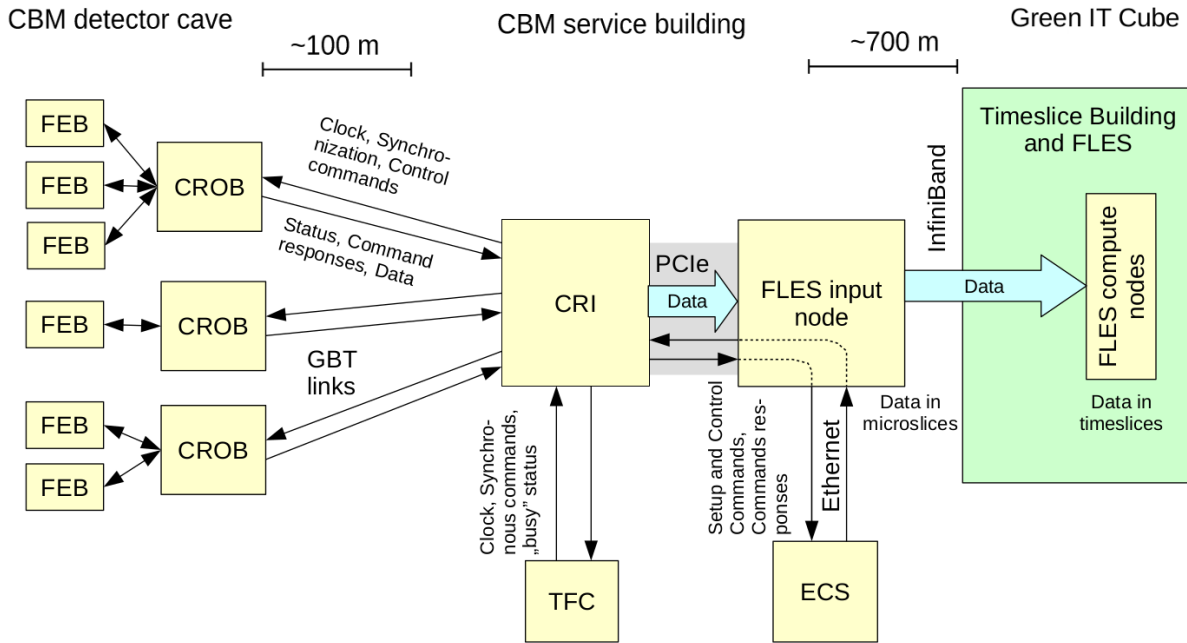


Figure 2.14: CBM DAQ chain for SIS100. A Common Readout Interface (CRI) will combine the functionalities of a Data Processing Board (DPB) and a First Level Event Selection (FLES) Input Boards (FLIB) in a single FPGA. It will serve as interface between the GigaBit Transceiver (GBT) links and FLES input nodes. Long range EDR InfiniBand will be used to transfer the micro-slices sent from the FLES input nodes to the Green IT Cube, where the data stream will be combined to time slices from the FLES computing nodes. Figure adapted from the mCBM@SIS18 proposal [102].

# Chapter 3

## The RICH detector of CBM

### 3.1 Principle of RICH detectors

#### 3.1.1 The Cherenkov effect

RICH detectors are based on the Cherenkov effect, discovered by P. Cherenkov in 1934 [103]. His work on the Cherenkov radiation allowed him to become the winner of the Nobel Prize in physics in 1958 along with I. Frank and I. Tamm.

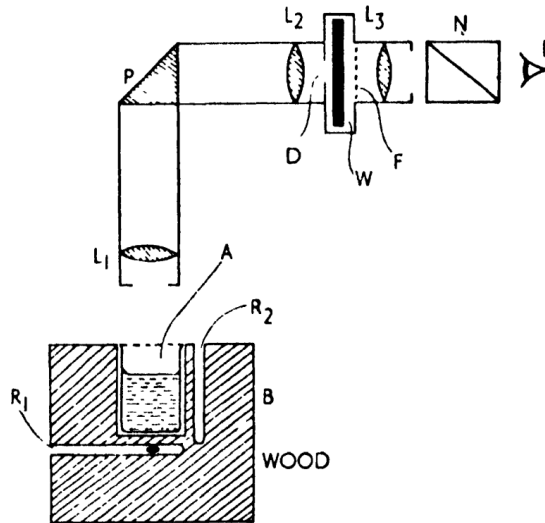


Figure 3.1: Experimental set-up used by P. Cherenkov for the characterisation of the radiation. A phial containing radium as gamma source is placed at R<sub>1</sub>, in a wood block. The liquid of interest is put in A. An optical system made of a collimator, a reflecting prism and a telescope was used to observe the radiation at E. A graded wedge, filters and a Nicol prism were used to determine its main properties. Figure taken from [104].

First documented observations of the emission of Cherenkov radiation were conducted by the French physician L. Mallet in 1926. Independently Cherenkov studied this phenomenon in his lab, too. Figure 3.1 illustrates Cherenkov's first experiment, with which he could observe Cherenkov radiation. He observed the Cherenkov light emitted from a phial containing radium, placed under different liquids. With an optical system made of

a collimator, a reflecting prisme and a telescope he measured the relative intensities of the light from the studied liquids. He also examined the polarisation of the emitted light and made a spectral analysis [104].

A qualitative description of the effect is given hereafter [104]. Suppose a charged particle entering a medium. At the atomic level, in the region close to the passage of the particle, the medium becomes polarised. At low velocities, the local polarisation vanishes, as the particle polarises another region of the medium. Due to the complete symmetry of the polarisation field, there will be no resultant field at large distances and thus no emission of radiation. At high velocities however, for a particle's velocity comparable to that of light, an asymmetry in the particle axis of propagation takes place. In this case a resulting dipole field will appear and each polarised atom will radiate an electromagnetic pulse one after the other. If the particle velocity is even higher than that of light, the radiated pulses will interfere constructively, similarly to wave interferences.

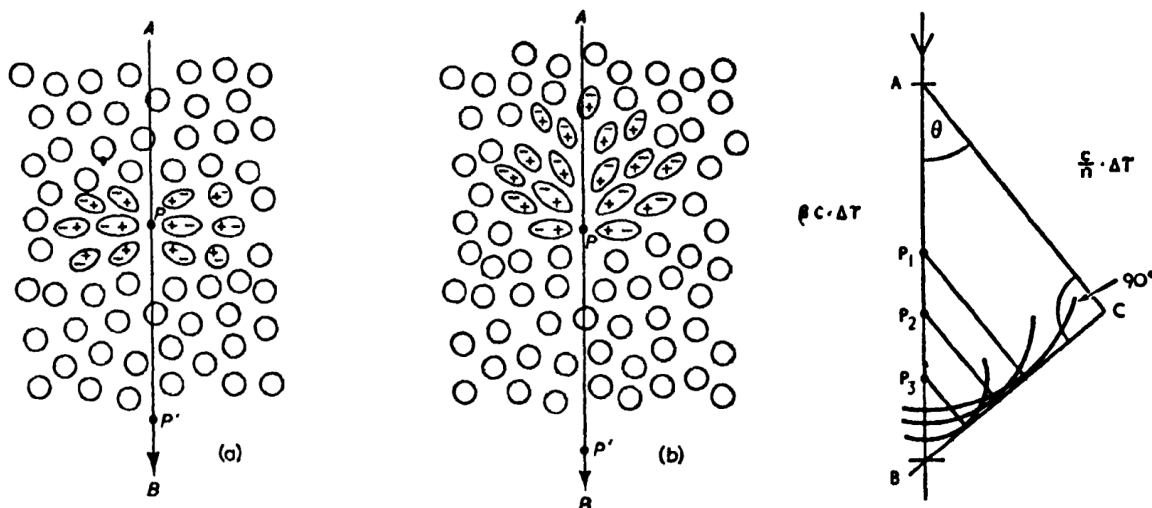


Figure 3.2: Illustration of a charged particle traversing a medium from A to B. At low velocities (a), the medium is locally polarised but no global effect is observed. At high velocities (b), the polarisation asymmetry is the source of an electromagnetic radiation. Right: Formation of the plane wave front (BC) at an angle  $\theta$ . The wave front is formed from wavelets stemming from emission points located along the particle path ( $P_1$ ,  $P_2$  and  $P_3$ ). Figures taken from [104].

The left and middle pictures of Figure 3.2 illustrate the polarisation phenomenon happening in the case of a charged particle travelling at low (left) and high (middle) velocities.

The right part of Figure 3.2 sketches how wavelets coherently interfere to form a plane wave front (BC). Each point located along the particle path ( $P_1$ ,  $P_2$  and  $P_3$ ) emits wavelets at a particular angle  $\theta$ , for which the wavelets will be coherent and combine on the plane wave front. The required condition for coherence to take place is that the particle travels from A to B in the same amount of time as light travels from A to C.

Geometrical calculations yields the Cherenkov relation:

$$\cos \theta_{Ch} = \frac{\Delta t \cdot \frac{c}{n(E)}}{\Delta t \cdot \beta c} = \frac{1}{\beta \cdot n(E)} \quad (3.1)$$

Equation 3.1 shows the dependence between the polar emission angle of Cherenkov photons ( $\theta_{Ch}$ ) produced by a charged particle and the refractive index ( $n(E)$ ) of the medium.  $\beta$  is the velocity of the particle relative to that of light.

The phenomenon was theoretically derived by I. Frank and I. Tamm afterwards. They calculated the number of photons produced by a charged particle per unit path length and per unit of energy [105]:

$$\frac{d^2 N}{dE dx} = \frac{\alpha Z^2}{\hbar c} \sin^2 \theta_{Ch} = \frac{\alpha Z^2}{\hbar c} \left( 1 - \frac{1}{(\beta \cdot n(E))^2} \right) \quad (3.2)$$

Where  $\alpha$  is the fine structure constant,  $Z$  is the electric charge of the particle in units of the elementary charge,  $\hbar = \frac{h}{2\pi}$  is the reduced Planck constant,  $N$  is the number of photons emitted with energy in the interval  $[E; E + dE]$  and  $l$  is the particle path length in the medium.

Applying the relation  $E = \frac{hc}{\lambda}$  to Equation 3.2 yields:

$$\frac{d^2 N}{d\lambda dl} = \frac{2\pi\alpha Z^2}{\lambda^2} \sin^2 \theta \quad (3.3)$$

Where  $\lambda$  is the wavelength of the emitted photons.

From Equation 3.1 and Equation 3.3, the following information can be extracted:

- Equation 3.1 shows that there is a threshold velocity  $\beta_{min} = 1/n$  below which no radiation can be emitted. In this case  $\theta_{Ch} = 0$ , that is the Cherenkov photons are produced in the direction of travel of the particle.
- A maximum emission angle can also be computed for ultra-relativistic particles from the relation:  $\theta_{Ch,max} = \cos^{-1}(\frac{1}{n})$
- Equation 3.3 reveals that the number of photons emitted per wavelength step  $d\lambda$  and per radiator length  $dl$  is inversely proportional to the square of the wavelength. The Cherenkov radiation is thus mostly emitted in the ultra-violet region. It can also be added that for the x-ray emission range the refractive index of media drops below 1, hindering Cherenkov emission.
- The number of emitted Cherenkov photons is proportional to the length of the medium, which is crossed

### 3.1.2 Evolution of detectors relying on the Cherenkov effect

The discovery of the Cherenkov effect led the way to new detector developments. The first use of Cherenkov radiation in particle physics coincides with the development of the first vacuum photomultiplier (PM). Gettings and Dicke proposed and demonstrated an original focusing system coupled to a PM in 1947, the first Cherenkov differential counter [106, 107]. Shortly after several types of Cherenkov counters were designed and improved, such as threshold Cherenkov counters, along with differential isochronous self-collimating (DISC) counters [105].

With an appropriate choice of the refractive index of the radiator and based on the particle momentum, threshold Cherenkov counters can differentiate light particles emitting Cherenkov radiation from heavy ones, which do not emit any radiation. The relation giving the threshold momentum in dependence on the particle mass and radiator refractive index is:

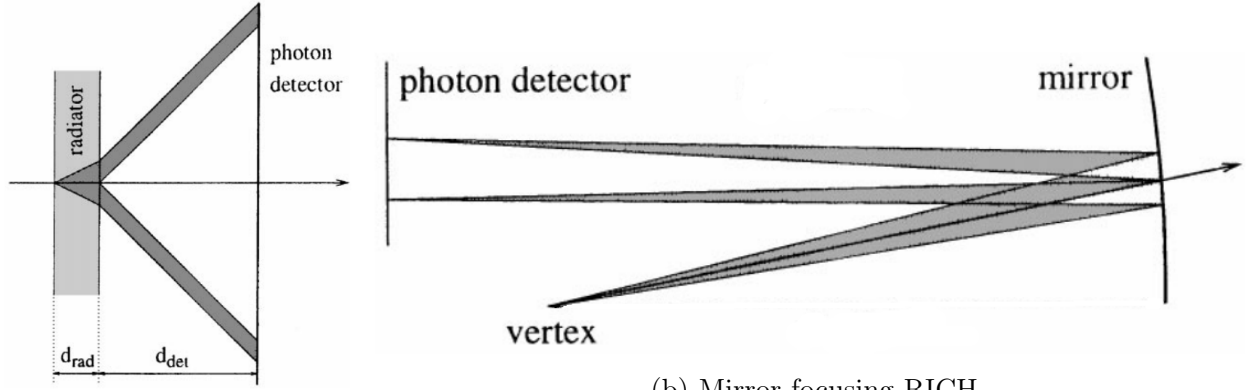
$$p = \frac{m}{\sqrt{n^2 - 1}} \quad (3.4)$$

The common part of these detectors is the use of a chamber filled with a radiator (for example Ne, Ar, CO<sub>2</sub> or N<sub>2</sub>), coupled to one or more photon sensors (for example PhotoMultiplier Tubes (PMTs)). Those Cherenkov counters are grouped in a category, which is called proximity focusing Cherenkov detectors, or threshold counters.

The combination of the good phase space acceptance of threshold counters with the better  $\beta$  resolution of differential counters was proposed by Roberts in 1960 [105, 109] (see Figure 3.3c). This association marked the beginning of Ring Imaging Cherenkov (RICH) counters, whose first practical prototype was developed by Seguinot and Ypsilantis [110]. Unlike the DISC detectors described above, which use annular diaphragm and chromatic corrector at the mirror focal plane, RICH counters make use of an additional focusing optical system. This method is called projective RICH detectors. Different types of focusing for RICH detectors are illustrated in Figure 3.3.

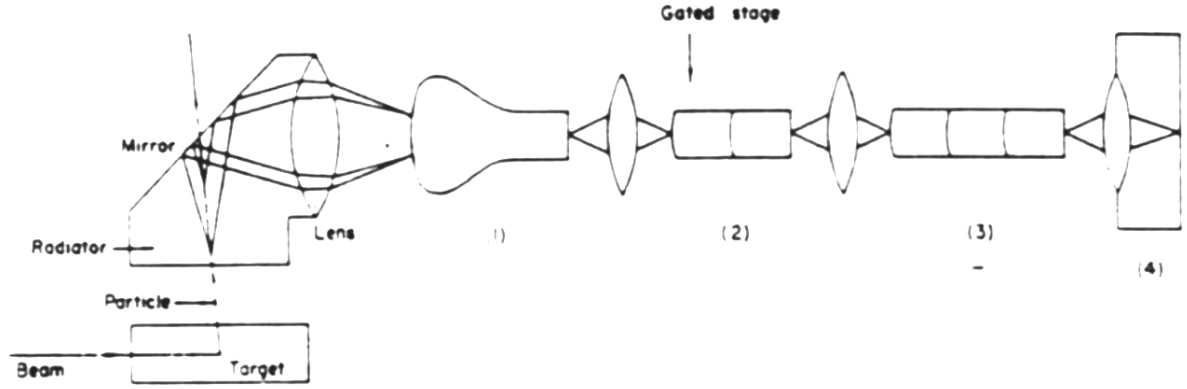
A special type of RICH detector is the Detection of Internally Reflected Cherenkov light (DIRC). For those RICH, the emitted Cherenkov photons are kept inside the radiator by total internal reflection and propagate to the photon sensors in a zigzag pattern, conserving their angle of reflection with the radiator surface. Those detectors are used for particle identification. They are compact and thus reduce both the material budget and the needed size of the subsequent detectors.

The first DIRC was proposed in 1994 for particle identification in B factories [111] and the design was first employed in the BaBar collaboration, which used the pinhole or proximity focusing technique to separate pions from kaons up to a momentum of 4.2 GeV/c [112]. Two other designs were later developed: the lens focusing and mirror focusing designs.



(a) Proximity focusing RICH

(b) Mirror focusing RICH



(c) Focusing RICH in its original version proposed by Roberts. 1: stage image intensifier, 2: 2-stage gated intensifier, 3: 3-stage intensifier, 4: photo-camera.

Figure 3.3: Different types of focusing RICH detectors. Figures taken from [105, 108].

The PANDA experiment, one of the pillars of FAIR (see Section 2.2), will employ a DIRC detector in the lens focusing mode with a lens made of LaK33B to improve the focusing. It will separate pions from kaons up to 3.5 GeV/c in an angular coverage ranging from 22° up to 140°.

The design of the barrel DIRC is presented in Figure 3.4. The Endcap Disc DIRC will encompass four identical quadrants made of a large fused silica radiator and 27 readout modules. The achieved Cherenkov angle resolution is foreseen to range between 1.2 and 2 mrad for a track with 16 to 25 detected photons. The Cherenkov opening angle  $\theta_c$  of a charged particle entering a radiator can be determined by the relation [113]:

$$\theta_c = \arccos(\sin(\theta_n) \cdot \cos(\Phi_{az}) \cdot \cos(\phi) + \cos(\theta_n) \cdot \sin(\phi)) \quad (3.5)$$

where  $\theta_n$  is the particle angle relative to the normal of the radiator plane,  $\Phi_{az}$  the azimuthal angle between the photon path and the particle trajectory on the radiator plane and  $\phi$  the angle between the photon path and the radiator surface.

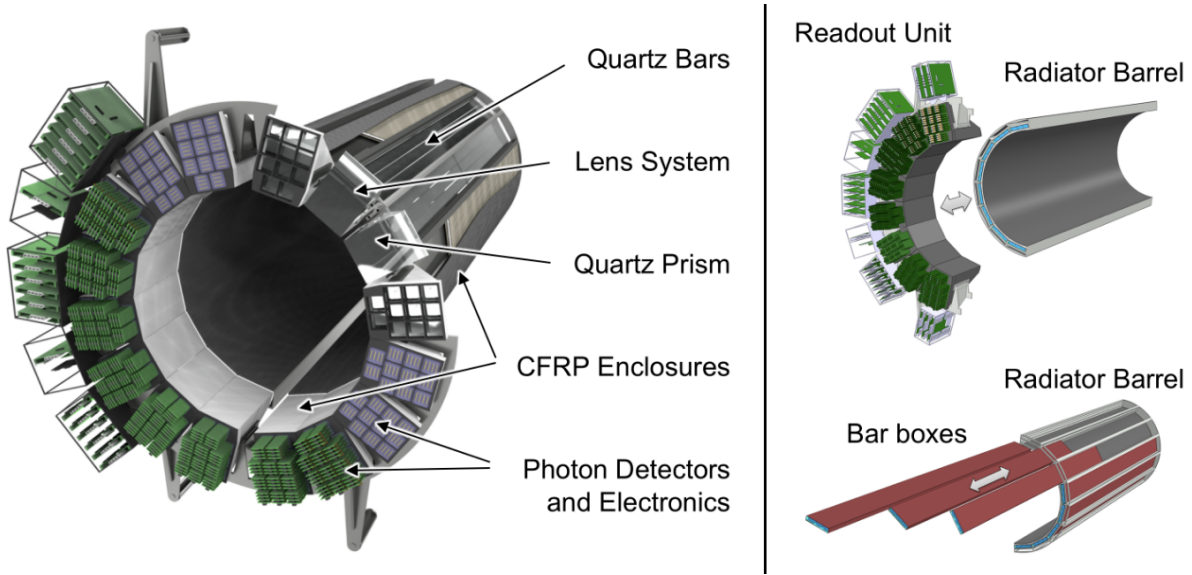


Figure 3.4: Schematic baseline design (left) and mechanical design (right) of the PANDA barrel DIRC. Figures taken from [114].

### 3.1.3 Functioning principle of the CBM RICH detector

The CBM RICH is based on the projective RICH principle and employs a radiator with spherical mirrors as focusing elements. Cherenkov photons are emitted in the form of a cone throughout the passage of the particle in the radiator. The cone is reflected by the spherical mirrors and focused on a photon detector plane placed at the mirror focal length, corresponding to half the spherical radius. In this configuration, the cone is observed as a ring on the photon sensor plane. The ring radius is in first approximation given by [110]:

$$r = f \cdot \tan(\theta_{Ch}) = \frac{R}{2} \cdot \tan(\theta_{Ch}) \quad (3.6)$$

Where  $r$  is the ring radius,  $f$  the focal length of the mirrors,  $\theta_{Ch}$  the Cherenkov emission angle of the particle and  $R$  the radius of curvature of the mirrors.

In the approximation of small angles and the mirror focal length being constant, it can be derived from Equation 3.6 [115]:

$$r = f \cdot \sqrt{2 - \frac{2}{n} \sqrt{1 + \left(\frac{mc}{p}\right)^2}} \quad (3.7)$$

With  $m$  and  $p$  the particle mass and momentum, respectively.

Thus, knowing the particle momentum and the ring radius resulting from the passage of the particle through the detector, the CBM RICH can be used for particle identification. For the CBM experiment, the momentum of the particle is given by the tracking information from the STS detector (see Section 2.3.3).

Integrating the Frank-Tamm relation (Equation 3.2), over the energy  $E$  and the path length  $l$  and supposing a constant Cherenkov angle (that is  $n\beta$  constant and neglecting the dispersion of the medium), it can be derived:

$$N = N_0 \cdot L \cdot \sin^2(\theta_{Ch}) \quad (3.8)$$

Where  $N$  corresponds to the number of detected photons and  $L$  the radiator length.  $N_0$  is the so called ‘figure of merit’, first introduced in [110] and describing the quality of RICH detectors. It is used as a mean of comparison between different RICH detectors. It is defined as:

$$N_0 = \frac{\alpha}{\hbar c} \int_{E_1}^{E_2} \epsilon(E) \epsilon_T(E) \epsilon_R(E) dE \quad (3.9)$$

Where  $\epsilon$  is the quantum efficiency for photon detection,  $\epsilon_T$  the transmittivity of the optical medium and  $\epsilon_R$  the reflectivity of the mirrors.

In Equation 3.2, the number of photons produced by a charged particle per unit path length and per unit of energy depends on the refractive index, which, due to the chromatic dispersion effect, depends on the energy as well. Equation 3.7 links the refractive index with the ring radius and can thus imply a loss in the ring radius resolution. The first Cherenkov counters, like DISC counters, corrected directly for this error. For RICH detectors usually a compromise has to be made between the photon yield and the ring radius resolution.

## 3.2 Physics objectives and detector requirements of the CBM RICH detector

RICH detectors have already been used in a wide variety of experiments, with various physics programs [116].

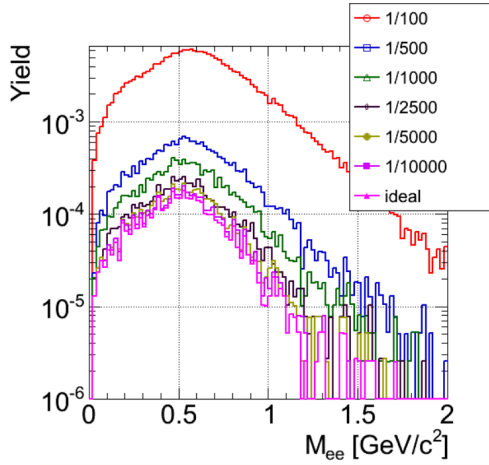
RICH detectors are used for example for flavours physics and CP violation measurements, via the hadron identification, such as in the ALICE, BaBar, BELLE, LHCb and NA62 experiments. COMPASS, MIPP and PANDA use RICH for the measurements of particle production rates and the study of hadron spectroscopy. In COMPASS and HERMES, RICH detectors are used to improve the charmed-hadron purity, via the separation of pions from kaons. RICH principles are also employed in neutrino physics, where a water Cherenkov detector is used for neutrino measurements in K2K and T2K.

In heavy ion physics, electrons are used as probes of the created fireball and are identified by RICH detectors. The pioneer experiment, who employed for the first time RICH detectors for electron identification is the CERES experiment. Other experiments followed, like JLAB, RHIC and soon CBM. The CBM-RICH requirements are reviewed in detail in the technical design report [94]. Some of the physics prerequisite and environmental limitations are specified in the following.

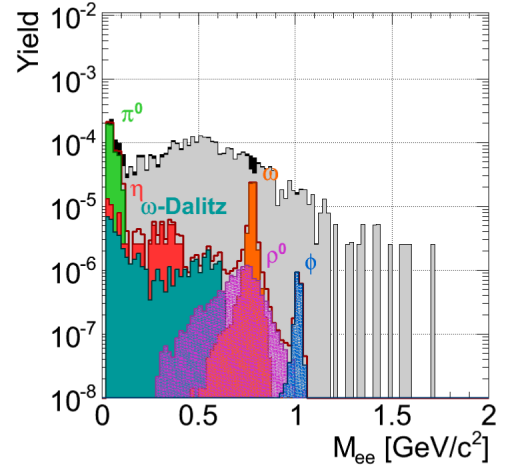
### 3.2.1 Physics objectives

One of the key probes for the CBM experiment are lepton pairs due to their penetrating nature, as discussed in Section 1.3.2. In the particular case of the RICH detector, dedicated to the identification of dielectrons, light vector mesons (such as the  $\rho^0$ ,  $\omega$  and  $\phi$  mesons), charmonium and direct photons via their conversion pairs can be investigated.

A key factor in the measurement of the low mass vector mesons is the pion suppression power of the detector. A study on the impact of the pion suppression factor on the combinatorial background underlying the low mass vector meson measurement has been conducted [94]. The pion suppression factor is defined as the number of pions reconstructed in the STS detector, with a track projection lying in the RICH acceptance divided by the number of pions wrongly identified as electrons. For this study the electron identification in the RICH software was performed using Monte-Carlo information. A certain pion suppression factor of 100; 500; 1,000; 2,500; 5,000; 10,000 and ‘ideal case’ was assumed. Figure 3.5a depicts the situation after all reconstruction cuts were applied for different pion suppression factors. Clearly a factor 1/5,000 is desirable, as with such a factor the background is not dominated by pion misidentification. Figure 3.5b shows, as a comparison, the invariant mass spectrum of electron pairs with the contributions from each physical signals in different colours for a full simulation of 100,000 events central Au+Au collisions at 8 AGeV beam energy after applying all reconstruction cuts.

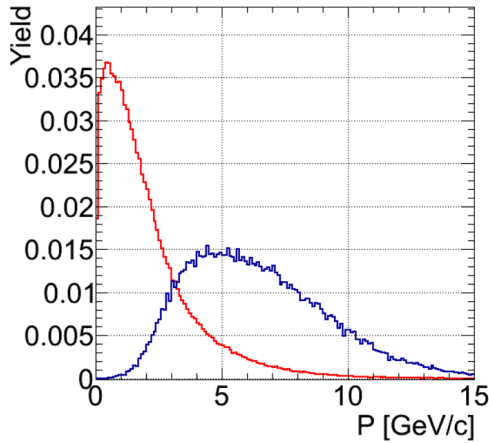


(a) Combinatorial background for different pion suppression factors after all reconstruction cuts are applied for central Au+Au collisions at 8 AGeV beam energy.

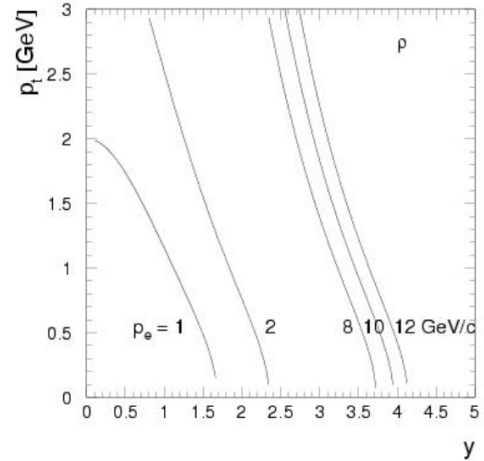


(b) Invariant mass spectra after all reconstruction cuts are applied for 100,000 central Au+Au collisions at 8 AGeV beam energy.

Figure 3.5: Figures taken from [94].



(a) Momentum distribution for electrons from the decay of  $\rho$  (red) and  $J/\Psi$  (blue) mesons for Au+Au collisions at 25 AGeV (SIS300 regime). The parameters of the PLUTO generation can be found in [94].



(b) Transverse momentum vs rapidity for the  $\rho$  meson. The lines represent constant momenta for the decay electrons. The centre of mass rapidities for 8, 15 and 25 AGeV beam energies amounts to 1.42, 1.75 and 2 respectively.

Figure 3.6: Figures taken from [94].

The momentum distribution of the  $\rho$  and  $J/\Psi$  mesons for Au+Au collisions at 25 AGeV is depicted in Figure 3.6a and shows the momentum range necessary for the electron identification. A momentum range up to 8 GeV/c will allow a measurement of the  $\rho$  meson in the full forward hemisphere also at lower energies. At these energies, the nominal magnetic field of CBM may be reduced to 70% in order to increase the acceptance for low momentum electrons while still keeping sufficient momentum resolution [94].

Several transverse momentum distributions in dependence on rapidity for the decay electrons of the  $\rho$  meson are shown in Figure 3.6b. Feasibility studies on the measurements of other physics signals such as the charmonium and direct photons are presented in [94].

The CBM RICH detector will thus provide electron identification for momenta up to 8 GeV/c with a pion suppression factor of at least 100. Its combination with the TRD increases the momentum range even further and the pion suppression factor up to 1,000 - 5,000.

### 3.2.2 Environmental conditions

In addition to the requirements expected to be achieved for the study of the discussed physics signals, the CBM RICH must satisfy specifications imposed by the environment of the CBM experiment.

First the high interaction rates, up to 10 MHz, are the source of high radiation levels and will produce about 1,000 charged particles per collisions in central Au+Au collisions at SIS300. These charged particles include secondary electrons, but also neutron. They are produced upstream of the detector and cause a high track density, translating into a high ring density in the RICH detector.

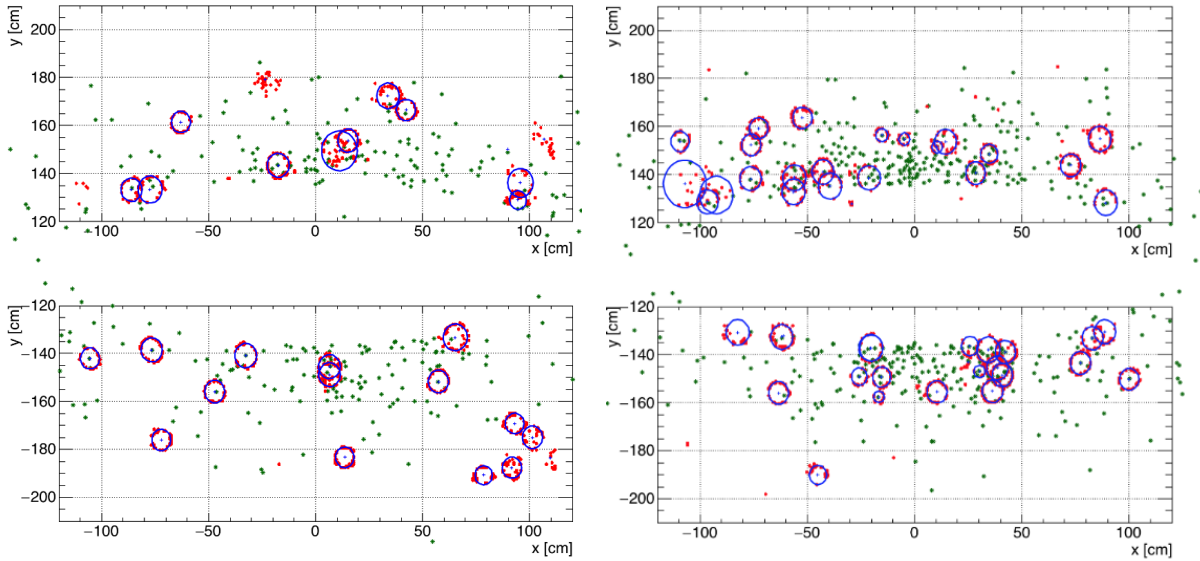


Figure 3.7: Typical event displays recorded by the upper and lower photon detector plane, for central Au+Au collisions at 8 (left) and 25 (right) AGeV beam energies. Blue circles: reconstructed rings, red points: photon detector hits, green points: reconstructed track projections. Figures taken from [94].

The secondary particles might decrease the detector efficiency, damage the mirror reflective coating and the glue used for fixing the mirrors, decrease the lifetime of the photon detectors and harm the electronics. It might also dissociate the radiator gas. Figure 3.7 shows the high ring densities seen by the upper and lower photon detectors in the RICH detector for simulated central Au+Au collisions at 8 (left-hand side of the

figure) and 25 (right-hand side) AGeV beam energies.

In order to limit the production of secondary particles by the detector, the material budget needs to remain as low as possible for both the RICH detector and the beam pipe. This will thus reduce background for the detectors positioned downstream of the CBM RICH. Figure 3.8 illustrates the material budget of the RICH detector, for the RICH set-up presented in [94] (left and middle) and for an optimised RICH geometry specified in [117].

Furthermore a full azimuthal angle coverage is required as well as a polar angle coverage of  $2.5^\circ \leq \theta \leq 25^\circ$  with a factor 1.5 in the x-direction due to the bending power of the magnet. Simulations of single particles stemming from the primary vertex with a transverse momentum  $p_t \leq 3$  GeV/c were conducted to compute the acceptance of the RICH detector.

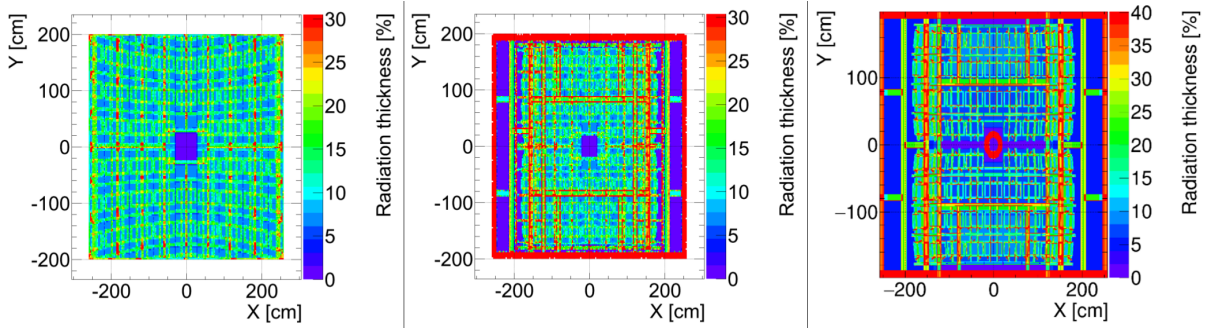


Figure 3.8: Material budget of the RICH detector. Left: Material budget at the time of writing of the RICH Technical Design Report, as seen for inclined particles coming from the primary vertex. Middle: Material budget at the time of writing of the RICH Technical Design Report, as seen for parallel tracks. Right: Material budget of the RICH detector for a more recent geometry. The major elements contributing to the material budget belong to the mirror supporting structure. This matter is still a subject of optimisation. The red frame at the edges of the figure is not in the acceptance any more. Figures taken from [94] (left and middle) and [117] (right).

Finally, the detector is placed in the vicinity of the magnetic stray field. The stray field might reduce the collection efficiency at the dynodes of the photon detectors, reducing the detection efficiencies. The RICH detector will also be exchanged approximately on a yearly basis with the MUCH detector, for independent dilepton measurements in the CBM energy range. The movements and stress applied during the exchange of the RICH with the MUCH may misalign the individual mirror tiles.

### 3.3 Detector design

To meet the physics and environmental specifications, a dedicated RICH detector has been designed and is being built for the future CBM experiment [118, 119]. The detector will consist of gaseous  $\text{CO}_2$  as radiator, spherical mirrors with reflective coating as focusing elements and a cylindrical photon detector plane, made of multianode photomultiplier tubes (MAPMT). Figure 3.9 represents the latest geometry of the RICH detector used in the simulation framework of CBM.

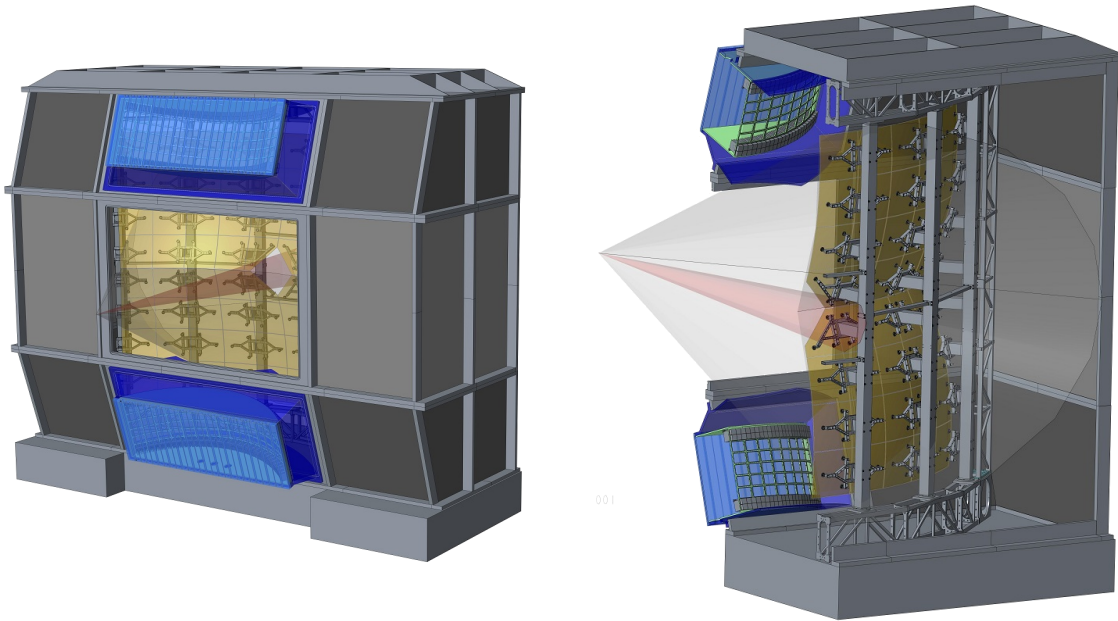


Figure 3.9: Front (left) and side (right) views of the CBM RICH detector designs. The geometrical acceptance is coloured in transparent grey, the mirror wall in yellow and the photon detector structure in blue. The detector and mirror supporting structures can be visualised, along with the photon sensor designs. Figures taken from [120].

An overview of the main components of the RICH detector is given in Table 3.1. In the following the different detector parts are discussed and performances are illustrated.

Concept	RICH gaseous detector
Dimensions	2 m × 5.14 m × 3.93 m (length × height × width)
Acceptance	0 - 35° (horizontal) and 0 - 25° (vertical)
Radiator	CO <sub>2</sub> gas at slight overpressure of ~ 2mbar
Radiator volume	~ 34 m <sup>3</sup>
Radiator length	1.7 m
Focussing elements	Spherical mirrors
Mirror design	Glass mirror (SIMAX), 6 mm thick Al+MgF <sub>2</sub> coating
Mirror effective area	14.4 m <sup>2</sup>
Focal length	1.5 m
Photon sensor	MAPMTs (H12700B-03 from Hamamatsu)
Active camera area	2.4 m <sup>2</sup>
Number of channels	~ 70,000 channels

Table 3.1: Summary of the CBM-RICH detector main components. Table inspired from [94].

### 3.3.1 Detector geometry and mechanics

The dimensions of the RICH detector will be 2 m × 5.14 m × 3.93 m (length × height × width) [94], which has a total volume of roughly 40 m<sup>3</sup>. The entrance window of the detector will offer an acceptance, which covers a range of scattering angles of up to 35° in the horizontal plane and up to 25° in the vertical plane, with respect to the target position. The angle in the horizontal plane is extended due to the widening of the particle tracks from the magnetic field. The detector will be filled with CO<sub>2</sub> gas with a slight overpressure of a few mbar (~ 2 mbar). A radiator length of 1.7 m and a radiator volume of about 34 m<sup>3</sup> are provided.

The refractive index of the radiator equals to  $n = 1.000449$  (at 0°C and atmospheric pressure), giving a Lorentz factor of  $\gamma_{th} = 1/\sqrt{1 - 1/n^2} = 33.4$  and yielding a saturated Cherenkov angle of  $\cos^{-1}(1/n) = 1.72^\circ$ . Thus the Cherenkov threshold momentum for pions amounts to [94]:

$$p_{th} = \gamma_{th} \cdot m_0 \cdot \frac{c}{n} = 4.66 \text{ GeV}/c \quad (3.10)$$

In comparison the Cherenkov threshold momentum for electrons and kaons is  $p = 17.1 \text{ MeV}/c$  and  $p = 16.5 \text{ GeV}/c$ , respectively. Furthermore the emitted Cherenkov radiation is absorbed by CO<sub>2</sub> for  $\lambda \leq 180 \text{ nm}$ , which coincides with the wavelength region, where effects of chromatic dispersion become more severe [94].

Figure 3.10 shows the ring radius versus the particle momentum in both the simulated and the beam test cases. In the shown momentum range ( $1 \leq p \leq 10 \text{ GeV}/c$ ) electrons emit Cherenkov photons and can be identified to 100% up to 4.7 GeV/c. At this point pions start emitting Cherenkov photons. For momenta below 10 GeV/c, the radii from pions remain small relative to the radii from electrons.

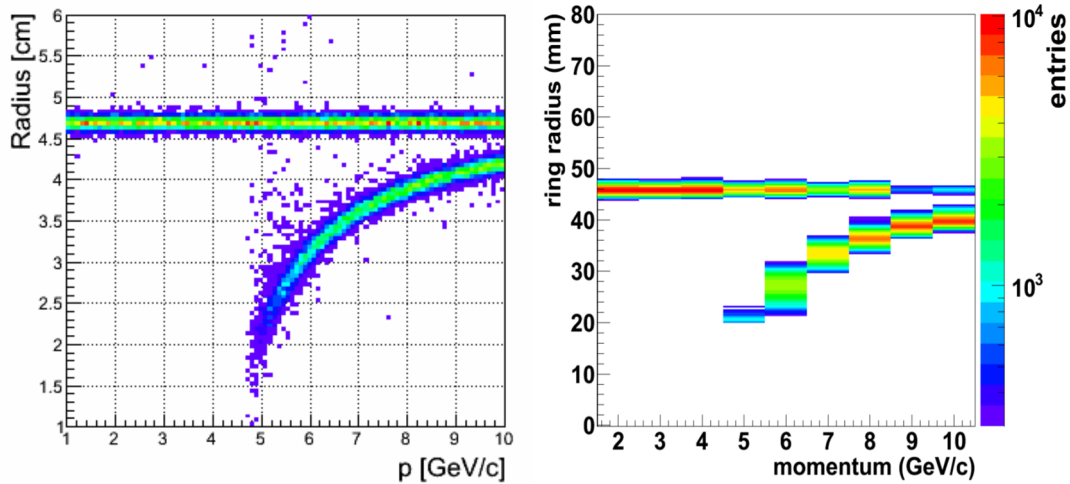


Figure 3.10: Radius versus incident particle momentum distributions in the simulation (left) case and with collected data from beam test (right). Figures taken from [121].

A good qualitative agreement is observed between the two cases of Figure 3.10. In addition, a pion identification efficiency was introduced to quantify the performances of the detector. It is defined as the number of pions identified as electrons over the total number of pions, at an electron efficiency of 95%. The pion suppression factor is defined as the inverse value of the pion identification efficiency.

In the beam test at CERN in 2012, the RICH test box yielded a pion efficiency below 0.00025 for all momenta below 10 GeV/c. These results are consistent with the results obtained from simulations and reveal a very good pion suppression capability of the detector.



Figure 3.11: RICH mirror supporting structures. Prototypes of supporting pillar (left) and mirror supporting frame (middle) are built and undergo tests. Right: detector and mirror supporting structures implemented in a detector model. Figures taken from [120].

The radiator box needs to be reinforced to allow its craning, when exchanging the RICH and MUCH detectors. The decided solution is the use of a frame reinforced with channel bars covered with rigid panels. Some panels can be removed to perform mainte-

nance works on the equipment placed inside. The front and rear panels are planned to be made out of kapton foil or, for the rear panel, to be a thin PCB plate. The supporting frame of the detector is sketched on the right-hand side of Figure 3.11.

In addition to the detector frame, a supporting frame for the reflective mirrors was developed. Figure 3.11 illustrates the latest prototypes of the RICH mirror supporting pillar (left) and the mirror support and mounts (middle). It also displays the mirror and detector supporting frames (right). The supporting structure will be made of pillars, each pillar supporting two mirror columns. This design will allow for a structure weight of 125 kg, which is an estimated weight for the pillars and mirror supporting frames without the mirror mounts and which provides a radiation length of  $\sim 4.4\%$  on average. Glue studies are also conducted to select a glue, which is resistant to mirror loads and radiation hard. Prototypes of both frames were produced and are being optimised by the PNPI institute.

### 3.3.2 Mirror wall

The mirror wall (visible on Figure 3.9) consists of 80 glass mirror tiles divided into two halves made of 40 tiles each. The halves are split into four rows of ten tiles each. The spherical focusing mirror tiles have a radius of curvature of 3 m and are made of a SIMAX glass substrate. They will be coated with a thin aluminium layer, providing good reflection properties in the UV-region. An additional layer of  $\text{MgF}_2$  is applied to prevent the oxidation of the aluminium layer, which strongly absorbs the Cherenkov emission in the UV region. Following mirror reflectivity studies [94], mirrors from JLO Olomouc have been ordered to be used in the beam test (see Section 4.2.2).

The mirror tiles will be trapezoidal and grouped into two categories depending on their dimensions. The two inner mirror rows will comprise trapezoidal mirrors of  $430/425.6$  mm  $\times$  425 mm with a reflective surface of  $0.182$  m<sup>2</sup>. The two outer mirror rows will have dimensions of  $425.5/412.6$  mm  $\times$  425 mm, yielding a reflective surface of  $0.178$  m<sup>2</sup>. The total effective mirror area will thus be  $14.4$  m<sup>2</sup>. Figure 3.12 summarises the dimensions of the two tile types.

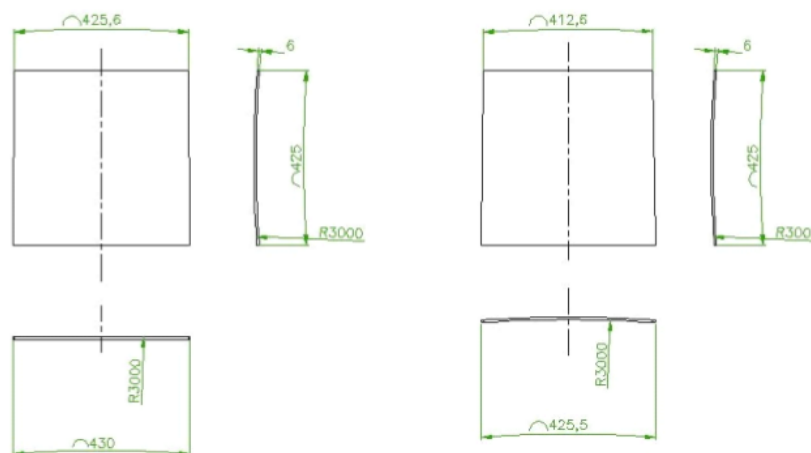


Figure 3.12: Dimensions of the mirror tiles. Figure taken from [94].

Shrinking the dimensions of the mirror segments makes the manufacturing easier and

reduces the gaps between mirrors down to 3 - 4 mm.

The mirror mounts (Figure 3.11, middle) will be fixed at three points on the back side of the tiles, forming a triangle. This will allow single tile rotations around the x and y axes of each individual tile to ensure global alignment between the mirrors. For optimal detector operation, an alignment of the mirror wall in two steps is foreseen, inspired by the strategy of the COMPASS experiment [122, 123].

Studies in beam time were conducted to determine the tolerated values of mirror displacements [124]. A mirror system with displacements of about 1 mrad around both the horizontal and vertical axes of mirror tiles relative to the neighbouring ones is accepted.

The principle of the alignment is to orient each mirror tile, such that the centre of curvature of all tiles coincide in one virtual point. During the initial mirror alignment, at the time of the detector assembly or during shut-down periods, a theodolite in auto-reflection method is planned to be employed [125]. This method provides a global accuracy of 0.1 mrad, ensuring an aligned mirror wall for optimal detector operation.

However this procedure is very time consuming (about 10 mirrors per day can be aligned) and access to the mirrors is required, exposing the mirrors to potential damages and pollution [126]. In order to monitor the mirror alignment, two approaches from the COMPASS [127] and the HERA-B [128] experiments will be employed in parallel. Their functioning principles and results obtained in the case of the CBM RICH detector are presented in Chapters 4 and 5.

### 3.3.3 Photon detector plane

A crucial requirement for the operation of the CBM RICH detector is a high efficiency in single photon detection. To that extent Multi-Anode Photomultiplier Tubes (MAPMTs) were selected as photon sensors. The photon sensor chosen for the CBM RICH is the H12700 MAPMT from Hamamatsu. Its inner structure and functioning principle is illustrated on Figure 3.13.

MAPMTs are PMTs with a quadratic photocathode window and a separated dynode and anode design. The H12700 has  $8 \times 8$  quadratic pixels with a surface of  $6 \times 6 \text{ mm}^2$  and a total effective area of  $48.5 \times 48.5 \text{ mm}^2$ . A blue-enhanced super-bialkali photocathode is used in parallel with a UV glass, to improve photon detection, given that Cherenkov radiation is mainly emitted in the ultra-violet region.

The main characteristics of the chosen H12700 MAPMT along with the requirements on the performances are listed below [131]:

- Quantum efficiency. The ring finding and ring resolution efficiencies rise up with an increased number of photons detected per ring, therefore increasing the efficiency of the ring-track matching algorithm and the performance of the detector (see Section 3.3.5). For those reasons a high quantum efficiency and single photon detection efficiency are required. More than 25% peak quantum efficiency for the bialkali photocathode type is required.

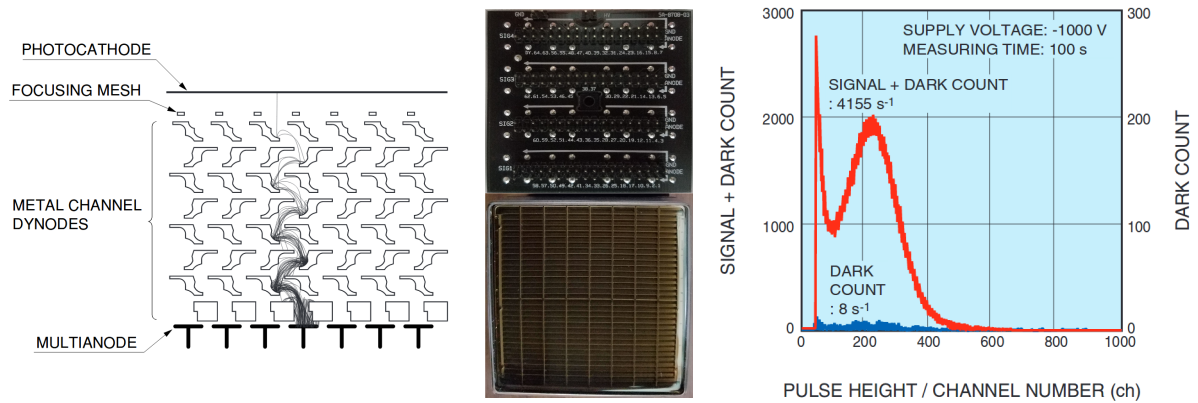


Figure 3.13: Left: Inner structure of the Multi-Anode Photomultiplier (MAPMTs) H12700 from Hamamatsu and typical electron trajectories. The illustrated metal channel dynodes present very low crosstalk during the multiplication stages, compared to other dynode types. Figure taken from [129]. Middle: front and rear views of the MAPMT. Right: single photoelectron spectrum. Figure taken from [130].

- Collection efficiency. This is the probability that a photoelectron produced by the photoelectric effect in the photocathode reaches the first dynode and creates an output signal.
- Dark current. This is the result of thermal electrons created from the photocathode, when high voltage is applied on a PMT. The electrons are accelerated to the first dynode and are responsible for a measurable current at the anode, referred to as dark current. At a supply voltage of 1kV, a limit for the dark current of less than 5 nA is specified. Moreover a very low dark count rate (average  $\leq 100$  Hz/pixel and individual  $\leq 1$  kHz/pixel) is required, given the self-triggered DAQ system of CBM.
- Single photoelectron spectrum. It corresponds to the output signal collected at the anode, which is seen as a pulse, whose shape depends on the PMT characteristics. A parameter of interest used to characterise single photoelectron spectra is the peak-to-valley ratio. It is the ratio between the single photoelectron peak and the valley separating it from the noise. A clear single photon peak and a peak-to-valley ratio larger than 1.2 in 61 out of 64 channels is needed (Figure 3.13, right).
- Afterpulsing. Sometimes, shortly after a pulse is measured at the anode, a secondary pulse can also be observed. Those pulses come from the positively charged ions, generated by thermal electrons or photoelectrons. The ions hit the photocathode, producing additional electrons, which are accelerated in the dynode structure and are a source of additional signals in the anode. These signals are called afterpulses. An afterpulse probability below 5% in a time span from 70 ns up to 1.7  $\mu$ s after the signal is required.
- Time resolution. The time resolution is characterised by two parameters. The rise time, corresponding to the time for the output signal to rise from 10% to 90% of the peak amplitude. The transit time is the time interval between the photon arrival on the entrance window and when the corresponding peak is read out at the anode.

At the highest rate in CBM, the time interval between events will be less than 100 ns. A typical transit time spread of  $\sim 1$  ns is required and compatible with the Hamamatsu data sheets, revealing a transit time spread of 0.35 ns [130].

- Life time. It corresponds to the integrated anode charge within one year of operation at maximum hit rates. A life time superior than  $10 \text{ C/cm}^2$  is required.
- In addition, an average gain at a supply voltage of 1 kV larger than  $0.8 \times 10^6$  at an operation rate up to 700 kHz is required.

Table 3.2 summarises the main properties of the H12700 MAPMT:

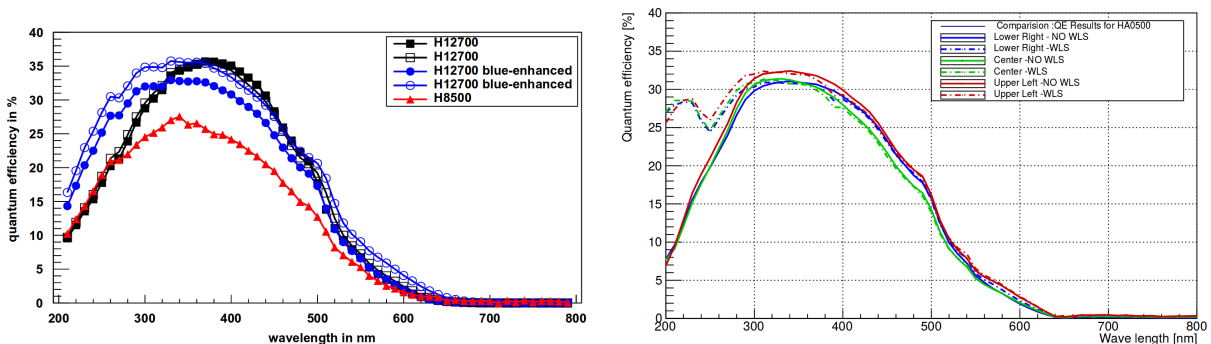
Multi-Anode PMT	H12700B-03		
Photocathode material	Blue-enhanced Super-Bialkali		
Window material	UV glass		
Dynode structure	10-stage metal channel		
Spectral response range	185 nm to 650 nm		
Peak quantum efficiency at about 380 nm	33%		
Anode	Gain		$1.5 \times 10^6$ (typ.)
	Dark current	per channel	0.1 nA (typ.)
		in total	6 nA (typ.)
	Time response	rise time	0.52 ns
		transit time	4.9 ns (typ.)
		transit time spread	0.35 ns (typ.)

Table 3.2: Hamamatsu H12700 main specifications. The figures are obtained for a tungsten filament lamp operated at 2,856 K and a MAPMT supply voltage of 150 V at the first dynode. Table inspired from [130].

Thorough measurements have been conducted, comparing the H12700 MAPMT to other PMTs, in particular also the H8500, the previous MAPMT of reference for the CBM RICH detector. The tests showed superior performances in most aspects, allowing an overall higher quantum efficiency and very good improvements in the UV region, better spacial resolution, less crosstalk, shorter after pulsing and improvements in the single photon response. Figure 3.14a shows a quantum efficiency comparison of the H12700 MAPMT with two differently configured photocathodes to the H8500 MAPMT.

Wavelength shifting (WLS) films are also planned to be employed on some MAPMTs to increase the quantum efficiency in the UV region. The p-terphenyl WLS films are organic materials absorbing incoming photons and re-emitting them via fluorescence to larger wavelength values. The performances of MAPMTs coated with WLS films revealed a significant increase in the wavelength region  $180 \text{ nm} \leq \lambda \leq 280 \text{ nm}$ , while no modifications

in the quantum efficiency were observed in the wavelength region  $\lambda > 280$  nm. Compared to uncoated PMTs, the photon yield increases by  $\sim 20\%$  [132, 133]. Figure 3.14b displays the quantum efficiency for bare and WLS coated H12700 MAPMTs.



(a) Comparison of quantum efficiencies for several H12700 MAPMTs and one H8500, used as reference. Two of the H12700 MAPMTs have a so-called blue shifted or blue enhanced super-bialkali photocathode for higher quantum efficiency at low wavelengths. An overall higher quantum efficiency is observed for the H12700 MAPMT, due to the super-bialkali photocathode. Figure taken from [119].

(b) Impact of wavelength shifting films on the QE of the H12700 MAPMT. The solid lines shows the QE for a MAPMT without the WLS film, the dashed line shows the QE with the WLS film. The colours correspond to different measurement positions on the photocathode: blue in the lower right corner, green in the center, red in the upper left corner. Figure taken from [134].

Eleven hundred H12700 MAPMTs were ordered for the CBM RICH detector and a list of specifications was set to ensure a high quality [135]. Upon delivery the MAPMTs were tested and those fulfilling the requirements kept. To that end, a single photon scanning test bench was built for the characterisation of each MAPMT [86].

The MAPMTs are planned to be distributed over two cylindrical shapes (one per mirror half), which was decided due to an overlap of the electronics modules placed behind them and is the result of an optimisation study [86]. The dimensions of the cylinders were adjusted to cover the detector acceptance and to be integer multiples of the readout modules presented in the following section. It was decided to distribute the MAPMTs over 14 strips in the horizontal direction, each with 7 modules spread in the vertical direction.

### 3.3.4 Readout chain and electronics

The MAPMTs will be read out with so-called DIRC RICH (DiRICH) readout modules, a common development for the CBM-RICH, HADES-RICH and PANDA-DIRC detectors [136, 137] (see Figure 3.15 and Figure 3.16). One such MAPMT readout module combines 6 MAPMTs and the readout on one PCB board (also referred to as the backplane), providing mechanical fixation for the PMTs. The PCB design is also gas and light tight, thus serving as border to the radiator gas volume. On its rear side, the backplane serves as interface for the readout front-end electronics, linking the different front-end electronics modules, which are plugged in. The PCB board thus minimises electronic cables, as it transfers data, power and clock information between the front-end modules. This makes the overall design very compact.

Three different front-end electronic modules are connected to this PCB board and are used in the readout chain: 12 DiRICH modules, a combiner module and a power module. Together they form the so-called DiRICH family illustrated in Figure 3.16.



Figure 3.15: MAPMT readout module developed for data digitisation and treatment of 6 MAPMTs. It is made of a PCB board, on which 6 MAPMTs are plugged on one side. One data combiner module, one power module and 12 DiRICHs (two per MAPMT) are connected on the other side.

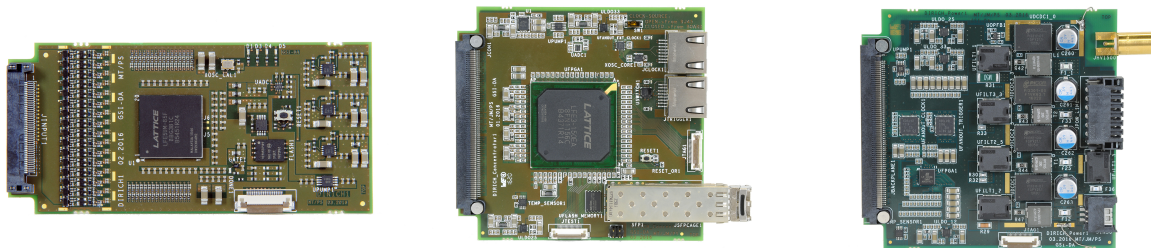


Figure 3.16: DiRICH family. Left: DiRICH readout module developed for data digitisation and treatment of 32 channels. Middle: data combiner module. Right: power module to supply the readout electronics with low voltage and distribute the high voltage to the 6 MAPMTs.

Each DiRICH module, the heart of the readout chain, is a front-end module made of analogous pre-amplifiers, a discriminator and a time to digital converter (TDC) [135]. The concept is optimised for low noise and good timing resolution. Each module reads out 32 individual channels. The analog MAPMT signal is amplified ( $\times 25$ ) and shaped with a high bandwidth transistor amplifier stage. The signal is then discriminated via input comparators of a low voltage differential signaling line from an on-board FPGA. Data from all 12 DiRICH (that is from six connected MAPMTs) is transmitted via the backplane to the data combiner module with a 2 Gbps serial link. The data combiner module gathers data from all PMTs to a signal output link. The link speed can be increased to 2.4 Gbps, which still needs enhancement to cope with the high data stream required in CBM.

The output data are currently read out with Go4 (GSI Object Oriented On-line Off-line system). All modules are powered via the backplane by the power module, distributing 1.1 V / 1.2 V / 2.5 V / 3.3 V DC power supply from external cables to the backplane. The external power supply lines are measured by the power module, which makes a remote supply voltage regulation easier. The power module also delivers high voltage (max -1,170 V) to the PMTs, via a high voltage supply line connected on the backplane.

In the CBM RICH detector, the MAPMT modules will be placed at the focal length of the mirror wall, for sharp ring detection. The assembly will follow a cylindrical shape, whose orientation and position has been optimised to yield minimal ring ellipticity and maximal ring resolution [135].

The DiRICH modules were successfully produced and tested under beam time conditions at the COSY accelerator located in the Jülich research center. The set-up employed was reduced to 2 PMT readout modules of 3 by 2 MAPMTs and used a lens and a quartz plate as radiators. Simulations in CbmRoot were conducted to determine key parameters of the set-up, such as the spacing between the modules and the position and thickness of the radiator material. Figure 3.17 shows the 2 configurations as mounted in the beam line, along with an integrated ring collected in the quartz plate configuration. The results obtained with this set-up were promising and confirmed the feasibility of the designed readout chain and electronics.

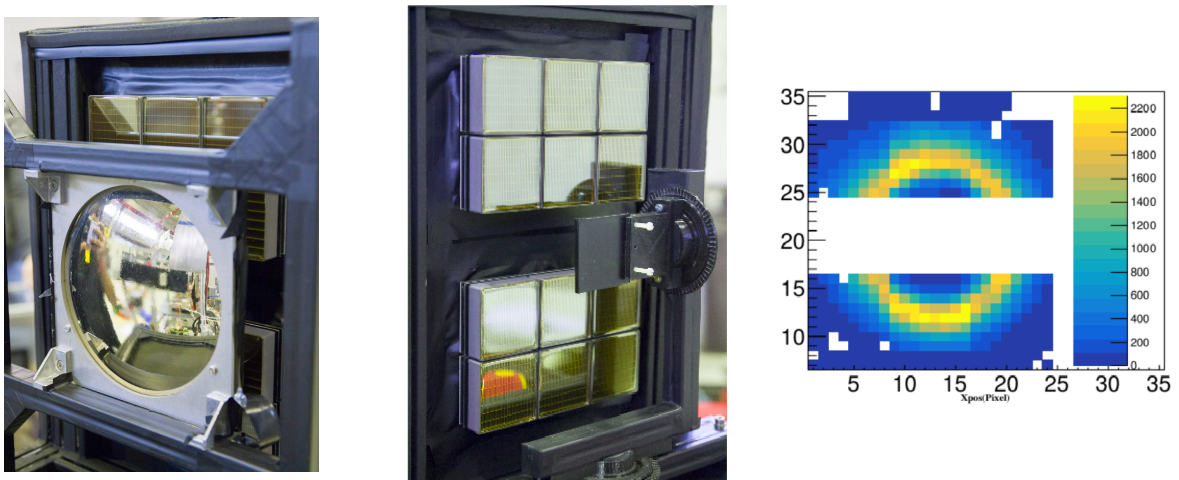


Figure 3.17: Set-up used in the COSY accelerator facility made of 2 DiRICH modules and a lens (left, focussing set-up) or a quartz plate (middle, proximity focussing set-up) used as radiators. The beam went between the two modules through the radiator. Right: Integrated ring collected in the quartz configuration.

Simulations done with the FLUKA software, assuming a realistic CBM operation scenario for 20 years, yield an estimated ionizing radiation dose of up to 100 Gy, at the place of the MAPMT plane. MAPMTs can be damaged by radiation in several parts, such as the photocathode, the entrance window, the housing made of COVAR (via  $^{60}\text{Co}$  production from neutron capture), the electronics and potential wavelength shifting films [135]. Both neutrons and gammas (from  $\text{Co}^{60}$  source) were employed to radiate the MAPMTs. A slight increase in the dark rate with radiation is seen, but both the

PMT gain and spectral shape were not affected after a 145 Gy irradiation dose. At 100 Gy radiation dose, a few percent loss of transmission in the window was noticed, which resulted in a slight decrease ( $\sim 6\%$ ) in single photon efficiency. Furthermore no impact was observed on the dynode chain with this radiation dose.

Another issue for the MAPMT plane comes from the residual stray field from the dipole magnet. The photon detector plane will be positioned close to the dipole magnet, inducing a residual stray field of 50 to 100 mT, which is too high for good photon detection efficiencies of the MAPMTs. To reduce the stray field in the region of the MAPMT plane a magnetic shielding box has been designed and optimised [138]. Figure 3.18 presents preliminary engineering drawings of the shielding box and a magnetic field map in the upper photon detector plane, obtained from calculations with the OPERA software. The residual stray field is reduced to 0.3 mT in the central part at the surface of the photon detector plane, which fulfils the specification of a magnetic field below 1 mT in the MAPMT region. The shielding box also has room for the readout modules and lateral holes for electronics cables and cooling. This part is still being optimised, according to the latest developments in the dipole magnet design.

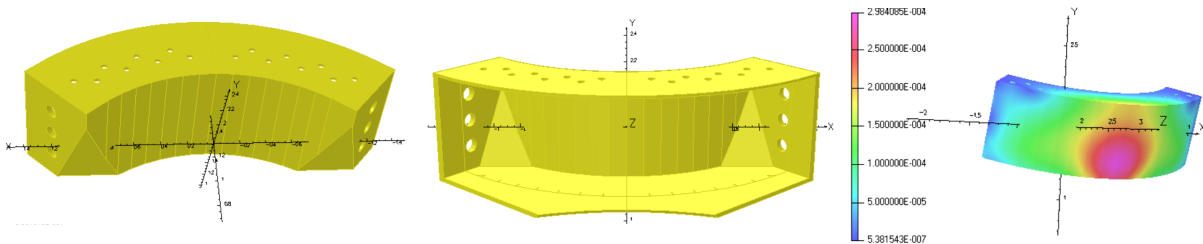


Figure 3.18: Front (left) and rear (middle) engineering drawings of the shielding box. The magnetic field map in the upper photon detector (right) is given in Tesla.

### 3.3.5 RICH Software

To embed experiment conditions and detector responses as close as possible to reality, a software framework has been developed for the CBM experiment, named *CbmRoot*. It combines the ROOT functionality for data analysis (developed in 1995 at CERN by R. Brun), with GEANT (used for detector simulation) and inputs (such as event generators) in order to simulate full events in the CBM detector set-up. Like ROOT for CERN, *CbmRoot* provides the scientific community of CBM a tool for specific physics simulation, big data processing, statistical analysis and visualisation and storage.

Each detector of CBM is being designed with computer-aided design (CAD) softwares, including the detailed detector geometry and the materials to be used. Based on these CAD models or even more simple designs, the detectors are implemented into *CbmRoot*.

In the case of the RICH detector, the geometry is designed with AutoCAD and transformed to CATIA from Dassault Systèmes. The CATIA geometry is then converted to a gdml file, used in the *CbmRoot* framework. Figure 3.19 represents a simplified CAD view of the RICH detector in CATIA. The corresponding simulation views in *CbmRoot*

are illustrated in Figure 3.20. The coordinate system of the RICH is the same as in CBM, which has the  $z$  axis towards downstream of the beam line, the  $y$  axis vertical positive to the top and the  $x$  axis, such as the  $(xyz)$  basis is right-handed. The centre  $(0; 0; 0)$  is located in the centre of the target.

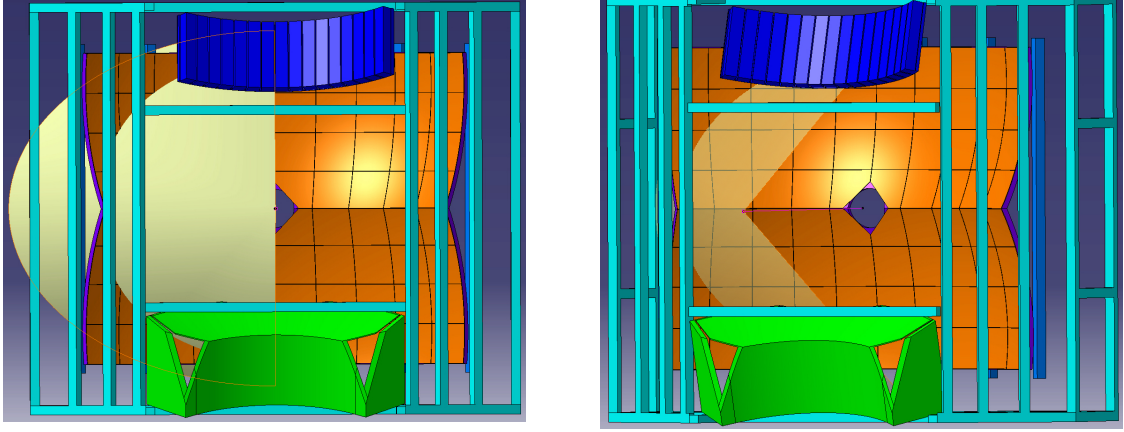


Figure 3.19: RICH geometry within the CATIA software. These are simplified models ready to be converted for CbmRoot. The supporting structure is coloured in light blue, the mirror wall in orange, the mirror supporting structure in blue, the MAPMTs in dark blue and the shielding box in green. The required acceptance is shown in beige: polar angle  $0^\circ \leq \theta_{hor} \leq 35^\circ$  in the horizontal direction and  $0^\circ \leq \theta_{ver} \leq 25^\circ$  in the vertical direction and the azimuthal angle  $0^\circ \leq \phi \leq 360^\circ$ .

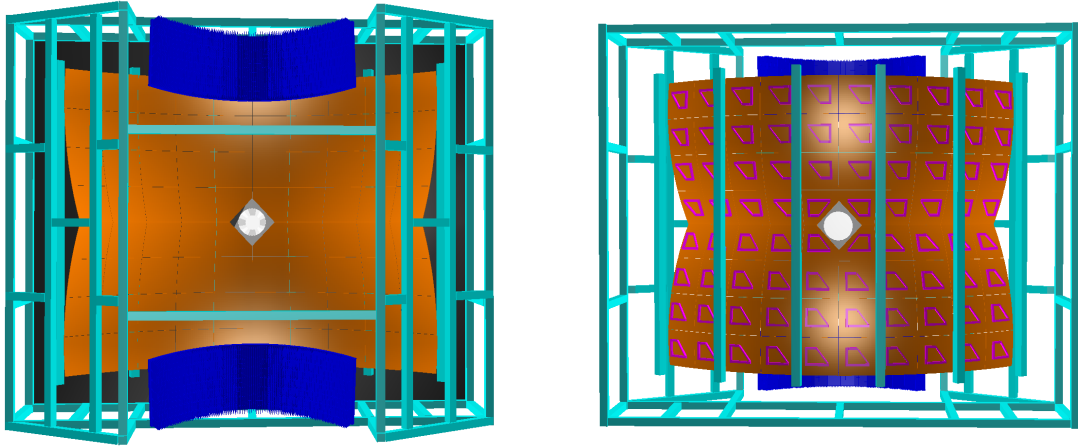


Figure 3.20: Front (left) and rear (right) views of the RICH detector in the simulation framework of CBM. The beam pipe is coloured in white, the supporting structure in light blue, the mirror tiles in orange, the mirror supporting structure in magenta and the MAPMTs grouped in two cylinders in blue. The shielding box is not yet included.

This geometry is the result of several optimisations, which were the subject of a thesis occurring during the presented thesis [139]. Therefore some results presented in the subsequent sections use an older version of the RICH geometry. This version is shown in Figure 3.21. It had a different mirror supporting structure and the MAPMTs were distributed over two rectangular planes per mirror sphere, thus its denomination: ‘two-wing geometry’.

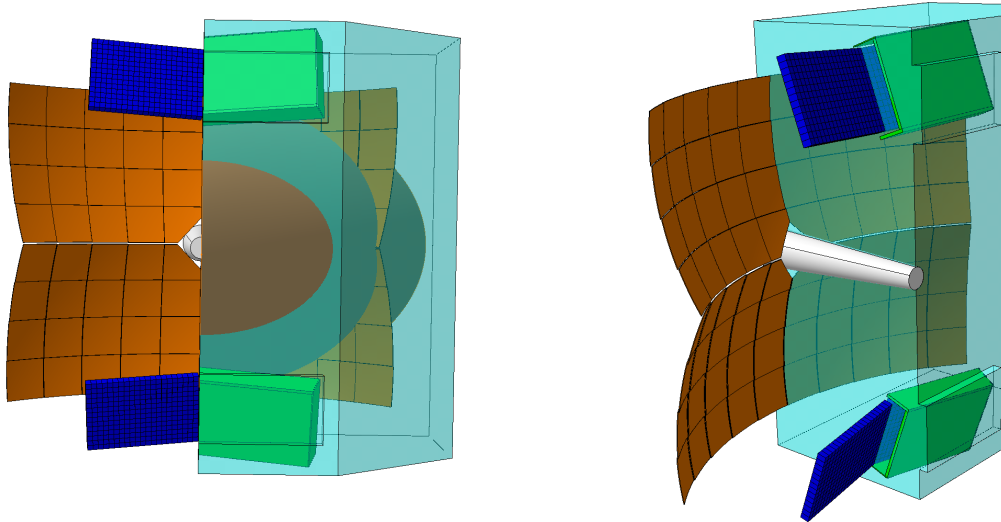


Figure 3.21: Front (left) and side (right) view of the RICH old two-wing geometry within the CATIA software. The beam pipe is coloured in white, the RICH box in light blue, the mirror wall in orange, the MAPMTs in blue and the shielding box in green. The detector and mirror supporting structures have been removed on purpose for better visualisation.

Figure 3.22 sketches the event reconstruction of the RICH software. Based on the information from the STS detector, particle tracks are extrapolated and projected on the photon detector plane, as if the tracks had been reflected by the mirrors (a). The MAPMT plane is scanned to search for rings and reconstruct them (b). The found rings are attached to incoming tracks, based on their projections (c). The latter process is referred to as ring-track matching.

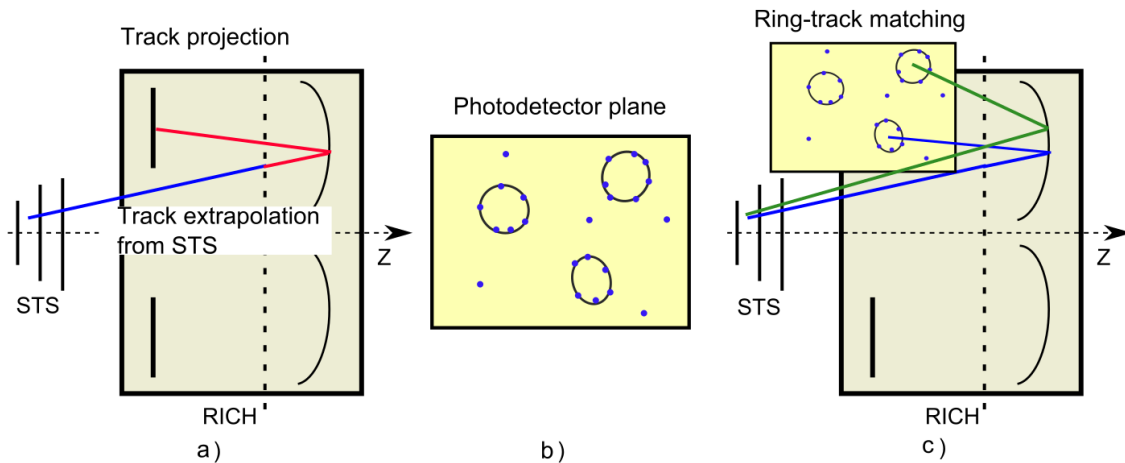
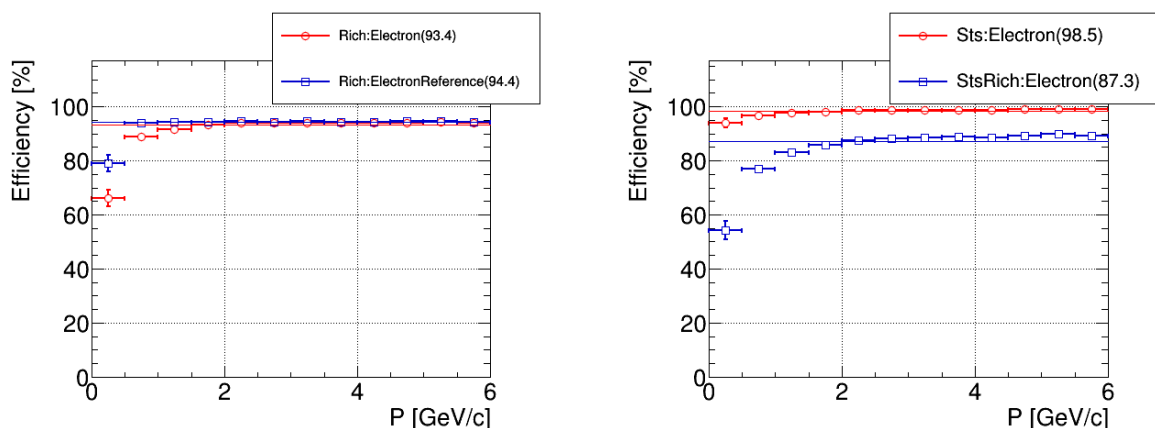


Figure 3.22: Reconstruction process of the RICH software. Incoming STS tracks are extrapolated and projected on the photon detector plane (a). Rings are searched for and reconstructed based on the photon hits on the MAPMT plane (b). The found rings are fitted to the projected tracks (c). Figure taken from [94].

To reconstruct rings, the Hough Transform method is employed to combine hit triplets forming potential rings. A ring rejection algorithm is used afterwards to reject fake rings, based on characteristics defining the quality of the found rings, such as the number of hits in the ring, the ring radius and the hit distribution uniformity on the ring [94]. For

the ring quality determination, an artificial neural network (ANN) is used.

The found rings, which are accepted by the ANN, are considered to have an elliptic shape. An ellipse fitting algorithm is applied with 5 characterisation parameters: the centre coordinates ( $X$ ;  $Y$ ), the major ( $A$ ) and minor ( $B$ ) semi-axes and a rotation angle. The reconstructed rings are then matched to the projected tracks on the MAPMT plane, which are obtained from the extrapolation of the STS detected tracks. To match the reconstructed ring and the projected track, the distance between the ellipse centre and the projected track coordinates is minimised. The correctly found and matched ring-tracks have a typical distance peaking at around 0.2 cm, and the wrong matched pairs usually have a distance larger than 1 cm.



(a) Ring reconstruction efficiencies for primary electrons with respect to momentum. The red points show the reconstruction efficiency for rings with at least 5 hits, whereas the blue points illustrate the reconstruction efficiency for rings with at least 15 hits.

(b) Matching efficiency between the STS and the RICH detectors for primary electrons versus momentum. The red points indicate the STS tracking efficiency, while the blue ones represent the matching efficiency between the STS and RICH detectors.

Figure 3.23: Ring reconstruction and STS-RICH matching efficiencies obtained for simulations of 16,000 events containing 5 electrons and 5 positrons ( $0 \leq p \leq 9.5$  GeV/c, polar angle  $2.5^\circ \leq \theta \leq 25^\circ$  and azimuthal angle  $0^\circ \leq \phi \leq 360^\circ$ ) embedded in Au+Au collisions at 10 AGeV beam energy.

The electron identification is done with an additional ANN and uses several parameters, such as the major and minor semi-axes, the rotation angle of the ellipse, the  $\chi^2$  of the ellipse fit, the radial angle and radial position of the ring, the number of hits, the distance to the closest track and the momentum of the track [94]. Using the radius of the reconstructed ring in dependence on the momentum of the matched track obtained from the STS detector, the particle can be identified. Electron rings have a constant radius, as their Cherenkov opening angle is maximum, regardless of the momentum. Yet, a source of pion misidentification comes from the combination between pions stemming from the primary vertex with a momentum below the Cherenkov threshold and secondary electrons produced somewhere in CBM. If these electrons are not seen in the tracking systems but leave rings in the RICH, wrong ring-track matches can accidentally occur.

Figure 3.23 illustrates the performances in ring reconstruction (left) and STS-RICH

matching (right) for simulations of 5 electrons and 5 positrons (momentum from 0 up to 9.5 GeV/c, polar angle  $2.5^\circ \leq \theta \leq 25^\circ$  and azimuthal angle  $0^\circ \leq \phi \leq 360^\circ$ ) embedded in UrQMD (Ultrarelativistic Quantum Molecular Dynamics) background, for 16,000 central Au+Au collisions at 10 AGeV beam energy. The set-up employed for this simulation contains the following: Magnet (version v15a, with the magnetic field map v12b), STS (version v16x), RICH (v17a\_1e) and beam pipe (v16c\_1e). In addition, the mirrors were all aligned and default parameters for characteristics of the MAPMTs were chosen.

Ring reconstruction efficiencies of 93.4% and 94.4% are obtained for rings with at least 5 hits and 15 hits per ring, respectively. The STS reconstruction efficiency for primary electrons is 98.5%. This figure decreases to 87.3% when combining information from the STS and RICH detectors. The latter efficiency corresponds to matching between reconstructed STS tracks and detected RICH rings. Efficiency losses are a combination of losses from ring finding and ring-track matching. These losses can for instance stem from high ring density, low number of reconstructed hits or rings, multiple scattering and high track density.

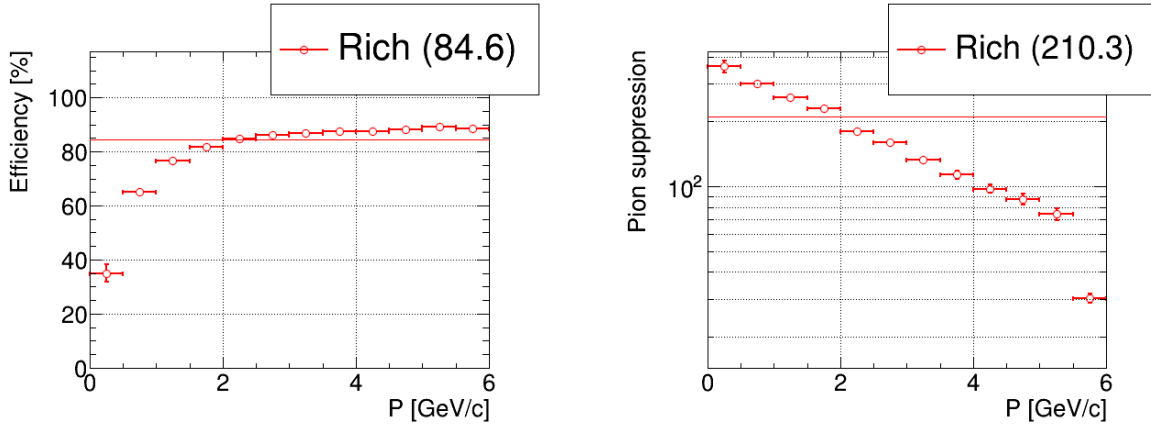


Figure 3.24: Electron identification efficiency (left) and pion suppression factor (right) achieved for simulations of 16,000 events containing 5 electrons and 5 positrons ( $0 \leq p \leq 9.5$  GeV/c, polar angle  $2.5^\circ \leq \theta \leq 25^\circ$  and azimuthal angle  $0^\circ \leq \phi \leq 360^\circ$ ) embedded in Au+Au collisions at 10 AGeV beam energy.

Figure 3.24 shows the electron identification and pion suppression capabilities with identical simulation parameters to the ones detailed in Figure 3.23. The electron identification efficiency amounts to 84.6% and the pion suppression factor is 210.3. For these numbers a RICH cut of -0.4 on the artificial neural network was applied. The same cut is used for all results presented later in this thesis.

Table 3.3 sums up the computed efficiencies for central Au+Au collisions at beam energies of 8 and 10 AGeV. In each event, 5 electrons and 5 positrons are embedded with the following parameters: momentum from 0 up to 9.5 GeV/c, polar angle  $2.5^\circ \leq \theta \leq 25^\circ$  and azimuthal angle  $0^\circ \leq \phi \leq 360^\circ$ . In addition, simulations were performed with only 10 electrons and positrons each per event. For these particles identical momentum range, polar and azimuthal angles were chosen.

Increasing energies generate in particular higher track and ring densities, which translates in a decrease in the efficiencies.

Efficiencies	8 AGeV	10 AGeV	single $e^-/e^+$
Ring reconstruction ( $\geq 5$ hits)	95.5%	93.4%	96.8%
Ring reconstruction ( $\geq 15$ hits)	96.4%	94.4%	97.5%
STS track reconstruction	98.9%	98.5%	99.8%
STS-RICH reconstruction and matching	90%	87.3%	90.7%
RICH identification	87.1%	84.6%	86.7%
Pion suppression factor ( $0 \text{ GeV}/c \leq p \leq 6 \text{ GeV}/c$ )	285.3	210.3	0 <sup>1</sup>

Table 3.3: Comparison of efficiencies for different simulations. Electrons were either embedded into UrQMD events at different beam energies, or simulated as only source (right column), with a momentum  $0 \leq p \leq 9.5 \text{ GeV}/c$ , a polar angle  $2.5^\circ \leq \theta \leq 25^\circ$  and an azimuthal angle  $0^\circ \leq \phi \leq 360^\circ$ . 16,000 events were simulated for each simulation run.

### 3.3.6 Real-size projects

Several RICH prototypes have already been tested successfully [94, 140]. As a next step for the construction of the CBM RICH and due to delays in the construction of the FAIR facility, components from the RICH detector will be used in other projects, namely the HADES experiment and the mini-CBM (mCBM) set-up.

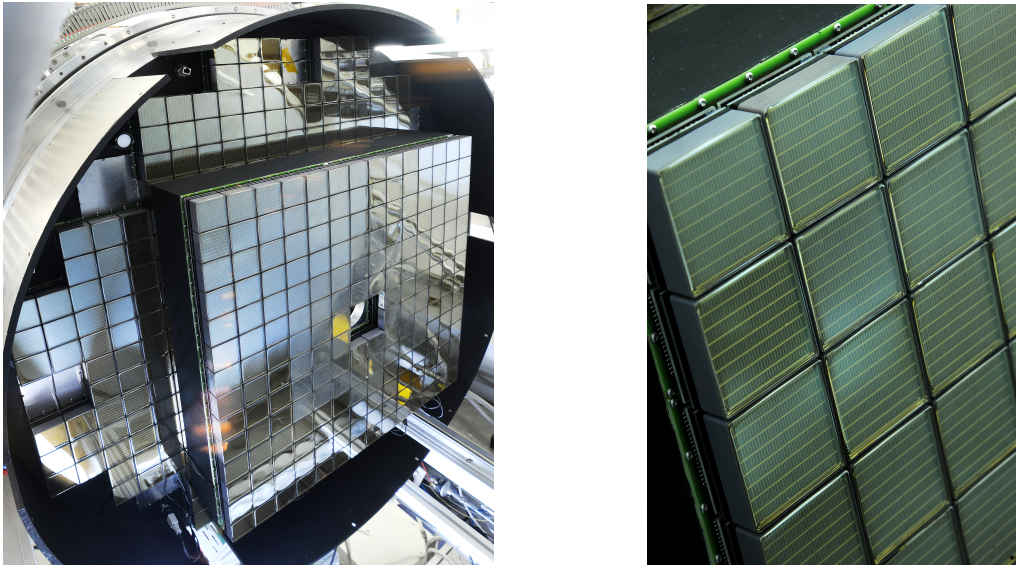


Figure 3.25: Left: Front view of the HADES RICH detector with the mounted H12700 Hamamatsu MAPMT. The central MAPMTs are coated with WLS films. Right: Close-up view of the MAPMTs.

<sup>1</sup>No pions were simulated

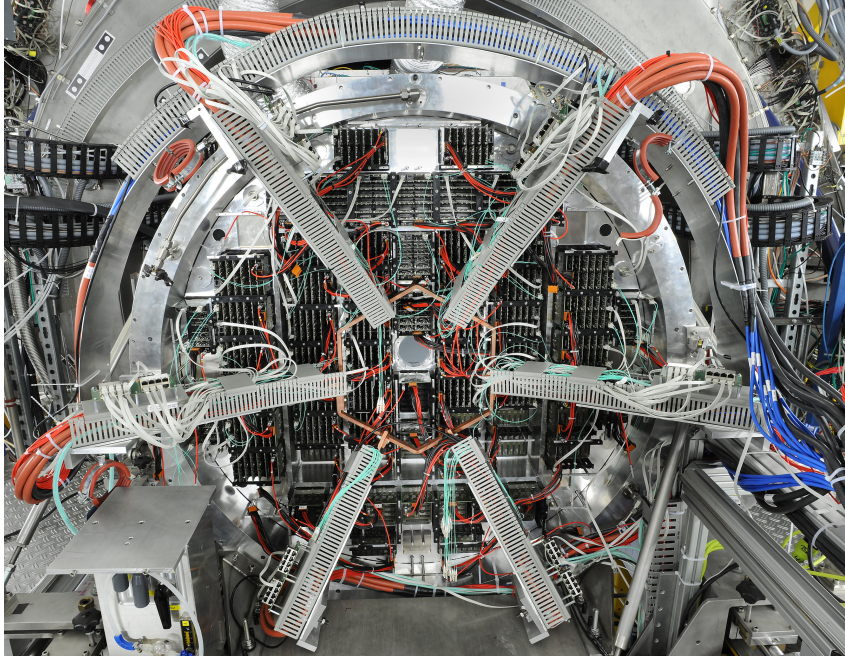


Figure 3.26: Rear view of the HADES RICH detector with electronics and cooling cables.

The upgrade of the HADES RICH detector was successfully carried out in a beam time in March of 2019 in GSI. One of the objectives was to change the reflective CsI photocathodes and corresponding gas detector with H12700 MAPMTs (see Figure 3.25). The HADES RICH detector uses  $C_4F_{10}$  as gas radiator and is thus blind to hadrons at HADES energies. With this upgrade, the number of photon hits per ring should increase from 3 - 4 hits with the aged set-up, to about 10 - 12 hits per ring, depending on the polar angle. These parameters were obtained with simulations.

Taking part in this real physics project is also a good opportunity for the RICH group to test the newly developed readout chain and electronics concept (see Section 3.3.4), whose successful assembly is shown on Figure 3.26.

A second project, in which the CBM-RICH detector will take part from summer 2019 on, is the mCBM at SIS18 energies at the GSI/FAIR facility [141]. The purpose of this project is mainly to test the self-triggered CBM DAQ system running with the different detectors involved. Also online and offline data processing and analysis will be tested.

The set-up of the mCBM project is presented on Figure 3.27. The RICH detector will use aerogel as radiator. A feasibility study with this set-up was successfully carried out in a beam time at the COSY accelerator facility. It will separate low momenta pions from kaons and from protons. In the basic set-up, two MAPMT readout modules will be used and the DiRICH data transfer between the TRBNet based DiRICH and the CBM DAQ will be established.

In addition, a mini-RICH was already implemented in the CbmRoot framework to run simulations of Au+Au collisions at 1.24 AGeV. Figure 3.28 shows a ring produced by a negatively charged pion in simulation in one of the four mRICH stations, along with an identification histogram, showing a clear separation between pions and kaons for momenta up to 3.5 GeV/c and allowing protons identification for momenta up to 5 GeV/c.

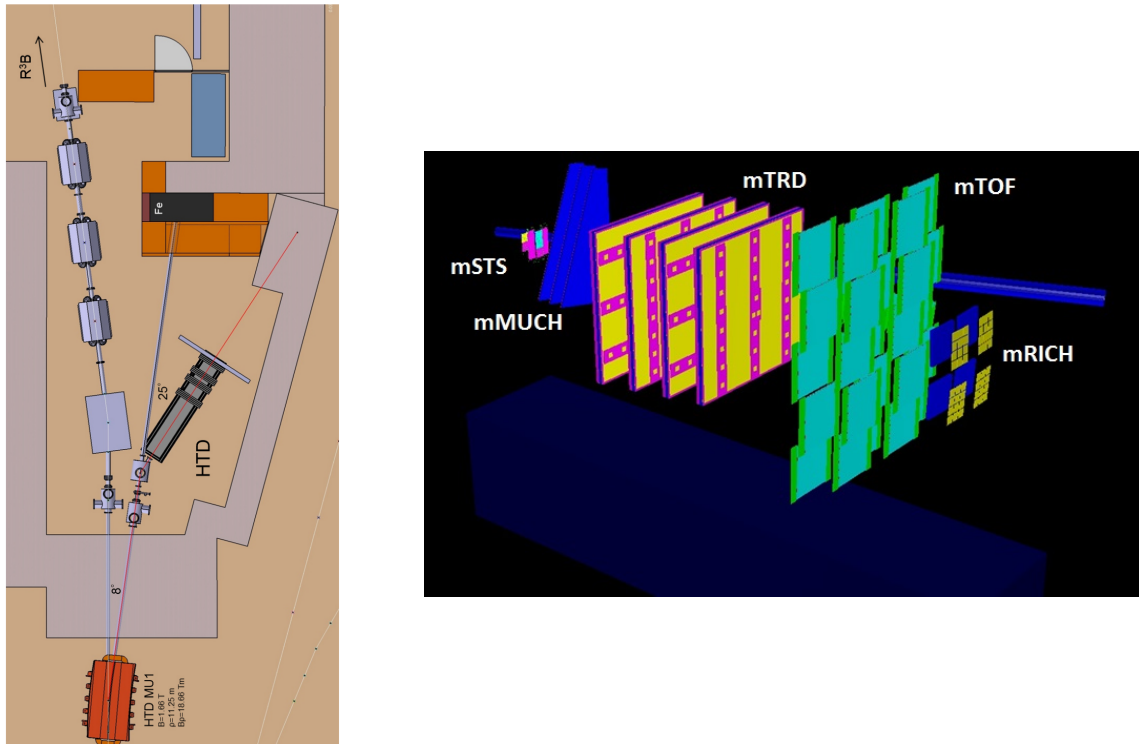


Figure 3.27: Left: Design of the detector test area HTD for the mCBM experiment at SIS18. Right: Top view of the mCBM test set-up. The coordinate axes are coloured in red (X), green (Y) and blue (Z). The detector subsystems are aligned at an angle of  $25^\circ$ , with respect to the beam pipe. Figures taken from [141].

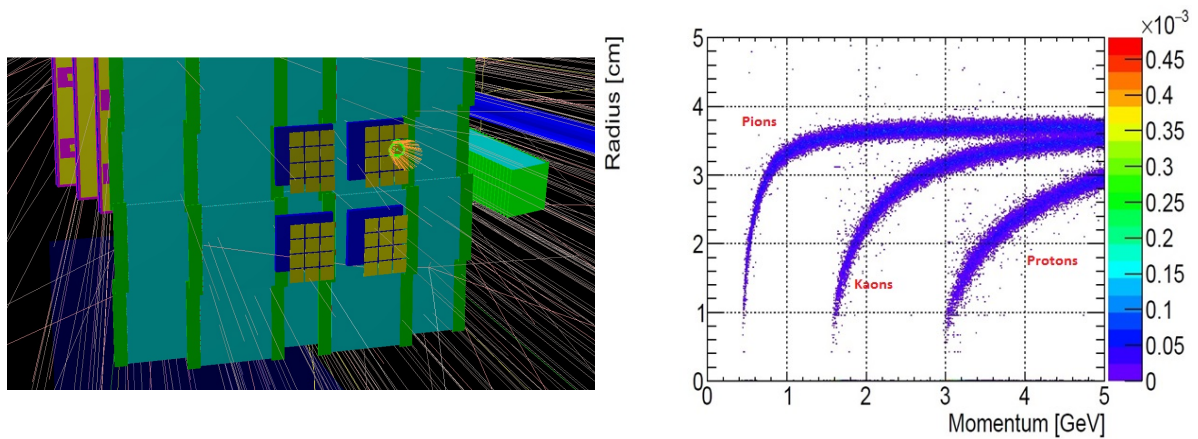


Figure 3.28: Left: Four simulated mRICH stations, where the dark blue, yellow and green parts correspond to the aerogel radiator, the photon sensors and a ring produced by a  $\pi^-$ , respectively. The coloured lines represent particle tracks. Right: Radius versus momentum histogram. A good separation between pions and kaons is observed for momenta below 3 GeV/c and pions and kaons are well separated from protons for momenta up to 5 GeV/c. Figures taken from [142].

### 3.4 The importance of mirror alignment - Scope of this work

One of the challenges for the RICH detector with respect to mirror alignment is the expected relatively high ring density. To that end a perfectly aligned and stable mirror system is required for an accurate and efficient ring reconstruction.

The simulated mirror system, as implemented for the RICH detector in the CbmRoot framework, provides, when mirrors are perfectly aligned, a ring reconstruction efficiency of 95.5% for at least 5 hits per ring and a STS-RICH reconstruction and matching efficiency of 90%. This was obtained in simulation of 16,000 events, each containing 5 electrons and 5 positrons embedded in UrQMD central Au+Au collisions at 8 AGeV beam energy (see Table 3.3).

A theodolite in auto reflection mode will be employed to ensure the initial mirror alignment, yielding a 0.1 mrad global accuracy (see Section 3.3.2).

However this method requires space to operate (at least the radius of curvature of the mirrors, which is for the CBM RICH detector 3 meters) and will be conducted outside of the experiment line. The detector will be thus craned after the initial alignment. In addition, the RICH detector will be craned out of the beam line when an exchange with the MUCH detector is required (on a yearly/biyearly basis).

This could harm the stability of the mirror system, which could consequently harm the detector overall performance.

In the case of misalignments, the Cherenkov angle measurement might be altered, which translates in efficiency losses in ring reconstruction. These efficiency losses might be caused by ring distortion, ring splitting and ring-track mismatching, which might in turn cause particle misidentification. This is detrimental to a good operation of the detector, as reduced ring finding efficiencies will harm the performances of the RICH.

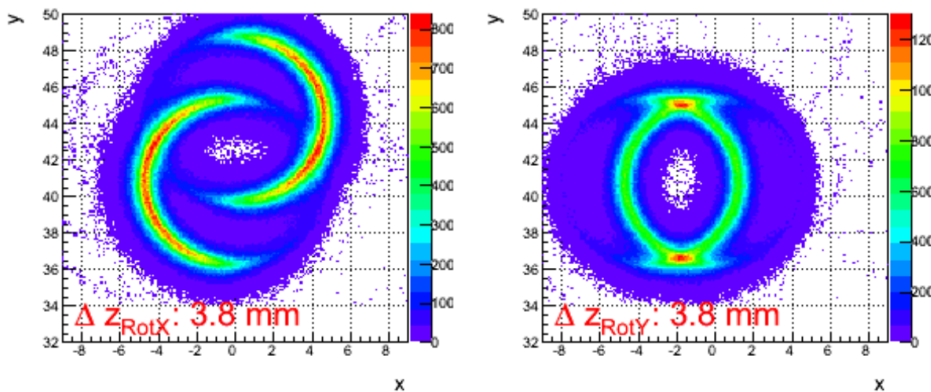


Figure 3.29: Integrated rings in the case of mirrors rotated around the horizontal (left) and vertical (right) axes. Figures taken from [94].

Figure 3.29 illustrates the ring splitting effect obtained from simulation. For this study the particle beam was oriented towards the middle of the two lower mirrors of the RICH prototype (see Section 4.2.1 and Figure 4.3). One of the mirrors was rotated, so that the

cone half reflected by it was shifted in the vertical direction or in the horizontal one.

Figure 3.30 shows the impact of misalignments on the ring reconstruction efficiency and on the STS-RICH reconstruction and matching efficiency.

Simulations have been carried out with a random mirror misalignment applied on all tiles in any direction, following a Gaussian distribution (see Section 6.2.2 for a definition of the induced misalignment). The mean misalignment was 0 mrad and the standard deviation was 5 mrad.

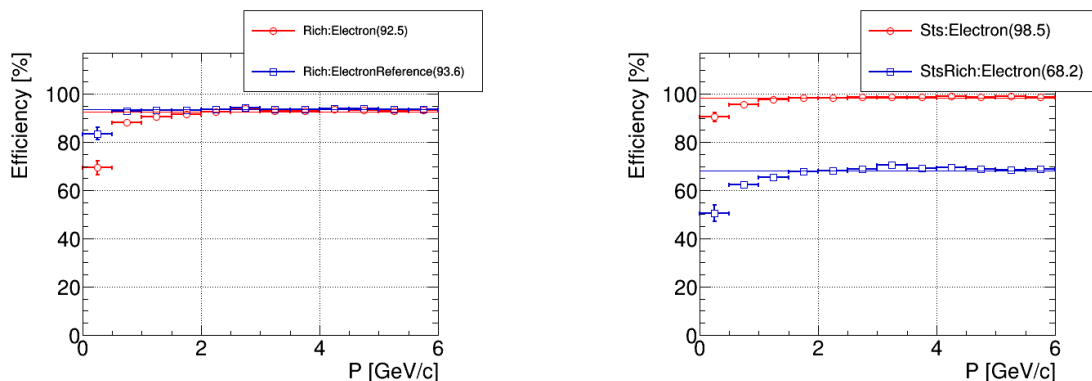


Figure 3.30: Ring reconstruction efficiencies (left) and STS reconstruction and STS-RICH matching efficiencies (right) for a 5 mrad Gaussian misalignment of the mirror wall. 16,000 events containing 5 electrons and 5 positrons embedded in Au+Au collisions at 10 AGeV beam energy were simulated. The colour code follows the one from Figure 3.23.

In this case and compared to the aligned case (Figure 3.23), the STS reconstruction efficiency is not affected. The ring reconstruction efficiency is only a little affected and still amounts to 92.5% for rings with at least 5 hits. However the STS-RICH reconstruction and matching efficiency drops down to 68.2%. As the ring reconstruction efficiency is almost constant, the ring shapes are not much altered by misalignments, due to ring distortions.

Instead mirror misalignments must perturb the ring-track matching, because of the decrease in the STS-RICH reconstruction and matching efficiency. Misalignments translate into rings being projected on the MAPMT plane in locations which do not match with the projected tracks obtained from the STS detector and calculated in the software. This overall increase in the ring-track distances results in losses in matching, which will cause losses in electron identification and pion suppression.

A more detailed study was conducted to investigate the impact of misalignments on different reconstruction efficiencies of the RICH detector and is presented in Table 3.4.

The results are displayed for two different beam energies: 8 and 10 AGeV. The misalignment values correspond to the standard deviations of the Gaussian distributions used to induce mirror rotations.

Just like in the case of Figure 3.30, the ring reconstruction efficiency and the STS reconstruction efficiency are not harmed by an increase in the mirror misalignment. But a clear drop can be observed already for a 2 mrad Gaussian misalignment in the STS-RICH reconstruction and matching efficiency, as well as for the electron identification

efficiency and the pion suppression factor.

This clearly shows the importance of mirror alignment in the performance of the CBM RICH detector.

UrQMD beam energies	8 AGeV				10 AGeV			
Misalignments	1 mrad	2 mrad	3 mrad	5 mrad	1 mrad	2 mrad	3 mrad	5 mrad
Ring reconstruction ( $\geq 5$ hits)	95.2	95.1	94.9	94.8	93.3	93	92.9	92.5
Ring reconstruction ( $\geq 15$ hits)	96.3	96.1	96	96	94.4	94	93.9	93.6
STS reconstruction	98.9	98.9	98.9	98.8	98.5	98.5	98.5	98.5
STS-RICH reconstruction and matching	88.9	86.1	82.2	72.5	86.3	83.1	78.8	68.2
RICH $e^-$ identification	85.4	78.5	68	47.2	82.9	76	65.3	45.2
Pion suppression factor	265.4	212.8	186.7	164.8	190.6	162.4	143	128.8

Table 3.4: Comparison of efficiencies for different geometries and simulation inputs. Two simulations are compared: central Au+Au collisions at 8 and 10 AGeV beam energy with 5 embedded electrons and 5 embedded positrons (momentum from 0 up to 9.5 GeV/c, polar angle  $2.5^\circ \leq \theta \leq 25^\circ$  and azimuthal angle  $0^\circ \leq \phi \leq 360^\circ$ ). For each of these simulations, several misaligned geometries were produced. Mirrors were randomly misaligned with values following a Gaussian distribution, whose mean was set to 0 mrad and whose standard deviation amounts to the values given in line 2 as ‘Misalignments’. 16,000 events were simulated for both energies. All numeric values are expressed in %, apart from the pion suppression factor.

A mirror alignment and control system was thus deemed necessary to allow proper operation of the CBM RICH detector under misalignments during the experiment data taking. It has been developed to tackle the revealed and explained efficiency losses and misidentification problems coming from mirror misalignments [143, 144].

In this thesis two methods are presented to determine possible mirror misalignments. They are inspired from other RICH detectors from two different experiments and were adapted to the RICH detector of CBM.

The first method relies on hardware and is inspired from the COMPASS RICH detector. It is presented in Chapter 4. The second method is based on the software and is adapted from the HERA-B experiment. Chapter 5 illustrates this method. In case of mirror misalignments the two methods allow for a double-check, making thus a more stable mirror system.

An alignment correction cycle is introduced in a third step in Chapter 6. It uses the inputs of the two determination methods to correct for the detected misalignment.

# Chapter 4

## Determination of mirror rotations with hardware

### 4.1 Principle of the method

The Continuous Line Alignment Monitoring (CLAM) method [127] was originally developed for the RICH-1 detector system of the COMPASS experiment [145]. The fundamental principle of the method is to use an object's reflection by a surface made of mirror tiles. In the case of misalignments between adjacent tiles, the image of the reflected object will appear broken [126, 146].

The equipment required to implement the CLAM method is listed below:

- Stripes and targets made of retroreflective material
- Camera(s) to image the mirror reflections of the retroreflective material
- Lightning system to illuminate the stripes and targets

A rectangular grid made of retroreflective stripes is placed near the entrance of the RICH vessel. Additionally, retroreflective targets are glued on the grid (for example at the stripes crossing) and close to the mirrors (for example on the mirror frame). Cameras (four in the case of COMPASS) are fixed inside the vessel, such that they point to the spherical mirrors and see the retroreflective grid by reflection. The lightning system (LEDs for COMPASS) are installed such that they illuminate the grid through the mirrors. Figure 4.1 sketches the apparatus and the principle of the CLAM method.

The method consists of two different approaches to estimate mirror misalignments. The first step supposes a previous initial alignment of all mirrors, such that the centres of curvature of the mirrors coincide in one point in space. This alignment is usually realised with a theodolite in autoreflexion method [125]. In this configuration pictures are taken to show the reflected grid with an aligned mirror system. These pictures are used as references for later comparisons. If at some point mirrors are displaced, the picture of the reflected grid changes and grid stripes will appear broken. Here the relative alignment of adjacent mirrors is measured. This step yields a quick qualitative assertion, as to whether mirrors are aligned or not.

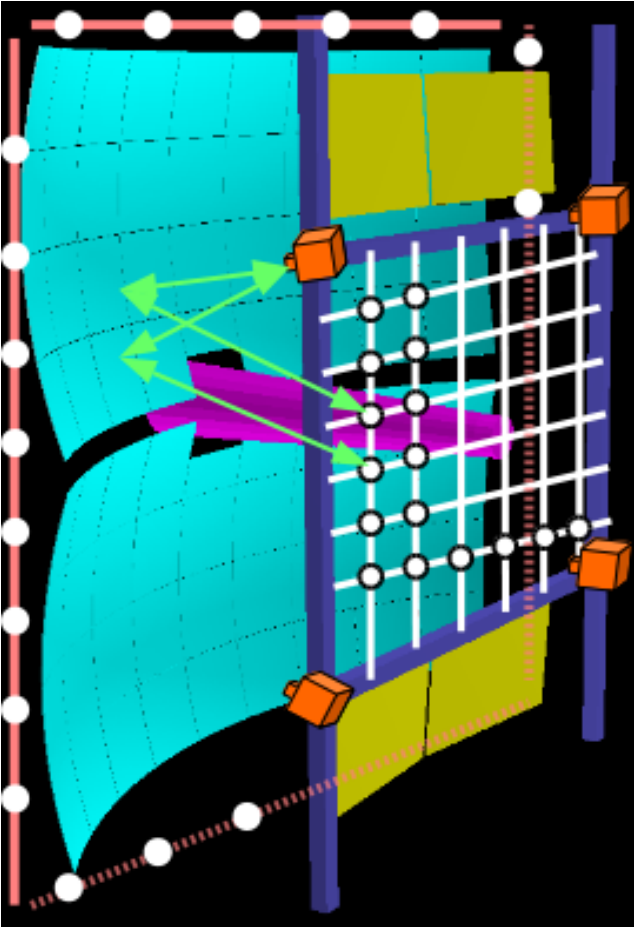


Figure 4.1: Sketched apparatus and principle of the CLAM method in the old two-wing geometry of the CBM-RICH detector. The mirror wall is in light blue, the outer mirror frame in salmon, the vessel frame in dark blue, the photon sensors in yellow and the beam pipe in light purple. LEDs are fixed close to the cameras (in orange) and shine light on the rectangular retroreflective grid (white) via the mirrors. The light is reflected back to the cameras and the lines reflected by misaligned mirrors will appear broken. Retroreflective target dots are also glued at the mirror and vessel frames for photogrammetry.

It is all the more possible, in a second step, to determine mirror rotations around the horizontal and vertical axes of the tile. To do so a previous calibration of mirror rotation is required. For this calibration mirrors are artificially rotated with a known rotation angle. A picture is taken after the rotation and is subtracted to the reference picture. A pixel shift between the stripes is extracted. This procedure is applied for several mirror rotations on both rotation axes. Thus, should the mirror pivot, its rotation can be determined by comparing the current grid reflection with the reference picture and extracting the corresponding pixel shift. Sections 4.4 and 4.5 focus on the quantification of mirror misalignments using this technique.

The feasibility of the CLAM method has already been shown by the COMPASS experiment [127, 147].

This strategy is however limited by several factors. Mirrors are supposed to be initially perfectly aligned, mirror rotations on both axes cannot be easily disentangled and the position of the cameras might be altered during the detector operation, too [126].

In addition to this method, photogrammetry can be employed, involving the targets and exact determination of their positions in space. This option requires the calibration of the CLAM cameras, to determine their interior orientation parameters and an external calibration, to establish the spatial position and orientation of the cameras in a global coordinate system. Analytical photogrammetry algorithms, such as collinearity equations [148], can be applied to derive the positions of all objects in the cameras' field of view.

## 4.2 CBM RICH prototype in 2014 beam time at CERN

### 4.2.1 Real size RICH prototype

To prove the feasibility of the proposed RICH detector design, several prototypes were realised. Among them, one was used in beam time conditions at CERN in 2011, 2012 and 2014 (see Figure 4.2). This prototype is of particular interest, as it complies with the real size radiator length, directly related to the number of emitted Cherenkov photons. Furthermore, the prototype is true to most of the components foreseen for the full RICH detector and defined in Section 3.3, such as the CO<sub>2</sub> gas system and the mirror tiles.

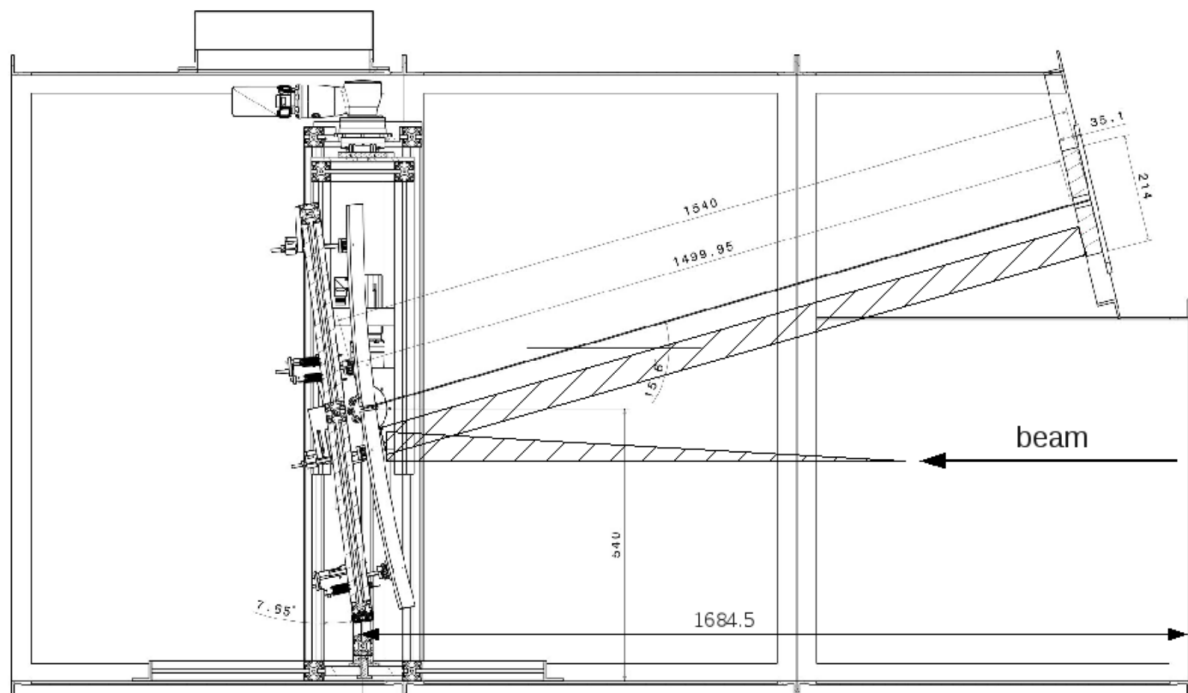


Figure 4.2: Technical drawing of the CBM-RICH prototype vessel. The mirrors and the rotation system are also drawn. The hatched area represents the emitted Cherenkov photon cone and its reflection by the mirror system onto the photon detector plane (upper right). Figure taken from [94].

Figure 4.2 sketches a side view of the RICH prototype, whose dimensions ( $2.4 \text{ m} \times 1.2 \text{ m} \times 1.4 \text{ m}$ ) provide a radiator length of about 1.7 m. The box is made of stainless steel and its front and rear sides consist of 10 mm and 20 mm thick plastic plate, respectively. An entrance and an exit window, each made of 2 mm thick plastic plate, are added to minimise multiple scattering.

### 4.2.2 2014 beam time set-up at CERN PS/T9 beamline

The prototype was filled with CO<sub>2</sub> by a computer-controlled gas system, in an overpressure of 2 mbar. The system guaranteed a stable gas supply, maintaining oxygen contamination to 100 ppm and water contamination to 200 ppm. This system provided a pion Cherenkov

threshold of 4.65 GeV/c, corresponding to the expected value used in the CBM-RICH detector [94].

Four 6 mm thick SIMAX glass mirror tiles manufactured by JLO Olomouc, Czech Republic, and coated with a protective layer of Al + MgF<sub>2</sub> constitute the mirror system (see Figure 4.3). Each mirror tile is held by the aluminium frame and controlled by three actuators. The actuators allow forward and backward tile movements within 3 cm, on the contact points, permitting mirror rotations. The whole frame can also rotate around a horizontal and vertical axis via motors (blue parts on the left side of Figure 4.3), controlled by a dedicated EPICS program described in Appendix A. During the detector operation, the mirrors are rotated by 7.65° around the horizontal axis to focus the Cherenkov photons on the photon sensor plane (see Figure 4.2). The rotation value was computed, considering an opening angle of 1.72° in CO<sub>2</sub> for relativistic electrons and pions.

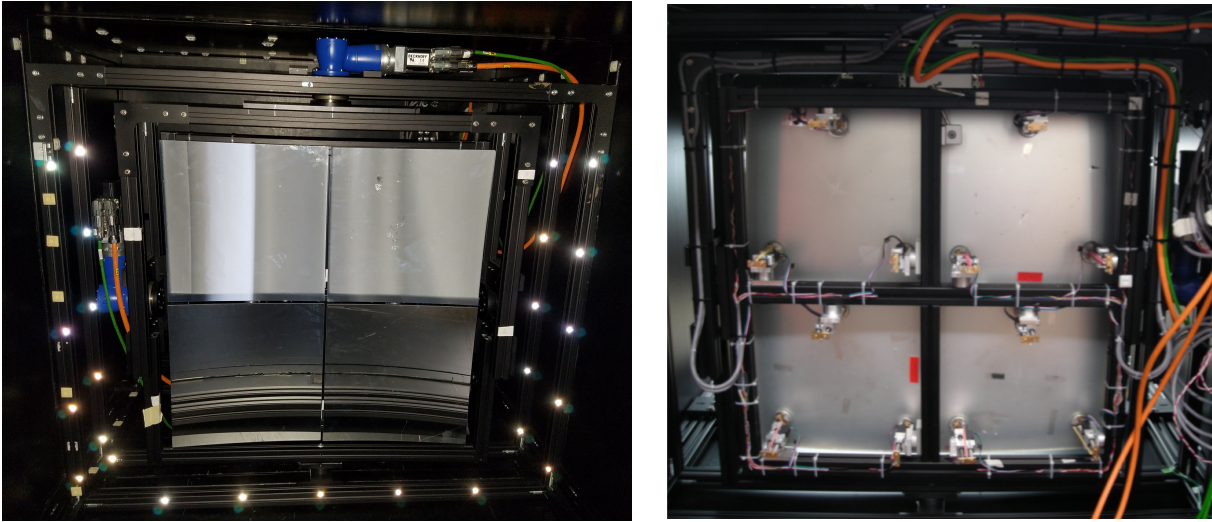
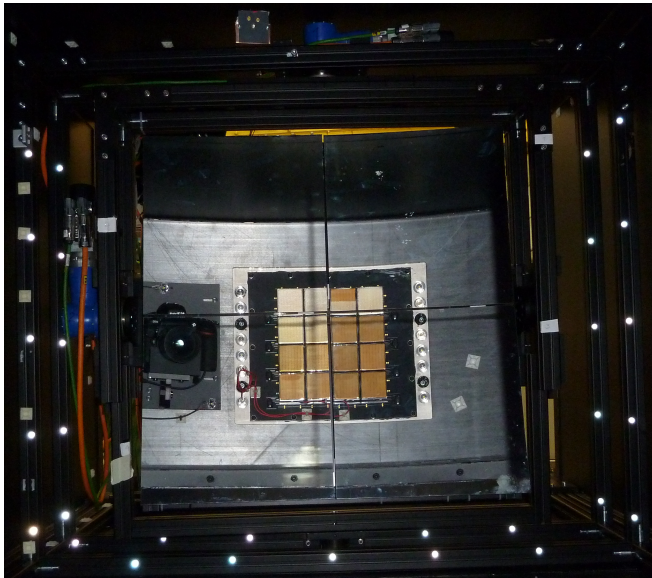


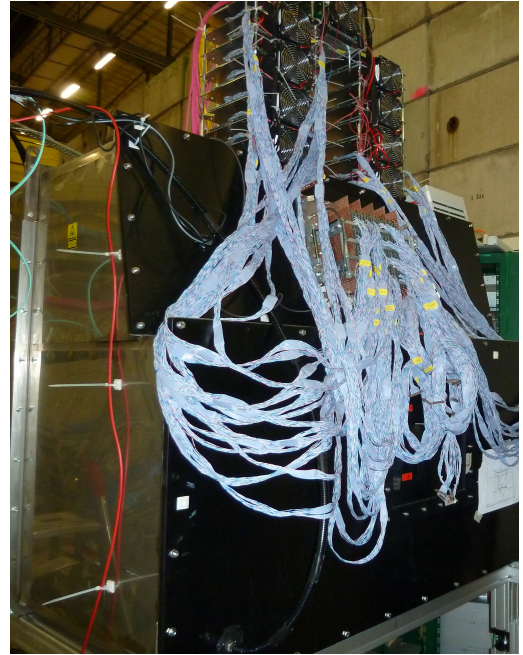
Figure 4.3: Front (left) and rear (right) view on the four mirror tiles mounted on the frame inside the CBM-RICH prototype.

The photon detector plane is located at a distance of about 1.5 m to the mirrors and is tilted to face the mirrors. One of the many goals of the 2014 CERN PS beamtime was an in-beam comparison between the Hamamatsu H8500, the MCPs XP85012 from Photonis and the newly released H12700 MAPMTs. In addition, a fully FPGA-based readout chain developed in the lab was also tested [117]. This readout chain is the predecessor of the finally developed DiRICH readout system. The MAPMTs were mounted on a gas-tight carrier board, acting as interface between the inner part of the prototype and its surroundings. The total coverage area of the carrier board was 21.4 cm × 21.4 cm and the spacing between the PMTs was 2 mm. Figure 4.4 shows the set-up in the beam line. The left-hand side represents a reflection on the mirror frame of the photon detector plane, along with the CLAM camera. The right-hand side shows the readout chain connected to the carrier board.

The signals were first processed by 64 PADIWA front-end modules, each PADIWA having 16 channels. The PADIWAs were used as signal discriminators and signals were further transported via flat cables to a second readout element. The second readout



(a) Mirror frame holder inside the CBM-RICH prototype. The photon sensor plane is also visible on the mirrors via reflection. Retroreflective target dots are visible on the frame, as well as the camera and LEDs to apply the CLAM method.



(b) Front side of RICH vessel with the readout electronics plugged in the photon detectors.

Figure 4.4: Mirror frame and readout system.

boards were made of TRB3 FPGA-TDCs and extrapolated several information from the input signal, such as leading and trailing time and thus also time over threshold. This idea was later abandoned and the much more compact DiRICH concept (see Section 3.3.4) was developed. The DiRICH readout system drastically reduces the equipment and cable loads (see Figure 4.4b) and thus reduces sources of background and signal losses during signal analysis.

This opportunity of a beam test was also used to test the impacts of mirror rotations on ring characteristics. For that purpose, two positions of the mirror frame were introduced. In the first one, the frame was placed such that the particle beam was passing in between the two lower mirrors. In the second position, the beam was crossing the mirror frame at its center, that is in between the four mirrors.

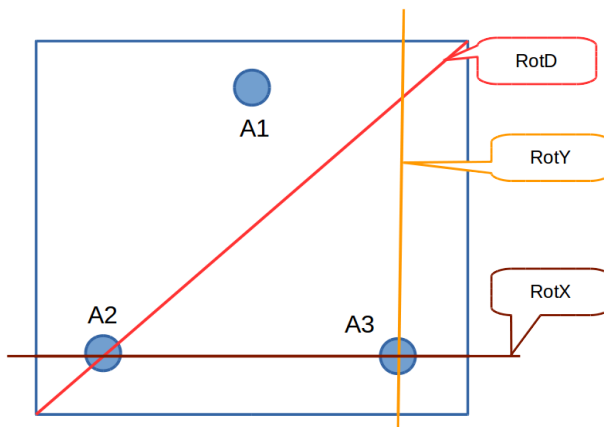


Figure 4.5: Front view of one mirror. Mirror rotation axes defined to artificially misalign mirrors during beamtime. The horizontal axis (brown) passes through the two lower actuators, the vertical (yellow) through the rightmost actuator and the diagonal (red) links the two mirror edges passing through the leftmost actuator.

To imply artificial misalignments, the mirrors were remotely controlled with actuators. Three rotation axes were defined: horizontal, vertical and diagonal (see Figure 4.5). Mirrors were rotated in several positions to investigate the impact of misalignments on ring characteristics.

The subsequent section presents results obtained with the presented prototype in real conditions at CERN.

### 4.3 Results from beam time at CERN

For the beam-test an initial mirror alignment was conducted. The procedure consists in aligning the reflection of a laser source (assumed to be point-like) by all four tiles on a single point at the focal plane of the mirrors.

The CLAM equipment is represented in Figure 4.6. A camera was mounted next to the photomultiplier plane and its position and orientation remained fixed until the end of the measurements (see Figure 4.6a). It was surrounded by three LEDs, which were supplied with a voltage of 3.2 V. For the CLAM measurements, the PMTs were turned off and the LEDs were switched on. The LEDs shined light through the mirrors on a grid of retroreflective stripes, glued at the entrance of the RICH vessel (see Figure 4.6b).

Figure 4.6c represents the reference CLAM picture, taken after the initial alignment procedure. The mirror edges appear as black cuts on the stripes. All stripes are continuous, which shows that the mirror system is aligned. In the following, mirrors will rotate and the stripes will appear broken at the mirror edges, indicating misalignments. This thus allows for a fast qualitative assessment regarding mirror alignment.

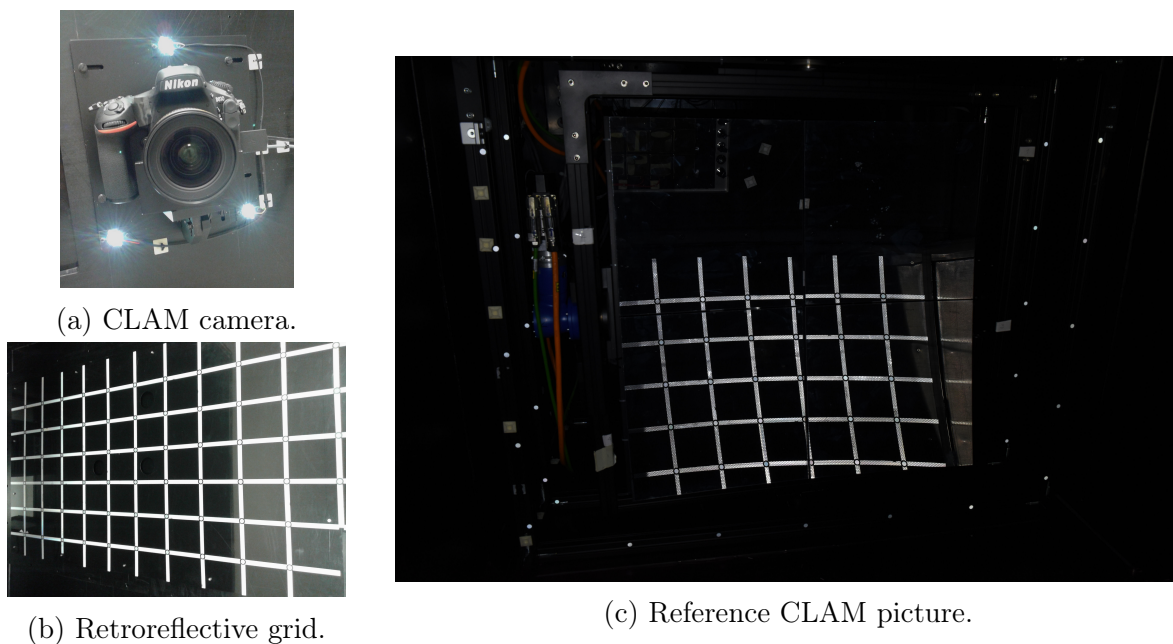


Figure 4.6: CLAM equipment and reference picture.

The vessel was placed in the beamline such that the beam passed in between the two lowest mirrors at their half-height. Figure 4.7 represents different histograms of ring characteristics in this configuration and for the case of an aligned mirror system. The sub-histograms represent the integrated rings (4.7a), the number of hits per photon sensor (4.7b), the radius (4.7c), the major semi-axis A (4.7d) and minor semi-axis B (4.7e) distributions and the B/A ratio (4.7f). The integrated rings histogram shows the sum of all events recorded in the aligned mirror configuration. The integrated ring resolution in this picture displays smearing, due to a diffuse beam. The rings do not appear elliptical,

as the mean values of the minor and major semi-axes are very close (Figures 4.7d and 4.7e).

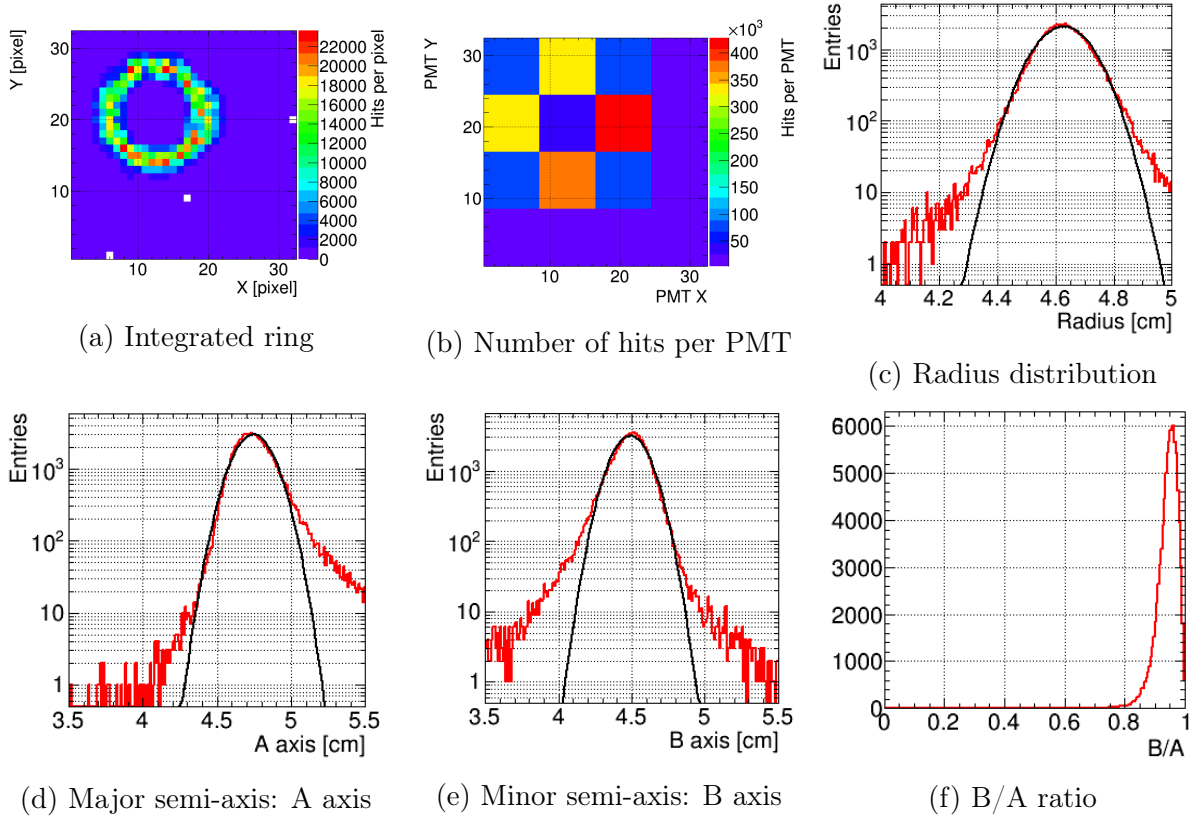
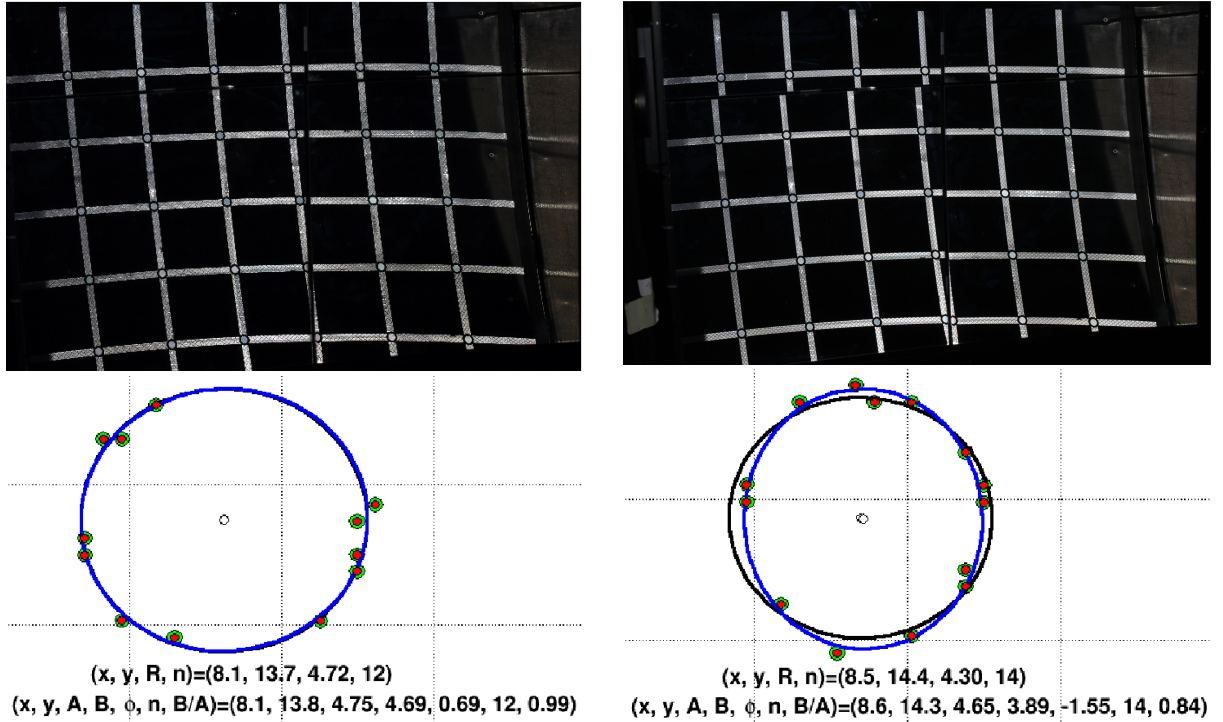


Figure 4.7: Distributions of main ring parameters with an aligned mirror system. The mean radius is 4.63 cm, the mean A and B axis are 4.75 cm and 4.49 cm, respectively. The number of events recorded is 90,669 with one ring per event.

The lower left mirror (in beam direction) was rotated afterwards, first around the vertical axis, defined as RotY in Figure 4.5. In this configuration half of the Cherenkov cone emitted by a particle crossing the vessel was reflected by the misaligned mirror, while the other half was reflected by an unchanged mirror.

In the cases reviewed here, the lower left mirror was rotated such that its left side rotated towards the observer (looking downstream). Thus the ring half reflected by this mirror would come closer to its other half reflected by the aligned lower right mirror on the photon detector. The ring in the MAPMT plane is thus squeezed. In order to improve the beam focussing and select only beam particles going exactly in between the two mirrors, a finger scintillator detector placed behind the mirror gap was additionally used as triggering device.

Figure 4.8a illustrates the mirror configuration after the initial alignment and a typical reconstructed single event ring. The situation once the mirror tile was rotated around its vertical axis, as described above, is depicted in Figure 4.8b, with a corresponding reconstructed single event ring. In the rotated configuration, misalignment is clearly visible, as the grid lines appear broken at the mirror edges, while the ring becomes more elliptical, as the two ring halves come closer to one another.



(a) Picture of the retroreflective grid reflected by the mirrors after the initial alignment (top). A corresponding single event ring reconstructed in this configuration is also shown (bottom).

(b) Picture of the retroreflective grid once the lower left mirror was rotated, along with a single event ring. Mirror misalignment is observable, as the grid lines appear broken at the mirror edges.

Figure 4.8: Impact of mirror rotation. For single event rings, the black and blue lines correspond to a ring and an ellipse shape, respectively. The fitted ring and ellipse parameters are drawn below the reconstructed ring.

Figure 4.9 shows analogous histograms to Figure 4.7 in the case of a rotation of 4 mrad of the lower left mirror around its vertical axis. As expected, rings seem more elliptical in the integrated ring picture (Figure 4.7a). The ring resolution is worse, which is a partial effect of misalignment, but also due to a dispersed beam. The increased ellipticity is measured by the mean values of the A and B axes. Their difference increased from 0.26 cm in the aligned case up to 0.43 cm. This increased ellipticity is also seen in a reduced B/A ratio (Figure 4.7f).

A split in two peaks in the B axis histogram is also observed. The first peak is reached for a B axis of about 3.95 cm, while the second one is located at around 4.45 cm. This feature suggests that two types of events were recorded. The first type ( $\bar{B} = 3.95$  cm) corresponds to the actual misaligned case. Here one ring half was reflected by the misaligned mirror closer to the other half. The second type of events ( $\bar{B} = 4.45$  cm) corresponds to cases where the Cherenkov cone was mainly reflected by one mirror (either misaligned or aligned). This is due to a rather unfocussed beam and reveals that the scintillator finger trigger was not sufficient to enhance the beam focussing.

Subsequently a cut on the data was applied to select only events, where the misalign-

ment is clearly seen. In this case, a B axis cut of 4.25 cm was implemented. This value was chosen, as it lies between the two observed peaks, allowing a rough separation between the two types of events. For the further discussion, the two types of events are called ‘misaligned’ and ‘aligned’. Comparing with the values obtained in the reference case, it can be assumed that events in which the B axis of the reconstructed ring is bigger than this threshold value are considered as ‘false’ misaligned events, while events with a B axis below the threshold are ‘true’ misaligned events.

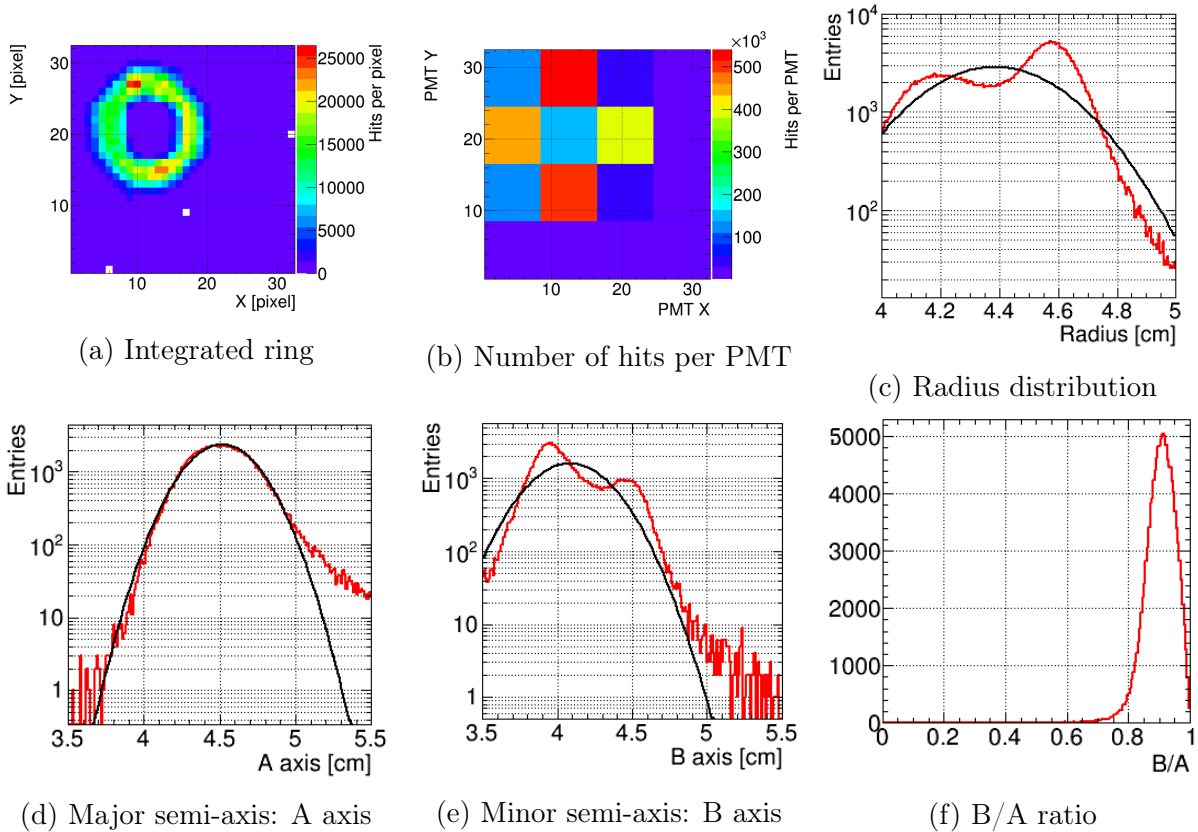


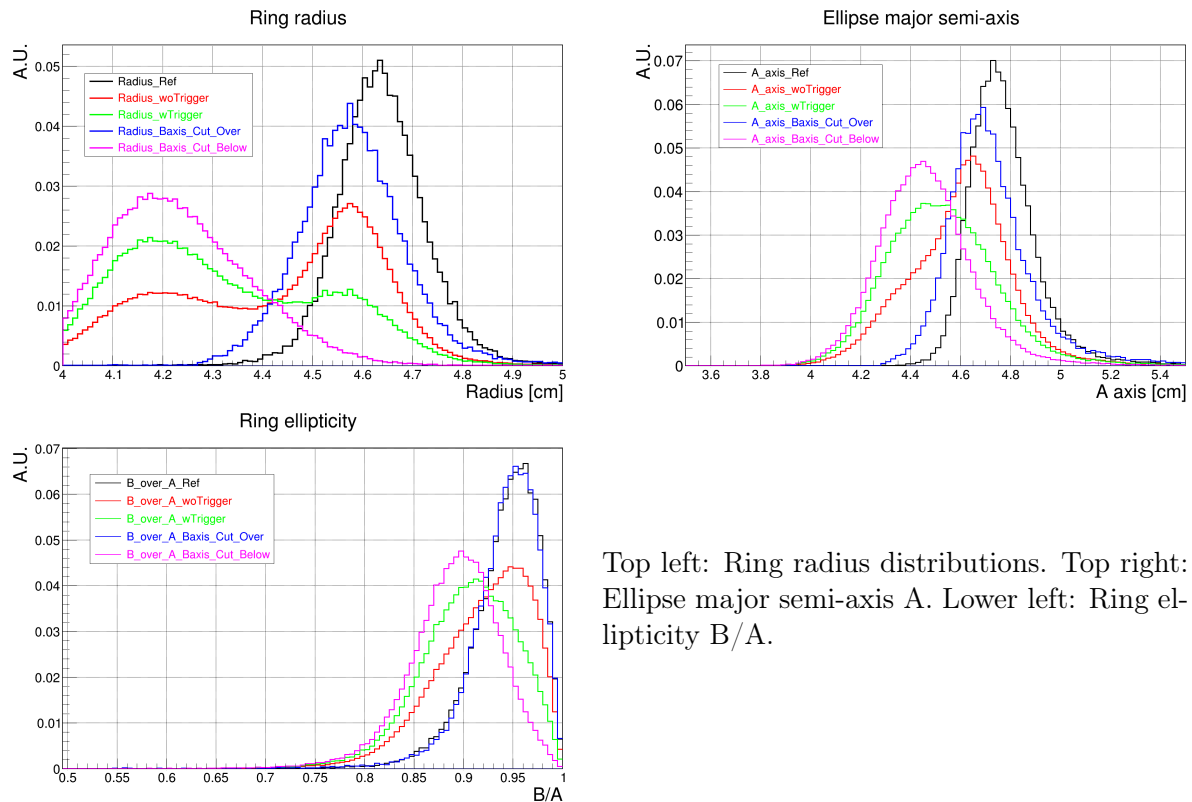
Figure 4.9: Distribution of main ring parameters with the lower left mirror rotated by 4 mrad around its vertical axis. The mean radius is 4.39 cm, the mean A and B axes are 4.52 cm and 4.09 cm, respectively. The number of events recorded is 121,849 with one ring per event.

Figure 4.10 illustrates the ring radius, the ellipse major semi-axis and the ring ellipticity histograms. In all the histograms the reference data set (black curve) is compared with the data set for which a 4 mrad rotation around the vertical axis of the mirror was carried out (coloured curves). The colour code correlates to different triggers used to select between rings strongly affected (B axis  $\leq 4.25$  cm) and rings only little affected (B axis  $> 4.25$  cm) by misalignment.

When applying a cut using the information from the finger scintillator detector, the number of ‘misaligned’ events extracted in the data set increases. This can be observed, for example, in the ring radius distribution, which compares the red (no trigger on finger scintillator) and the green lines (trigger on finger scintillator). As described the misalignment was done such that the ring is squeezed, thus the reconstructed ring should have a smaller radius. This effect is clearly seen and enhanced by selecting events more precisely

going in between the two mirrors with the finger scintillator. As a result, the lower values of the ring radius histogram from Figure 4.10 should correspond to the ‘misaligned’ events. For these events the Cherenkov cone was partially reflected on the aligned mirror and partially on the rotated one.

This described phenomenon is observed in all presented histograms.



Top left: Ring radius distributions. Top right: Ellipse major semi-axis A. Lower left: Ring ellipticity B/A.

Figure 4.10: Histograms of ring radius, A axis and ring ellipticity B/A. The reference data for an aligned system (black curves), the selected data without (red curves) and with (green curves) triggering and the data obtained above (blue curves) and below (magenta curves) the proposed cut (4.25 cm on the B axis). The histograms were normalised to the number of entries. The number of events recorded is 145,676 with one ring per event.

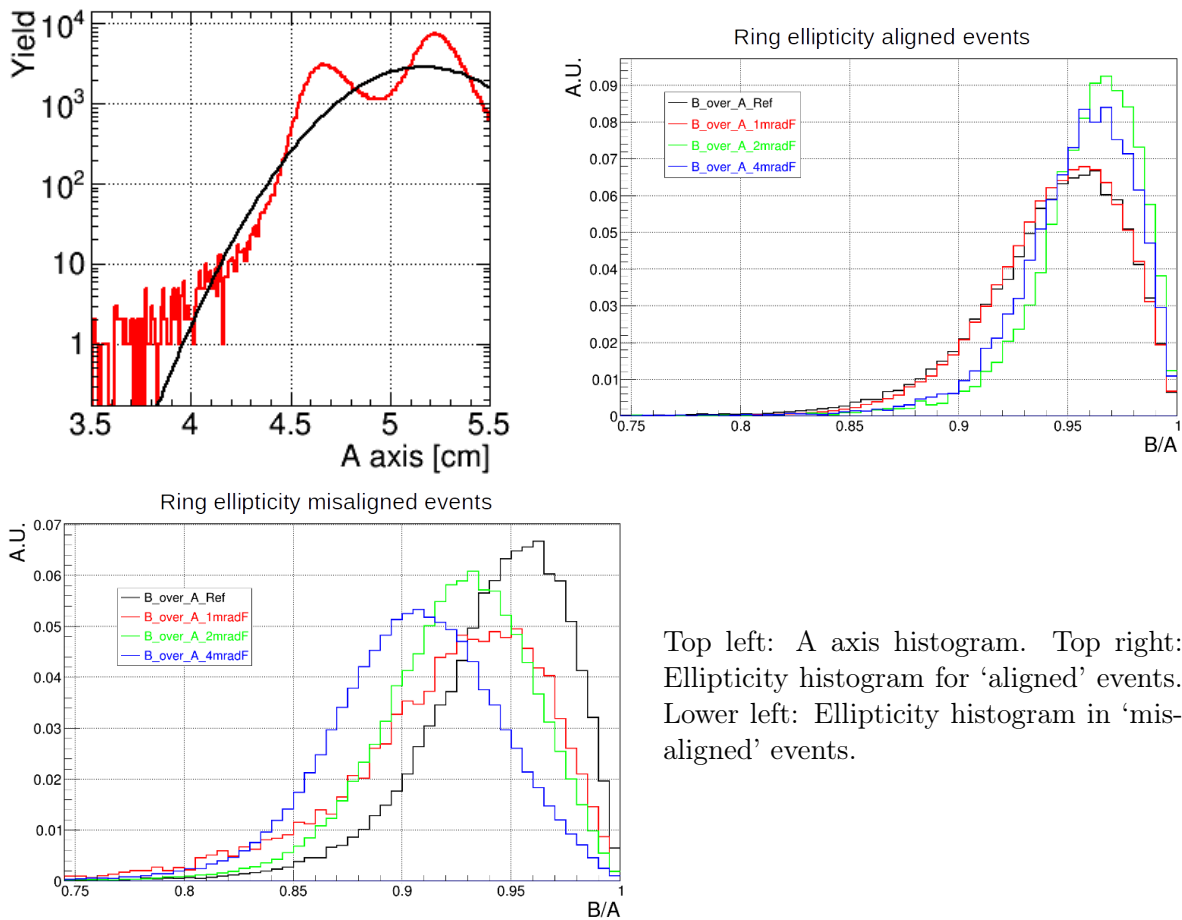
Furthermore, implementing the proposed cut on the B axis ( $B \text{ axis} \leq 4.25 \text{ cm}$ ), the selection of ‘misaligned’ events can be enhanced. This statement is supported by all histograms and in particular by the ring ellipticity histogram, in the lower left panel of Figure 4.10. The ring ellipticity, B/A, gives information on the shape of the reconstructed ring. For ‘aligned’ events (the blue line), the reconstructed ring should not be elliptical and should thus have an ellipticity close to 1. For ‘misaligned’ events (the magenta curve), the ellipticity increases thus B/A becomes smaller.

Indeed the blue curve lies closely to the black one (reference data set) and peaks at around 0.95 in B/A, while the magenta curve is the furthestmost curve on the left side, peaking at around 0.9 and thus gathering all elliptical events from the misaligned data set.

The study was extended to smaller rotation values and different rotation axes as well. Figure 4.11 shows results from the lower left mirror after rotation around its vertical axis,

however in the opposite direction than for the previous case (Figure 4.10), thus stretching the reflected rings. The rotation values were 1, 2 and 4 mrad. The beam diffusion translated into two peaks visible in the A axis distribution. The histogram presented in the upper left panel of Figure 4.11 illustrates the 4 mrad rotation. In the cases of 1 and 2 mrad rotations the peaks were still distinguishable but less pronounced.

In this example, a cut on the A axis at 5 cm was chosen, to differentiate the ‘misaligned’ events from the ‘aligned’ events. The same was done for the 1 and 2 mrad data set. The resulting ellipticities are plotted in the top right and the lower left panels of Figure 4.11. The reference data set is plotted as a mean of comparison (black line). The 1, 2 and 4 mrad rotations (red, green and blue curves, respectively) are superimposed on the histogram, too. Events below the threshold correspond to the ‘aligned’ events, while the ones above correspond to the ‘misaligned’ case.



Top left: A axis histogram. Top right: Ellipticity histogram for ‘aligned’ events. Lower left: Ellipticity histogram in ‘misaligned’ events.

Figure 4.11: Results from a misalignment study applying different rotations around the lower left mirror tile. In the A axis distribution the red curve corresponds to data and the black line to a Gaussian fit of the data. In the ellipticity histograms (top right and lower left panels), the reference data set is represented in black, the 1, 2 and 4 mrad rotations are in red, green and blue, respectively.

Analogous studies were conducted for mirror rotations around the horizontal and diagonal axes, with various rotation values. Studies were also done in the case of a beam passing between the four mirror tiles. Similar behaviours and results were detected and obtained, when applying threshold on ring parameters to select misaligned events.

Figure 4.12 displays integrated rings obtained in different rotation cases. The integrated ring obtained in the aligned case (Figure 4.12a) is also shown for comparison. Notable consequences of misalignment are ring half shifts, or ring splits.

Effects of misalignments on rings were observed, only if rings are equally split between two (or four) mirrors. If the two halves are unequally distributed, the largest half dominates, which reduces the impacts of misalignments on the reconstructed rings. Misalignment effects remain however small for rotations of 1 mrad, which goes along with the detector specifications.

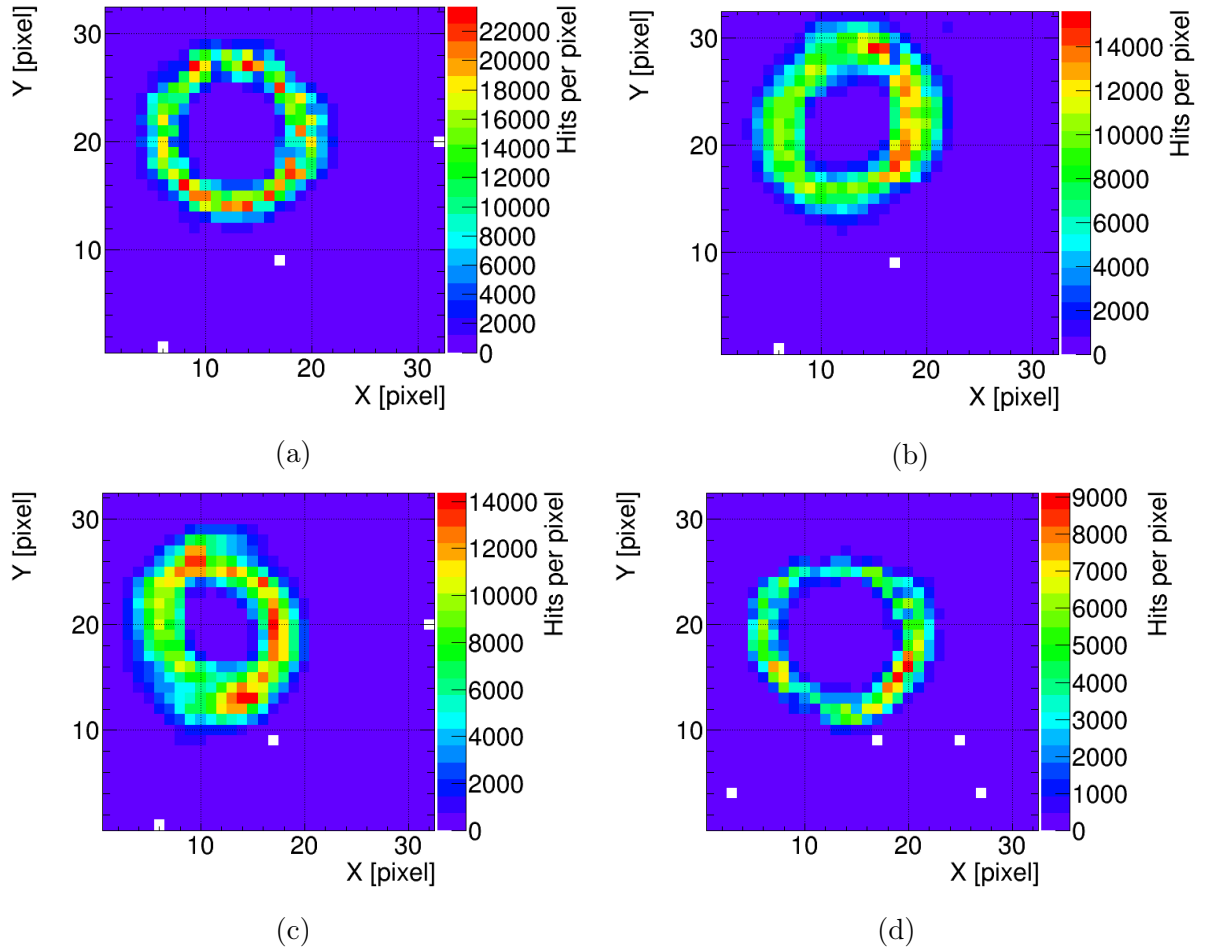


Figure 4.12: Integrated rings for different configurations of the rotated mirror wall. Upper left: Aligned mirror wall. Upper right: 4 mrad rotation around the horizontal axis of the lower left mirror tile. Lower left: 4 mrad rotation around the diagonal axis of the lower left mirror tile. Lower right: 4 mrad rotation around the vertical axis of the upper left mirror tile and 2 mrad rotation around the diagonal axis of the lower left mirror tile. The number of events acquired to obtain the figures are 90,669 (Figure 4.12a), 80,900 (Figure 4.12b), 64,783 (Figure 4.12c) and 18,205 (Figure 4.12d).

## 4.4 Mirror calibration for the CLAM method

As explained in Section 4.1, it is possible to infer the mirror rotations directly from CLAM pictures. To do so, a laboratory calibration is required and was conducted for the prototype set-up.

For the laboratory calibration, a reference image is taken when the mirrors are aligned and is used as comparison with pictures of the same mirrors, once they were rotated with defined rotation values. The reference and rotated pictures are subtracted and a threshold is applied on the resulting image. Thus only pixels which do not coincide between the reference and rotated pictures and whose levels of white exceed the applied threshold are observed on the resulting image. In case of misalignments, the resulting image exhibits duplicated bands. These image processing operations were carried out with the program *Mathematica*.

If double bands are obtained after the image processing, band widths are calculated. They are defined as the difference in pixels between the leftmost and rightmost lines for vertical mirror rotations and between the lowermost and the uppermost lines for horizontal mirror rotations (see Figure 4.15). In total four band widths are measured on four points of measurement chosen on the resulting picture either along the pixel rows or the pixel columns, depending on the applied rotations. Mirror rotations ranging from 0 to 5 mrad in both directions around the vertical and horizontal axes were applied and the corresponding pixel bands were measured.

	Upper actuator	Lower left actuator	Lower right actuator
Upper right mirror	1.65	2.35	0.67
Upper left mirror	2.838	3.76	2.278
Lower right mirror	1.72	2.3	0.26
Lower left mirror	4.04	3.88	2.73

Table 4.1: Reference actuator values of different mirrors for the mirror calibration study. The actuator values are given in volts and were applied to the system to obtain the initial alignment.

these steps are illustrated in a study conducted in the laboratory. For this study the LEDs were powered with  $0.12A \times 3.3V = 0.4W$ . The mirror outer frame was rotated by  $-30.5^\circ$  around its horizontal axis and  $-14.65^\circ$  around its vertical axis<sup>1</sup>. The mirror tile actuator values are given in Table 4.1. They were obtained after the mirror alignment procedure conducted at CERN.

Figure 4.13 shows a picture obtained after the initial alignment and which was used as reference for this study (left), along with a picture obtained after a 3 mrad rotation of the lower left mirror (right) around the vertical axis (such a rotation is illustrated on Figure 4.5 as RotY). To achieve the 3 mrad rotation of the lower left mirror tile, a voltage

<sup>1</sup>In EPICS the corresponding rotation values for the mirror frame are  $329.5^\circ$  around the horizontal axis and  $345.35^\circ$  around the vertical one.

of 4.1, 4.01 and 2.73 Volts were applied on the upper, lower left and lower right actuators, respectively. On the rotated picture the stripes clearly appear broken, revealing quickly the presence of misalignment.

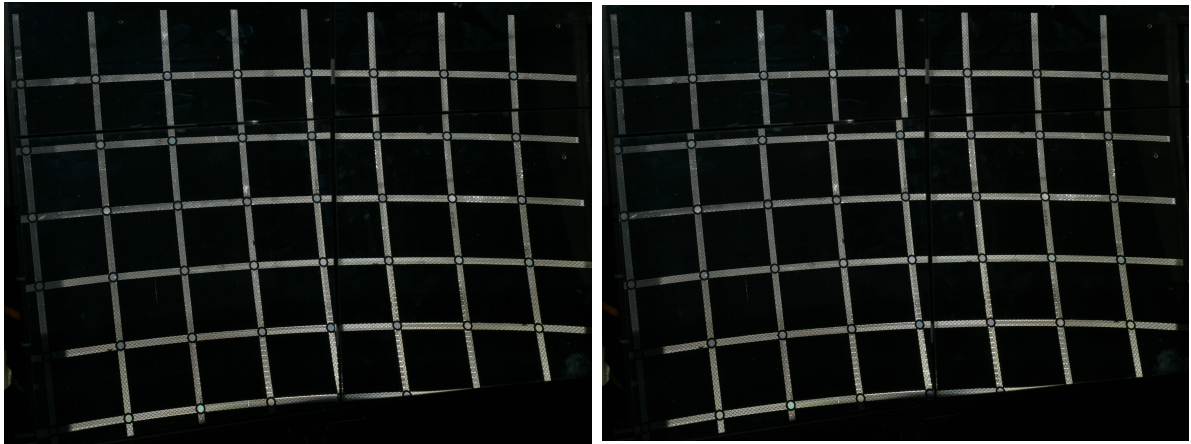


Figure 4.13: Left: Reference picture obtained after the initial alignment in the laboratory. Right: Picture obtained after a 3 mrad rotation of the lower left mirror around its vertical axis. The stripes appear broken at the mirror edges, revealing quickly the presence of misalignment.

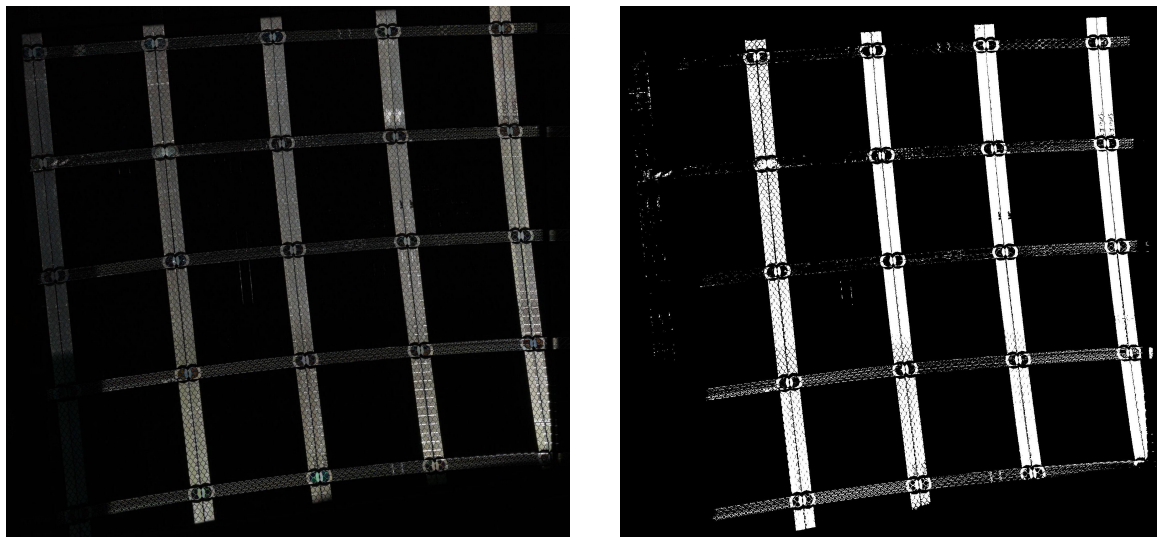
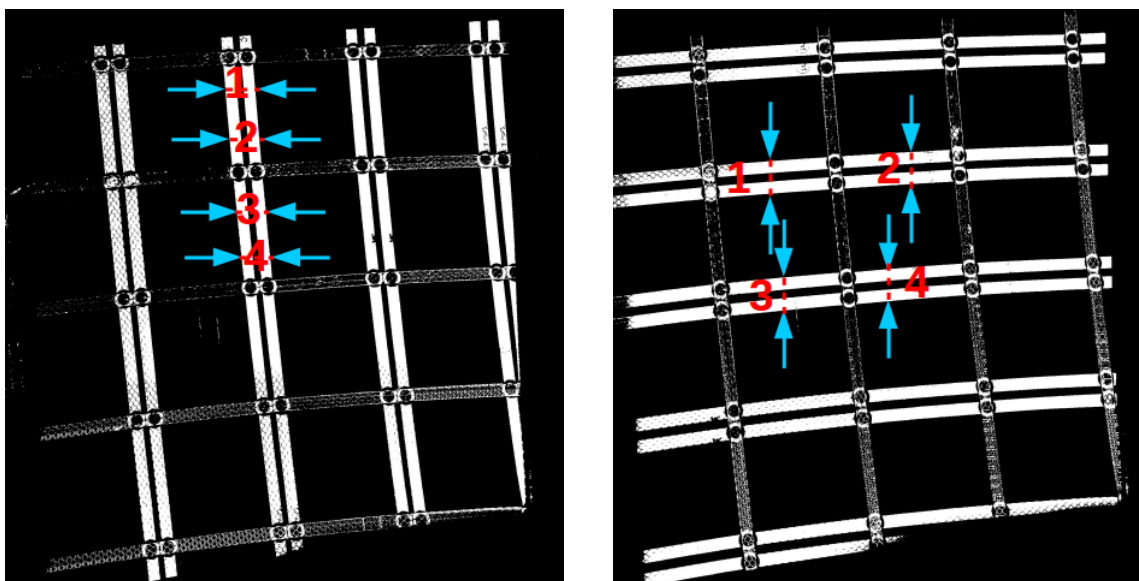


Figure 4.14: Left: Subtraction between the two pictures presented in Figure 4.13, where a 3 mrad rotation of the lower left mirror around its vertical axis has been applied. Right: Picture obtained after application of an appropriate threshold on the subtracted picture.

On the left side of Figure 4.14, the subtraction of the two CLAM pictures from Figure 4.13 is shown. To obtain this picture, pixel values between the reference picture and the misaligned one are compared and the relative difference is plotted in a gray scale. The right side of Figure 4.14 displays the subtracted figure after an appropriate threshold was applied. There only black and white pixels are visible. The application of the threshold facilitates the measurement of the different pixel bands, which corresponds to the next step of the calibration.

The rows and columns, where the band widths are measured are defined on Figure 4.15. The width of the pixel bands are measured either horizontally (Figure 4.15a) or vertically (Figure 4.15b) or both in the indicated areas, depending on the applied mirror rotations.



(a) Chosen measurement bands on the thresh- (b) Chosen measurement bands on the thresh-  
old picture for a horizontal rotation. old picture for a vertical rotation.

Figure 4.15: For both pictures a rotation of 5 mrad was induced.

For rotations around the vertical axis of the mirror tile (Figure 4.15a), four measurement rows are chosen along the middle stripe. For rotations around the horizontal axis (Figure 4.15b), two measurement columns are chosen along the second stripe and the third stripe, counting from the top one.

Thus a mirror rotation in mrad corresponds to a width of pixels. This measurement is done automatically from the first until the last detected white pixel in an area surrounding the band to be measured.

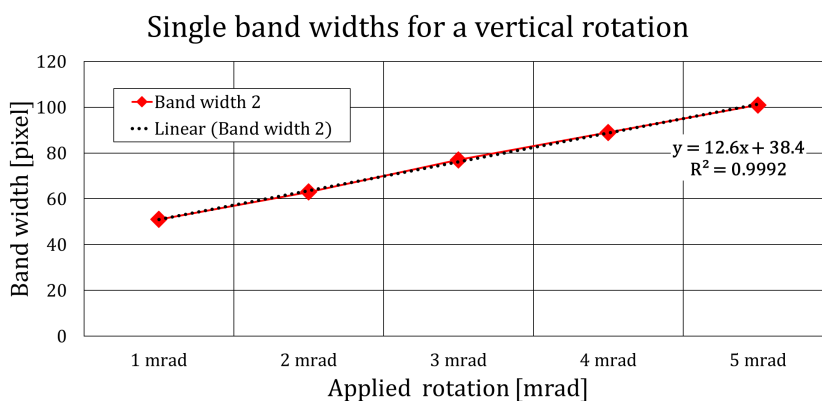


Figure 4.16: Band widths (in pixel) obtained for the measurement on the band number 2 (see Figure 4.15a) for vertical rotations ranging from 0 to 5 mrad applied on the lower left mirror tile. The data are well described by a linear fit, plotted with black dots and whose fit is given. The intercept of 38.4 corresponds to the width of a single band.

Figure 4.16 displays for example a band width obtained for the second measurement row (Figure 4.15a, measurement band number 2) for a vertical rotation ranging from 0 to 5 mrad. A linear fit is plotted, with a determination coefficient of nearly one, showing a very close to ideal fit. The parameters extracted from the fit are plotted, too.

The dependence of the band width on the mirror rotation is shown in Figure 4.17. All four measurement points for vertical and horizontal rotations are displayed. A linear trend is observed for all measurements, which agrees with the report from the COMPASS experiment [127]. This makes it possible to infer the applied rotation from a rotated picture, provided that a previous calibration measurement has been performed.

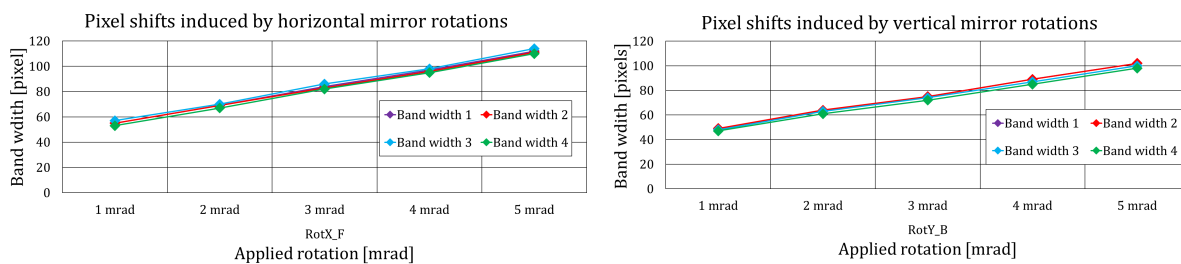


Figure 4.17: Relation between the band widths and the horizontal (left) and vertical (right) rotations for all measurement rows and columns for the lower left mirror of the wall. The same linear behaviour is observed in all positions of each applied rotations.

A similar study has been carried out for the lower right mirror tile and fit results are presented in Figure 4.18. In this case the linear fits were slightly worse than in the previous one. For all measurement bands, the fits yield good results, even though the data points do not seem to lie on a straight line.

For the lower right mirror, a loss in the intensity of the grid was observed. This caused fluctuations in the threshold picture for smaller rotations. Increasing the power of the LEDs to  $0.19A \times 3.7V = 0.7W$  did not solve the problem. The band widths were thus measured manually.

## Single band widths for a vertical rotation

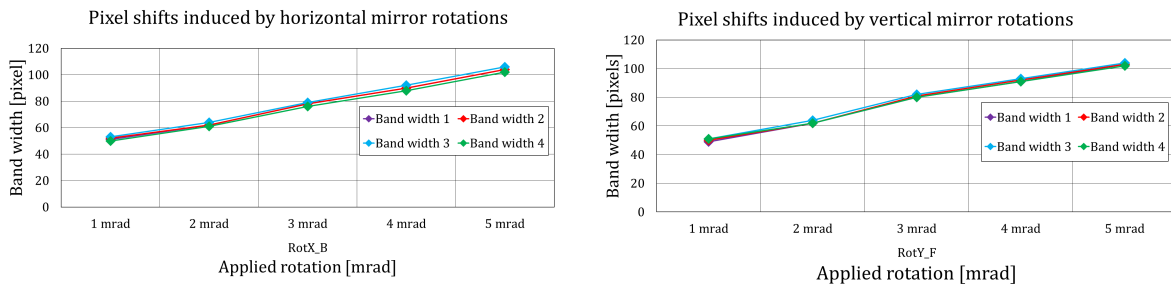
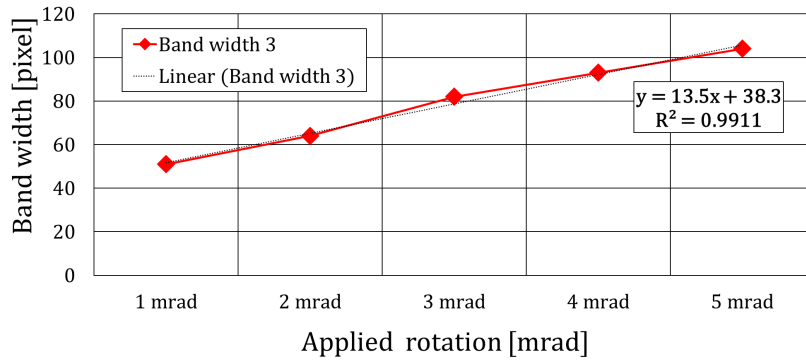


Figure 4.18: Upper panel: Band widths obtained for the measurement band number 3 (see Figure 4.15a) for vertical rotations of the lower right mirror tile ranging from 0 to 5 mrad. Two lower panels: Relation between the band widths and the horizontal (left) and vertical (right) rotations for all measurement rows and columns for the lower right mirror of the wall. A linear behaviour is still visible, although it is slightly worse than in the previous example.

## 4.5 Application of the CLAM calibration on pictures taken at CERN

The previously presented calibration of the mirror wall with the CLAM method was subsequently used on pictures taken during the beam time at CERN (see Section 4.2.2). From these pictures, mirror rotations were deduced in order to test the method, even though the calibration was carried out at a later time and with a slightly different set-up.

Figure 4.19 exhibits pictures of the mirror wall taken after the initial alignment (top left), after a 4 mrad rotation around the vertical axis (top right) and after a subtraction between the two pictures and once a threshold has been applied (lower picture).

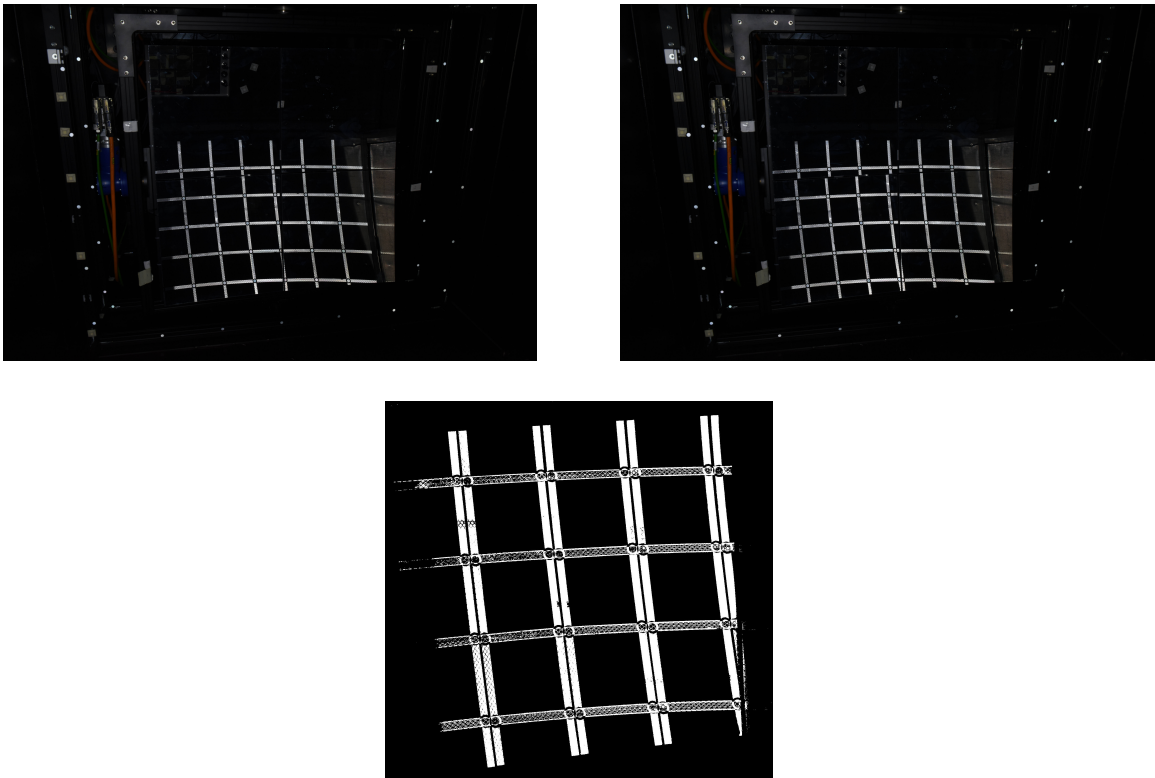


Figure 4.19: Pictures obtained after the initial mirror alignment (top left), after a 4 mrad rotation around the vertical axis of the lower left mirror tile (top right) and after subtraction of the two upper pictures and application of a threshold (lower picture).

The band widths of each measurement points used in the case of a vertical rotation (defined on Figure 4.15a) were measured in pixels. From the fits obtained for each measurement band during the calibration in the laboratory (see for example the equation on Figure 4.16 for the measurement band number 2), the following rotation values were retrieved:

- point 1: 4.09 mrad
- point 2: 4.08 mrad
- point 3: 3.98 mrad
- point 4: 4.3 mrad

The mean of these values amount to 4.11 mrad, which is only 2.75% more than the actual applied rotation.

these results are obtained with the fit curves extracted for a rotation around the vertical axis in the same direction. In this case the left side of the mirror comes towards the observer and the right side of the mirror goes away from him (called ‘Backward’ rotation). In addition, the measured band widths (in pixel) were fit to the results obtained for the same vertical rotation in the different direction. In this case, the left side of the mirror goes away from the observer and the right side of the mirror comes towards him (called ‘Forward’ rotation). The following rotations were extracted:

- point 1: 4.01 mrad
- point 2: 4.1 mrad
- point 3: 3.98 mrad
- point 4: 4.25 mrad

The mean of these values amount to 4.09 mrad, which is 2.25% more than the applied rotation and lies even closer than the value obtained previously.

The same study has been conducted in the case of a 2 mrad ‘Forward’ rotation and a 1 mrad ‘Backward’ rotation around the vertical axis of the lower left mirror. The results are displayed in Table 4.2.

	2 mrad rotation ‘Forward’		1 mrad rotation ‘Backward’	
	‘Backward’ calibration	‘Forward’ calibration	‘Backward’ calibration	‘Forward’ calibration
Measurement point 1	2.35	2.22	0.98	0.81
Measurement point 2	2.56	2.51	1.03	0.92
Measurement point 3	2.34	2.23	0.94	0.86
Measurement point 4	2.56	2.46	1.13	1
Mean	2.45	2.36	1.02	0.9

Table 4.2: Retrieved mirror rotations in the case of a vertical rotation of the lower left mirror. The numbers are given in mrad.

In this case, the rotation values obtained for a 2 mrad rotation diverge more from the applied rotation. The mean is about 22.5% more than the applied rotation for the ‘Backward’ calibration and about 18% more for the ‘Forward’ rotation. In the case of the 1 mrad rotation, the calculated rotations are in very good agreement with the applied ones. They diverge by 2% and 10% for the ‘Backward’ and ‘Forward’ calibrations, respectively.

The discrepancy shown for the 2 mrad rotation can be due to a slightly different mirror set-up used during the laboratory calibration from the one employed at CERN.

For example the orientation of the camera could not be exactly reproduced. Also the light intensity was different.

For comparison purposes, Table 4.3 shows the equations obtained once the presented image processing operations have been applied to the pictures taken at CERN and fitted with a linear fit. They are similar to the equations retrieved from the laboratory calibration displayed on Figures 4.16 and 4.18.

	Measurement point 1	Measurement point 2	Measurement point 3	Measurement point 4
Equations from the 'Backward' calibration	$y = 13.2x + 36$	$y = 13.1x + 36.5$	$y = 12.8x + 36$	$y = 12.6x + 34.8$
Equations from the 'Forward' calibration	$y = 12.8x + 38.6$	$y = 12.6x + 38.4$	$y = 12.5x + 37.3$	$y = 12.3x + 36.7$

Table 4.3: Equations obtained from the pictures taken at CERN, once the image processing operations have been applied and the resulting threshold pictures have been fitted with a linear fit.  $x$  represents the mirror rotation values in mrad and  $y$  the corresponding pixel width values. The equations can be compared to the ones obtained in Figures 4.16 and 4.18 from the previous section.

The same study was carried out for a 'Backward' diagonal rotation of 4 mrad of the lower left mirror, that is, a rotation on both the vertical and the horizontal axes in the 'Backward' direction. Figure 4.20 illustrates the mirror wall after initial alignment (top left), after the rotation was applied (top right) and after the subtraction and threshold were implemented (lower figure).

The rotation values of the mirrors retrieved from the pixel shifts are presented in Table 4.4. The calculated vertical rotation is consistent with the applied one. The overestimation amounts to 1.75% of the applied rotation, in the case of the 'Backward' calibration, which corresponds to the actual direction of rotation. In the case of the horizontal rotation, a discrepancy appears, which translates to 14.25% and 9.75% of the applied mirror rotation in the 'Backward' and 'Forward' calibrations, respectively.

In this case, the pictures taken at CERN look quite different from the ones taken in the laboratory during the calibration. Figure 4.21 displays the two different pictures taken at CERN (left) and in the laboratory (right). This reveals that the vertical rotation is not so much affected by the conditions under which the calibration is carried out, such as camera orientation and light intensity. However the horizontal rotation seems to be more sensitive to the calibration set-up.

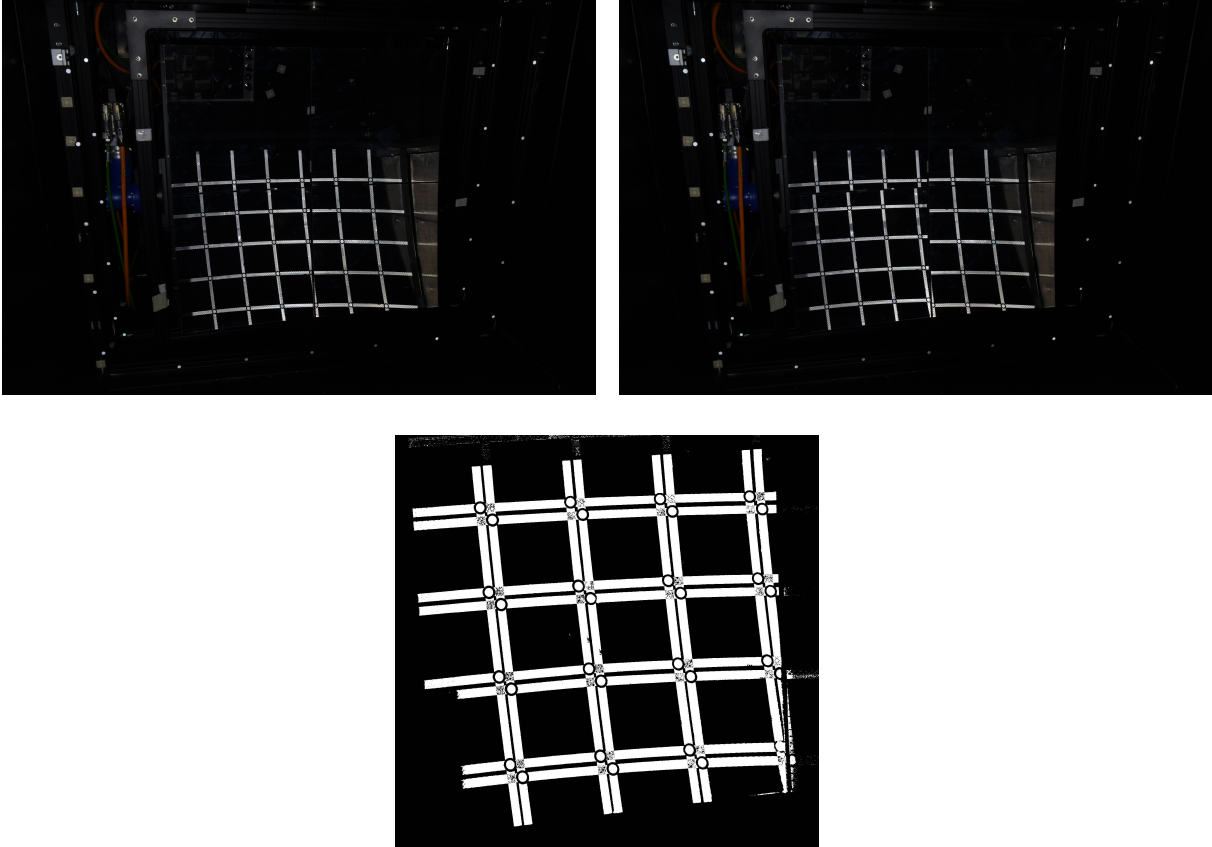


Figure 4.20: Pictures obtained after the initial mirror alignment (top left), after a 4 mrad rotation around the diagonal axis of the lower left mirror tile (top right) and after subtraction of the two upper pictures and application of a threshold (lower picture).

	Vertical rotation		Horizontal rotation	
	'Backward' calibration	'Forward' calibration	'Backward' calibration	'Forward' calibration
Measurement point 1	4.09	4.02	4.55	4.38
Measurement point 2	4.24	4.25	4.62	4.38
Measurement point 3	4.02	4.14	4.48	4.34
Measurement point 4	3.94	4.17	4.64	4.45
Mean	4.07	4.15	4.57	4.39

Table 4.4: Retrieved mirror rotations in the case of a diagonal rotation of the lower left mirror. The vertical and horizontal components of the applied rotation are separated. The numbers are given in mrad.

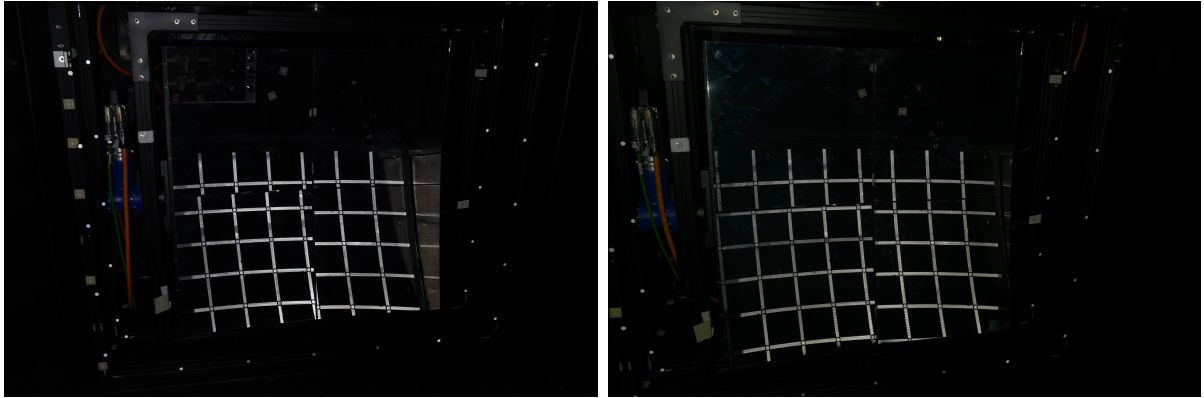


Figure 4.21: Mirror system as observed by the CLAM camera at CERN (left) and during the calibration in the laboratory (right), after a ‘Backward’ diagonal rotation of 4 mrad induced on the lower left mirror tile.

Another technique to quantify mirror rotations would be to use photogrammetry calculations, which is briefly discussed in Section 7.2.

In summary, the so-called CLAM method was successfully implemented in the CBM-RICH prototype. The method yields a quick qualitative assertion to monitor mirror alignment. In addition, it can be used to quantify mirror rotations, provided that a previous laboratory calibration was conducted. This calibration is required for each mirror, which can be time consuming. Also the conditions during the calibration (camera orientation, illumination) have to stay stable, so that the yielded results remain comparable.

Moreover in the event that mirror rotations are detected and calculated with the CLAM method, the rotation values can be written to a text file. This file is then used as input for the correction cycle presented in Chapter 6 to allow a proper operation of the RICH detector with mirror misalignments.



# Chapter 5

## Quantification of mirror rotations with software

### 5.1 Principle of the technique

In addition to the CLAM method employing an external hardware, a technique inspired from the HERA-B experiment was implemented in the CbmRoot simulation framework for the CBM-RICH detector [128, 149]. This technique aims at quantifying mirror rotations, based on software and recorded data. Its principle is illustrated in Figure 5.1.

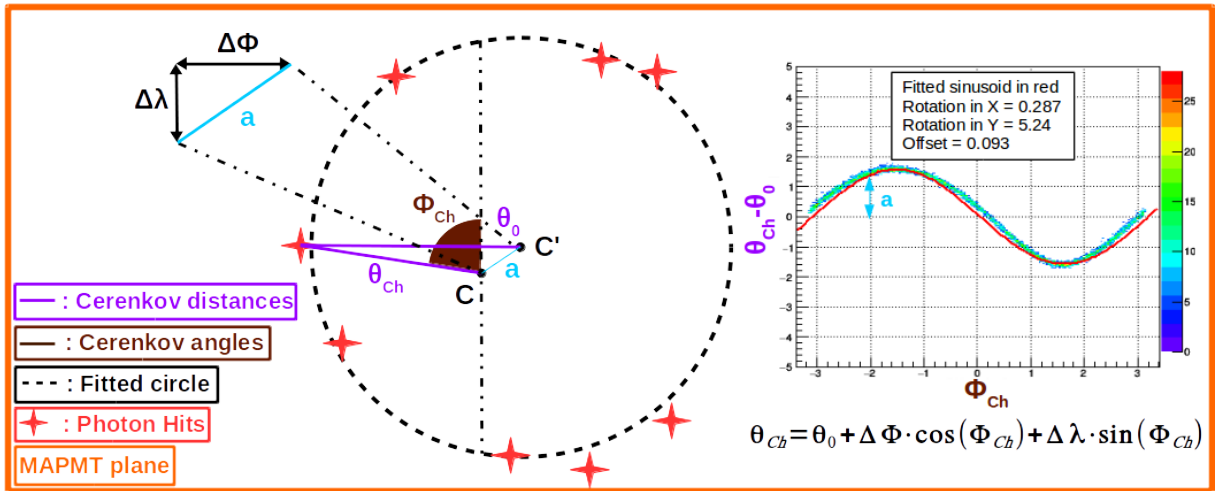


Figure 5.1: Principle of the quantification technique developed by the HERA-B experiment.

Assume an event, where a Cherenkov cone is reflected on one particular mirror tile, focused on the MAPMT plane as a ring and reconstructed by the software. The red crosses in Figure 5.1 represent photon hits on the MAPMT plane and are fitted by the software into a ring (dashed black line), whose centre is denoted  $C'$ . If the track, which produced this ring, had been reflected by the same mirror in its aligned position, its extrapolation on the MAPMT plane, as it is implemented in the RICH software, is indicated as  $C$ . For a perfectly aligned system,  $C$  and  $C'$  would overlap. If misalignments are present,  $C'$  is shifted horizontally ( $\Delta\lambda$ ) and vertically ( $\Delta\Phi$ ), depending on the rotation angles of the

misaligned mirror tile. These shifts, when combined together, correspond to the distance  $a$  between  $C$  and  $C'$ .

Subsequently two parameters are measured, namely the Cherenkov distance and the Cherenkov angle, defined as  $\theta_{Ch}$  and  $\Phi_{Ch}$  in Figure 5.1.  $\theta_{Ch}$  (in violet) is the distance between each photon hit (red cross) and the extrapolated track hit  $C$ .  $\Phi_{Ch}$  (in brown) is calculated as the angle between  $\theta_{Ch}$  and the vertical passing through  $C$ . In parallel  $\theta_0$  is defined as the distance between a photon hit and the reconstructed ring center.

In case of mirror rotations, a sinusoidal behaviour is revealed when plotting  $\theta_{Ch} - \theta_0$  versus  $\Phi_{Ch}$ . This sinusoid can be used to extract the rotation values of the mirror tile. Indeed, it has been demonstrated that [128]:

$$\theta_{Ch} = \theta_0 + \Delta\Phi \cdot \cos \Phi_{Ch} + \Delta\lambda \cdot \sin \Phi_{Ch} \quad (5.1)$$

$\Delta\lambda$  and  $\Delta\Phi$  are illustrated in Figure 5.1 and correspond to the horizontal and vertical projections of the distance between  $C$  and  $C'$ :  $a$ . These shifts can be correlated to mirror rotations around a vertical axis and a horizontal axis, with the rotation axes passing through the center of the mirror tile.

To compute the correlation between a shift on the MAPMT plane and a mirror rotation, the following formula can be derived, using geometric considerations:

$$shift = \tan(2\sigma) \cdot R \quad (5.2)$$

*Shift* is the shift on the photon detector plane in meter ( $\Delta\lambda$  or  $\Delta\Phi$  for example),  $R$  is the radius of curvature of the mirror in meter and  $\sigma$  the rotation applied on one axis of the mirror tile in mrad.

A rotation around the horizontal axis of the mirror tile will induce a shift along the vertical axis on the photon detector plane, while a rotation around the vertical axis of the tile will induce a shift along the horizontal axis.

Thus, for a sufficient number of accumulated events fully hitting a particular mirror tile, mirror rotations around a horizontal and a vertical axis can be quantified by the software. The right side of Figure 5.1 gives a first example. It represents in a histogram  $\theta_{Ch} - \theta_0$  as a function of  $\Phi_{Ch}$  in the case of a mirror rotated by 5 mrad around its vertical axis and after a threshold was applied to enhance the sinusoidal behaviour. Fitting the data to Equation 5.1, misalignments of 0.29 mrad and 5.24 mrad were reconstructed around the horizontal and vertical axes, respectively. The red curve illustrates the sinusoid with these parameters.

## 5.2 Implementation of misalignments in the RICH geometry

The implementation of the RICH geometry in the CbmRoot framework was presented in detail in Section 3.3.5. In addition to the presented RICH detector geometry, the possibility of mirror rotation was implemented, using the CATIA software. This feature allows for artificial mirror tile rotations around the horizontal and vertical axes of the tile, both independently and simultaneously. The rotation axes are defined locally for each tile as the tangent (for the horizontal axis) and the binormal (for the vertical axis) of the tile passing through its center. Horizontal and vertical mirror rotations are illustrated on Figure 5.2, where two rows of mirrors have been rotated.

Mirror rotations can be set in a .gdml file, which first needs to be converted to the .root format, before being used for simulations. Studies have shown [94] that, during the operation of the RICH detector, a mirror misalignment of 1 mrad per axis is tolerated.

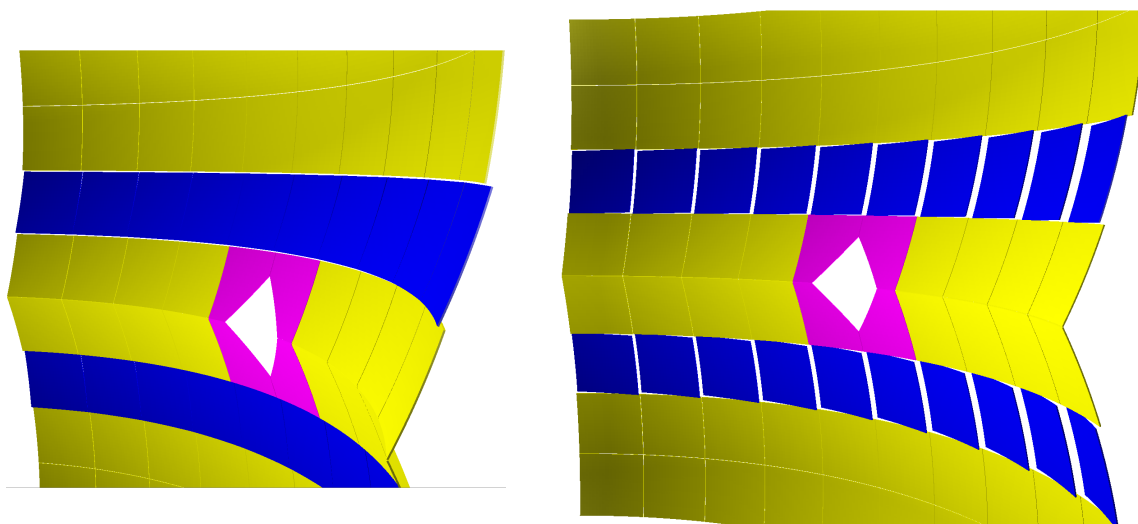


Figure 5.2: Mirror rotations around the horizontal (left) and vertical (right) axes. The misaligned row of mirrors are coloured in blue, while the aligned rows are in yellow. The beam-pipe, mirror supporting frame and holding structure were removed and an exaggerated rotation value of 100 mrad was applied for better visualisation.

As explained in Section 3.4, inducing misalignments will alter the reconstruction process of the RICH software illustrated in Figure 3.22. Indeed the reflection of an incoming track extrapolated from the STS detector is calculated by the software, supposing mirrors in their ideal aligned configuration. However, the emitted Cherenkov photons will be reflected by the mirrors in their actual state, which is rotated in case of misalignments. This will lead to shifts between the reconstructed ring centres  $C'$  and the extrapolated track positions  $C$ , corresponding to an increase in  $a$  from Figure 5.1.

Figure 5.3 represents four situations of mirror misalignments. Four different mirror tiles (marked by the red boxes) were rotated by 3 mrad around a single axis.

As explained in the previous section, a vertical rotation, corresponding to a rotation around the Y axis, should induce a shift only (in the ideal case) in the horizontal direction ( $\Delta\Phi$  on Figure 5.1, while  $\Delta\lambda$  remains unchanged). Analogously, a horizontal rotation, referred to as a rotation around the X axis, should induce a shift only in the vertical direction ( $\Delta\lambda$  on Figure 5.1, while  $\Delta\Phi$  remains unchanged).

In addition, a direction of rotation is defined. A positive rotation around the Y axis (for example +3 mrad around the Y axis) is such that when looking at the front of a mirror tile, the right side of the tile will rotate towards the observer and the left side of the tile will rotate away from him. Analogously, a positive rotation around the X axis (for example +3 mrad around the X axis) is such that the upper part of the mirror tile will rotate towards the observer and the lower part will rotate away from him.

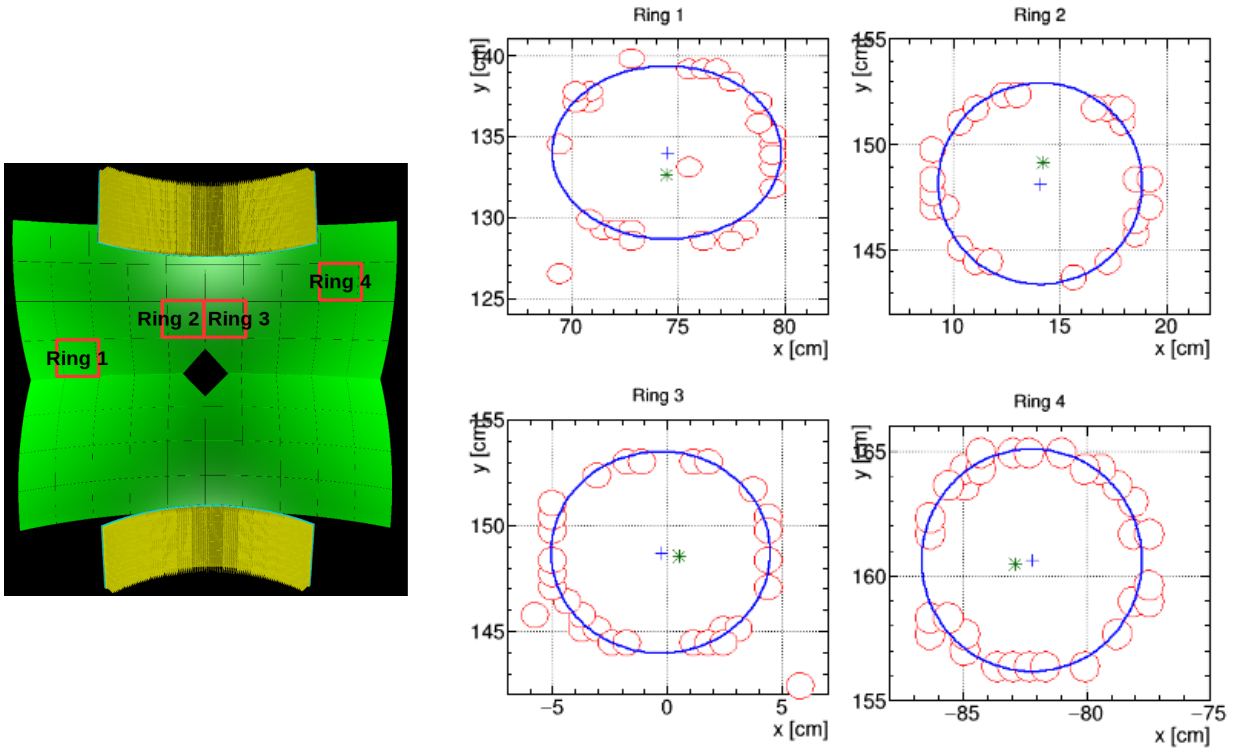


Figure 5.3: Reconstructed rings (blue) and measured photoelectrons (red) in the MAPMT plane for different mirror rotations and mirror tile positions, as depicted on the left figure. Right, from top left (Ring 1) to bottom right (Ring 4): -3 mrad around the X axis, +3 mrad around the X axis, -3 mrad around the Y axis, +3 mrad around the Y axis. Ring centres are depicted with the blue cross, extrapolated tracks with the green stars. A 3 mrad rotation corresponds to a shift of 0.9 cm of the ring centre  $C'$  on the photon detector plane. In all cases the ring centre was shifted in the expected direction from the extrapolated track hit by around 1 cm.

The rings reflected by the different mirror tiles are labelled from 1 to 4 on Figure 5.3. The ring centres were shifted by 1.3 cm in the horizontal direction in the case of rings 1 and 2 and by 0.8 cm and 0.7 cm in the case of rings 3 and 4, respectively. Moreover, a shift in the other direction was observed, which amounts to 0.1 cm for rings 1 and 2 and 0.2 cm for rings 3 and 4.

Using the Equation 5.2, a rotation of 3 mrad is equivalent to a shift of 0.9 cm on the photon detector plane. The errors observed in Figure 5.3 amount in average to 44% of the calculated value for a horizontal rotation, while for a vertical rotation they amount to 17% of the calculated value.

The observed discrepancies can be attributed to the detector geometry, such as the cylindrical shape of the photon detectors.

### 5.3 Quantification of mirror rotation

In this first example, a single mirror tile, whose ID number is 5\_3, was rotated by 4 mrad around its vertical axis. 2,500 events were simulated, each event containing 1 electron shot directly at the tile of study. The following lists the set-up used on CbmRoot for this study: Magnet (version v15a, with the magnetic field map v12b), STS (version v16x), RICH (version v17a\_1e) and beam pipe (version v16c\_1e).

The minimum number of points required for the STS detector was four and it was seven for the RICH detector. The standard routines of the RICH detector for ring finding and ring-track matching were employed. The results presented were obtained with the class *CbmRichMirrorSortingAlignment*, with a threshold of 400 to reduce the background.

The intersection between the track and the photomultiplier is done by computing first the intersection between the particle and the mirror tile. This is implemented using a particle propagation method from the Geometry Manager class. Then the reflection on the mirror is calculated from the mirror normal computed at the intersection point. Finally the intersection with the MAPMT is calculated, by extrapolating the reflection to the MAPMT plane.

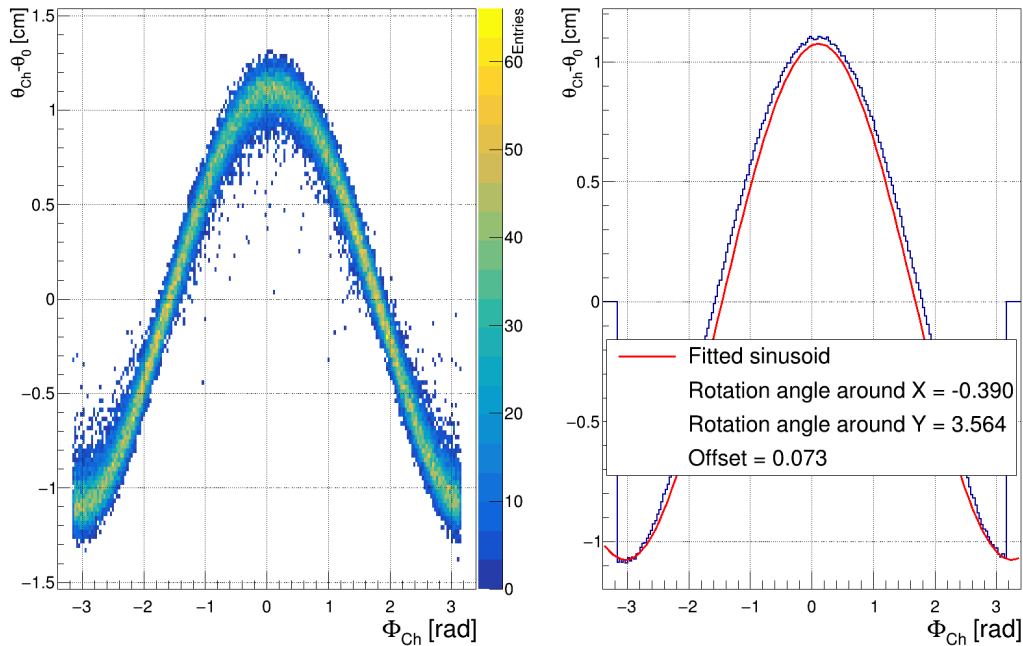


Figure 5.4: Left: Histogram of  $\theta_{Ch} - \theta_0$  versus  $\Phi_{Ch}$  in the case of a mirror tile rotated by 4 mrad around its vertical axis. The distribution is clearly that of a sinusoid. Right: Resulting sinusoidal fit from the left histogram coloured in red. The extracted rotation parameters around the horizontal and vertical axes are -0.39 mrad and 3.56 mrad respectively. The blue curve represents the maximum of each vertical slice from the histogram on the left-hand side. 2,500 electrons were simulated and a threshold of 400 was applied.

From the accumulated statistics, the variables  $\theta_{Ch} - \theta_0$  and  $\Phi_{Ch}$  were calculated. They were put together in a histogram, shown on the left side of Figure 5.4. A sinusoidal behaviour is apparent.

To fit the resulting histogram with a sinusoid from Equation 5.1, a preliminary search

of maximum was conducted for each vertical slice of the histogram. The resulting sinusoid is shown on the right side of Figure 5.4. The extracted rotation values are -0.39 mrad around the X axis and 3.56 mrad around the vertical axis.

According to Figure 5.3, a vertical rotation will mostly translate in an increase in  $\Delta\Phi$ , while  $\Delta\lambda$  remains unchanged. This implies, according to Equation 5.1 that the fitted curve will mainly look like a cosine function, which is the case on Figure 5.4.

The binning of the histogram on Figure 5.4 can be tuned to optimise the quantification of mirror rotations. A finer binning yields more reliable results but also requires more statistics, which can become difficult to achieve for example for mirrors located away from the beam pipe. In the end a trade-off needs to be found.

The rotation values do not correspond exactly to the applied rotation, partially due to the RICH detector geometry. Indeed a rotation around a single axis implies both vertical and horizontal displacements of  $C'$  on the PMT plane, which is detected from the sinusoid shape. This phenomenon is more apparent for the CBM RICH detector, as the radius of curvature of the mirrors is 3 m and the mirror wall is tilted by  $10^\circ$  around the horizontal axis, whereas the radius of curvature is 11.4 m in the case of the HERA-B RICH and the mirrors are tilted by  $9^\circ$ .

The technique has been also adapted to the RICH detector geometry nomenclature, such that the mirror tile name from the geometry file is extracted and used. It was also further improved to detect misalignments on different mirror tiles simultaneously. These changes have been included in the class *CbmRichMirrorSortingAlignment* in the *Exec* and *DrawFitAndExtractAngles* methods.

## 5.4 Performances of the technique

The performances of the quantification technique were further investigated. Simultaneous misalignments on both rotation axes of a given mirror tile can be extracted. The situation is illustrated in Figure 5.5. In this example, the mirror tile 5\_3 was rotated by 4 mrad around its horizontal axis and by 2 mrad around its vertical axis. The simulation parameters were identical to the ones detailed in the previous section. A rotation of 3.96 mrad around the horizontal axis and 1.97 mrad around the vertical axis were calculated by the software.

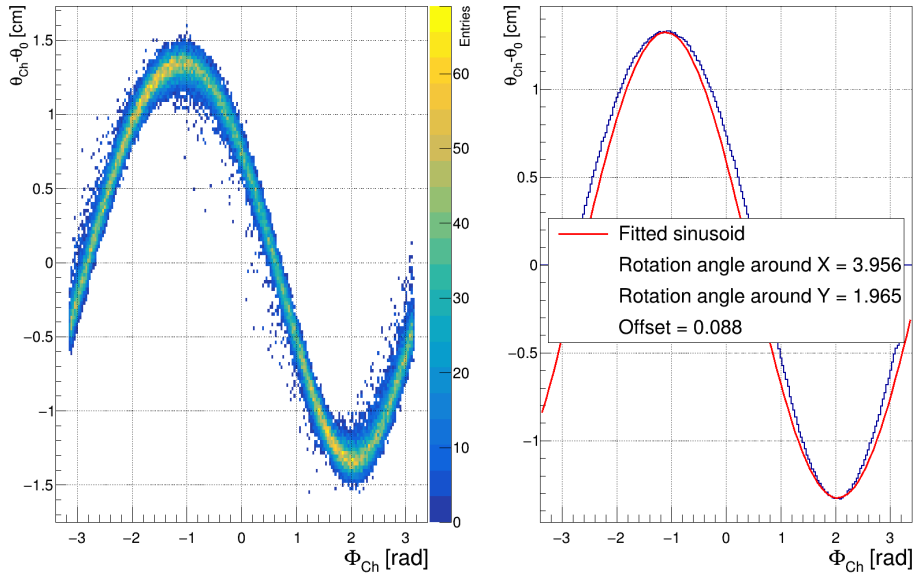


Figure 5.5: Detection of misalignments on both mirror tile axes simultaneously. Left: histogram obtained from data. Right: corresponding sinusoid. Rotation values were 4 mrad around the horizontal axis and 2 mrad around the vertical axis. Detected values are 3.96 mrad and 1.97 mrad, respectively.

The detection limits and the performances in the inner and outer regions of the mirror wall are reviewed in the following subsections.

### 5.4.1 Detection limits

The detection limits of the technique were examined, namely the minimal and maximal misalignments on a mirror tile, which can be correctly derived. Misalignments were applied on the tile 5\_3 and 2,500 events, each containing one electron for better reconstruction, were simulated and shot towards the mirror tile. The chosen set-up in CbmRoot is similar to the one already presented in the previous section.

For rotations only around the horizontal axis of the mirror tile, misalignments down to 0.3 mrad and up to 14 mrad can be retrieved. The reconstruction errors amount to 19.7% of the applied rotation for the 0.3 mrad misalignment case and it amounts to 16% of the applied rotation for the 14 mrad misalignment case. The sinusoids and fits obtained in these two cases are represented on Figure 5.6.

For rotations only around the vertical axis of the mirror tile, misalignments down to 0.4 mrad and up to 15 mrad can be reconstructed as well, with reconstruction errors equal to 21% and 19.3% of the applied rotation, respectively. The two cases are illustrated on Figure 5.7.

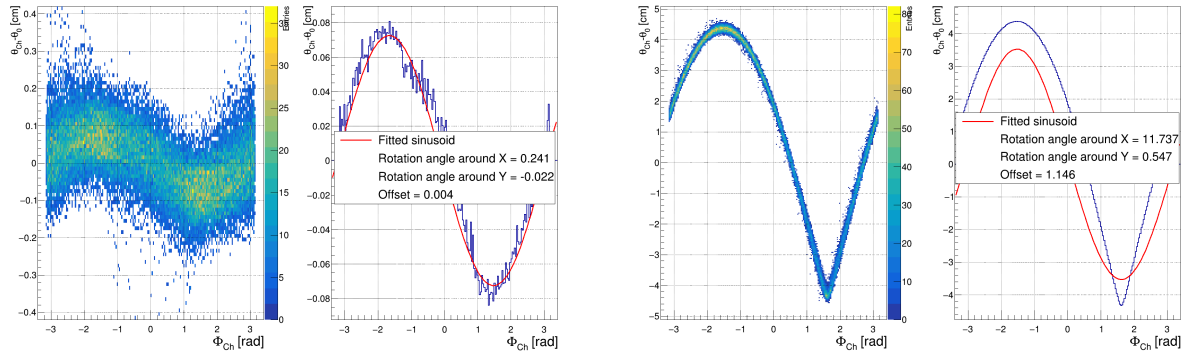


Figure 5.6: Minimal (left) and maximal (right) detected misalignments on the mirror tile 5\_3 for a horizontal rotation. In the minimal case, a rotation of 0.3 mrad around the horizontal axis was applied on the mirror 5\_3, yielding a reconstructed misalignment of 0.24 mrad around the horizontal axis and -0.02 mrad around the vertical axis. In the maximal case, a rotation of 14 mrad around the horizontal axis was applied. The reconstructed values amount to 11.74 mrad for the horizontal axis and 0.55 mrad for the vertical one.

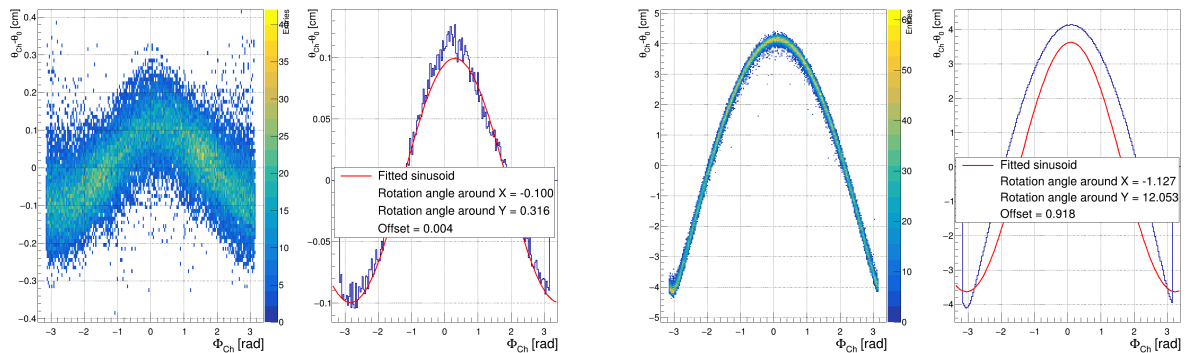


Figure 5.7: Minimal (left) and maximal (right) detected misalignments on the mirror tile 5\_3 for a vertical rotation. In the minimal case, a rotation of 0.4 mrad around the horizontal axis was applied, yielding a reconstructed misalignment of -0.1 mrad around the horizontal axis and 0.32 mrad around the vertical axis. In the maximal case, a rotation of 15 mrad around the horizontal axis was applied. The reconstructed values amount to -1.13 mrad for the horizontal axis and 12.05 mrad for the vertical one.

For lower mirror rotations, a sinusoid is still detected (see Figure B.1). However the reconstructed values contain huge errors ( $\sim 70\%$  of the applied rotation) on both axes of the mirror tile with respect to the actually applied misalignments. Thus the technique is, for these rotation values, not reliable any more. The sinusoids corresponding to a 0.1 mrad rotation around the horizontal and vertical mirror axes are shown in the appendix B.1.

For misalignments of more than 14 mrad for a horizontal rotation and of more than 15 mrad for a vertical one, the technique reaches a maximum value for the detected mirror

misalignment. The calculated mirror rotation for higher rotation values stagnate around this maximum. In fact the point  $C$  (from Figure 5.1) does not lie within the ring radius any more. This distorts the resulting sinusoid, thus higher offsets appear in the fits, which makes the technique not applicable any more.

In the RICH technical design report [94], the maximum mirror misalignment to be tolerated is specified to 1 mrad on average, which lies within the working range of the quantification technique.

### 5.4.2 Performances in the inner and outer regions of the mirror wall

Due to the observed dependence of the technique on the CBM-RICH detector geometry, causing a reduced precision in the quantification of mirror misalignments, a subsequent study was conducted to compare the performances of the technique between the inner and the outer regions of the mirror wall. The main concern was that tracks reflected by mirrors situated in the outer region of the mirror wall could be more influenced by the detector geometry. This may be attributed to the low momentum of the majority of tracks reaching the outer mirrors, combined with the large reflection angles.

For this study, a previous geometry of the RICH detector was used, named *rich\_v16a\_1e*. In this geometry, the photon sensors were grouped in rectangular planes. Two MAPMT planes were installed per mirror half, that is four planes in total. They are partially represented in dark blue on the upper and lower edges of Figure 5.8a. The set-up used differs from the previous one: Magnet (version v15a, with the magnetic field map v12b), STS (version v15c), RICH (version v16a\_1e) and beam pipe (version v14l). In addition, the number of events was increased to 5,000 per mirror tile, to collect sufficient statistics.

Additionally the previous nomenclature going along with the detector geometry was used for mirror labelling. The mirrors used for this study are labelled 1\_4 for the inner part and 2\_1 and 0\_8 for the outer part of the mirror wall. Their locations are highlighted on Figure 5.8a. With the new nomenclature, these mirrors would have the labels 5\_4, 6\_1 and 4\_8, respectively.

Misalignments ranging from 0.1 mrad up to 5 mrad with a step of 0.1 mrad in the interval [0.1 mrad; 2 mrad] and a step of 1 mrad in the interval [3 mrad; 5 mrad] were applied on mirror tiles located in the inner (mirror 1\_4) and outer (mirrors 2\_1 and 0\_8) regions of the mirror wall. Rotations on separate axis and on both axes simultaneously were implemented. The class used to quantify mirror misalignments was called *CbmRichAlignment*. The mirror nomenclature from the *rich\_v16a\_1e* geometry was implemented accordingly in the class.

Figure 5.8 shows the applied and reconstructed misalignments for different types of mirror rotations applied on an inner and an outer mirror tile. Figure 5.9 displays the

deviations between the applied and reconstructed misalignments.

For the inner mirror tile 1\_4 and for mirror rotations applied on the X axis only, the reconstructed misalignments on the rotated axis is excellent, while the reconstructed misalignment on the non-rotated axis is negligible. The error on the misalignment reconstruction on the X axis is 3.3% on average of the applied rotation and the average reconstructed misalignment on the Y axis amounts to 0.1 mrad. The errors obtained for rotations and misalignment reconstruction on the X axis are illustrated in yellow on Figure 5.9a.

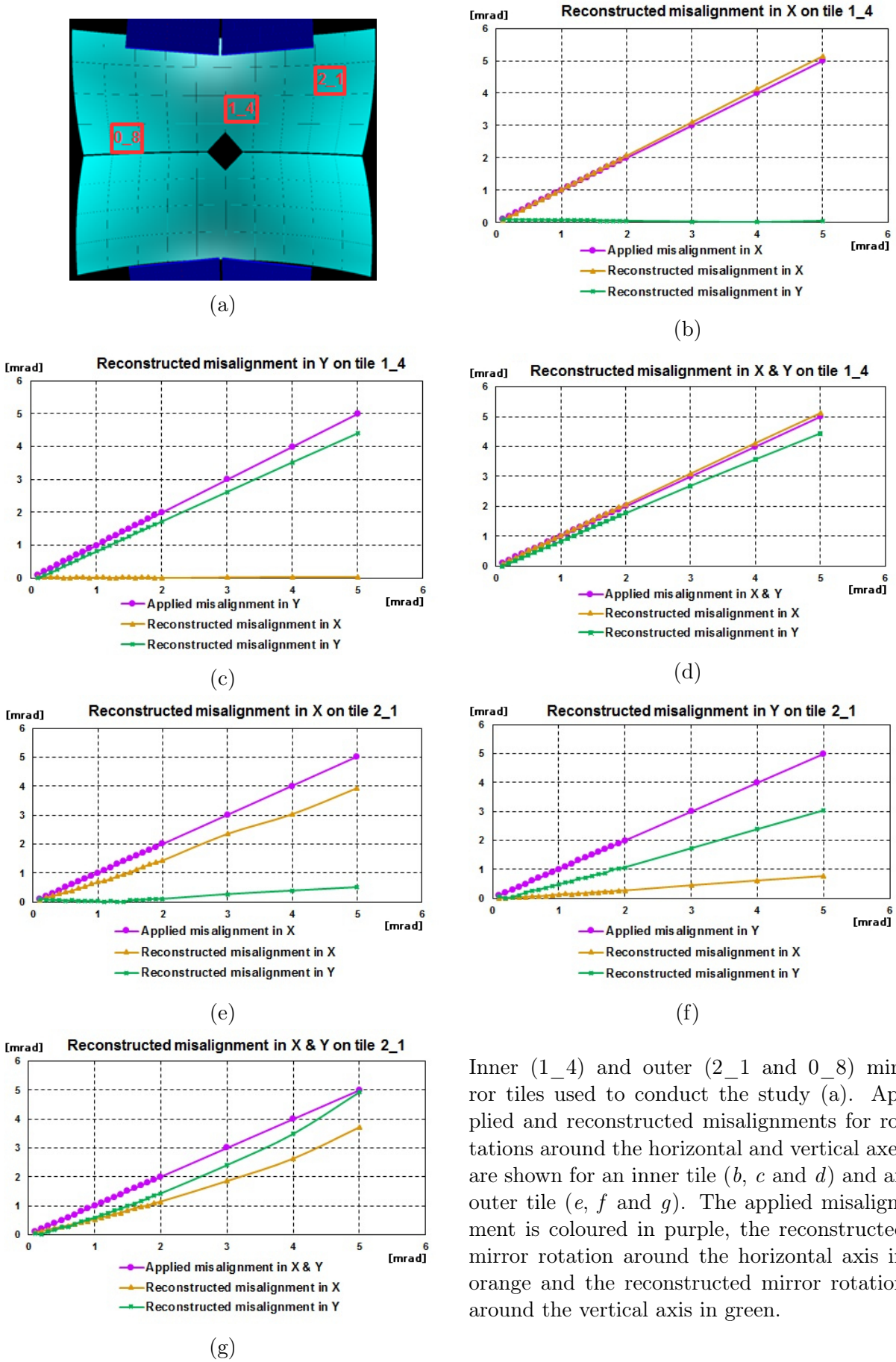
For mirror rotations applied on the Y axis of the same mirror tile, a small discrepancy is observed on the rotated axis, where an error of 18.9% on average of the applied rotation is observed for mirror rotations ranging from 0.3 mrad up to 5 mrad. The errors on the misalignment reconstruction for vertical rotations are represented in purple on Figure 5.9a. The higher the applied rotation, the smaller the reconstruction errors. In this case, the reconstructed misalignment on the non-rotated axis is negligible and close to 0 mrad.

Applying the same mirror rotation on both axes of tile 1\_4 yields errors in the reconstructed misalignments on the X axis of about 3% of the applied rotation for misalignments ranging between 0.3 and 5 mrad. On the Y axis, the errors obtained in the calculation of mirror misalignments amount to 16.9% within the same rotation range. These errors are illustrated in Figure 5.9b.

As shown in the previous subsection, the method works for the inner mirror tile 1\_4 with acceptable errors for misalignments starting at 0.3 mrad on the horizontal axis and 0.4 mrad on the vertical one. Furthermore, the errors in the misalignment reconstruction decrease with increasing mirror rotations. The deviations for small mirror rotations are large, however the corrections are anyway tiny in this range, thus no large influence is expected.

The study of the software-based method performances for an outer mirror tile has been conducted with the tile 2\_1. In this case, larger errors in the calculation of mirror rotations on the rotated and non-rotated axes than in the inner mirror tile case are observed.

For mirror rotations applied only on the X axis, errors on the reconstructed misalignments on the X axis amount to 28.6% of the applied rotation on average, over the complete mirror rotation range. In addition, rotations on the non-rotated Y axis are detected and keep increasing with increasing rotations around the X axis. On average a misalignment of 0.1 mrad is calculated on the Y axis and errors amounting to 7.9% are calculated. The errors obtained for rotations and misalignment reconstruction on the horizontal axis are shown in yellow on Figure 5.9c.

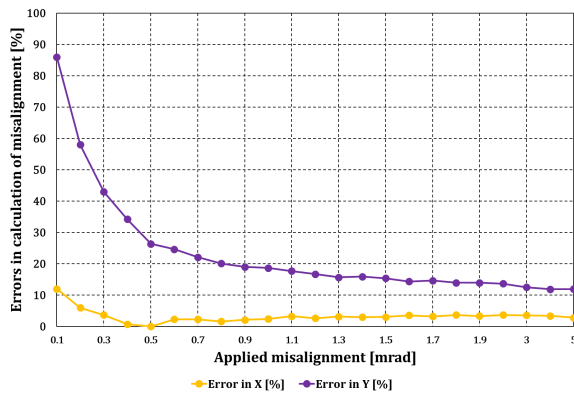


Inner (1\_4) and outer (2\_1 and 0\_8) mirror tiles used to conduct the study (a). Applied and reconstructed misalignments for rotations around the horizontal and vertical axes are shown for an inner tile (b, c and d) and an outer tile (e, f and g). The applied misalignment is coloured in purple, the reconstructed mirror rotation around the horizontal axis in orange and the reconstructed mirror rotation around the vertical axis in green.

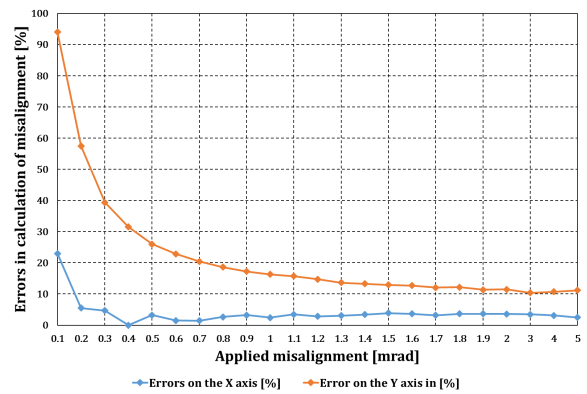
Figure 5.8

For mirror rotations on the Y axis of the tile 2\_1, errors in the misalignment reconstruction on the rotated as well as the non-rotated axes are larger than in the case of a horizontal rotation. The errors on the misalignment reconstruction on the Y axis are 47.1% of the applied rotation on average, for mirror rotations ranging between 0.5 and 5 mrad. An average misalignment of 0.2 mrad on the non-rotated X axis is calculated for the same rotation range. The errors for rotations on the Y axis are displayed in purple on Figure 5.9c.

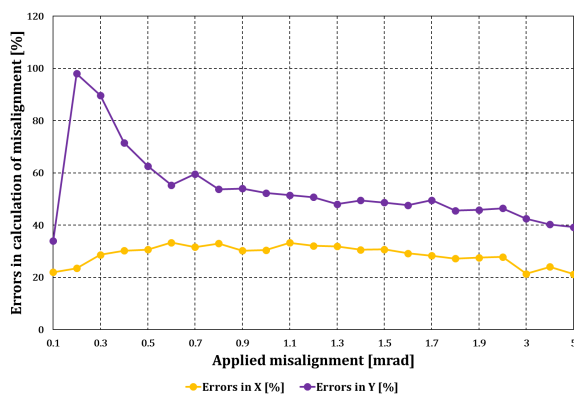
For a simultaneous rotation applied on both axes of the same outer mirror, errors on the reconstructed misalignment on the X and Y axes amount to 43.5% and 36.4% of the applied rotation on average, respectively. In this case, the chosen mirror rotation range goes from 0.3 mrad up to 5 mrad. The errors in the misalignment reconstruction on both axes are represented on Figure 5.9d. For the 5 mrad rotation case, reconstruction errors might cancel each other out, which translates in the observed behaviour (see last point of the green curve on Figure 5.8g).



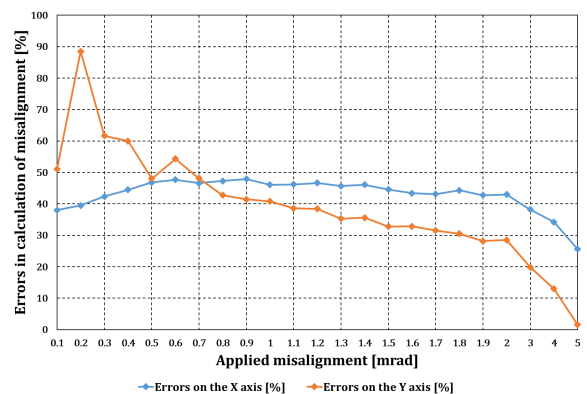
(a)



(b)



(c)



(d)

Figure 5.9: Difference between the applied and reconstructed mirror rotations obtained by the software technique for rotations applied on the inner mirror tile 1\_4 (a and b) and on the outer mirror tile 2\_1 (c and d). Errors for single axes rotations (left column) and for mirror rotations on both axes (right column) are displayed. For single axis rotations, the errors on the X axis are represented in yellow and the errors on the Y axis in purple. For simultaneous rotations the errors on the X axis are in blue and the errors on the Y axis in orange.

A similar study conducted on another outer mirror tile labelled 0\_8 is detailed in the appendix B.2. Results are shown on Figure B.2. Errors on the rotated axis were smaller than for the mirror tile 2\_1, meanwhile larger errors on the non rotated axis were reconstructed. For simultaneous mirror rotations, errors on separate axes reach a plateau and amount to 32.2% and 33.9% of the applied rotation for the X and Y axes, respectively.

In summary, this study demonstrates that the software-based technique yields better results for an inner mirror tile than for an outer mirror. This is observed for misalignment reconstruction on the rotated axis as well as on the non-rotated one.

Furthermore, the errors in the calculations of misalignments decrease with increasing mirror rotation for both mirror tile types. Also for both mirror types, the calculation of the mirror rotation is better for horizontal than for vertical rotations.

Yet the method still works for misalignments within the working range of the CBM-RICH detector, starting at 0.3 mrad for a horizontal rotation and 0.4 mrad for a vertical rotation.

The detector geometry plays an important role in the quantification of misalignments for the proposed software-based technique. The RICH geometry has been subject to optimisations, resulting in a cylindrical shape for the photon detector. A study showing the variations of the ring-track distance on the photon detector plane in different regions has been conducted on a more global scale (for a complete mirror half) with this geometry and is shown in Section 6.2.1.

In this chapter, it has been demonstrated that the quantification technique inspired from the HERA-B experiment yields overall satisfying results for the CBM RICH detector and a reasonable precision for mirror misalignments ranging between 0.3 mrad and 5 mrad. The misalignment information is written in an output text file, where the tile name and corresponding mirror rotations on both axes are listed. This text file will be later used as input in an alignment correction cycle, which was subsequently developed and is the subject of the following chapter.

# Chapter 6

## Correction cycle developed for the RICH software

### 6.1 Correction cycle with the former RICH geometry

The correction cycle employs the two presented methods from Chapters 4 and 5 to detect and calculate mirror misalignments. If misalignment is detected and quantified, the information is used to correct the track extrapolation onto the photon detector plane, which reduces the distance between the reconstructed ring centre and the track extrapolation hit, denoted  $a$  in Figure 5.1. This correction will thus reduce the impact of misalignments on the RICH detector performance.

#### 6.1.1 Principle of the correction cycle

As explained in Section 5.1 and illustrated on Figure 5.3, in case of mirror rotations, the reflected ring is shifted on the photon detector plane. However, the extrapolated track hit does not change, as it is calculated from the ideal mirror position. Therefore the distance  $a$  between ring center and track extrapolation increases.

In principle two approaches could be applied to correct for the misalignment. The first one would work on either the position of the ring centre alone, or the positions of the photon hits and thus of the ring center. This approach would aim at correcting these positions by shifting them of the photon sensor plane. The second approach would displace the track extrapolation as if it were reflected by a rotated mirror tile similar to the one which shifted the ring on the MAPMT plane.

It turns out it is easier to proceed with the second strategy, as only single tracks need to be corrected and a single track can be clearly allocated to a certain mirror. For photons from one track however, they may be reflected by more than one mirror tile. Furthermore it might not always be clear which photon corresponds to which ring under the CBM

conditions.

The second strategy, which was chosen for the correction cycle, is sketched in Figure 6.1. The ideal track extrapolation (point C in blue) is recomputed, as if the mirror was rotated, which shifts it closer to the ring center. This is illustrated on the right-hand side of Figure 6.1, where the point C (in green) lies closer to the ring center (in red).

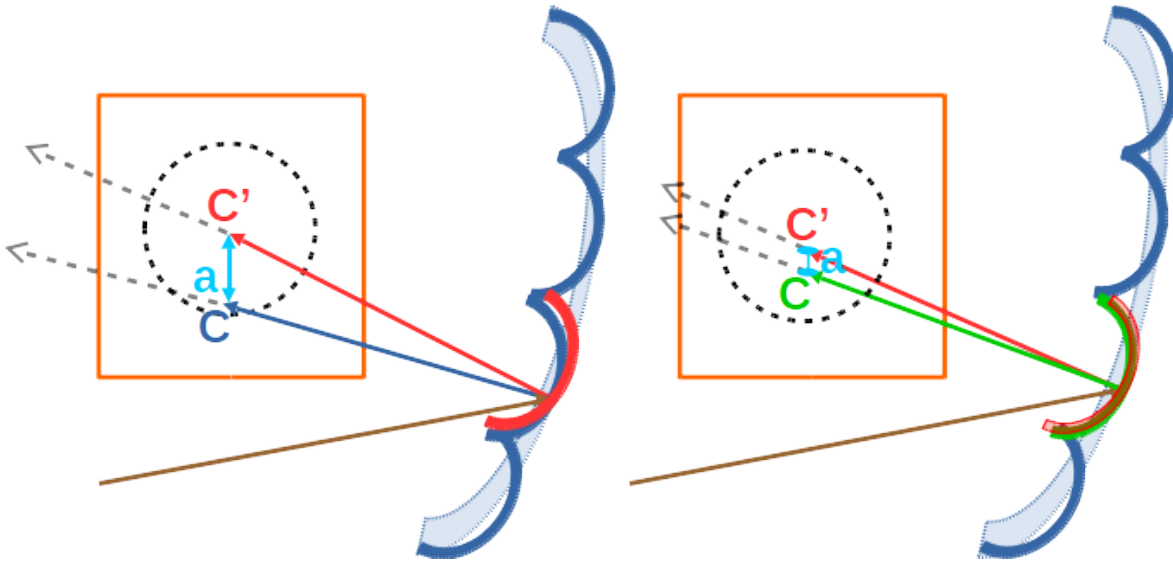


Figure 6.1: Sketched correction method, which is based on the correction of the track extrapolation. The blue elements represent the ideally aligned mirrors used for the track extrapolation (point C in blue on the left). In case of a misaligned mirror (in red on the left), the reflected ring (in dashed black) is shifted on the MAPMT plane (in orange). After correction, the mirror orientation is adjusted closer to the misaligned mirror (in green on the right). This shifts the track extrapolation (point C in green on the right) closer to the ring center (point C' in red) and thus reduces the distance  $a$  between them (in light blue).

The correction cycle as implemented in the software for simulation and reconstruction runs is illustrated in the case of the software-based technique in Figure 6.2. It depicts the underlying implemented classes and their interlacing and gives a detailed description of the different implemented methods.

For the hardware-based method, the first reconstruction run is replaced by the CLAM measurement, as explained in Section 4.4 and a text file containing the mirror rotations has to be manually created.

For the software-based method, the correction cycle occurs with two instances of the event reconstruction. The misalignment information is determined in a first reconstruction run (third brown box in Figure 6.2), employing the technique described in Chapter 5. It is stored as an array in a text file, where the tile name, along with the measured rotations around the horizontal and vertical axes of each mirror tile are written. In the case of the software-based method, a threshold on the number of measurements per tile can be set to ensure enough statistics are obtained for each tile and optimise the quantification technique.

The misalignment information can be subsequently used during a second reconstruction run to correct the track projections. From the text file created for both the hardware-based and the software-based methods, the misalignment information is extracted and stored in a correction map.

The corrections are applied when a track is reflected on a mirror tile. To calculate mirror reflections, the crossing points between a given track reflected by a given mirror are calculated. The normal of the mirror at this point is then computed. If a correction information is available in the correction map, it is at this step used to modify the mirror normal. Thus the track projection is calculated with the misaligned mirror tile and it gets shifted on the photon detector closer to its corresponding ring, which decreases the ring-track distance  $a$ .

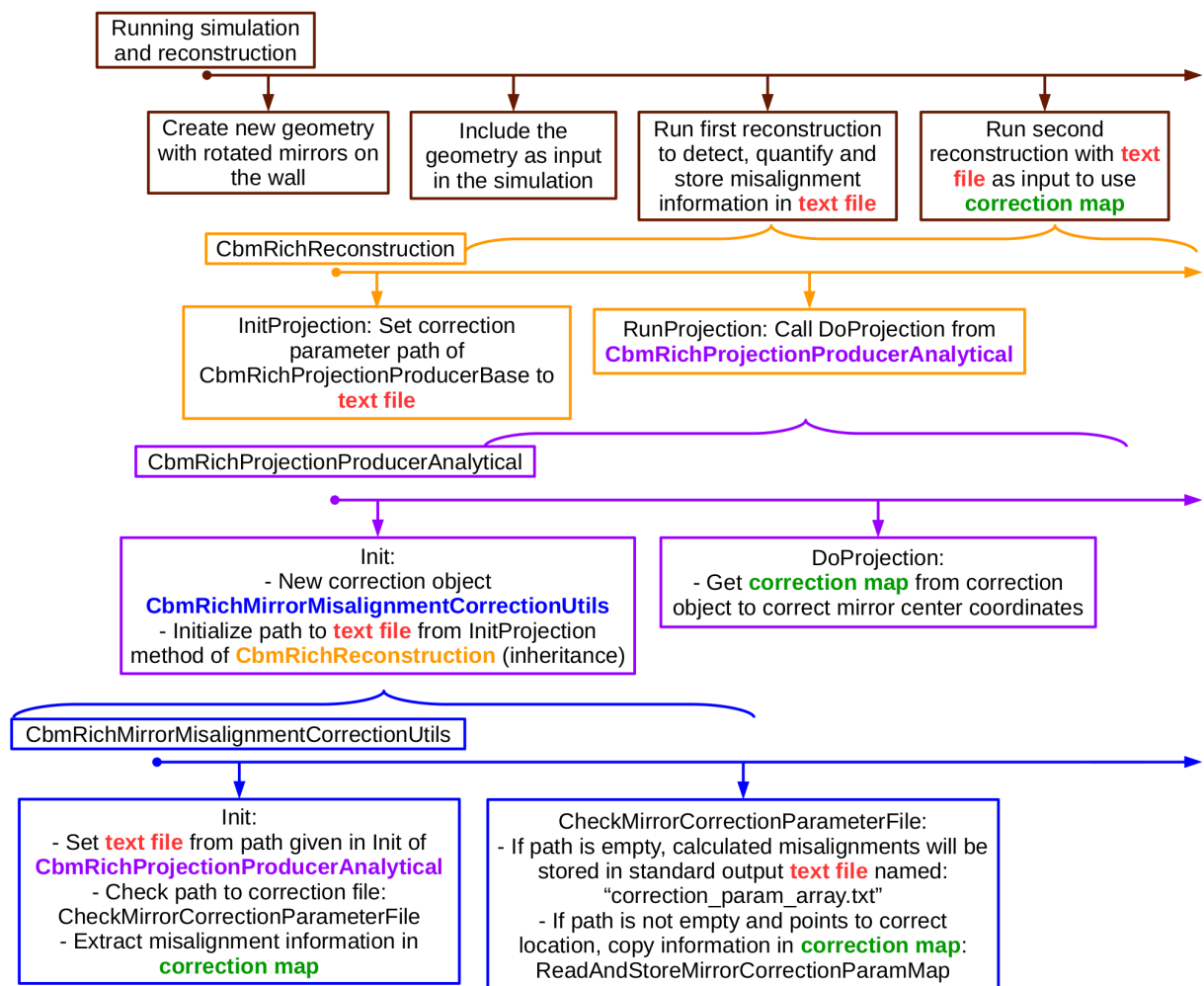


Figure 6.2: The correction cycle as implemented for the software-based technique occurs during a first and a second reconstruction run. The text file path is provided in the first event reconstruction and read in the second event reconstruction. The sequence in which the functions are called inside the classes is from left to right. In the hardware-based method, the first reconstruction run is replaced by the CLAM measurement and a text file has to be manually written.

### 6.1.2 Correction cycle for a single mirror tile

To quantify the performances of the correction cycle, single mirror tiles were first investigated. For this study, the geometry version used is the *rich\_v16a\_1e* with four MAPMT wings. This geometry is described in detail in Section 5.4.2 and so the previous mirror tile nomenclature is used. The resulting distance between fitted ring center and track extrapolation,  $a$ , is projected along the horizontal and vertical axes and is in the following referred to as ‘Difference in X’ and ‘Difference in Y’, respectively. These projections correspond to the variables  $\Delta\Phi$  and  $\Delta\lambda$  introduced in Figure 5.1.

In the following, first horizontal and vertical projections without corrections are plotted. Then the evolution of these projections when corrections are implemented is displayed for a mirror tile located in the central region of the mirror wall and a mirror tile located in the outer region. For the corrections, the software-based quantification technique presented in Section 5.3 was employed in a first reconstruction run to derive mirror rotations. The rotation values were stored in an output text file and used as input in a second reconstruction run to calculate the new intersection point of the incoming track with the photon detector plane, as illustrated in Figure 6.1 and explained in Figure 6.2.

Figure 6.3 represents horizontal and vertical projections of the ring-track distance  $a$  for rotations around a single axis, ranging from 0 to 4 mrad with a step of 1 mrad. The mirror tile used for this study is located in the centre of the mirror wall and labelled 1\_3. The expected behaviour is observed for both induced rotations. Namely the rotation of the mirror tile around its vertical axis (upper histograms in Figure 6.3), entails a shift in the horizontal direction (X direction), while no shift is observed in the vertical direction (Y direction). Similarly a mirror tile rotation around its horizontal axis (lower histograms in Figure 6.3) results in a shift in the vertical direction and no changes are observed in the horizontal one.

Using Equation 5.2, a one mrad rotation corresponds to a shift of 0.3 cm on the photon detector plane. This is observed on the top left and lower right histograms of Figure 6.3, where the distribution peaks are spaced by about 0.3 cm. In addition, a rotation around the horizontal axis hardly induces a shift in the horizontal direction, which is expected. However a vertical rotation does imply a shift in the vertical direction, as seen on the top right histogram of Figure 6.3, in particular for the three and four mrad rotation cases. For these cases, a shift of approximately 0.1 cm was detected, which is in agreement with the results from the study conducted in Section 5.4.2 and shown on Figure 5.8d.

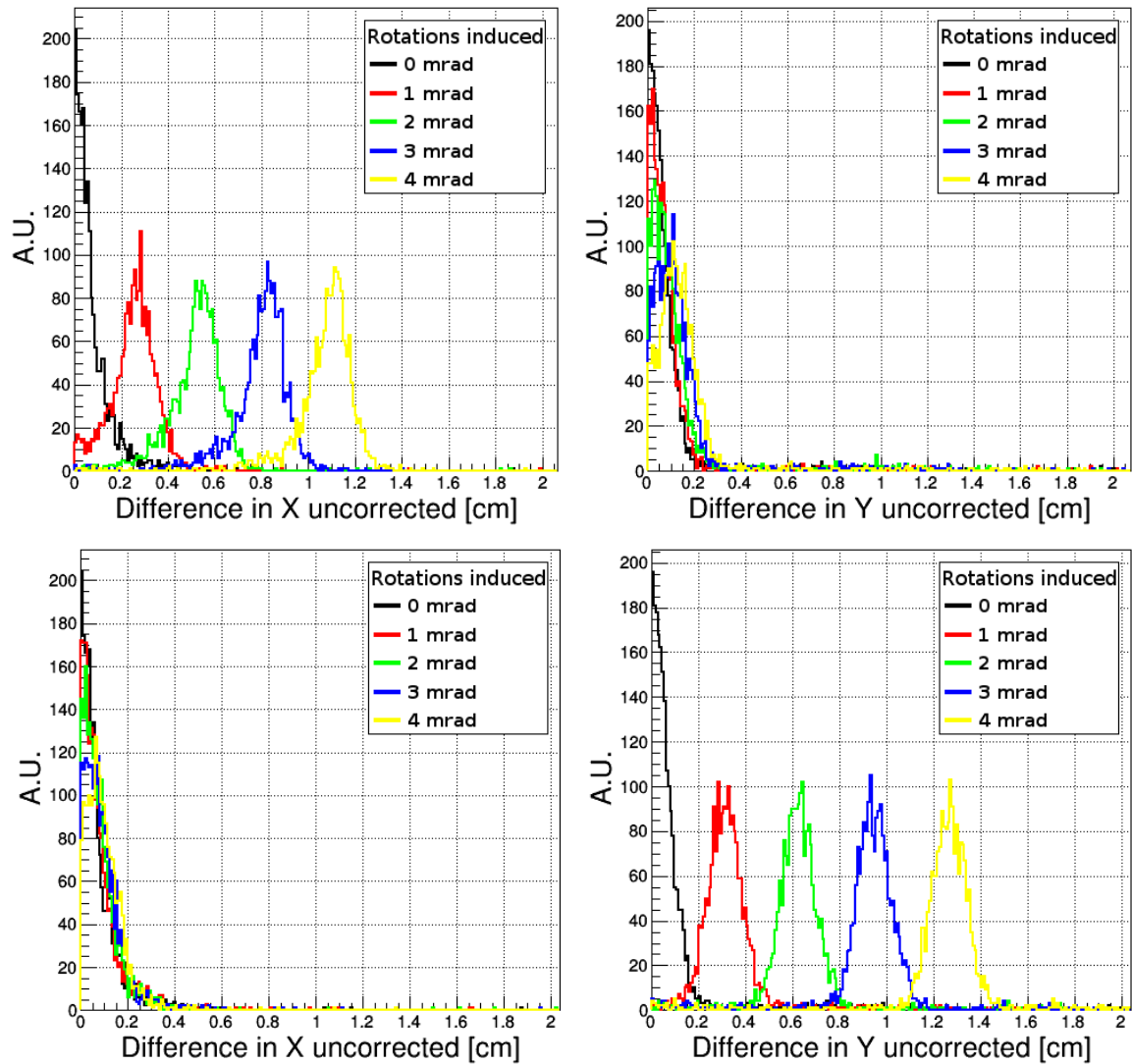


Figure 6.3: Horizontal and vertical projections of the ring-track distance  $a$  for rotations ranging between 0 and 4 mrad with a step of 1 mrad. The mirror tile used for this study lies in the central region of the mirror wall and is labelled 1\_3. The upper histograms depict the horizontal and vertical projections of the ring-track distance for a tile rotation around its vertical axis. The lower histograms display the same projections for a tile rotation around its horizontal axis.

Figure 6.4 shows projections of ring-track distances obtained before (coloured in red in Figure 6.4) and after (in green) the presented correction cycle has been applied. In addition, the ideal correction case is plotted (in blue). The ideal correction was calculated with the mirror tile center directly extracted from the geometry (with the TGeoManager class) and stored in the text file. Two mirror rotations are presented: a 4 mrad rotation around the horizontal axis of the mirror tile (upper histograms in Figure 6.4) and a 1 mrad rotation around the vertical axis of the tile (lower histograms). The same mirror tile was investigated, which lies in the centre of the mirror wall and is labelled 1\_3.

In both examples, the corrected values are in good agreement with the ideal ones, revealing a proper operation of the correction cycle. In the upper example, where a

rotation of 4 mrad around the vertical axis of the mirror tile was induced, the software-based quantification technique yields mirror rotations of 0.05 mrad around the horizontal axis and 3.76 mrad around the vertical one. Even though a discrepancy of 6% of the applied rotation is measured, the ring-track distances along the vertical and the horizontal axes in the corrected case lie close to the ideal distances. The bottom example shows the results obtained for a 1 mrad rotation around the X axis, where rotations angles of 0.06 mrad and 1.02 mrad around the X and Y axes were reconstructed, respectively. In this case a clear improvement brought by the correction cycle is observed as well.

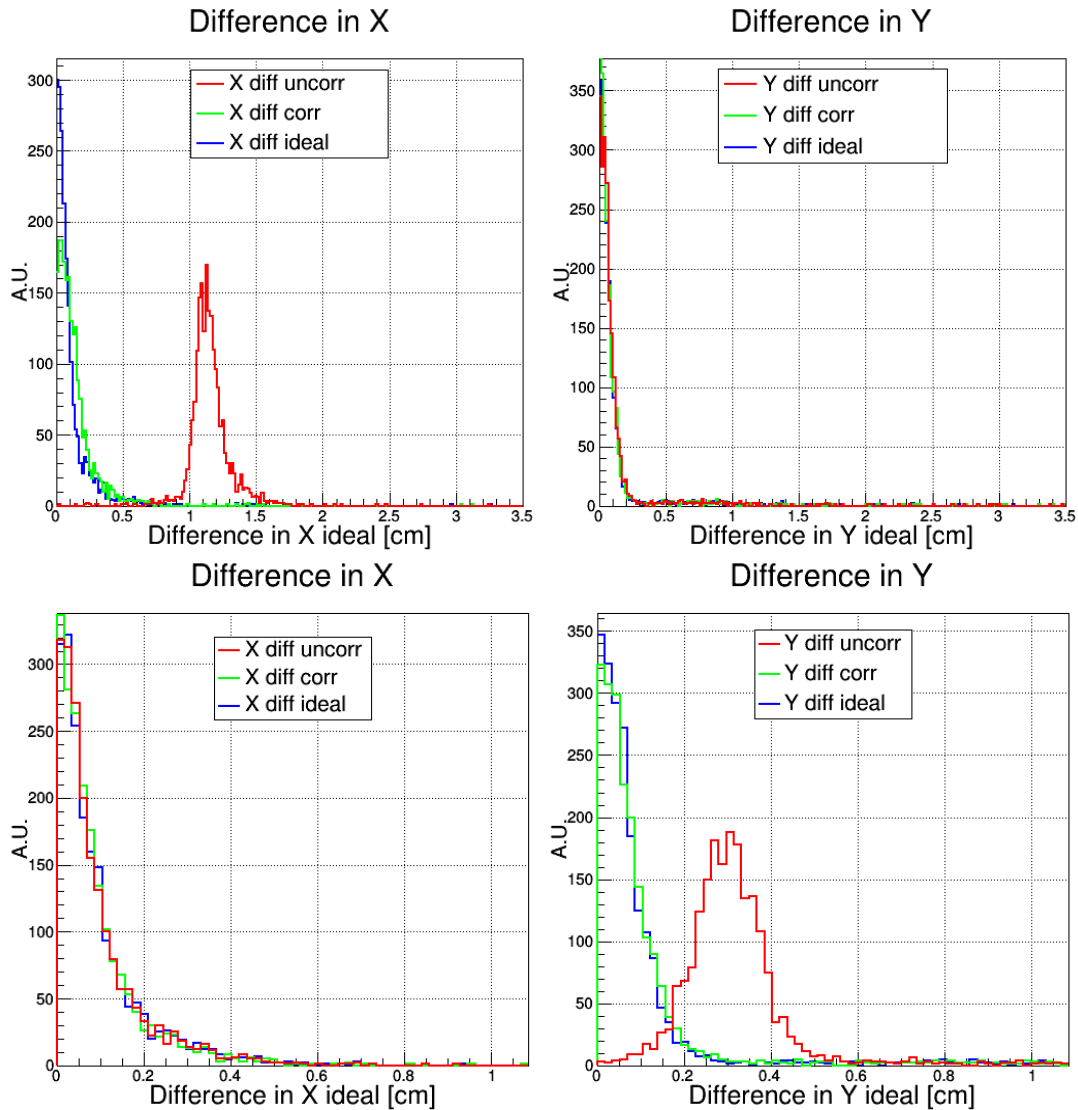


Figure 6.4: Uncorrected (red), corrected (green) and ideally corrected (blue) projections of the ring-track distance in the horizontal (left) and vertical (right) directions. The applied misalignments are 4 mrad around the horizontal axis (up) and 1 mrad around the vertical axis (bottom). The mirror tile used for this study lies in the central region of the mirror wall and is labelled 1\_3.

The results obtained with the correction cycle for a mirror tile located in the outer region of the mirror wall are displayed in Figure 6.5. In this study, the mirror tile labelled 2\_8 was investigated. It is located in the upper left corner of the mirror wall when looking in beam direction. A misalignment of 5 mrad was induced on the X axis only (upper histograms in Figure 6.5), on the Y axis only (middle histograms) and on both axes simultaneously (lower histograms). Similarly to the previous studies, the mirror rotations were derived with the software-based technique to correct the track reflection by the mirror and its intersection with the photon detector plane.

For both cases, where a rotation around a single axis was carried out (upper and middle histograms in Figure 6.5), it can be first noticed that the ring-track distances increased with mirror misalignments (red curves) along both directions, unlike for the more central tile 1\_3. This correlates with the results displayed in Figures 5.8e and 5.8f. Once the corrections are applied, residuals of misalignments can still be observed, such as in the upper right and lower left histograms in Figure 6.5. In other cases no clear improvements are noticed, that is on the top left and middle right histograms.

These problems are caused by the software-based quantification technique, whose performances for mirror tiles located in the outer region of the mirror wall become less reliable, as already demonstrated in Section 5.4.2. The tracks hitting the outer mirror tiles have a low momentum and are thus strongly bent by the magnet field. In addition and due to the detector geometry, these tracks have large reflection angles. These factors make the track extrapolation on the photon detector plane less accurate and make it thus more difficult to disentangle rotations around the horizontal axis from rotations around the vertical one. As a consequence, the performances of the software-based technique are harmed and those of the correction cycle, too.

Moreover, for the software-based technique to yield reliable results, mirror tiles should be hit by tracks as uniformly as possible. The mirrors located in the outer region of the mirror wall can however be only partially illuminated and present a lack of statistics. This also affects the performances of the quantification technique.

Nevertheless, as the track and ring densities are lower in the outer region of the mirror wall, looser cuts on the ring-track distance can be applied. This, combined with the partial correction brought by the correction cycle could enhance the ring-track matching efficiency of the RICH detector. Also, a new version of the RICH geometry named *rich\_v17a\_1e* was designed. It includes a cylindrical shape of the photon detector plane, which reduces the detector geometry effects mentioned above. In the following section, the correction cycle was tested with this new geometry.

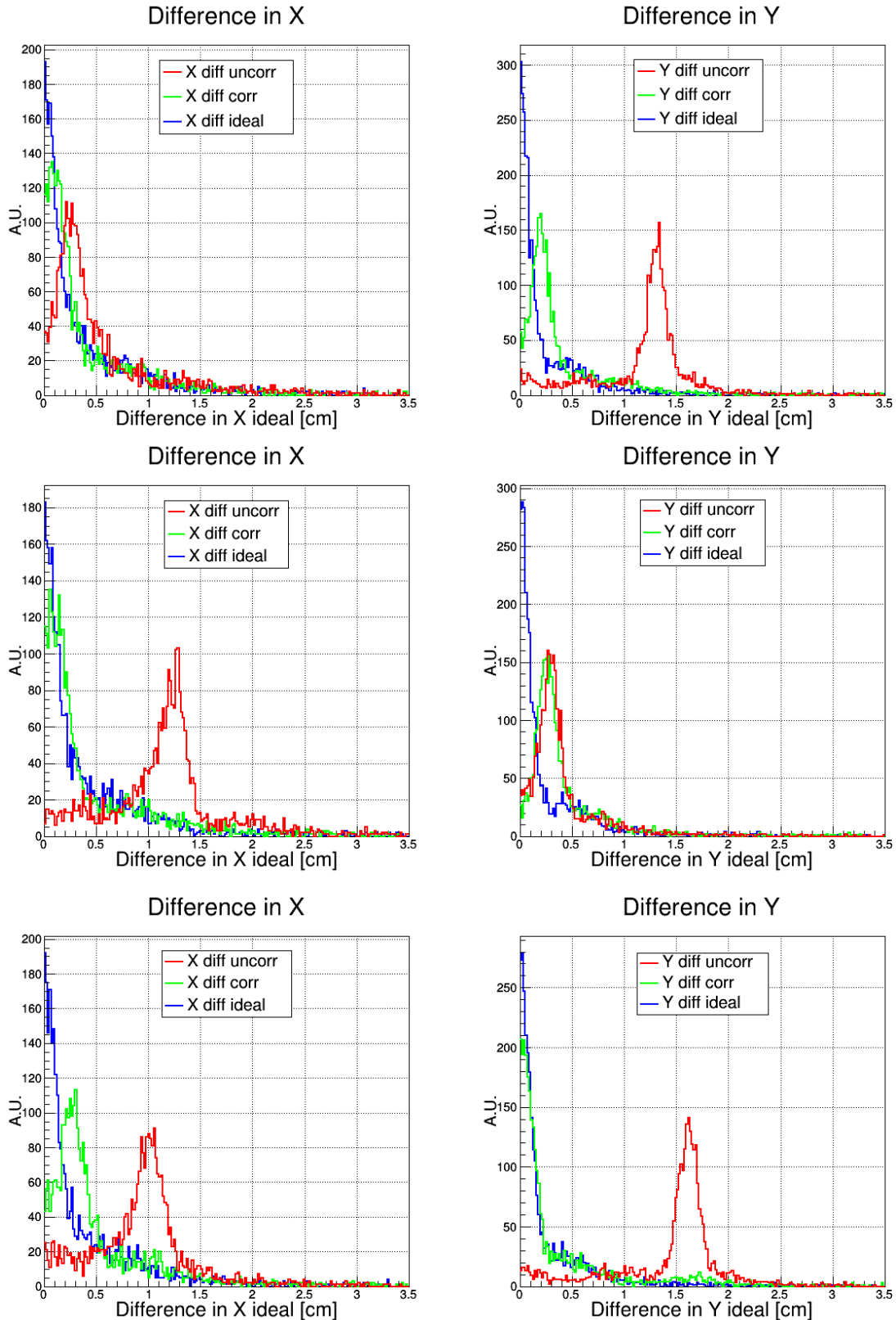


Figure 6.5: Performances of the correction cycle for the outer mirror tile labelled 2\_8. A rotation of 5 mrad was induced around the horizontal axis only (upper histograms), around the vertical axis only (middle histograms) and on both the horizontal and vertical axes simultaneously (lower histograms). For all histograms the same colour code is used, namely: the red, green and blue lines correspond to the uncorrected, corrected and ideally corrected cases, respectively.

## 6.2 Results with the RICH geometry v17a\_1e

### 6.2.1 Identical rotation of each mirror tile in the upper half of the mirror wall

The presented correction cycle, implemented in the RICH software, has been adapted to the most recent RICH geometry named *rich\_v17a\_1e* and automatised for the full mirror wall of the RICH detector. The performances of the correction cycle were further investigated with this new geometry, on which the MAPMTs were distributed over a cylindrical shape. For this study, 100,000 events were simulated, each containing 10 electrons and 10 positrons with a momentum ranging from 0.5 GeV/c up to 9 GeV/c, a polar angle varying between 2.5° up to 25° and an azimuthal angle varying between 0° and 180°. These parameters allowed a full coverage of the upper half of the mirror wall within the acceptance of the CBM experiment. In addition to these parameters, the following set-up was employed: Magnet (version v15a with the magnetic field map v12b), STS (version v16x), RICH (version v17a\_1e) and beam pipe (version v16b\_1e).

Figure 6.6 shows, in the case of an aligned mirror wall, the average distance between the fitted ring centres and the extrapolated track hits (ring-track distance  $a$  from Figure 5.1) together with the projections of the ring-track distance along the horizontal and vertical axes. The upper left histogram illustrates the average ring-track distance over the upper photon detector plane. The horizontal and vertical components of the average ring-track distances are displayed on the upper middle and right histograms, respectively. The lower histograms in Figure 6.6 reveal the horizontal and vertical projections of the ring-track distance distribution. In each figure, the local mean distance is shown in dependence on the position of the photon detector plane.

For an aligned mirror wall, the average ring-track distance amounts to 0.3 cm in the central region of the photon detector plane. The distance  $a$  increases on the borders, along the horizontal and vertical directions, up to roughly 1 cm. From the upper right histogram in Figure 6.6, a dependence along the vertical direction is observed, which can be attributed to the detector geometry and the tilt of both the mirror wall and the photon detector plane. In addition, an increase in the ring-track distance at the edges of the MAPMT plane is observed, which can be attributed to insufficient statistics but also to the ring reconstruction limit at the edges of the photon sensor plane.

All mirrors were afterwards rotated by -3 mrad around their horizontal axis and by +3 mrad around their vertical axis in two different simulation runs. The resulting ring-track distance distributions before the corrections were applied are shown in Figures 6.7 and 6.8. The arrangement of the figures is identical to that of Figure 6.6.

For both rotations an increase in the ring-track distance is observed. For the horizontal rotation of -3 mrad, the ring-track distance rose in average up to more than 1 cm in the central part of the photon detector. For the vertical rotation of +3 mrad, an increase in the ring-track distance of 0.9 cm is observed in the central part of the photon detector.

This is consistent with the expected shift induced by a 3 mrad mirror rotation, which corresponds to a translation of 0.9 cm of the ring center from the extrapolated track hit.

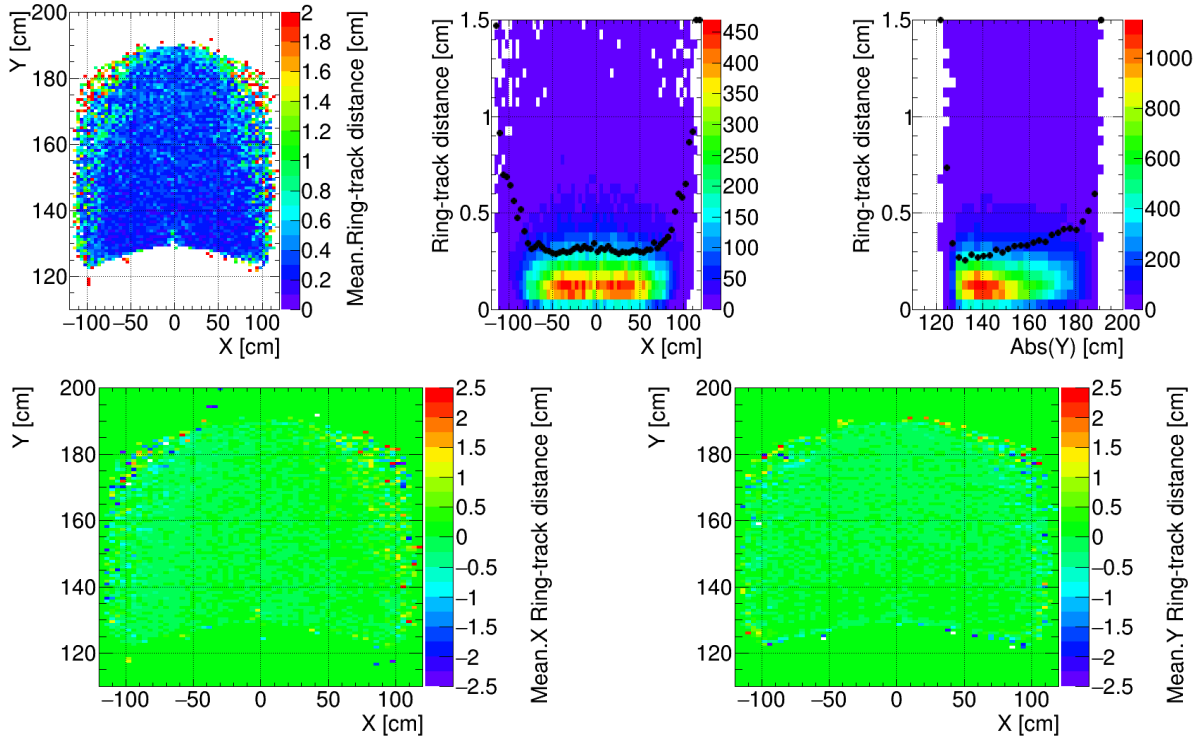


Figure 6.6: Histograms of the mean distances between fitted ring centres and extrapolated track hits for the aligned mirror wall. The upper histograms display from left to right, the distribution of the local average ring-track distance on the upper photon detector plane and the ring-track distance projected horizontally and vertically. For the projection histograms, black dots represent the mean ring-track distance obtained for each vertical slice. However the maximum of the distribution lies around 0.14 cm. The lower histograms represent the horizontal (left) and vertical (right) projections of the average ring-track distances.

As already illustrated in Section 5.2, the histograms showing the horizontal and vertical components of the ring-track distance in Figure 6.8 reveal that a vertical rotation of each mirror tiles translates into an increase in the ring-track distance along the horizontal direction and thus a horizontal shift of the ring centre on the photon detector plane. Thus the histogram corresponding to the vertical component of the ring-track distance for a vertical rotation by +3 mrad appears empty (lower right histogram in Figure 6.8).

Analogously, a horizontal rotation translates into an increase along the vertical direction and thus a vertical shift of the ring centre, as observed on the lower right histogram in Figure 6.7.

Furthermore, the vertical dependence of the ring-track distance, already observed in the aligned case, is in opposite direction in both rotated cases. For the horizontal rotation, the asymmetry is increased, while it is less pronounced with the vertical rotation. This behaviour is observed for rotations in both directions, in particular a +3 mrad rotation around the horizontal axis and a -3 mrad rotation around the vertical axis.

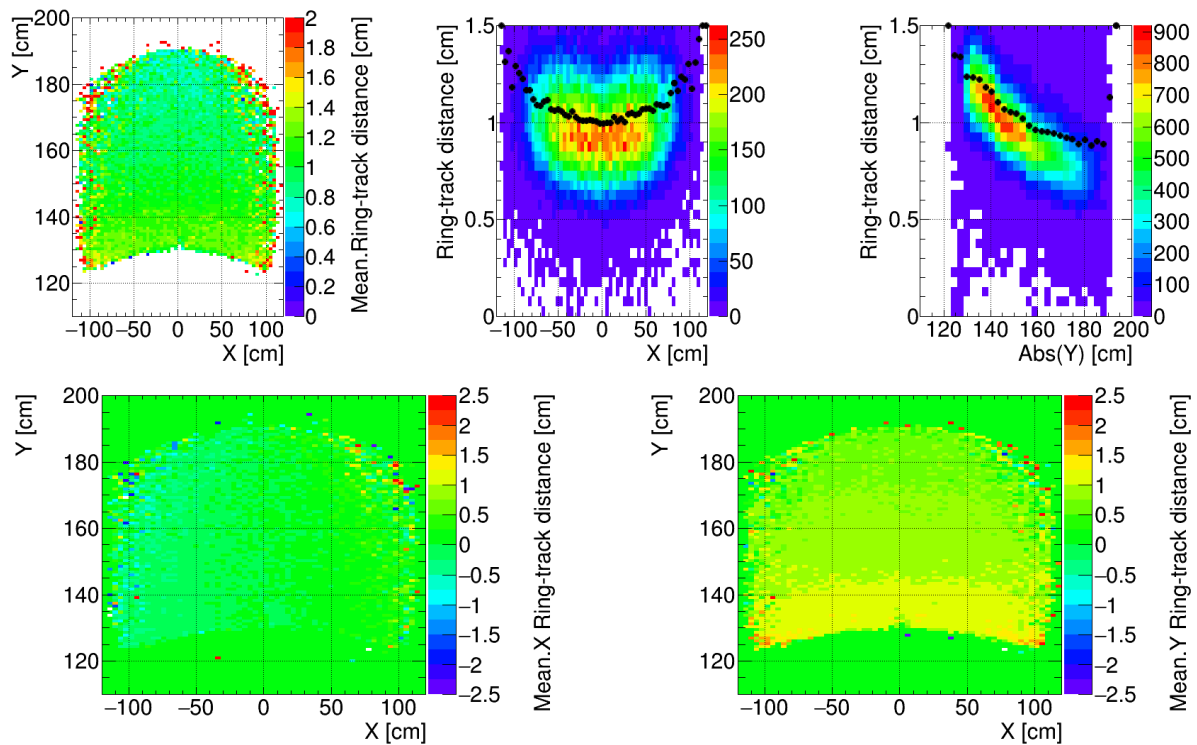


Figure 6.7: Histograms of the mean distances between fitted ring centres and extrapolated track hits for a rotation of all tiles of the upper mirror wall around the horizontal axis by  $-3$  mrad and before the correction cycle was applied.

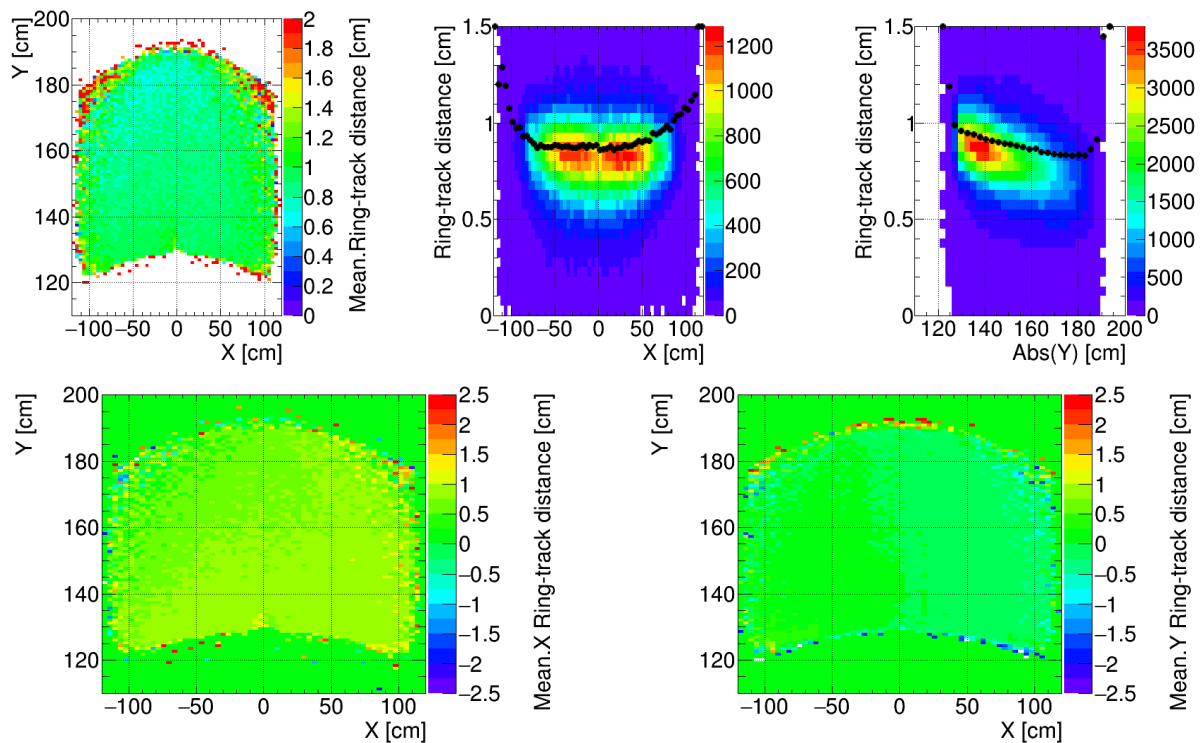


Figure 6.8: Histograms of the mean distances between fitted ring centres and extrapolated track hits for a rotation of all tiles of the upper mirror wall around the vertical axis by  $+3$  mrad and before the correction cycle was applied.

Figures 6.9 and 6.10 display the ring-track distance for the rotation cases presented above, once the correction cycle has been applied. In both cases, the overall ring-track distance was reduced to about 0.35 cm in the central region of the photon detector plane, which is close to the average distance of 0.3 cm obtained in the aligned case. Also the direction of the vertical dependence of the ring-track distance has become identical to the one from the aligned figure. Overall the pictures obtained after corrections for both rotation cases are similar to the ones from the aligned case in Figure 6.6. This thus demonstrates a good operation of the correction cycle for an identical rotation applied on all mirrors.

Yet the average ring-track distance appears to be not fully corrected at the edges of the photon detector plane. These residual distances at the edges are however not necessarily critical to the performances of the RICH software, as less track and ring densities are observed in these regions. Thus, looser cuts on the ring-track distance can be applied during the ring-track matching phase in the RICH software.

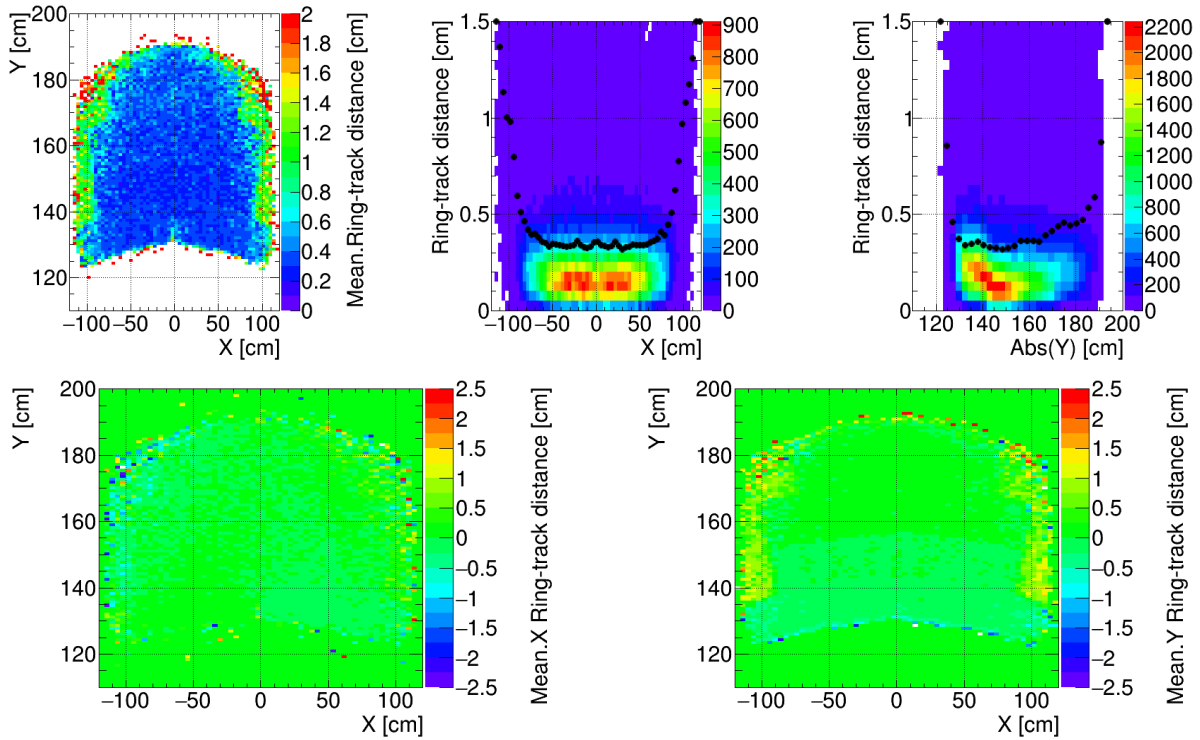


Figure 6.9: Histograms of the mean distances between fitted ring centres and extrapolated track hits for a rotation around the horizontal axis of all tiles of the upper mirror wall by  $-3$  mrad, once the correction cycle has been applied.

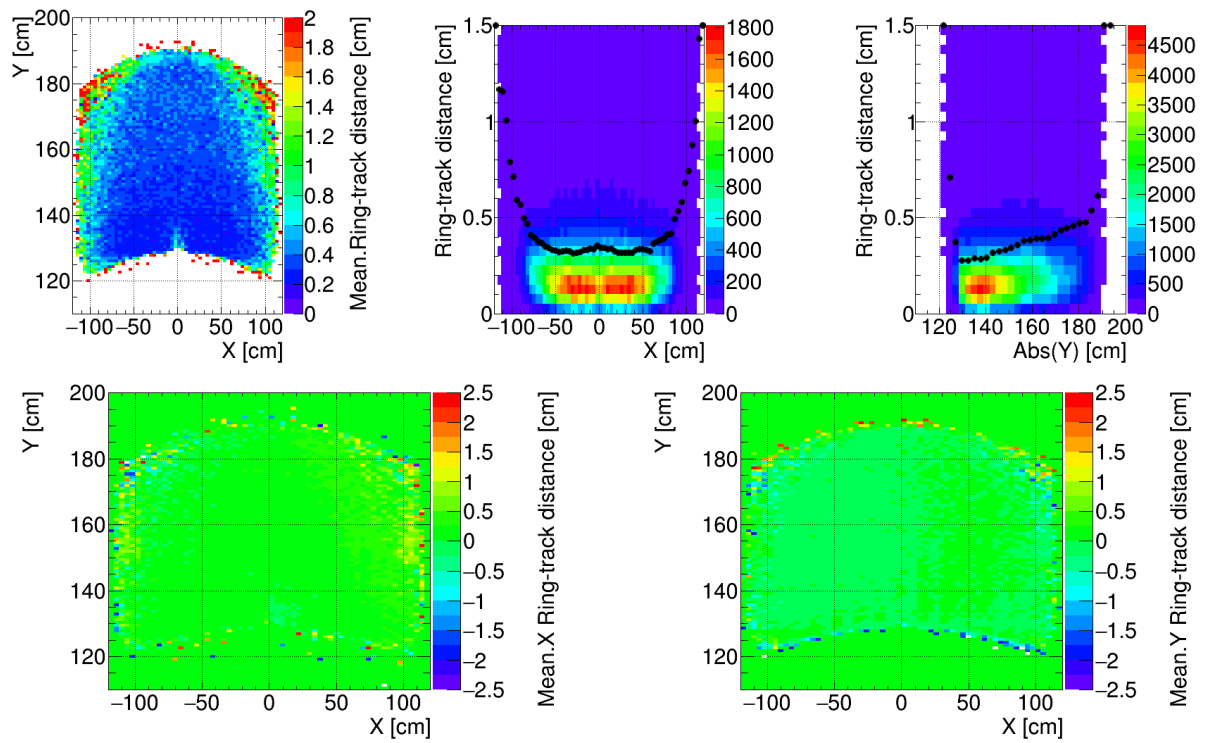


Figure 6.10: Histograms of the mean distances between fitted ring centres and extrapolated track hits for a rotation around the vertical axis of all tiles of the upper mirror wall by +3 mrad, once the correction cycle has been applied.

### 6.2.2 1 mrad Gaussian misalignment

A subsequent study was conducted in which all 80 mirror tiles were rotated randomly around their horizontal and vertical axes. The applied misalignment values followed a Gaussian distribution, whose standard deviation was chosen as 1 mrad. For each tile, two rotation values were randomly extracted from the Gaussian and applied on one rotation axis. Mirror misalignment with this technique will be called in the following a ‘1 mrad Gaussian misalignment’.

For this study, 100,000 events were simulated, each containing 10 electrons and 10 positrons with a momentum ranging from 0.5 GeV/c up to 9 GeV/c. The angular and azimuthal angles were chosen such that the full mirror wall was illuminated within the acceptance of the CBM experiment ( $\theta \in [0^\circ; 180^\circ]$  and  $\Phi \in [0^\circ; 360^\circ]$ ). The following set-up was employed: Magnet (version v15a with the field map v12b), STS (version v16x), RICH (version v17a\_1e) and beam pipe (version v16c\_1e).

Figure 6.11 shows the average ring-track distance, denoted hereafter  $a$ , distribution obtained with the ‘1 mrad Gaussian misalignment’ geometry. The upper row shows the absolute value of  $a$  for the upper (left) and lower (right) MAPMT planes. The middle and bottom rows display the horizontal and vertical projections of  $a$  for the upper (middle row) and lower (bottom row) MAPMT planes.

The rotated mirrors can be distinguished on the photon planes as coloured slabs, whose values indicate the local mean value of  $a$ . In the upper row the average  $a$  ranges from 0.2 cm up to more than 1 cm. The middle and lower rows reveal the projection components of  $a$  in both directions, which shows an applied misalignment different on the two rotation axes of all mirror tiles.

Figure 6.12 depicts the situation after the correction cycle has been implemented. The mosaic-like structure has disappeared in the global picture (top row) as well as in the histograms of the projections of  $a$  (middle and lower rows).

The mean values of  $a$  distributed over the complete MAPMT plane are presented in Figure 6.13 for the aligned, misaligned and corrected cases. A Gaussian fit is applied on the ring-track distance distributions. The mean of the Gaussian fit allows the extraction of the maximum of the distribution. In the aligned ring-track distance distribution, the mean of the Gaussian fit amounts to 0.14 cm. With the ‘1 mrad Gaussian misalignment’ geometry, the mean of the Gaussian fit is 0.47 cm. It decreases to 0.17 cm in the corrected case, which is close to the ideal case. The specifications for the RICH detector required mirror misalignments to be kept below 1 mrad (see Section 3.3.2), which corresponds to an average 0.3 cm shift on the photon detector plane. Thus the correction cycle fulfils the RICH specifications.

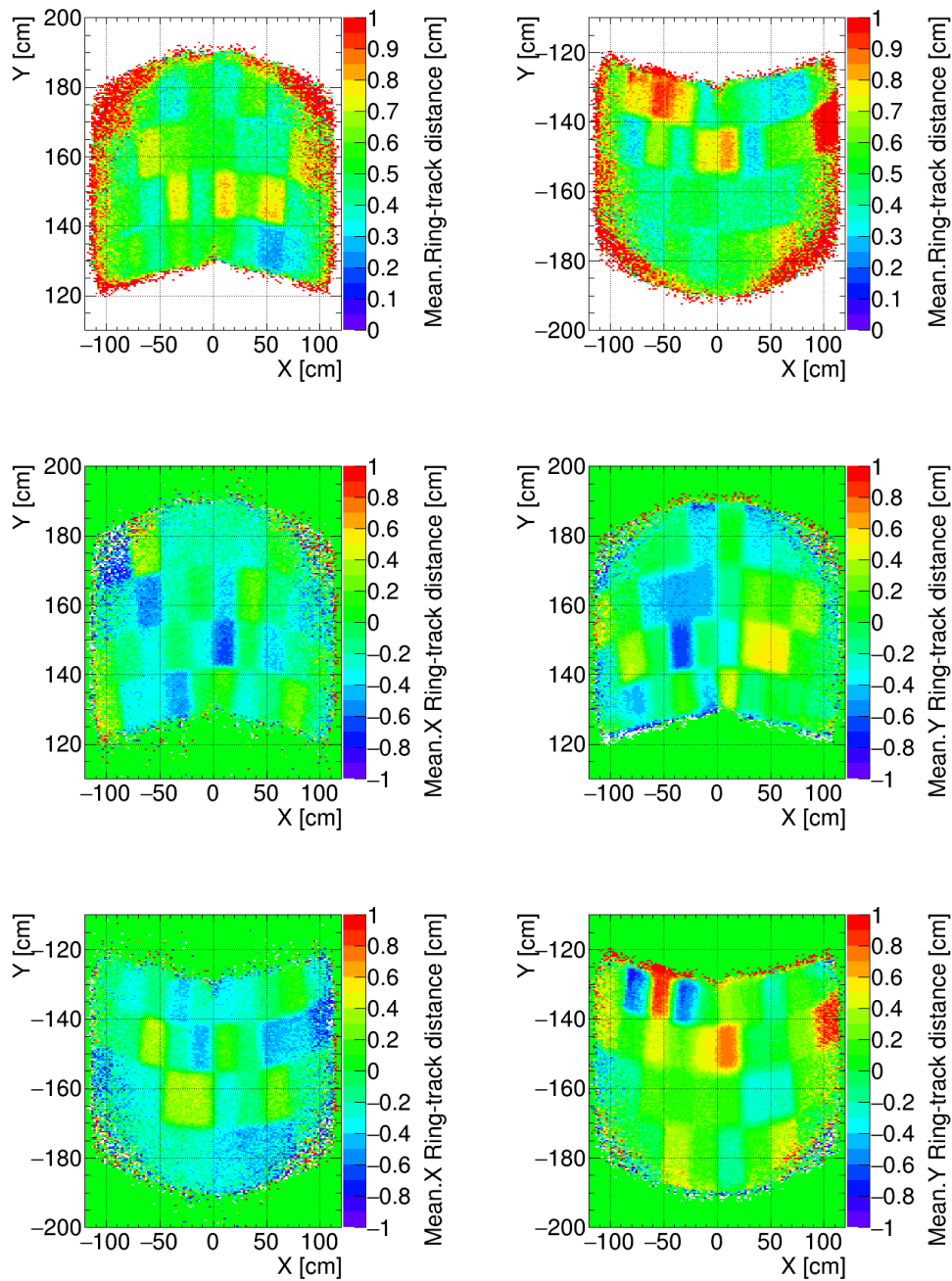


Figure 6.11: Average  $a$  distribution for a randomly rotated mirror wall. The mean of  $a$  is presented in the upper row, where the upper photon detector plane is shown on the left side and the lower photon detector plane on the right side. The horizontal projections of  $a$  are illustrated in the middle and lower left histograms for the upper and lower MAPMT planes, respectively. The vertical projections are displayed in the middle and lower right histograms for the upper and lower MAPMT plane, respectively. The applied mirror rotations are extracted from a Gaussian distribution, whose standard deviation amounts to 1 mrad. The rotation values on both tile axes are different. Individual mirror tiles are well visible on the photon sensor plane.

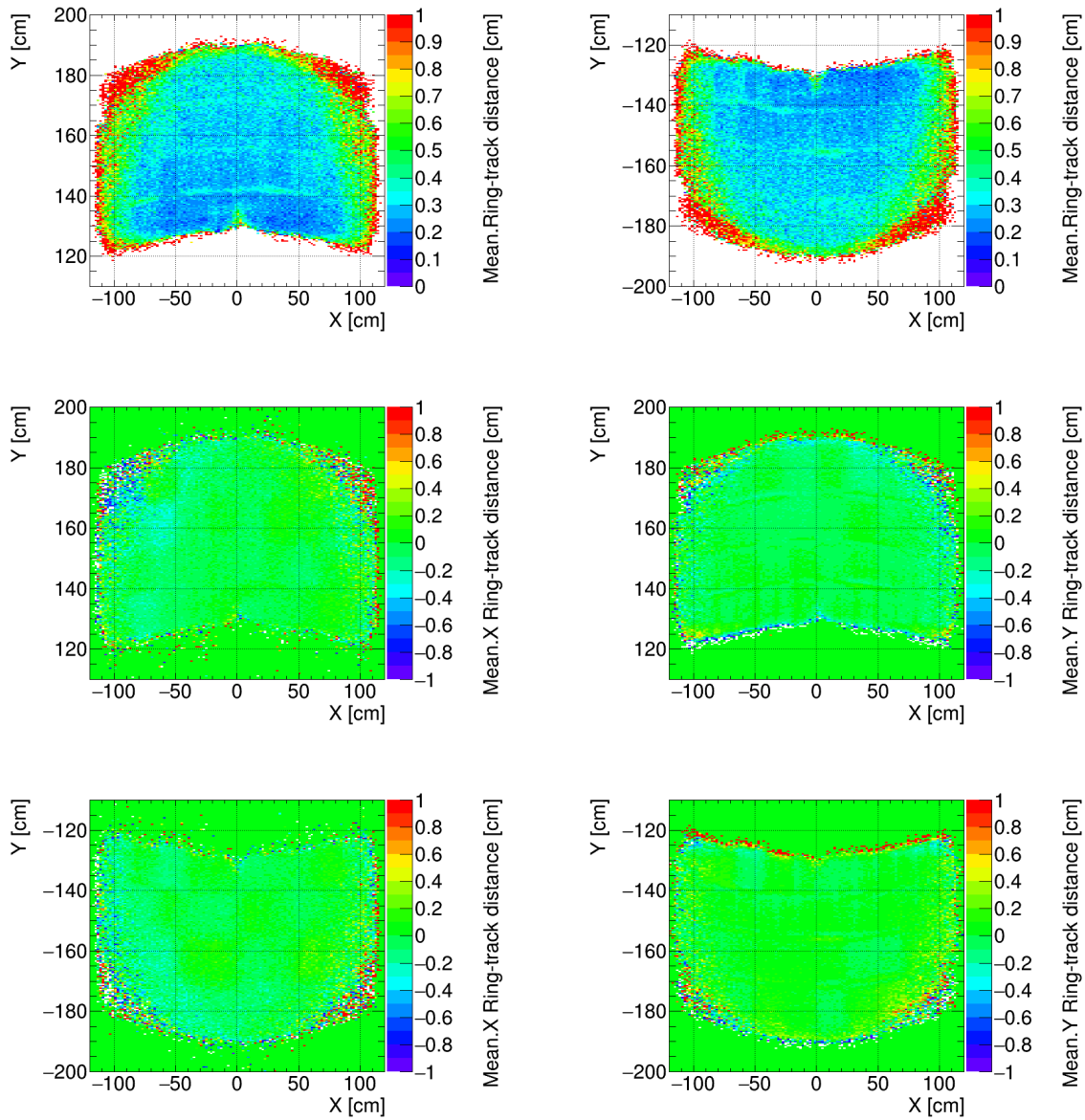


Figure 6.12: Average  $a$  distribution after the correction cycle has been applied, using the ‘1 mrad Gaussian misalignment’ geometry. The  $a$  distribution is more uniform and reduced to 0.2 – 0.3 cm in the central region of the photon sensor planes. Edge effects are still visible.

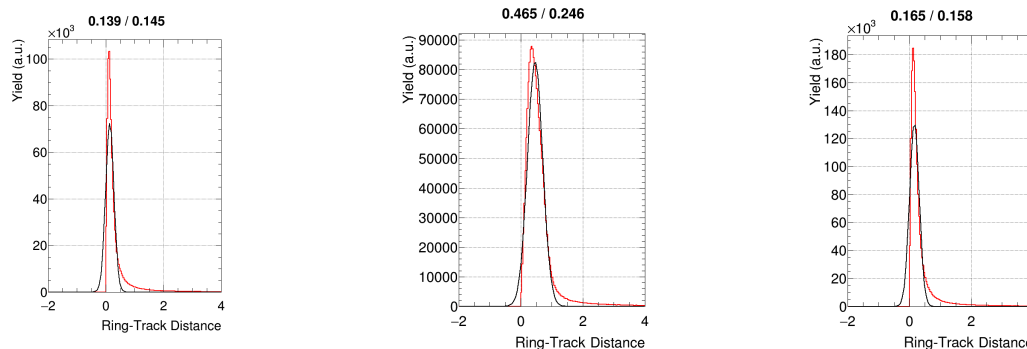


Figure 6.13:  $a$  distribution over the complete MAPMT plane for the aligned (left), rotated with a ‘1 mrad Gaussian misalignment’ geometry (middle) and corrected (right) cases. A Gaussian fit was applied on the data (black curves). The mean (left number) and standard deviation (right number) of the fitted Gaussian are displayed on the top of each histogram. The mean of the Gaussian fits roughly corresponds to the maximum of the distributions.

### 6.2.3 3 mrad Gaussian misalignment

Similar to the ‘1 mrad Gaussian misalignment’, a study has been carried out for misalignments following a Gaussian distribution whose standard deviation amounts to 3 mrad. Identical simulation parameters and statistics have been used. Analogous histograms to the ones presented in the previous subsection are shown in Figures 6.14, 6.15 and 6.16. In Figures 6.14 and 6.15, the scale range of  $a$  has been increased by a factor of two to avoid saturation in the histogram:  $a \in [-2 \text{ cm}; +2 \text{ cm}]$ .

The observed shifts with a ‘3 mrad Gaussian misalignment’ geometry are significantly larger than in the previous misalignment case. Even with such shifts, the correction cycle greatly reduces the average distance  $a$ , except at the edges of the photon sensor plane, where the situation is slightly worse than the previous case. The mean of the Gaussian fit applied on the ring-track distance distribution before the corrections are implemented is 1.3 cm. Once the correction cycle has been used, the mean of the Gaussian fit is reduced to 0.25 cm, which still fulfils the detector requirements.

Edge effects are still visible but not detrimental to the detector operation. The situation in the corners of the photon detector plane could be enhanced with higher statistics and by extending the lower momentum range of the particles to  $p \in [0 \text{ GeV}/c; 9 \text{ GeV}/c]$ . In addition a second iteration of the correction cycle on the corrected geometry could be applied.

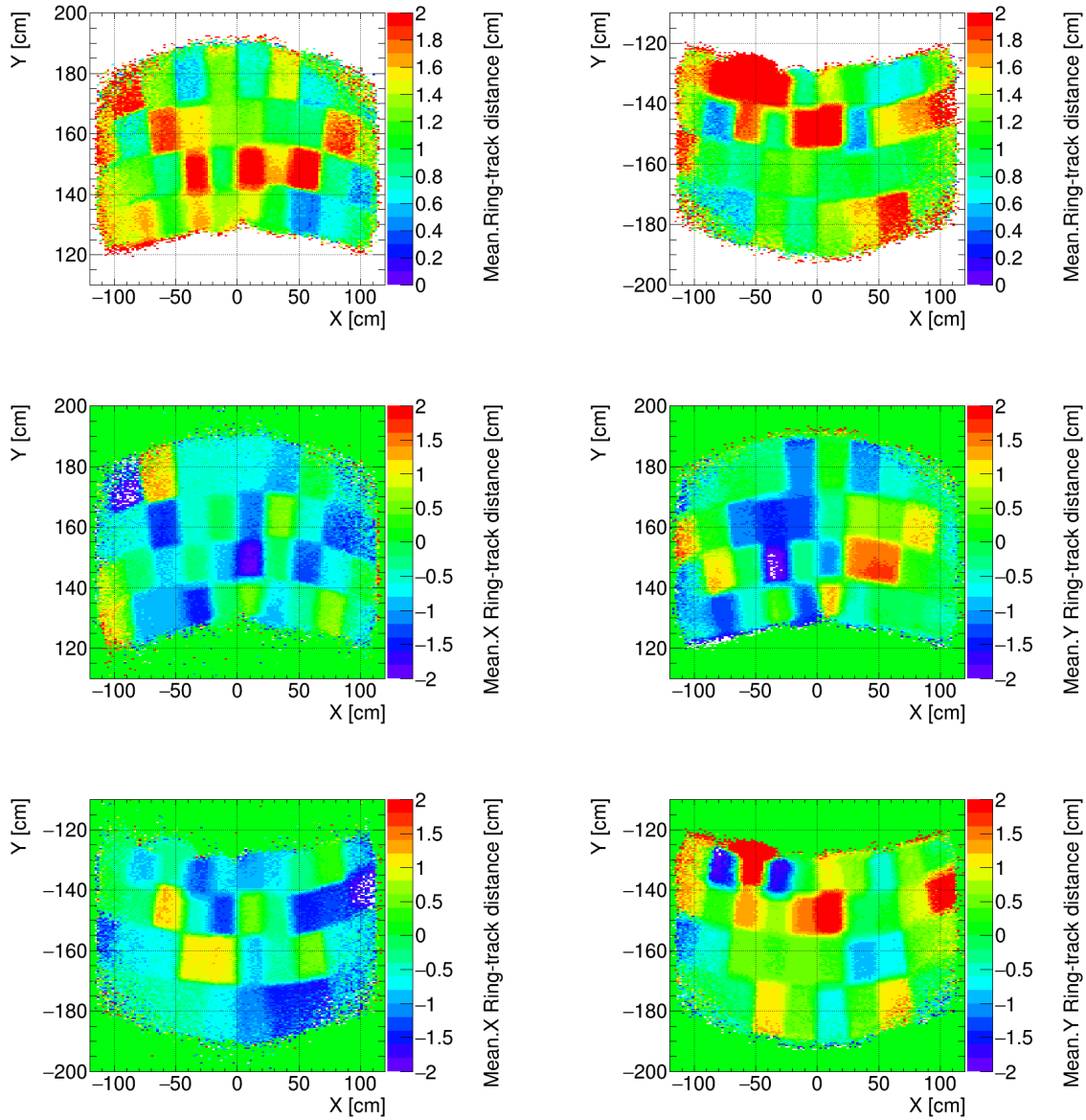


Figure 6.14: Average  $a$  distribution for a randomly rotated mirror wall following a ‘3 mrad Gaussian distribution’. The mean of  $a$  is presented in the upper row, where the upper photon detector plane is shown on the left side and the lower photon detector plane on the right. The horizontal projections of  $a$  are illustrated in the middle and lower left histograms for the upper and lower MAPMT planes, respectively. The vertical projections are displayed in the middle and lower right histograms for the upper and lower MAPMT plane, respectively. The rotation values on both tile axes are different. Individual mirror tiles are well visible on the photon sensor plane. The scale range of  $a$  has been increased by a factor of 2 in all histograms, with respect to Figure 6.11.

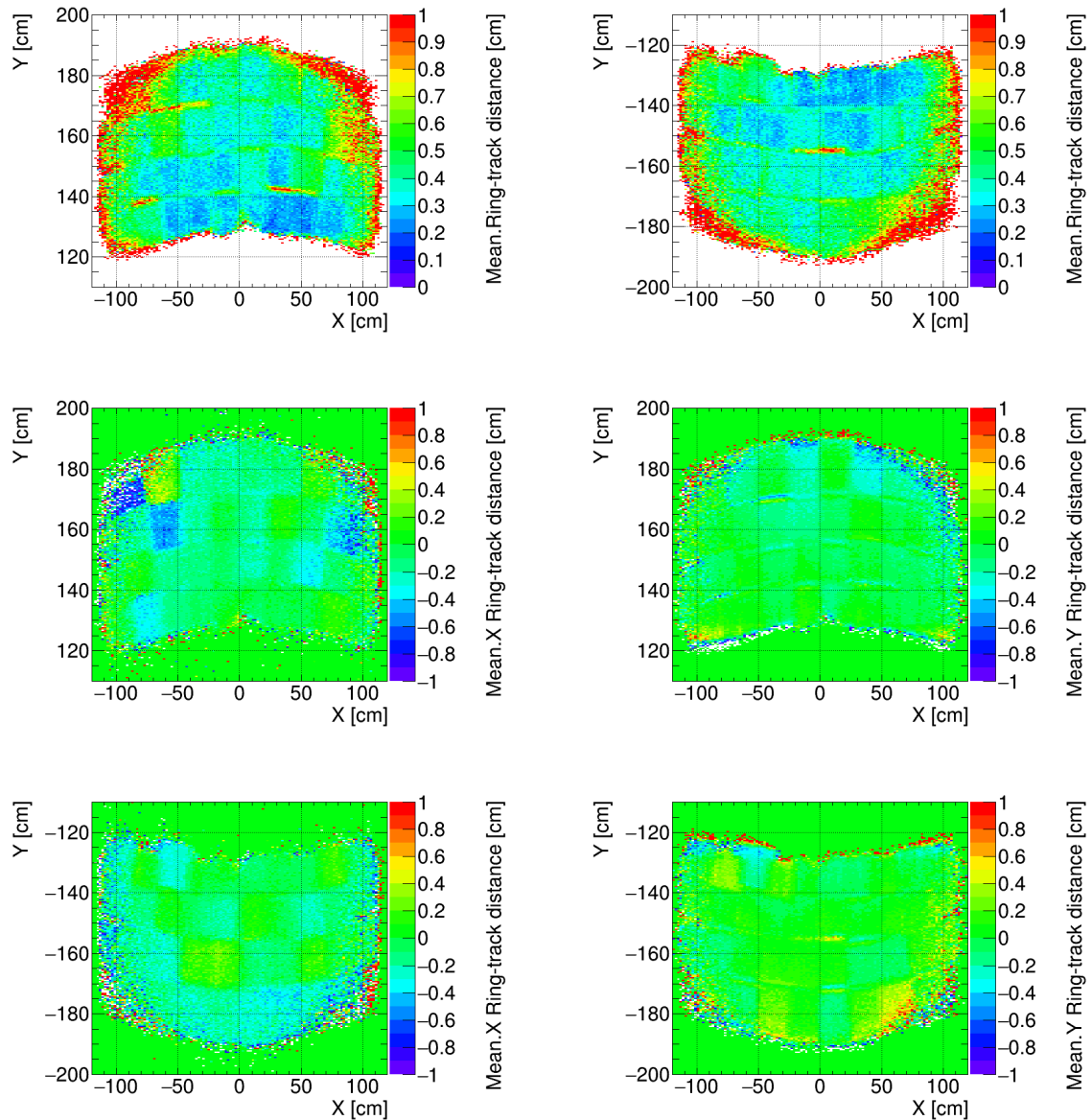


Figure 6.15: Average  $a$  distribution after the correction cycle has been applied, for the ‘3 mrad Gaussian misalignment’ geometry. The  $a$  distribution is more uniform, although a mosaic-like structure can still be observed. The mean  $a$  is reduced to 0.2 – 0.3 cm in the central region of the photon sensor planes, where misalignment residuals can still be observed. Edge effects are slightly more pronounced than for the aligned case. The scale range of  $a$  has been increased by a factor of 2 in all histograms, with respect to Figure 6.12.

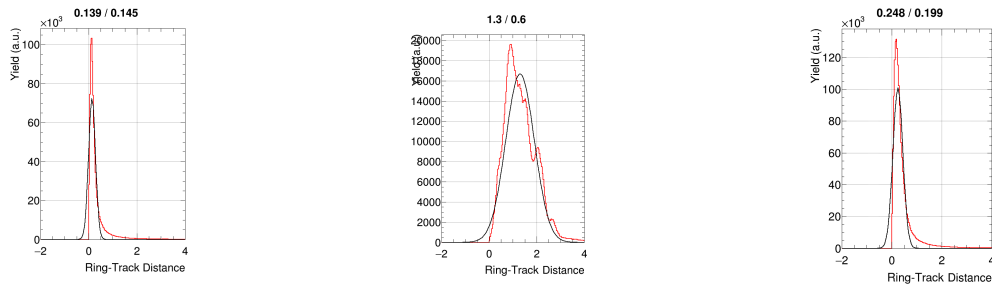


Figure 6.16:  $a$  distribution over the complete MAPMT plane for the aligned (left), rotated with a ‘3 mrad Gaussian misalignment’ (middle) and corrected (right) cases. A Gaussian fit was applied on the data (black curves). The mean (left number) and standard deviation (right number) of the fitted Gaussian are displayed on the top of each histogram. The mean of the Gaussian fits roughly corresponds to the maximum of the distributions.

### 6.3 Improvements from the correction cycle on reconstruction efficiencies

In Section 3.4 and Table 3.4, the impact of mirror misalignments on the STS-RICH matching, combined with the ring finding efficiency, and RICH identification efficiencies has already been demonstrated.

This study was conducted for 16,000 central Au+Au collisions at 10 AGeV beam energy, with 5 embedded electrons and 5 embedded positrons. It showed a clear drop in the STS-RICH matching and ring finding efficiency with both the ‘1 mrad Gaussian misalignment’ and ‘3 mrad Gaussian misalignment’ geometries (see Section 6.2.2 for a definition of the implemented mirror rotation). The efficiency was reduced from 87.3% in the aligned case to 86.3% and 78.8% for the 1 and 3 mrad cases, respectively. Similarly, this study showed a decrease in the RICH identification efficiency from 84.6% at a pion suppression factor of 210.3 in the aligned case to 82.9% with a pion suppression factor of 190.6 and 65.3% with a pion suppression factor of 143 with the ‘1 mrad Gaussian misalignment’ and ‘3 mrad Gaussian misalignment’ geometries, respectively.

Thus mirror misalignments are clearly harming the operation of the detector under real data taking, as physics signals are lost. In the following the impact of the correction cycle on these reconstruction efficiencies will be investigated.

To do so, 16,000 events were simulated, each containing 5 electrons and 5 positrons with a momentum ranging from 0 GeV/c up to 9.5 GeV/c and embedded in Au+Au collisions at 10 AGeV beam energy. The angular  $\theta \in [0^\circ; 180^\circ]$  and azimuthal  $\Phi \in [0^\circ; 360^\circ]$  angles were chosen to cover the complete mirror wall within the acceptance of the CBM experiment. And the following set-up was employed: Magnet (version v15a with the field map v12b), STS (version v16x), RICH (version v17a\_1e) and beam pipe (version v16c\_1e).

The upper row of Figure 6.17 displays the STS reconstruction (red curve) and the STS-RICH reconstruction and ring-track matching efficiency (blue curve). The STS-RICH reconstruction combines the STS reconstruction efficiency with the RICH ring finding efficiency. The middle and lower rows of Figure 6.17 show the electron efficiency and the obtained pion suppression factor. These efficiencies are shown for the aligned case, with a ‘1 mrad Gaussian misalignment’ geometry and once the correction cycle has been applied.

It can be stressed, that even for small mirror rotations in the order of 1 mrad, the STS-RICH reconstruction and ring-track matching efficiency is reduced by 1%, the electron identification efficiency by 1.7% and the pion suppression factor by 10%. The difference in these efficiencies after the correction cycle has been applied is reduced to 0.2% for the ring-track matching efficiency, 0.4% for the electron identification efficiency and provides a pion suppression factor similar to the one obtained in the aligned case. Thus an improvement of the correction cycle is observed for these efficiencies.

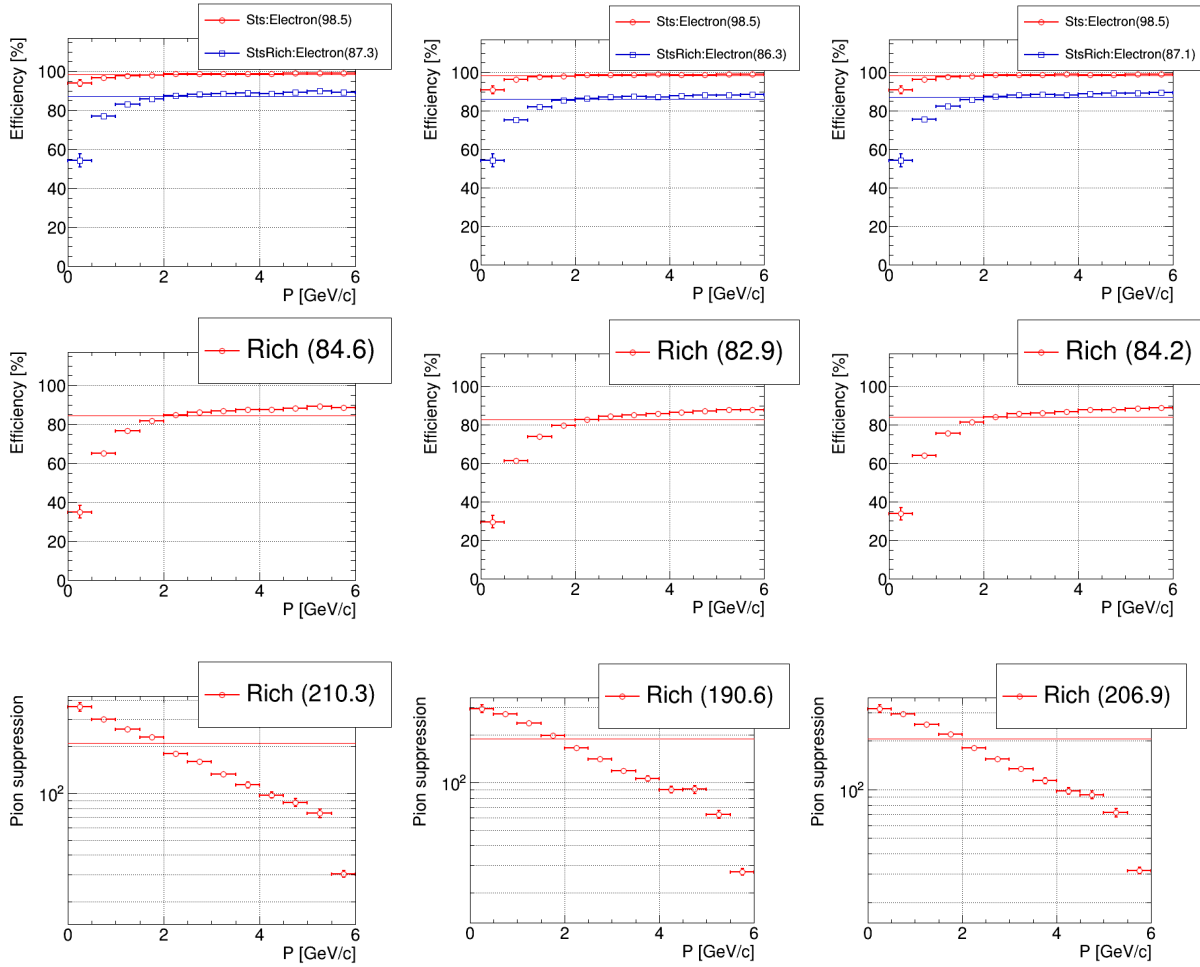


Figure 6.17: STS-RICH matching efficiency combined with the ring finding efficiency (upper row), electron identification efficiency (middle row) and pion suppression factor (lower row). The presented efficiencies are given for the aligned (left column), rotated (middle column) and corrected (right column) cases. A ‘1 mrad Gaussian misalignment’ was induced.

A study with identical simulation parameters and an identical set-up has been carried out for a ‘3 mrad Gaussian misalignment’ geometry. The results are shown in Figure 6.18.

Once the ‘3 mrad Gaussian misalignment’ has been applied, the STS-RICH reconstruction and ring-track matching efficiency, the electron identification efficiency and the pion suppression factor decreased to 78.8%, 65.3% and 143, respectively. With the correction cycle these efficiencies amount to 86%, 81.9% and the pion suppression factor is 202. This demonstrates an improvement in the reconstruction efficiencies and the pion suppression factor back to a situation very close to the one with an aligned mirror wall.

In both cases, the effects of misalignments are largest on the electron identification efficiency. This is due to the fact that the ring-track distance is used as input parameter by the ANN employed for the electron identification (as explained in Section 3.3.5).

These results reveal a clear enhancement in the operation of the CBM-RICH detector by the developed correction cycle, which was presented in this chapter.

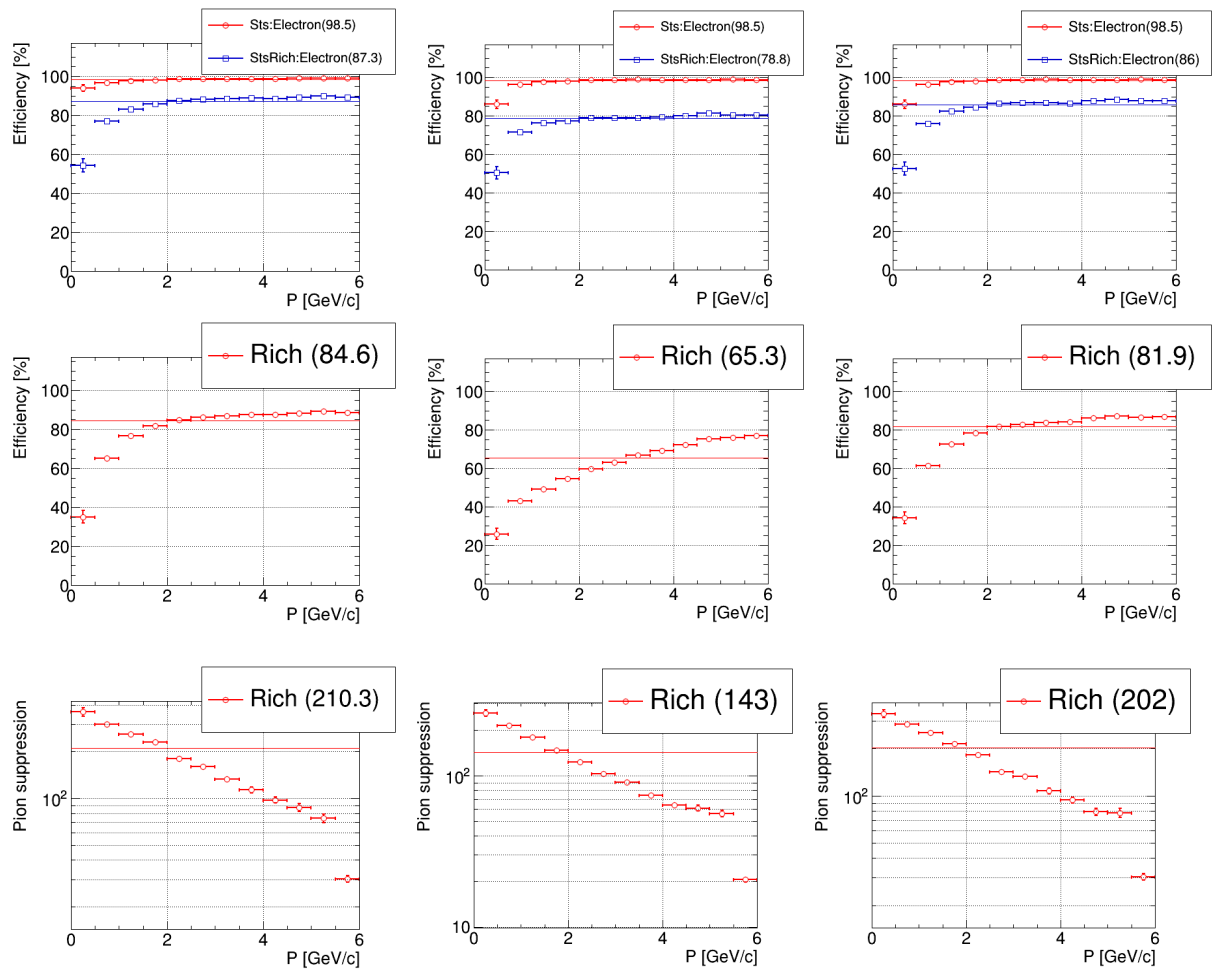


Figure 6.18: STS-RICH matching efficiency combined with the ring finding efficiency (upper row), electron identification efficiency (middle row) and pion suppression factor (lower row). The presented efficiencies are given for the aligned (left column), rotated (middle column) and corrected (right column) cases. A ‘3 mrad Gaussian misalignment’ was induced.



# Chapter 7

## Summary and outlook

### 7.1 Summary

The presented work and results in this thesis focus on the development of the Ring Imaging Cherenkov detector for the CBM experiment. They aim at a proper detector operation under possibly occurring mirror misalignments. To do so two techniques were investigated to observe and quantify misalignments. Once the detected misalignments were measured, the RICH reconstruction software was updated to correct them. The main results of this thesis are summed up in the following.

The CLAM method introduced in Chapter 4 is inspired from the COMPASS experiment and is based on hardware. It uses dedicated reflecting equipment and lighting apparatus inside the RICH detector for a quick and qualitative mirror misalignment detection. This method has been implemented during a beam time at CERN and tested in detail.

The study shown in Section 4.3 focuses on the event, where the Cherenkov cone is reflected by more than one mirror. The impact of such events on the histograms of the main ring parameters has revealed the apparition of a two peak structure on the ring radius distribution and on either the major or the minor semi-axis distribution (Figure 4.9). However, only for very unlikely cases where the Cherenkov cone is reflected right in between two or more mirrors, a large effect is seen.

In addition, the CLAM method can be employed to quantify mirror misalignments. It requires a previous calibration in the laboratory, presented in Section 4.4. The feasibility of the method has then been demonstrated on pictures taken during a previous beamtime at CERN in 2014. The results are presented in Section 4.5. The method could reconstruct mirror misalignments for single axis and diagonal rotations with errors amounting up to 18% of the applied mirror rotation (see Figures 4.19, 4.20 and Tables 4.2, 4.4). For the calibration in the laboratory, the mirror frame position and mirror orientations were chosen such that the CERN beamtime set-up was reproduced.

A misalignment quantification technique developed by the HERA-B experiment has been subsequently presented in Chapter 5. It is based on software and requires only data. Its adaptation to the CbmRoot framework and the CBM-RICH geometry has been demonstrated. The technique works for horizontal rotations ranging between 0.3 mrad and 14 mrad, while keeping an error of 20% of the applied rotation (Figure 5.6). For vertical rotations, the technique showed errors up to 20% of the applied rotation for misalignments ranging from 0.4 mrad up to 15 mrad (Figure 5.7). In a last step the behaviour of the technique for inner and outer mirror tiles has been studied (Figures 5.8 and B.2).

This method requires, when employed during real data taking, a clean electron sample from the data. It also needs a sufficient number of particles reconstructed by the STS and RICH detectors, which hit each individual mirror tile. The studies have shown that 2,500 electrons per mirror tile are enough to apply the technique. Azimuthal and polar angles from the target towards each individual tile can be defined and applied as a cut on the recorded data to select ‘good’ electrons or positrons. The ideal data taking case would be experiments yielding low multiplicity electrons and positrons, to have a better electron identification.

Given that possible misalignments can be measured, a correction cycle has been developed and is explained in Chapter 6. It includes the information of mirror tile rotations calculated with the technique from Chapter 5 and uses it inside the RICH software routines. It could also use the mirror orientation information given by the CLAM method as input for the RICH software. The misalignment information is used to correct track extrapolations onto the photon sensor plane (Figure 6.1). The influence of the correction is shown through the evolution of the distance between fitted ring centres and extrapolated track hits on the photon plane (Figure 6.4).

Extensive studies have been conducted with various mirror rotations and the presented correction cycle has been automatised for the full mirror wall (Figure 6.11 and 6.12). The correction software improved the mean ring-track distance from 0.47 cm in the case of a ‘1 mrad Gaussian misalignment’ down to 0.17 cm (Figure 6.13). For a ‘3 mrad Gaussian misalignment’, the ring-track distance was corrected from 1.3 cm down to 0.25 cm (Figure 6.16). In the aligned case, the average distance amounts to 0.14 cm and the average distance accepted in the detector specifications amounts to 0.3 cm, which corresponds to a 1 mrad rotation angle.

The impact of the correction cycle in the STS-RICH reconstruction and matching efficiency, the electron identification efficiency and in the pion suppression factor of the RICH detector has also been examined. Clear losses in these efficiencies and in the pion suppression factor have been shown, with different misaligned mirror geometries. However the developed correction routine improves both efficiencies and the pion suppression factor close to the values obtained in the aligned case, for a ‘1 mrad Gaussian misalignment’ (Figure 6.17) and for a ‘3 mrad Gaussian misalignment’ as well (Figure 6.18). Thus the developed correction cycle allows a proper operation of the CBM RICH detector under misalignments.

## 7.2 Future developments to optimise the correction procedure

To improve the quantification of mirror misalignments using the CLAM technique, photogrammetry can be employed (see Sections 3.3.2 and 4.2 of [148]). For this variant of the method, an apparatus similar to the one presented in Section 4.1 is required, with, in addition, calibrated cameras. From the calibration, the parameters of the camera's interior orientation, which describes the imaging process within the camera, are accessible. Moreover, the exterior orientation of the camera needs to be established via six parameters, characterizing the spatial position and orientation of the camera with respect to a chosen global coordinate system. This can be done with target dots glued on the mirror frame and on the RICH box. The defined parameters of interior and exterior orientation of the camera can then be used to solve the collinearity equations.

Another option would be to use commercial software, such as the MoveInspect DPA software module from Aicon. Here the main issue is that the software was not conceived to work with mirrors. When mirrors are misaligned, it becomes unclear which target moved in which direction. A possible workaround would be to have cameras looking at the backside of the mirrors. There space is a constraint and one could resort to rails, so that the cameras might still cover the full mirror wall.

Concerning the quantification technique using data, the next step would be to develop a strategy on how to extract good particle candidates from the data collected in real beam conditions. For example, the use of low multiplicity data would ensure a better electron identification. Also the implementation of proper cuts on the azimuthal and polar angles to help select particles for each mirror tile is required.

Furthermore, the technique has shown some limitations for the outer mirror wall region. An optimisation of the technique using data for mirrors located in this region could be undertaken. Indeed, in this region, incoming particles have low momentum and are thus more deviated by the remaining magnetic stray field. In addition, single axis rotations imply shifts in both directions due to the detector geometry. These effects consequently harm the performances of the technique.

A possible further development of the correction cycle would be to carry out multiple runs to enhance the results. The correction cycle would be applied on a given misaligned geometry first. The quantified mirror rotations would be used to correct the misaligned geometry, producing a new corrected mirror geometry. The correction cycle would then run on this new corrected geometry. This step could in turn produce a second corrected geometry, on which the correction cycle could be run again. The number of iterations required until the technique does not improve could also be examined.



# Appendix A

## EPICS based control systems for the CBM RICH prototype

In this appendix, control systems for the CBM-RICH prototype operated by EPICS are presented. They were implemented for beamtimes at CERN in 2011 and 2012 and have been updated for the 2014 beamtime (see Figures 4.3 and 4.4 from Section 4.2.2). They were used to obtain, among other things, the results presented in Section 4.3.

First the hardware is presented. How to run the software TwinCAT on windows and Linux is the subject of the two following sections. In a final section, the operation of the high voltage with EPICS is shown.

### A.1 Hardware installation

Connect the cables to the Beckhoff system (also called IPC, for industrial PC), as shown in Figure A.1.

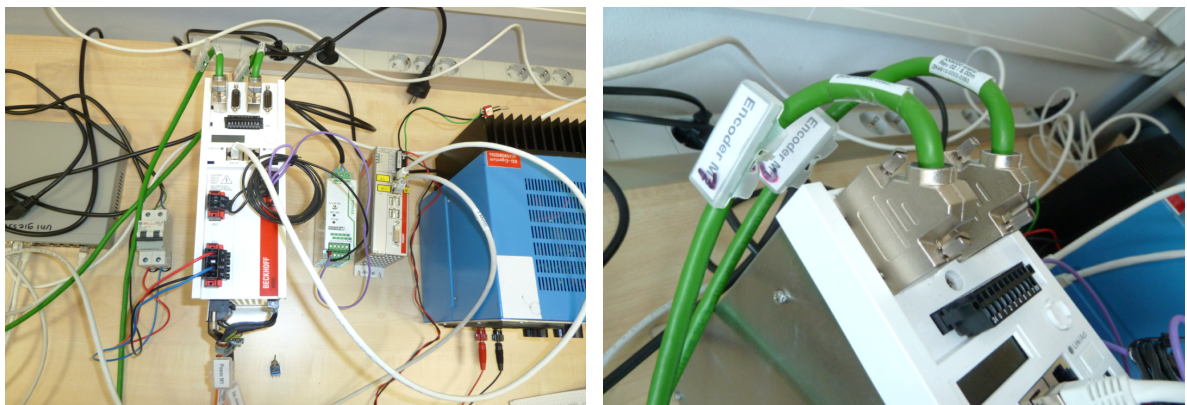


Figure A.1: Cabling of the IPC system.

Then connect the power supply cables for the motors (see Figure A.2).

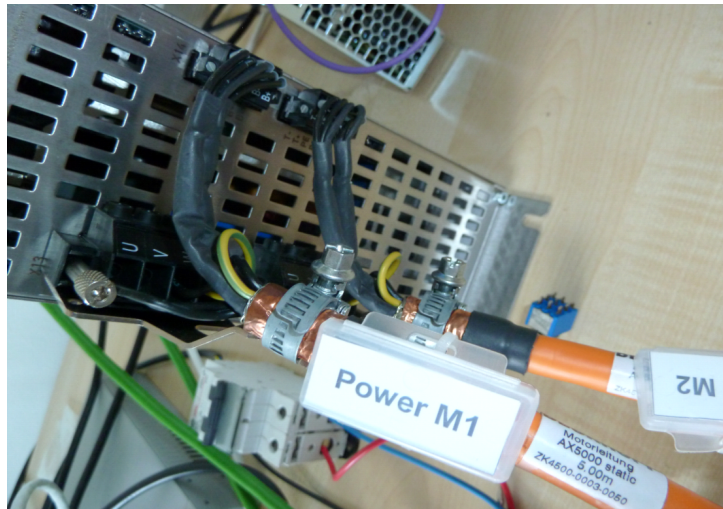


Figure A.2: Cabling of the Motors to the Beckhoff system.

Start the Beckhoff system, by connecting the power supply cables of the whole Beckhoff system into the wall sockets.

If the Windows computer workstation is not already running, turn it on. Do the same for the Linux one. Then connect the Windows and Linux workstations and the Beckhoff system together via a main switch (see Figure A.3).

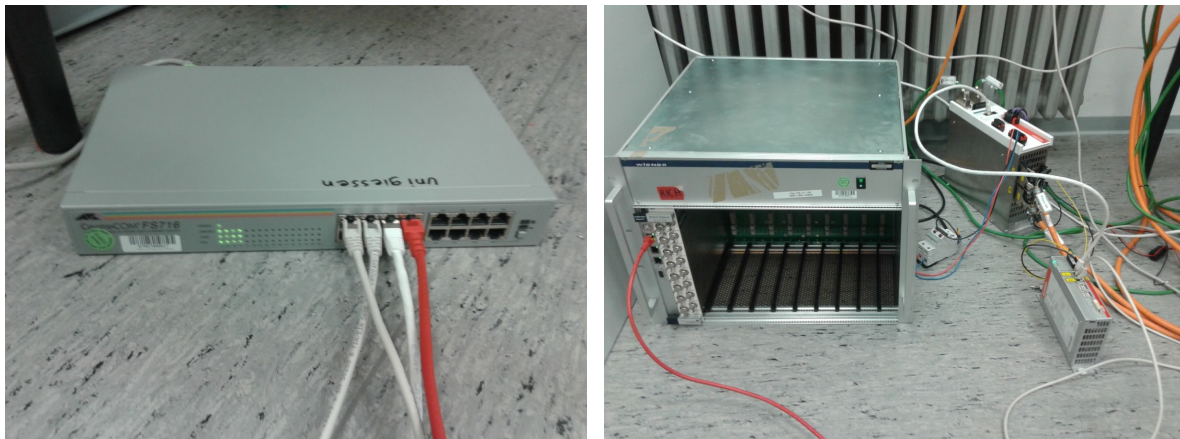


Figure A.3: Switch (left) and High voltage (right) connections.

## A.2 Run TwinCAT on the windows machine

### A.2.1 Numerical control (local without PLC program and without EPICS)

On the windows machine, go to the:

‘Desktop/TwinCAT PLC Control Versions/Version\_2012\_CBM\_RICH/’ folder. For the local control, execute ‘Test\_2Motors\_without\_Program’ (see Figure A.4).

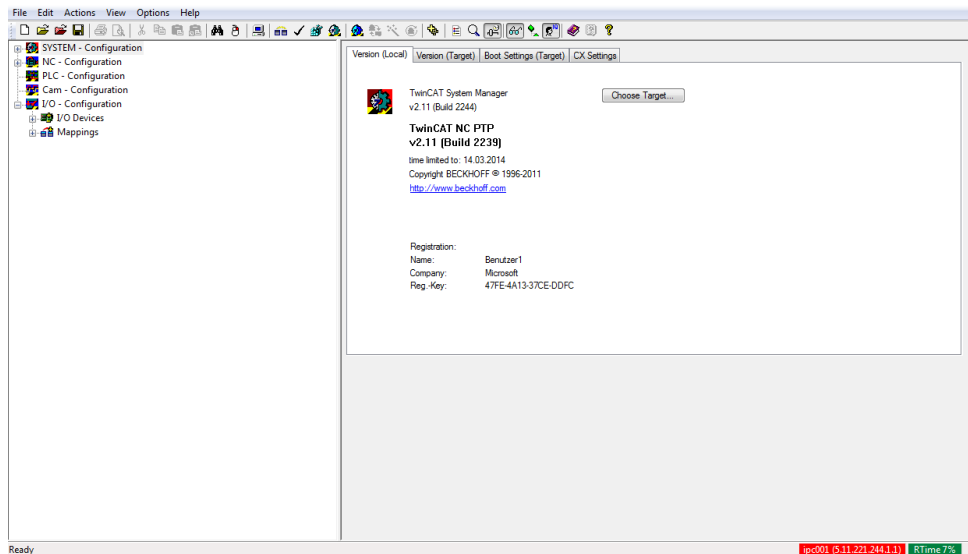


Figure A.4: TwinCAT software interface.

When the TwinCAT window appears, check whether the status is in “run mode” or “config mode” (configuration mode) - you can see the current status of the system on the bottom right of the window (see Figure A.5).



Figure A.5: TwinCAT status in runtime mode (left) and config mode (right).

Figure A.6 illustrates the buttons used to switch between the run and configuration modes. Below is a description of their functionality, the number corresponding to the number on Figure A.6:

1. Activate Configuration
2. Restart in Run mode
3. Restart in configuration mode

If the system is not in configuration mode, select the button “2” to restart TwinCAT in run mode.



Figure A.6: Different modes in TwinCAT.

### What to do if the computer cannot connect to the Beckhoff system?

In case the system status is “Time-Out”, this means that either:

- The Beckhoff system is not running (check if the system is on: check the power supply cables and the circuit breaker)
- Or it is not connected to the windows workstation (then check the Ethernet cables and the switch status. You can also check the connection between the Beckhoff system and the windows PC, with the Cerhost program, located on the desktop)
- Or it has been recently connected (in this case the program is trying to find the IPC).

If the two machines are well connected, go to the “SYSTEM – Configuration” entry of the tree on the left. Click on the “Choose target” button (see Figure A.7). Click “Search (Ethernet)”, then “Broadcast search”. The connection to the ipc001 should be established, then press close. On the “Choose target system” window, select the ipc001 in the tree and click OK.

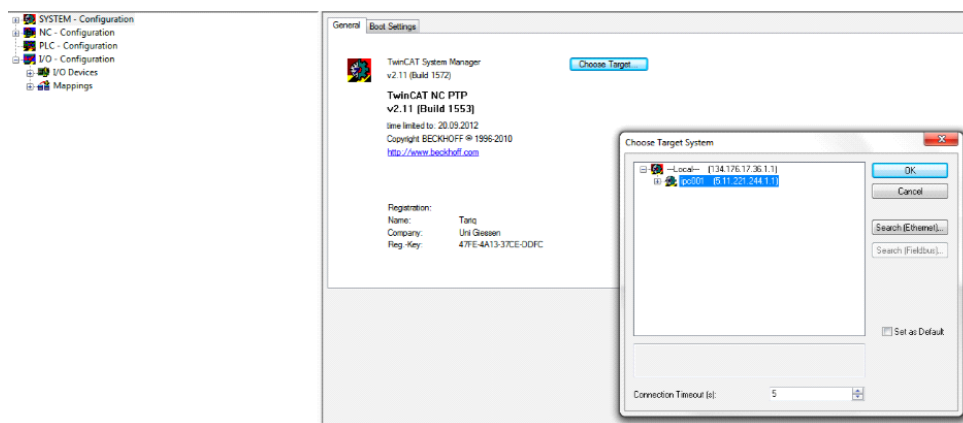


Figure A.7: Searching for the IPC on the network in TwinCAT.

If everything is well installed and connected but there is no connection between the IPC and the windows PC, try to disable the connection to the switch and enable it again.

You can also reset the router connection. To do so, right click on the icon called “TwinCAT Konfig Modus” (lower right on the windows desktop) and choose “Eigenschaften” option. Then under the AMS router tab, in the Router window, select the current IPC

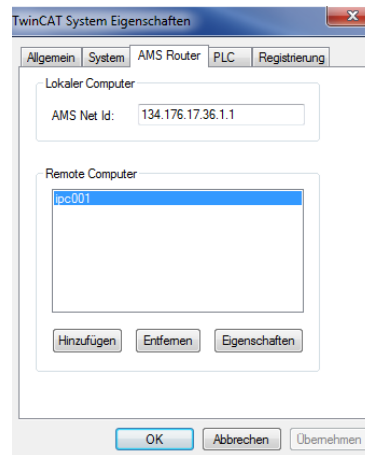


Figure A.8: Reset the router connection on TwinCAT.

connection and delete it (entfernen). Add (hinzufügen) a new connection to the IPC (see Figure A.8).

In case the system is still not running after the previous steps have been conducted, see the annex of this document ‘How to configure EtherCAT card’ to either check that each parameter has the right value seen on the figures or to configure a new program from zero.

Once the System Manager Program has been successfully launched and is in run mode, the user finds several entries on the left tree.

1. System Configuration: TwinCAT PC.  
Select the IPC using the ‘Choose Target’ button.
2. I/O – Configuration: Drive scan.  
Scan the drivers connected to the system. On the left tree, right click on the icon ‘Device 1 (Ether-CAT)’ located under I/O Devices.
3. NC – Configuration: Drive.  
Check connection between Drive and hardware under the entry “Axes”.
4. PLC – Configuration: TwinCAT PLC.  
Connect the hardware (input/output) to the PLC Program. Check the project name and PATH inside the IEC entry on the left tree, called: ‘MirrorControl\_new\_js\_TT\_ver3\_withEPICS’.

Remarks on the possible movements of the system:

- Motor 1: Rotation around horizontal axis (when increasing the axis value, the upper part comes towards the observer, when looking at the front of the mirror)
- Motor 2: Rotation around vertical axis (when increasing the axis value, the right side comes towards the observer, when looking at the front of the mirror)

## A.2.2 TwinCAT with PLC program but without EPICS

On the ‘Desktop/TwinCAT PLC Control Versions/Version\_2012\_CBM\_RICH/’ folder, choose the program: ‘Test\_2Motors\_with\_Program\_v3’ and go to run mode. Then, in the ‘Version\_2012\_CBM\_RICH/’ directory, choose the ‘MirrorControl\_new\_js\_TT\_ver3’ program. On the right tree at the bottom, choose the ‘visualisation’ tab and double click on the ‘CBM\_MIRROR\_CONTR’ entry. Figure A.9 shows the Graphical User Interface (GUI), which should come up.

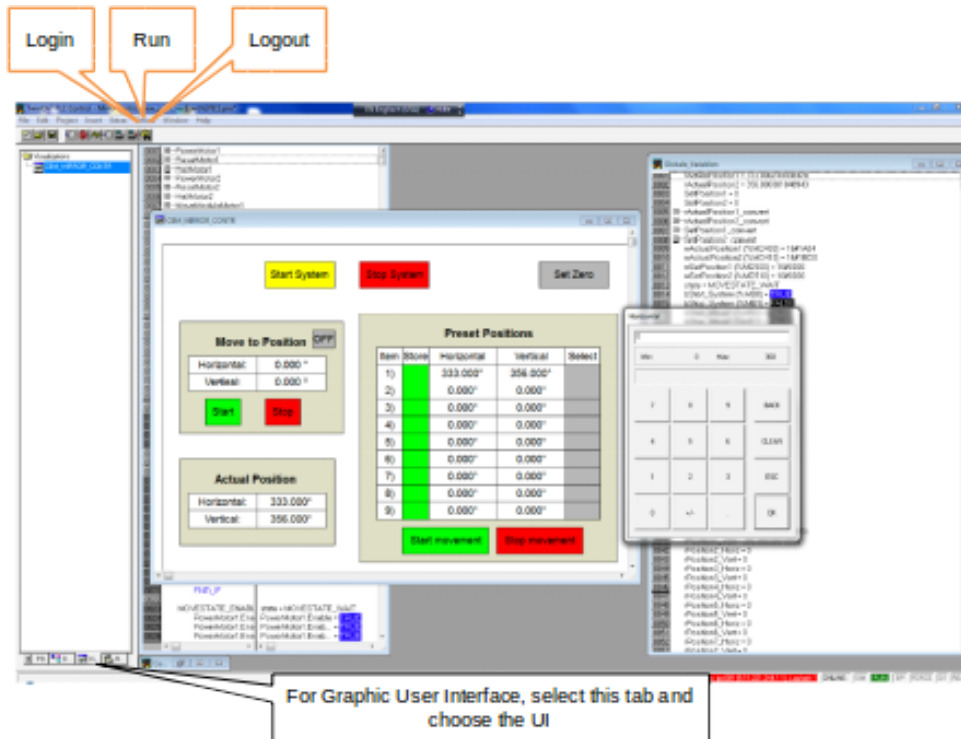


Figure A.9: TwinCAT PLC graphical user interface.

### How to run the system?

In the ‘Online’ tab, on the top of the window, select the ‘login’ entry and when asked to download the new program, answer ‘Ja’. Then select the ‘run’ entry in the ‘Online’ tab. Now the PLC program should be running.

It is very important, when starting the PLC program, to first login and then run; and when turning off, to stop the program and then logout!

To control the motors, click the ‘Start System’ rectangular button (this button should become yellow). Then in the ‘Move to position’ window, switch the button to ‘ON’ (the button becomes green). Set the horizontal and vertical positions to the desired values, using the numerical pad and click the ‘Start’ button. The system should start moving. In case the user wants to stop the motors while moving, click on the red ‘Stop System’ button.

Below is a description of the main options, which can be used by the user (see Figure A.10).

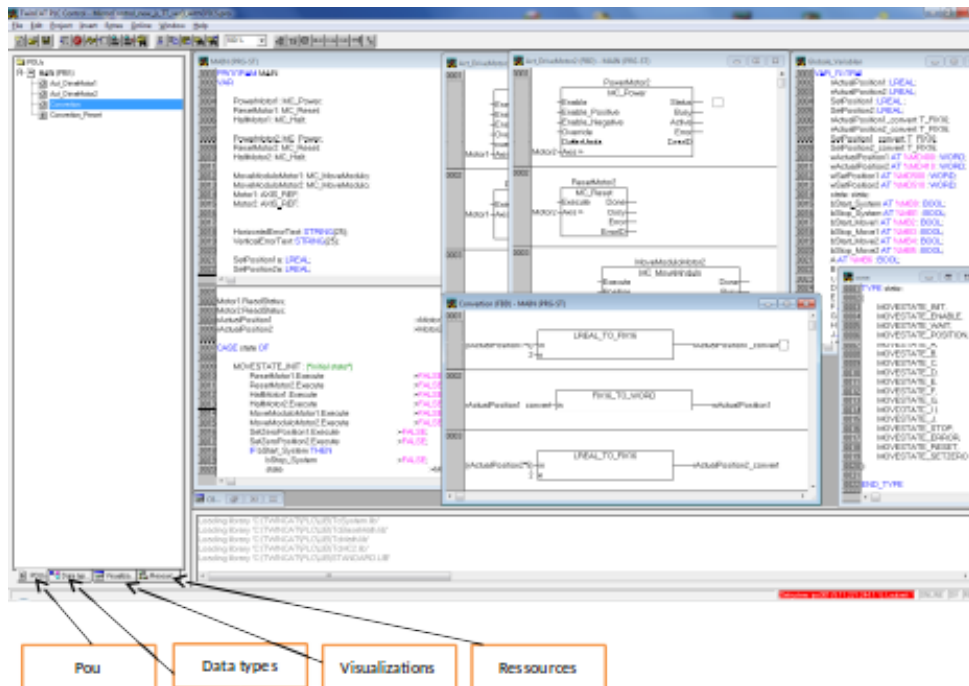


Figure A.10: Detailed view of the PLC program.

On the left tree, choose the ‘POUs’ (Program Organisation Unit) tab, one can open several windows:

- Main
- Act\_DriveMotor1
- Act\_DriveMotor2
- Conversion

In the ‘Main’ program under the tab POUs, there are many state functions, defined as `MOVESTATE_*`, where  $*$  = [A-H and J]. These states correspond to the items (1-9), which are stored inside the Preset Positions of the GUI. These positions correspond to mirror adjustments, reflecting on defined areas of the PMT plane.

To add a function in the Act\_DriveMotor1/2 or the Conversion windows, right click on the left border of the window and choose the ‘Network before’ or ‘Network after’ option. After changing anything in the code, go to the ‘Project’ tab (on top of the window) and use the ‘Rebuild all’ function.

To simulate the program before testing it on the motors, one can run a ‘Simulation Mode’, located in the ‘Online’ tab, once a ‘Login’ has been previously performed. The function block `MC_MoveModulo`, using `MC_Shortest_Way` as Direction input moves the motor to the requested position using the shortest way.

To stop the motor while moving, use `MC_Aborting` as input to the BufferMode of the `MC_Halt` function.

On the ‘Date types’ tab, one can open the states window, where one can add new

states to the program.

On the ‘Visualisations’ tab, a GUI is available. It can be modified using the upper menu to add remove or change blocks and by double clicking on any box, to change its characteristics.

When double clicking on a box, the ‘input’ and ‘variables’ entries are used to modify the variable linked to this box. In the case of a box with input values, one can change how the user enters a value inside the box, under the ‘Input’ entry and by ticking the ‘Text’ input of variable ‘Textdisplay’ option. Here one can specify the min and max values accepted inside the box and choose how the text is entered using the drop-down menu (with Numpad or Keypad, etc.).

On the ‘Resources’ tab, the ‘Globale\_Variablen’ window can be opened, where one can find all the variables linked to the program. While the system is running, the user can check the states of each variable in this window as well.

Table A.1 explains the address rules and specifies the meaning of the values stored inside the ‘Globale\_Variablen’ window.

Prefix	Description
I	Input
O	Output
M	Memory location
X	Single bit
B	Byte (8 Bits)
W	Word (16 Bits)
D	Double word (32 bits)

Table A.1: Address ruling of the TwinCAT PLC system.

Reference values for the current system in the lab are for the horizontal axis  $331.5^\circ$  (or  $-28.5^\circ$ ) and for the vertical axis  $353.15^\circ$  (or  $-6.85^\circ$ ). They correspond to horizontal and vertical rotations of the mirror frame.

## A.3 Linux with EPICS to run TwinCAT remotely

### A.3.1 In the case EPICS is not installed

The following is described for a Linux OS, with 64 bit architecture. Use the text file ‘Cookbook\_complete.txt’ in the ‘~/EPICS’ folder and follow the instructions, to install the EPICS system, with its extensions and modules and also the CSS program.

In this file, the installation process is explained in details and one only needs to copy and paste the commands on a terminal.

### A.3.2 Run TwinCAT via EPICS

On the windows workstation, go first to the:

‘Desktop/TwinCAT PLC Control Versions/Version\_2012\_CBM\_RICH/’ folder. Then choose the ‘Test\_2Motors\_with\_Program\_v4\_withEPICS’ program and go to run mode. Execute also the ‘MirrorControl\_new\_js\_TT\_ver4\_withEPICS’ PLC program. At the top of the window, in the ‘Online’ tab, press ‘login’ and then ‘run’.

Note: in this program, you cannot use the GUI in the PLC to set position values of the motors. The values can only be set from the CSS program on the Linux station. Now on the Linux workstation, open a new terminal.

#### If the programs are not installed

Follow the instructions from the ‘Cookbook\_complete.txt’ file.

#### If the programs are already installed

Go to the directory: ‘~/EPICS/’. In this directory, there is a hidden file, called ‘.profile’. To set the environment variables, enter the command: ‘source .profile’ in the terminal.

Then change the IP address of the Beckhoff system on EPICS. Go to the directory ‘~/EPICS/modules/synApps\_5\_7/support/modbus\_cbm\_2014/iocBoot/iocModbus/’ and open the ‘cbm.cmd’ file with an editor (for instance ‘vi cbm.cmd’).

At the line ‘drvAsynIPPortConfigure’, change the IP address to the desired value. Current set-up: `drvAsynIPPortConfigure(‘cbm’,‘10.160.0.51:502’,0,0,1)`.

After that, go to the:

‘~/EPICS/modules/synApps\_5\_7/support/modbus\_cbm\_2014/iocBoot/iocModbus/’ directory and enter the command: ‘../../bin/linux-x86\_64/modbusApp cbm.cmd’. The connection via EPICS to the Beckhoff system should be settled.

Finally, start the CSS graphic user interface. Go to the:

‘~/Desktop/CSS\_EPICS\_3.1.2/’ folder and execute the program, by double clicking on the script, called ‘start\_css’.

If needed, click Browse to select the wanted workspace:

‘~/CSS-Workspace/SlowControlPanel’. To change the PC’s IP address, go to Preferences in the edit tab. Choose the ‘CSS Core’ and ‘EPICS’ entries on the left tree and change the IP address on the ‘addr\_list’ field. The current set-up is represented in Figure A.11, left. Then restart the CSS program.

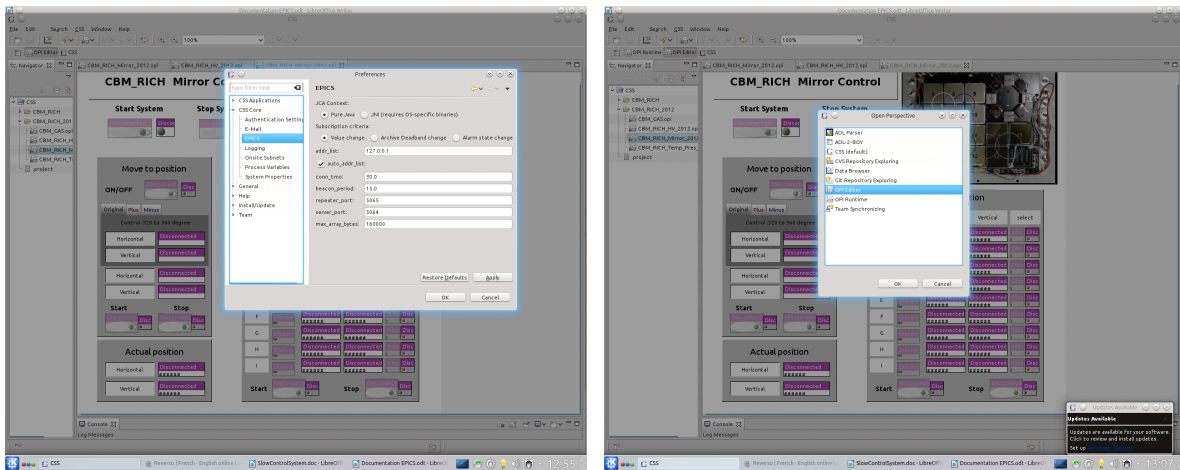


Figure A.11: EPICS default set-up (left) and switching to the edit mode (right).

In CSS there are two modes, the ‘edit mode’ and the ‘run mode’. To switch to the edit mode, go to the window tab, choose open perspective and other. Then select the ‘OPI Editor’ entry (see Figure A.11, right).

On the left-side tree, select the ‘CBM\_RICH\_Mirror\_2014\_Validated.opi’ file in the ‘CBM\_RICH\_2014’ folder.

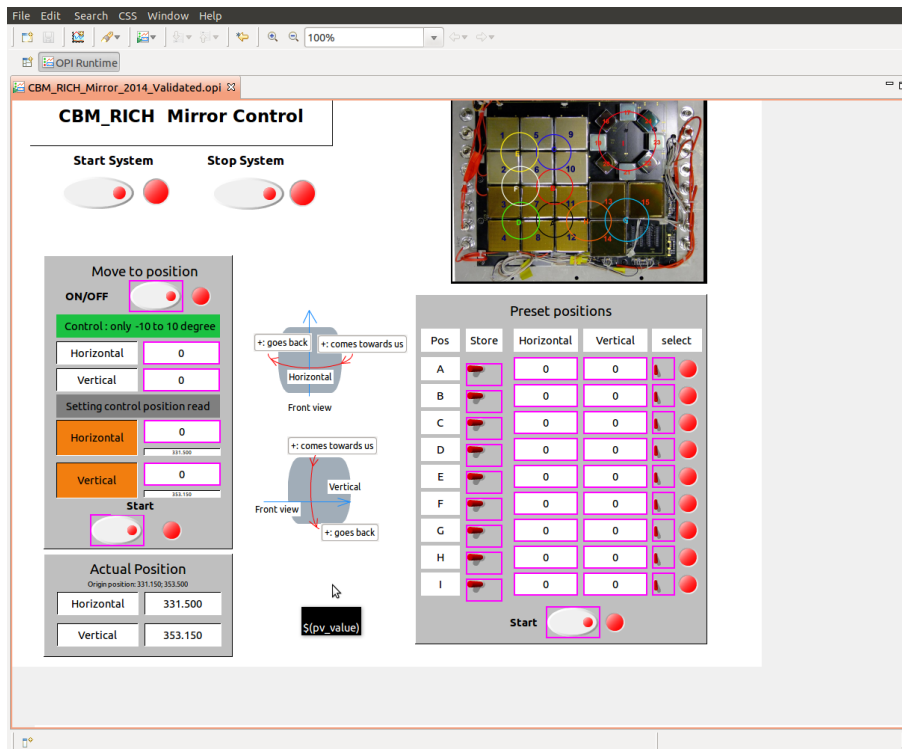


Figure A.12: EPICS editor view.

### How to edit changes in the editor mode?

In the editor mode, when clicking on a box (containing a variable or entry), one can change its value via the PV (Process Variable) name entry on the right-side window (this

variable name can be retrieved from the ‘dbl’ command of EPICS in a terminal).

The min and max values can be changed on the right side window. The style can be modified under the monitoring and/or control menu (click on the small white arrow on the top left of the right-side window).

### How to start the system?

Switch to run mode, (go to the window tab, choose open perspective – other and select ‘OPI Runtime’), or click on the green arrow (right side of the top menu bar). This window should appear (see picture on the previous page).

To start the system, click the ‘Start System’ button; you should hear a click emitted by the motors. Then switch the button to ‘ON’ in the ‘move to position’ window and set the desired horizontal and vertical values you wish to position the frame to (click on the box, enter the wished value and press ‘return’ key). To start rotating the frame, click on the ‘Start’ button.

To see which way the mirrors will rotate when increasing or decreasing the horizontal and/or vertical values, refer to the sketches in the centre of the Graphical Interface. To stop the motors while the frame is moving, click on the ‘Stop System’ button, located next to the ‘Start System’ one.

In the lab, the reference positions, also called zero positions, (that is when all frames are flat) were recorded as follow: Motor 1: 331.5 (horizontal/motor1) ; Motor 2: 353.15 (vertical/motor2).

### Additional commands

To control the system from the terminal, go to ‘~/EPICS/base/bin/linux’ to see the list of commands to change variables from EPICS in a terminal.

Useful commands to run while EPICS is running on a terminal (‘../../bin/linux86\_64/modbusApp (or snmp) cbm.cmd’, command in a terminal from ‘/Modbus\_cbm\_2014/iocBoot/iocTest’ or from ‘/snmp\_2014/iocBoot/iocsnmp’):

- ‘dbl’ (database list) command to see every current variables of the system
- ‘dbpr’ VAR\_NAME: current position/status of the variable
- ‘dbpf’ VAR\_NAME 1/0: set new value for the variable VAR\_NAME

To change values from the CSS program, one needs to go to the ‘~/EPICS/modules/synApps\_5\_7/support/Modbus\_cbm\_2014/modbusApp/Db’ folder and edit the changes inside the cbm\_2014.substitutions file. Concerning the logical code, a detailed description of the functions is available at this webpage: <http://www.aps.anl.gov/epics/EpicsDocumentation/AppDevManuals/RecordRef/Recordref-14.html>. Once the changes are done, save the file and go to previous directory and call ‘make’ to apply the changes on the ‘cbm\_2014.db’ file. The ‘.db’ file should have the same name as the ‘.substitutions’ one. There are many templates inside the ‘.substitutions’ file, which can be edited, such as the ‘ao2.template’ (send command value to TwinCAT) and the ‘ai2.template’ (read value from TwinCAT) blocks. These templates are defined inside the ‘Db/’ folder.

For more information the Beckhoff and EPICS websites can be consulted. The possibility to modify a CSS program is also included but not explained here.

## A.4 Run high voltage via EPICS

First connect the router and High Voltage using Ethernet cables. Then turn on the main switch of the High Voltage crate. The machine employed was a Wiener crate from ISEG.

Open a new terminal on the Linux workstation. Go to the directory ‘~/EPICS’. In this directory, there is a hidden file, called ‘.profile’. To set the environment variables, enter the command: ‘source .profile’ in the terminal.

Then change the IP address of the HV system on EPICS. Go to the directory ‘~/EPICS/modules/synApps\_5\_7/support/snmp\_2014/iocBoot/iocsnmp/’ and open the ‘cbm.cmd’ file with an editor (using for example ‘vi cbm.cmd’).

At the line ‘dbLoadRecords’, change the IP address to the desired value. Current set-up: dbLoadRecords (‘db/my\_iseg2.db’,‘HOST=10.160.0.50’).

After that, go to the ‘~/EPICS/modules/synApps\_5\_7/support/snmp\_2014/iocBoot/iocsnmp/’ directory and enter the command: ‘../../bin/linux-x86\_64/snmp cbm.cmd’. The connection via EPICS to the windows system should be settled.

Finally, start the CSS graphic user interface. Go to the ‘~/Desktop/CSS\_EPICS\_3.1.2/’ folder and execute the program, by double clicking on the script, called ‘start\_css’.

If needed, click ‘Browse’ to select the wanted workspace: ‘~/CSS-Workspace/SlowControlPanel’. Select the ‘CBM\_RICH\_HV\_2014.opi’ file, which is located in the ‘CBM\_RICH\_2014’ folder.

Then switch to run mode (go to the window tab, choose open perspective – other and select ‘OPI Runtime’) to open a window analogous to Figure A.13.

Start the system by clicking on the ‘Main Switch’ button. To modify a value, enter a number in the window (under the ‘Set Voltage’ column), then on the right side of the window (not shown here), turn the button ON to increase the voltage.

To modify the fan speed, change the value in the ‘Set’ box (under the ‘Fan Speed Control’ indicator). Put the wished value with the numerical pad and press the ‘return’ key.

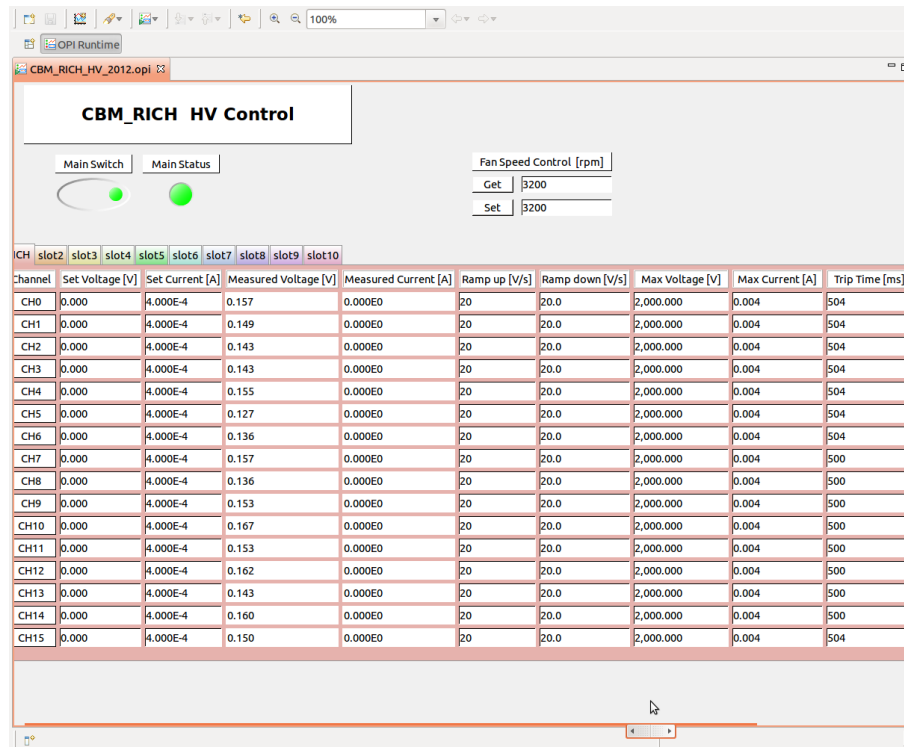


Figure A.13: EPICS high voltage GUI.



# Appendix B

## Complements to Chapter 5

### B.1 Reconstruction of mirror rotation for a 0.1 mrad misalignment

In Section 5.4.1, it has been shown, that the minimal detected misalignment with reconstruction errors within 20% of the applied rotation is 0.3 mrad for a rotation around the horizontal axis and 0.4 mrad for a rotation around the vertical one.

For lower mirror rotations, a sinusoid is still observed and can still be fitted to calculate the corresponding misalignment. However the errors obtained in these cases are such, that the technique is not reliable any more.

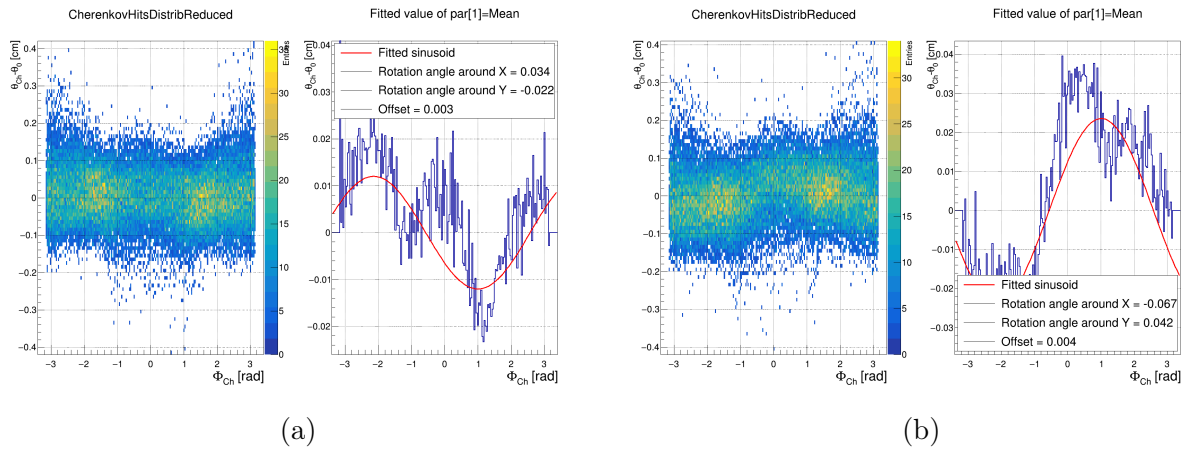


Figure B.1: Reconstructed misalignments for a 0.1 mrad rotation of the mirror tile 5\_3 around its horizontal (left) and vertical (right) axes. For the horizontal rotation, reconstructed misalignments of 0.034 mrad around the horizontal axis and -0.022 mrad around the vertical axis were obtained. In the vertical rotation, reconstructed misalignments of -0.067 mrad for the horizontal axis and 0.042 mrad for the vertical one were calculated.

For these results, 2,500 events, each containing one electron sent towards the mirror tile labelled 5\_3 were simulated. The mirror tile was previously rotated by 0.1 mrad either around its horizontal, or around its vertical axis. The following CbmRoot set-up was employed: Magnet (version 15a, with the magnetic field map v12b), STS (version 16x), RICH (version 17a\_1e) and beam pipe (version 16c\_1e).

Figure B.1a illustrates the sinusoid obtained and fitted in the case of a horizontal rotation. A reconstructed mirror rotation of 0.034 mrad was obtained, which corresponds to a reconstruction error of 68% of the applied rotation. In addition, the calculated rotation around the vertical axis amounts to -0.022. This shows that, for such small misalignments, the reconstructed values are equally distributed on both axes by the software.

Figure B.1b shows a similar behaviour for a vertical rotation of 0.1 mrad, with an even bigger reconstruction error, amounting to 72% of the applied rotation. On the non rotated axis, a misalignment of -0.067 mrad is reconstructed by the software, which is higher than the calculated rotation of 0.042 mrad for the rotated axis.

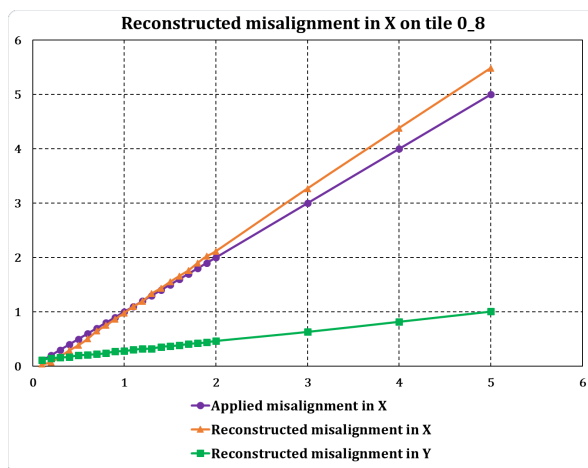
## B.2 Calculation of mirror rotations with the software for mirror tile 0\_8

Analogously to the study presented in Section 5.4.2, results showing the mirror rotation calculations for the outer mirror tile labelled 0\_8 are shown on Figure B.2. Mirror rotations range from 0.1 mrad up to 5 mrad and the set-up employed for this study is identical to the one detailed in the afore-mentioned section.

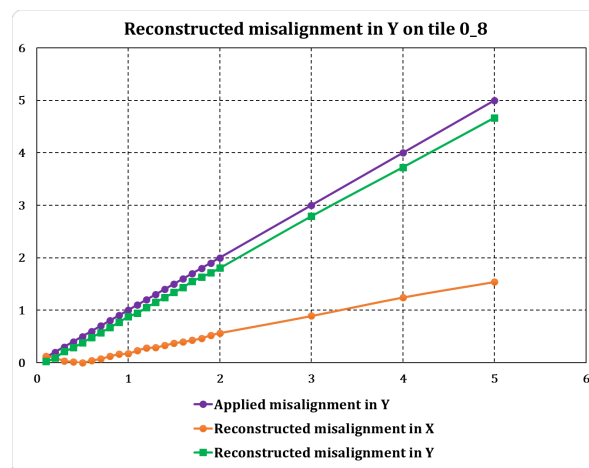
For mirror rotations applied on the X axis, errors in the misalignment reconstruction on the rotated axis amount to 8.9% of the applied rotation value for rotations ranging between 0.3 and 5 mrad. Rotations on the non-rotated Y axis are detected and amount in average to 27.4% of the applied rotation value in the range between 0.4 and 5 mrad. The errors obtained for rotations and misalignment reconstruction on the horizontal axis are illustrated in yellow on Figure B.2d.

For rotations around the Y axis, errors in the calculation of mirror rotation amount to 13.8% of the applied rotation value in average in the rotation range of 0.3 mrad up to 5 mrad. On the non-rotated axis X and for the same mirror rotation range, the detected rotations amount to 20.2% in average. The errors obtained for rotations and misalignment reconstruction on the vertical axis are shown in purple on Figure B.2d.

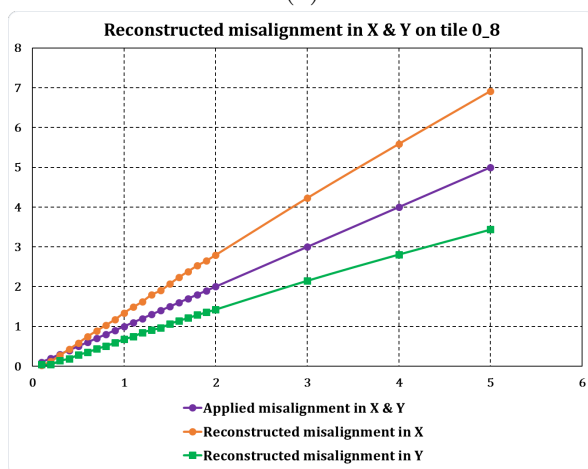
For a simultaneous mirror rotation on both axes, errors in the misalignment reconstruction amount in average to 32.2% and 33.9% of the applied rotation for the X and Y axis, respectively. The mirror rotation range spans from 0.3 mrad up to 5 mrad. These errors are illustrated in Figure B.2e.



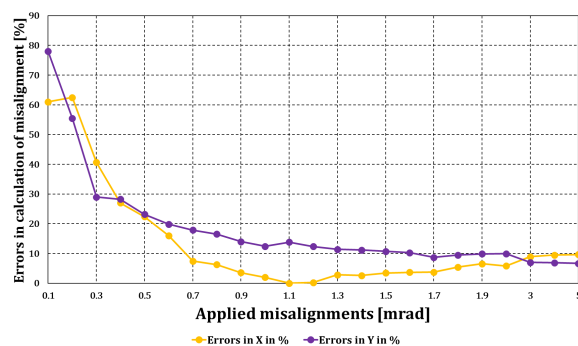
(a)



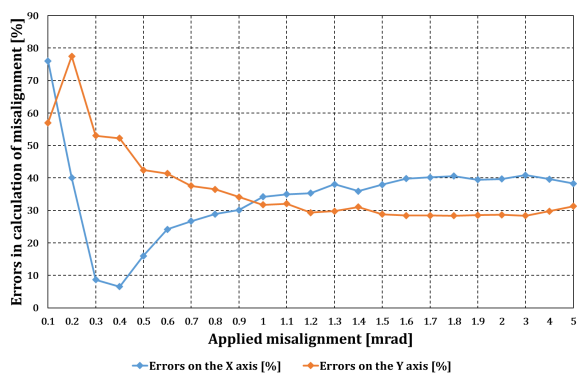
(b)



(c)



(d)



(e)

Calculations of mirror rotations with the software technique from Chapter 5 for the mirror tile 0\_8. Applied and reconstructed misalignments for rotations around the horizontal and vertical axes are shown (a, b and c). The applied misalignment is coloured in purple, the reconstructed mirror rotation around the horizontal axis in orange and the reconstructed mirror rotation around the vertical axis in green. The corresponding errors in calculation of misalignments for single axis rotations (d) and for simultaneous rotations (e) are illustrated as well. For single axis rotations, the errors on the X axis are represented in yellow and the errors on the Y axis in purple. For simultaneous rotations, the errors on the X axis are in blue and the errors on the Y axis in orange.

Figure B.2



# Bibliography

- [1] John Dalton. *Memoirs of the Literary and Philosophical Society of Manchester*. Vol. ser.2:v.1 (1805). <https://www.bio-diversitylibrary.org/bibliography/50808>. Manchester :The Society, 1805, pp. 271–287. URL: <https://www.biodiversitylibrary.org/item/20167>.
- [2] J.J. Thomson F.R.S. “XXIV. On the structure of the atom: an investigation of the stability and periods of oscillation of a number of corpuscles arranged at equal intervals around the circumference of a circle; with application of the results to the theory of atomic structure”. In: *Philosophical Magazine* 7.39 (1904), pp. 237–265. DOI: 10.1080/14786440409463107. URL: <http://dx.doi.org/10.1080/14786440409463107>.
- [3] Professor E. Rutherford F.R.S. “LXXIX. The scattering of  $\alpha$  and  $\beta$  particles by matter and the structure of the atom”. In: *Philosophical Magazine* 21.125 (1911), pp. 669–688. DOI: 10.1080/14786440508637080. URL: <http://dx.doi.org/10.1080/14786440508637080>.
- [4] N. Bohr Dr. phil. “I. On the constitution of atoms and molecules”. In: *Philosophical Magazine* 26.151 (1913), pp. 1–25. DOI: 10.1080/14786441308634955. URL: <http://dx.doi.org/10.1080/14786441308634955>.
- [5] N. Bohr Dr. phil. “XXXVII. On the constitution of atoms and molecules”. In: *Philosophical Magazine* 26.153 (1913), pp. 476–502. DOI: 10.1080/14786441308634993. URL: <http://dx.doi.org/10.1080/14786441308634993>.
- [6] N. Bohr. “LXXIII. On the constitution of atoms and molecules”. In: *Philosophical Magazine* 26.155 (1913), pp. 857–875. DOI: 10.1080/14786441308635031. URL: <http://dx.doi.org/10.1080/14786441308635031>.
- [7] J. Chadwick. “Possible Existence of a Neutron”. In: *Nature* 129 (3252 1932), p. 312. DOI: 10.1038/129312a0. URL: <http://adsabs.harvard.edu/abs/1932Natur.129Q.312C>.
- [8] J. Chadwick. “Bakerian Lecture. The Neutron”. In: *Proceedings of the Royal Society of London A: Mathematical, Physical and Engineering Sciences* 142.846 (1933), pp. 1–25. ISSN: 0950-1207. DOI: 10.1098/rspa.1933.0152. URL: <http://rspa.royalsocietypublishing.org/content/142/846/1>.
- [9] P. A. M. Dirac. “The Quantum Theory of the Electron”. In: *Proceedings of the Royal Society of London A: Mathematical, Physical and Engineering Sciences* 117.778 (1928), pp. 610–624. ISSN: 0950-1207. DOI: 10.1098/rspa.1928.0023. URL: <http://rspa.royalsocietypublishing.org/content/117/778/610>.
- [10] David J Griffiths. *Introduction to elementary particles; 2nd rev. version*. Physics textbook. New York, NY: Wiley, 2008. URL: <https://cds.cern.ch/record/111880>.
- [11] G Zweig. *An  $SU_3$  model for strong interaction symmetry and its breaking; Version 1*. Tech. rep. CERN-TH-401. Geneva: CERN, 1964. URL: <https://cds.cern.ch/record/352337>.
- [12] M. Gell-Mann. “A schematic model of baryons and mesons”. In: *Physics Letters* 8.3 (1964), pp. 214–215. ISSN: 0031-9163. DOI: [https://doi.org/10.1016/S0031-9163\(64\)92001-3](https://doi.org/10.1016/S0031-9163(64)92001-3). URL: <http://www.sciencedirect.com/science/article/pii/S0031916364920013>.
- [13] O. W. Greenberg. “Spin and Unitary-Spin Independence in a Paraquark Model of Baryons and Mesons”. In: *Phys. Rev. Lett.* 13 (20 1964), pp. 598–602. DOI: 10.1103/PhysRevLett.13.598. URL: <https://link.aps.org/doi/10.1103/PhysRevLett.13.598>.

- [14] J. J. Aubert et al. “Experimental Observation of a Heavy Particle  $J$ ”. In: *Phys. Rev. Lett.* 33 (23 1974), pp. 1404–1406. DOI: 10.1103/PhysRevLett.33.1404. URL: <https://link.aps.org/doi/10.1103/PhysRevLett.33.1404>.
- [15] J. E. Augustin et al. “Discovery of a Narrow Resonance in  $e^+e^-$  Annihilation”. In: *Phys. Rev. Lett.* 33 (23 1974), pp. 1406–1408. DOI: 10.1103/PhysRevLett.33.1406. URL: <https://link.aps.org/doi/10.1103/PhysRevLett.33.1406>.
- [16] S. W. Herb et al. “Observation of a Dimuon Resonance at 9.5 GeV in 400-GeV Proton-Nucleus Collisions”. In: *Phys. Rev. Lett.* 39 (5 1977), pp. 252–255. DOI: 10.1103/PhysRevLett.39.252. URL: <https://link.aps.org/doi/10.1103/PhysRevLett.39.252>.
- [17] C. M. G. Lattes et al. “PROCESSES INVOLVING CHARGED MESONS”. In: *Nature* 159 (1947). [42(1947)], pp. 694–697. DOI: 10.1038/159694a0. URL: <https://www.nature.com/articles/159694a0.pdf>.
- [18] R. Brown et al. “Observations With Electron Sensitive Plates Exposed to Cosmic Radiation”. In: *Nature* 163 (1949). [223(1949)], p. 82. DOI: 10.1038/163082a0. URL: <https://www.nature.com/articles/163082a0.pdf>.
- [19] F. Reines and C. L. Cowan. “Detection of the Free Neutrino”. In: *Phys. Rev.* 92 (3 1953), pp. 830–831. DOI: 10.1103/PhysRev.92.830. URL: <https://link.aps.org/doi/10.1103/PhysRev.92.830>.
- [20] M. Planck. *Planck’s Original papers in quantum physics / annotated by Hans Kangro ; translated by D. ter Haar and Stephen G. Brush*. English. German and English ed. Taylor and Francis London, 1972, viii, 60 p. ; ISBN: 0850660602. URL: <http://nla.gov.au/nla.cat-vn390274>.
- [21] Albert Einstein. “Concerning an heuristic point of view toward the emission and transformation of light”. In: *American Journal of Physics* 33.5 (1965), p. 367. URL: <http://users.isy.liu.se/en/icg/jalar/kurser/QF/references/Einstein1905b.pdf>.
- [22] Arthur H. Compton. “A Quantum Theory of the Scattering of X-rays by Light Elements”. In: *Phys. Rev.* 21 (5 1923), pp. 483–502. DOI: 10.1103/PhysRev.21.483. URL: <https://link.aps.org/doi/10.1103/PhysRev.21.483>.
- [23] Harald Fritzsch and Karl-Heinz Streng. “Three-jet structures in the decay of heavy quarkonium states”. In: *Physics Letters B* 74.1 (1978), pp. 90–94. ISSN: 0370-2693. DOI: [https://doi.org/10.1016/0370-2693\(78\)90067-9](https://doi.org/10.1016/0370-2693(78)90067-9). URL: <http://www.sciencedirect.com/science/article/pii/0370269378900679>.
- [24] Berger Ch. et al. PLUTO Collab. “Evidence for gluon bremsstrahlung in  $e^+e^-$  annihilations at high energies”. In: *Physics Letters B* 86.3 (1979), pp. 418–425. ISSN: 0370-2693. DOI: [https://doi.org/10.1016/0370-2693\(79\)90869-4](https://doi.org/10.1016/0370-2693(79)90869-4). URL: <http://www.sciencedirect.com/science/article/pii/0370269379908694>.
- [25] Barber D. P. et al. MARK-J Collab. “Discovery of Three-Jet Events and a Test of Quantum Chromodynamics at PETRA”. In: *Phys. Rev. Lett.* 43 (12 1979), pp. 830–833. DOI: 10.1103/PhysRevLett.43.830. URL: <https://link.aps.org/doi/10.1103/PhysRevLett.43.830>.
- [26] Brandelik R. et al. TASSO Collab. “Evidence for planar events in  $e^+e^-$  annihilation at high energies”. In: *Physics Letters B* 86.2 (1979), pp. 243–249. ISSN: 0370-2693. DOI: [https://doi.org/10.1016/0370-2693\(79\)90830-X](https://doi.org/10.1016/0370-2693(79)90830-X). URL: <http://www.sciencedirect.com/science/article/pii/037026937990830X>.
- [27] Arnison G. et al. UA1 Collab. “Experimental observation of isolated large transverse energy electrons with associated missing energy at  $s=540$  GeV”. In: *Physics Letters B* 122.1 (1983), pp. 103–116. ISSN: 0370-2693. DOI: [https://doi.org/10.1016/0370-2693\(83\)91177-2](https://doi.org/10.1016/0370-2693(83)91177-2). URL: <http://www.sciencedirect.com/science/article/pii/0370269383911772>.
- [28] Arnison G. et al. UA1 Collab. “Experimental observation of lepton pairs of invariant mass around 95 GeV/c<sup>2</sup> at the CERN SPS collider”. In: *Physics Letters B* 126.5 (1983), pp. 398–410. ISSN: 0370-2693. DOI: [https://doi.org/10.1016/0370-2693\(83\)90188-0](https://doi.org/10.1016/0370-2693(83)90188-0). URL: <http://www.sciencedirect.com/science/article/pii/0370269383901880>.

- [29] Bagnaia P. et al. UA2 Collab. “Evidence for  $Z_0 \rightarrow e^+e^-$  at the CERN pp collider”. In: *Physics Letters B* 129.1 (1983), pp. 130–140. ISSN: 0370-2693. DOI: [https://doi.org/10.1016/0370-2693\(83\)90744-X](https://doi.org/10.1016/0370-2693(83)90744-X). URL: <http://www.sciencedirect.com/science/article/pii/037026938390744X>.
- [30] LIGO Collab. and Abbott B. P. et al. Virgo Collab. “Observation of Gravitational Waves from a Binary Black Hole Merger”. In: *Phys. Rev. Lett.* 116 (6 2016), p. 061102. DOI: 10.1103/PhysRevLett.116.061102. URL: <https://link.aps.org/doi/10.1103/PhysRevLett.116.061102>.
- [31] CMS Collab. “Observation of a new boson at a mass of 125 GeV with the CMS experiment at the LHC”. In: *Physics Letters B* 716.1 (2012), pp. 30–61. ISSN: 0370-2693. DOI: <https://doi.org/10.1016/j.physletb.2012.08.021>. URL: <http://www.sciencedirect.com/science/article/pii/S0370269312008581>.
- [32] ATLAS Collab. “Observation of a new particle in the search for the Standard Model Higgs boson with the ATLAS detector at the LHC”. In: *Physics Letters B* 716.1 (2012), pp. 1–29. ISSN: 0370-2693. DOI: <https://doi.org/10.1016/j.physletb.2012.08.020>. URL: <http://www.sciencedirect.com/science/article/pii/S037026931200857X>.
- [33] N. Cabibbo and G. Parisi. “Exponential hadronic spectrum and quark liberation”. In: *Physics Letters B* 59.1 (1975), pp. 67–69. ISSN: 0370-2693. DOI: [https://doi.org/10.1016/0370-2693\(75\)90158-6](https://doi.org/10.1016/0370-2693(75)90158-6). URL: <http://www.sciencedirect.com/science/article/pii/0370269375901586>.
- [34] Kenji Fukushima and Tetsuo Hatsuda. “The phase diagram of dense QCD”. In: *Reports on Progress in Physics* 74.1 (2011), p. 014001. URL: <http://stacks.iop.org/0034-4885/74/i=1/a=014001>.
- [35] R. Hagedorn. “Statistical thermodynamics of strong interactions at high-energies”. In: *Nuovo Cim. Suppl.* 3 (1965), pp. 147–186. URL: <http://cds.cern.ch/record/346206/files/CM-P00057114.pdf>.
- [36] Hans-Ake Gustafsson. “LHC experiments”. In: *Nuclear Physics A* 774. Supplement C (2006). QUARK MATTER 2005, pp. 361–368. ISSN: 0375-9474. DOI: <https://doi.org/10.1016/j.nuclphysa.2006.06.056>. URL: <http://www.sciencedirect.com/science/article/pii/S0375947406002752>.
- [37] T.S. Virdee. “The LHC project: The accelerator and the experiments”. In: *Nuclear Instruments and Methods in Physics Research Section A: Accelerators, Spectrometers, Detectors and Associated Equipment* 623.1 (2010). 1st International Conference on Technology and Instrumentation in Particle Physics, pp. 1–10. ISSN: 0168-9002. DOI: <https://doi.org/10.1016/j.nima.2010.02.142>. URL: <http://www.sciencedirect.com/science/article/pii/S0168900210004092>.
- [38] M. Harrison, T. Ludlam, and S. Ozaki. “RHIC project overview”. In: *Nuclear Instruments and Methods in Physics Research Section A: Accelerators, Spectrometers, Detectors and Associated Equipment* 499.2 (2003). The Relativistic Heavy Ion Collider Project: RHIC and its Detectors, pp. 235–244. ISSN: 0168-9002. DOI: [https://doi.org/10.1016/S0168-9002\(02\)01937-X](https://doi.org/10.1016/S0168-9002(02)01937-X). URL: <http://www.sciencedirect.com/science/article/pii/S016890020201937X>.
- [39] Y. Aoki et al. “The Order of the quantum chromodynamics transition predicted by the standard model of particle physics”. In: *Nature* 443 (2006), pp. 675–678. DOI: 10.1038/nature05120. URL: <https://arxiv.org/pdf/hep-lat/0611014.pdf>.
- [40] J. Stachel et al. “Confronting LHC data with the statistical hadronization model”. In: *J. Phys. Conf. Ser.* 509 (2014), p. 012019. DOI: 10.1088/1742-6596/509/1/012019. URL: <https://arxiv.org/pdf/1311.4662.pdf>.
- [41] N. Armesto et al. “Heavy Ion Collisions at the LHC - Last Call for Predictions”. In: *J. Phys.* G35 (2008), p. 054001. DOI: 10.1088/0954-3899/35/5/054001. URL: <https://arxiv.org/pdf/0711.0974.pdf>.
- [42] M. Bluhm et al. “Determination of freeze-out conditions from fluctuation observables measured at RHIC”. In: *Nuclear Physics A* 931. Supplement C (2014). QUARK MATTER 2014, pp. 814–819. ISSN: 0375-9474. DOI: <https://doi.org/10.1016/j.nuclphysa.2014.08.016>. URL: <http://www.sciencedirect.com/science/article/pii/S0375947414002656>.

- [43] Francesco Becattini et al. “Hadron Formation in Relativistic Nuclear Collisions and the QCD Phase Diagram”. In: *Phys. Rev. Lett.* 111 (8 2013), p. 082302. DOI: 10.1103/PhysRevLett.111.082302. URL: <https://link.aps.org/doi/10.1103/PhysRevLett.111.082302>.
- [44] Alejandro Ayala et al. “The effective QCD phase diagram and the critical end point”. In: *Nuclear Physics B* 897.Supplement C (2015), pp. 77–86. ISSN: 0550-3213. DOI: <https://doi.org/10.1016/j.nuclphysb.2015.05.014>. URL: <http://www.sciencedirect.com/science/article/pii/S0550321315001741>.
- [45] Alexander Schmah. “Highlights of the beam energy scan from STAR”. In: *Central European Journal of Physics* 10.6 (2012), pp. 1238–1241. ISSN: 1644-3608. DOI: 10.2478/s11534-012-0149-1. URL: <https://doi.org/10.2478/s11534-012-0149-1>.
- [46] Lokesh Kumar. “STAR Results from the RHIC Beam Energy Scan-I”. In: *Nucl. Phys.* A904-905 (2013), pp. 256c–263c. DOI: 10.1016/j.nuclphysa.2013.01.070. URL: <https://arxiv.org/pdf/1211.1350.pdf>.
- [47] Yoshimasa Hidaka, Larry D. McLerran, and Robert D. Pisarski. “Baryons and the phase diagram for a large number of colors and flavors”. In: *Nuclear Physics A* 808.1 (2008), pp. 117–123. ISSN: 0375-9474. DOI: <https://doi.org/10.1016/j.nuclphysa.2008.05.009>. URL: <http://www.sciencedirect.com/science/article/pii/S0375947408005630>.
- [48] Kouji Kashiwa et al. “Critical endpoint in the Polyakov-loop extended NJL model”. In: *Physics Letters B* 662.1 (2008), pp. 26–32. ISSN: 0370-2693. DOI: <https://doi.org/10.1016/j.physletb.2008.01.075>. URL: <http://www.sciencedirect.com/science/article/pii/S037026930800258X>.
- [49] Bengt Friman et al. *The CBM physics book: Compressed baryonic matter in laboratory experiments*. Vol. 814. 2011, pp. 1–980. DOI: 10.1007/978-3-642-13293-3. URL: [https://link.springer.com/chapter/10.1007/978-3-642-13293-3\\_4](https://link.springer.com/chapter/10.1007/978-3-642-13293-3_4).
- [50] ALEPH Collaboration. “Measurement of the spectral functions of axial-vector hadronic  $\tau$  decays and determination of  $\alpha_s(M_\tau^2)$ ”. In: *Eur. Phys. J. C* 4.CERN-EP-98-012 (1998), 409–431. 44 p. URL: <http://cds.cern.ch/record/345764>.
- [51] Masayasu Harada and Chihiro Sasaki. “Dropping rho and A(1) meson masses at the chiral phase transition in the generalized hidden local symmetry”. In: (2007), pp. 109–115. DOI: 10.1142/9789812790750\_0011. URL: <https://arxiv.org/pdf/hep-ph/0703238.pdf>.
- [52] Larry McLerran, Krzysztof Redlich, and Chihiro Sasaki. “Quarkyonic matter and chiral symmetry breaking”. In: *Nuclear Physics A* 824.1 (2009), pp. 86–100. ISSN: 0375-9474. DOI: <https://doi.org/10.1016/j.nuclphysa.2009.04.001>. URL: <http://www.sciencedirect.com/science/article/pii/S0375947409002036>.
- [53] Larry McLerran and Robert D. Pisarski. “Phases of dense quarks at large  $N_c$ ”. In: *Nuclear Physics A* 796.1 (2007), pp. 83–100. ISSN: 0375-9474. DOI: <https://doi.org/10.1016/j.nuclphysa.2007.08.013>. URL: <http://www.sciencedirect.com/science/article/pii/S0375947407006823>.
- [54] A. Andronic et al. “Hadron Production in Ultra-relativistic Nuclear Collisions: Quarkyonic Matter and a Triple Point in the Phase Diagram of QCD”. In: *Nucl. Phys.* A837 (2010), pp. 65–86. DOI: 10.1016/j.nuclphysa.2010.02.005. URL: <https://arxiv.org/pdf/0911.4806.pdf>.
- [55] David Blaschke et al. “Topical issue on Exploring Strongly Interacting Matter at High Densities - NICA White Paper”. In: *The European Physical Journal A* 52.8 (2016), p. 267. ISSN: 1434-601X. DOI: 10.1140/epja/i2016-16267-x. URL: <https://doi.org/10.1140/epja/i2016-16267-x>.
- [56] T. et al. for the CBM collaboration Ablyazimov. “Challenges in QCD matter physics –The scientific programme of the Compressed Baryonic Matter experiment at FAIR”. In: *The European Physical Journal A* 53.3 (2017), p. 60. ISSN: 1434-601X. DOI: 10.1140/epja/i2017-12248-y. URL: <https://doi.org/10.1140/epja/i2017-12248-y>.
- [57] Henning Heiselberg and Morten Hjorth-Jensen. “Phases of dense matter in neutron stars”. In: *Phys. Rept.* 328 (2000), pp. 237–327. DOI: 10.1016/S0370-1573(99)00110-6. URL: <https://arxiv.org/pdf/nucl-th/9902033.pdf>.

- [58] Stanley Humphries. *Principles of charged particle acceleration*. 1999, pp. 1–561. ISBN: 0-471-87878-2. URL: [http://www.feldp.com/documents/ParticleAccelerators\\_9927.pdf](http://www.feldp.com/documents/ParticleAccelerators_9927.pdf).
- [59] Michael A. Lisa. “Size matters: spacetime geometry in subatomic collisions”. In: (2004), pp. 1–22. URL: <https://www.physics.ohio-state.edu/~lisa/SizeMattersSambamurti2004.pdf>.
- [60] Ralf Rapp and Hendrik van Hees. “Thermal dileptons as fireball thermometer and chronometer”. In: *Physics Letters B* 753 (2016), pp. 586–590. ISSN: 0370-2693. DOI: <https://doi.org/10.1016/j.physletb.2015.12.065>. URL: <http://www.sciencedirect.com/science/article/pii/S0370269315010138>.
- [61] L. D. McLerran and T. Toimela. “Photon and dilepton emission from the quark-gluon plasma: Some general considerations”. In: *Phys. Rev. D* 31 (3 1985), pp. 545–563. DOI: 10.1103/PhysRevD.31.545. URL: <https://link.aps.org/doi/10.1103/PhysRevD.31.545>.
- [62] Galatyuk, Tetyana et al. “Thermal dileptons from coarse-grained transport as fireball probes at SIS energies”. In: *Eur. Phys. J. A* 52.5 (2016), p. 131. DOI: 10.1140/epja/i2016-16131-1. URL: <https://doi.org/10.1140/epja/i2016-16131-1>.
- [63] Patrick Sellheim. “Reconstruction of the low-mass dielectron signal in 1.23A GeV Au+Au collisions”. PhD thesis. 2017, pp. X, 212.
- [64] Giorgio Torrieri, Sascha Vogel, and Bjørn Bäuchle. “Photon Signals from Quarkyonic Matter”. In: *Phys. Rev. Lett.* 111.1 (2013), p. 012301. DOI: 10.1103/PhysRevLett.111.012301. arXiv: 1302.1119 [nucl-th].
- [65] Elena Lebedeva. “Figures taken from a talk given at the 27<sup>th</sup> CBM collaboration meeting”. In: (2016), p. 18.
- [66] S. Voloshin and Y. Zhang. “Flow study in relativistic nuclear collisions by Fourier expansion of Azimuthal particle distributions”. In: *Z. Phys. C* 70 (1996), pp. 665–672. DOI: 10.1007/s002880050141. arXiv: hep-ph/9407282 [hep-ph].
- [67] C. Alt et al. “Directed and elliptic flow of charged pions and protons in Pb + Pb collisions at 40A and 158A GeV”. In: *Phys. Rev. C* 68 (3 2003), p. 034903. DOI: 10.1103/PhysRevC.68.034903. URL: <https://link.aps.org/doi/10.1103/PhysRevC.68.034903>.
- [68] V. Khachatryan et al. “Observation of long-range, near-side angular correlations in proton-proton collisions at the LHC”. In: *Journal of High Energy Physics* 2010.9 (2010), p. 91. ISSN: 1029-8479. DOI: 10.1007/JHEP09(2010)091. URL: [https://doi.org/10.1007/JHEP09\(2010\)091](https://doi.org/10.1007/JHEP09(2010)091).
- [69] Adrian Dumitru et al. “The Ridge in proton-proton collisions at the LHC”. In: *Phys. Lett.* B697 (2011), pp. 21–25. DOI: 10.1016/j.physletb.2011.01.024. arXiv: 1009.5295 [hep-ph].
- [70] Jochen Thäder. “Higher Moments of Net-Particle Multiplicity Distributions”. In: *Nuclear Physics A* 956 (2016). The XXV International Conference on Ultrarelativistic Nucleus-Nucleus Collisions: Quark Matter 2015, pp. 320–323. ISSN: 0375-9474. DOI: <https://doi.org/10.1016/j.nuclphysa.2016.02.047>. URL: <http://www.sciencedirect.com/science/article/pii/S0375947416001342>.
- [71] A. Adare et al. “ $J/\psi$  Production versus Centrality, Transverse Momentum, and Rapidity in Au+Au Collisions at  $\sqrt{s_{NN}} = 200$  GeV”. In: *Phys. Rev. Lett.* 98 (23 2007), p. 232301. DOI: 10.1103/PhysRevLett.98.232301. URL: <https://link.aps.org/doi/10.1103/PhysRevLett.98.232301>.
- [72] A. Andronic et al. “Production of light nuclei, hypernuclei and their antiparticles in relativistic nuclear collisions”. In: *Physics Letters B* 697.3 (2011), pp. 203–207. ISSN: 0370-2693. DOI: <https://doi.org/10.1016/j.physletb.2011.01.053>. URL: <http://www.sciencedirect.com/science/article/pii/S0370269311001006>.
- [73] H. Stoecker and C. Sturm. “The FAIR start”. In: *Nuclear Physics A* 855.1 (2011). Proceedings of the 4th International Conference on Hard and Electromagnetic Probes of High-Energy Nuclear Collisions – HP2010, pp. 506–509. ISSN: 0375-9474. DOI: <https://doi.org/10.1016/j.nuclphysa.2011.02.117>. URL: <http://www.sciencedirect.com/science/article/pii/S0375947411002041>.

- [74] FAIR GmbH and GSI. *[MSV] Green Paper, The Modularized Start Version : FAIR - Facility for Antiproton and Ion Research*. Darmstadt: FAIR, 2009, 19p. URL: <http://repository.gsi.de/record/54094>.
- [75] N. Herrmann. “Talk given at the 30<sup>th</sup> CBM collaboration meeting”. In: (September 2017).
- [76] C. Sturm, B. Sharkov, and H. Stöcker. “1, 2, 3 ... FAIR !” In: *Nuclear Physics A* 834.1 (2010). The 10th International Conference on Nucleus-Nucleus Collisions (NN2009), pp. 682c–687c. ISSN: 0375-9474. DOI: <https://doi.org/10.1016/j.nuclphysa.2010.01.124>. URL: <http://www.sciencedirect.com/science/article/pii/S0375947410001259>.
- [77] “FAIR website”. In: (2019). URL: <http://www.fair-center.eu/>.
- [78] Th. et al. for the APPA Collaboration Stöhlker. “APPA at FAIR: From fundamental to applied research”. In: *Nuclear Instruments and Methods in Physics Research Section B: Beam Interactions with Materials and Atoms* 365 (2015). Swift Heavy Ions in Matter, 18 – 21 May, 2015, Darmstadt, Germany, pp. 680–685. ISSN: 0168-583X. DOI: <https://doi.org/10.1016/j.nimb.2015.07.077>. URL: <http://www.sciencedirect.com/science/article/pii/S0168583X15006552>.
- [79] G. et al. for the HADES Collaboration Agakichiev. “The high-acceptance dielectron spectrometer HADES”. In: *Eur. Phys. J. A* 41.2 (2009), pp. 243–277. DOI: 10.1140/epja/i2009-10807-5. URL: <https://doi.org/10.1140/epja/i2009-10807-5>.
- [80] Thomas Nilsson and for the NUSTAR collaboration. “The NUSTAR project at FAIR”. In: *Physica Scripta* 2015.T166 (2015), p. 014070. URL: <http://stacks.iop.org/1402-4896/2015/i=T166/a=014070>.
- [81] J. Gerl, A. Herlert, and T. for the NUSTAR Collaboration Nilsson. “NUSTAR Progress Report”. In: (2012). URL: [http://www.fair-center.eu/fileadmin/fair/experiments/NUSTAR/Pdf/NUSTAR\\_ProgressReport\\_SC\\_Nov2012\\_final.pdf](http://www.fair-center.eu/fileadmin/fair/experiments/NUSTAR/Pdf/NUSTAR_ProgressReport_SC_Nov2012_final.pdf).
- [82] M. F. M. et al. Lutz. *Physics Performance Report for PANDA: Strong Interaction Studies with Antiprotons*. 2009. URL: <https://arxiv.org/pdf/0903.3905.pdf>.
- [83] P. Senger. “Talk given at the 30<sup>th</sup> CBM collaboration meeting”. In: (September 2017).
- [84] “FAIR website”. In: (2019). URL: [https://fair-center.eu/fileadmin/fair/experiments/CBM/documents/CBM\\_flyer\\_english.pdf](https://fair-center.eu/fileadmin/fair/experiments/CBM/documents/CBM_flyer_english.pdf).
- [85] Johann M. Heuser. “The Compressed Baryonic Matter Experiment at FAIR”. In: *Nuclear Physics A* 904-905 (2013). The Quark Matter 2012, pp. 941c–944c. ISSN: 0375-9474. DOI: <https://doi.org/10.1016/j.nuclphysa.2013.02.170>. URL: <http://www.sciencedirect.com/science/article/pii/S0375947413002960>.
- [86] Ilya Selyuzhenkov and Alberica Toia, eds. *CBM Progress Report 2016*. Literaturangaben. Darmstadt: GSI, 2017, 223 Seiten : Illustrationen, grafische Darstellungen. ISBN: 978-3-9815227-4-7. URL: <http://repository.gsi.de/record/201318>.
- [87] “GSI website”. In: (2019). URL: <https://www.gsi.de/work/forschung/cbmnqm/cbm.html>.
- [88] Alexander Malakhov and Alexey Shabunov, eds. *Technical Design Report for the CBM Superconducting Dipole Magnet*. Darmstadt: GSI, 2013, 80 S. URL: <http://repository.gsi.de/record/109025>.
- [89] Mikhail Kholopov. “Conceptual Design Report on the superconducting Dipole Magnet for CBM”. In: (April 2018), p. 16.
- [90] Michal Koziel et al. “Vacuum-compatible, ultra-low material budget Micro-Vertex Detector of the compressed baryonic matter experiment at FAIR”. In: *Nuclear Instruments and Methods in Physics Research Section A: Accelerators, Spectrometers, Detectors and Associated Equipment* 845 (2017). Proceedings of the Vienna Conference on Instrumentation 2016, pp. 110–113. ISSN: 0168-9002. DOI: <https://doi.org/10.1016/j.nima.2016.05.093>. URL: <http://www.sciencedirect.com/science/article/pii/S0168900216304867>.

- [91] A. Dorokhov et al. “High resistivity CMOS pixel sensors and their application to the STAR PXL detector”. In: *Nuclear Instruments and Methods in Physics Research Section A: Accelerators, Spectrometers, Detectors and Associated Equipment* 650.1 (2011). International Workshop on Semiconductor Pixel Detectors for Particles and Imaging 2010, pp. 174–177. ISSN: 0168-9002. DOI: <https://doi.org/10.1016/j.nima.2010.12.112>. URL: <http://www.sciencedirect.com/science/article/pii/S0168900210028925>.
- [92] Tomáš Balog. “Overview of the CBM detector system”. In: *Journal of Physics: Conference Series* 503.1 (2014), p. 012019. URL: <http://stacks.iop.org/1742-6596/503/i=1/a=012019>.
- [93] Johann Heuser et al., eds. *[GSI Report 2013-4] Technical Design Report for the CBM Silicon Tracking System (STS)*. Darmstadt: GSI, 2013, 167 p. URL: <http://repository.gsi.de/record/54798>.
- [94] Claudia Höhne, ed. *Technical Design Report for the CBM Ring Imaging Cherenkov Detector*. CBM Technical Design Reports. 2013, 215 p. URL: <http://repository.gsi.de/record/65526>.
- [95] Subhasis Chattopadhyay et al., eds. *Technical Design Report for the CBM : Muon Chambers (MuCh)*. Darmstadt: GSI, 2015, 190 S. URL: <http://repository.gsi.de/record/161297>.
- [96] NA60 Collaboration et al. “NA60 results on thermal dimuons”. In: *The European Physical Journal C* 61.4 (2009), pp. 711–720. ISSN: 1434-6052. DOI: 10.1140/epjc/s10052-009-0878-5. URL: <https://doi.org/10.1140/epjc/s10052-009-0878-5>.
- [97] Christoph Blume, ed. *Technical Design Report for the CBM Transition Radiation Detector (TRD)*. Darmstadt: GSI, 2017, 196 S. URL: <https://indico.gsi.de/event/5654/material/0/0.pdf>.
- [98] Norbert Herrmann, ed. *Technical Design Report for the CBM Time-of-Flight System (TOF)*. Darmstadt: GSI, 2014, 182 S. URL: <http://repository.gsi.de/record/109024>.
- [99] I E Korolko, M S Prokudin, and Yu M Zaitsev. “The CBM ECAL”. In: *Journal of Physics: Conference Series* 798.1 (2017), p. 012164. URL: <http://stacks.iop.org/1742-6596/798/i=1/a=012164>.
- [100] Fedor Guber and Ilya Selyuzhenkov, eds. *Technical Design Report for the CBM Projectile Spectator Detector (PSD)*. Darmstadt: GSI, 2015, 75 S. URL: <http://repository.gsi.de/record/109059>.
- [101] V Friese and CBM Collaboration. “The high-rate data challenge: computing for the CBM experiment”. In: *Journal of Physics: Conference Series* 898.11 (2017), p. 112003. URL: <http://stacks.iop.org/1742-6596/898/i=11/a=112003>.
- [102] The CBM Collaboration. “Mini CBM proposal”. In: (June 19th 2017). URL: <http://www.fair-center.eu/for-users/experiments/nuclear-matter-physics/cbm/projects/mcbm.html>.
- [103] P. A. Čerenkov. “Visible Radiation Produced by Electrons Moving in a Medium with Velocities Exceeding that of Light”. In: *Phys. Rev.* 52 (4 1937), pp. 378–379. DOI: 10.1103/PhysRev.52.378. URL: <https://link.aps.org/doi/10.1103/PhysRev.52.378>.
- [104] J.V. Jelley. *Čerenkov Radiation, and Its Applications*. United Kingdom Atomic Energy Authority, 1958. URL: <https://books.google.de/books?id=odlEAAAIAAJ>.
- [105] T. Ypsilantis and J. Seguinot. “Theory of ring imaging Cherenkov counters”. In: *Nuclear Instruments and Methods in Physics Research Section A: Accelerators, Spectrometers, Detectors and Associated Equipment* 343.1 (1994), pp. 30–51. ISSN: 0168-9002. DOI: [https://doi.org/10.1016/0168-9002\(94\)90532-0](https://doi.org/10.1016/0168-9002(94)90532-0). URL: <http://www.sciencedirect.com/science/article/pii/0168900294905320>.
- [106] I. A. Getting. “A Proposed Detector for High Energy Electrons and Mesons”. In: *Phys. Rev.* 71 (2 1947), pp. 123–124. DOI: 10.1103/PhysRev.71.123. URL: <https://link.aps.org/doi/10.1103/PhysRev.71.123>.
- [107] R. H. Dicke. “Čerenkov Radiation Counter”. In: *Phys. Rev.* 71 (10 1947), pp. 737–737. DOI: 10.1103/PhysRev.71.737. URL: <https://link.aps.org/doi/10.1103/PhysRev.71.737>.

- [108] P. Glässel. “The limits of the ring image Cherenkov technique”. In: *Nuclear Instruments and Methods in Physics Research Section A: Accelerators, Spectrometers, Detectors and Associated Equipment* 433.1 (1999), pp. 17–23. ISSN: 0168-9002. DOI: [https://doi.org/10.1016/S0168-9002\(99\)00315-0](https://doi.org/10.1016/S0168-9002(99)00315-0). URL: <http://www.sciencedirect.com/science/article/pii/S0168900299003150>.
- [109] Arthur Roberts. “A new type of Čerenkov detector for the accurate measurement of particle velocity and direction”. In: *Nuclear Instruments and Methods* 9.1 (1960), pp. 55–66. ISSN: 0029-554X. DOI: [https://doi.org/10.1016/0029-554X\(60\)90049-5](https://doi.org/10.1016/0029-554X(60)90049-5). URL: <http://www.sciencedirect.com/science/article/pii/0029554X60900495>.
- [110] J. Seguinot and T. Ypsilantis. “Photo-ionization and Cherenkov ring imaging”. In: *Nuclear Instruments and Methods* 142.3 (1977), pp. 377–391. ISSN: 0029-554X. DOI: [https://doi.org/10.1016/0029-554X\(77\)90671-1](https://doi.org/10.1016/0029-554X(77)90671-1). URL: <http://www.sciencedirect.com/science/article/pii/0029554X77906711>.
- [111] P. Coyle et al. “The DIRC counter: a new type of particle identification device for B factories”. In: *Nuclear Instruments and Methods in Physics Research Section A: Accelerators, Spectrometers, Detectors and Associated Equipment* 343.1 (1994), pp. 292–299. ISSN: 0168-9002. DOI: [https://doi.org/10.1016/0168-9002\(94\)90568-1](https://doi.org/10.1016/0168-9002(94)90568-1). URL: <http://www.sciencedirect.com/science/article/pii/0168900294905681>.
- [112] I. Adam et al. “The DIRC particle identification system for the BaBar experiment”. In: *Nuclear Instruments and Methods in Physics Research Section A: Accelerators, Spectrometers, Detectors and Associated Equipment* 538.1 (2005), pp. 281–357. ISSN: 0168-9002. DOI: <https://doi.org/10.1016/j.nima.2004.08.129>. URL: <http://www.sciencedirect.com/science/article/pii/S0168900204020753>.
- [113] Erik Etzelmüller. “Developments towards the Technical Design and Prototype Evaluation of the PANDA Endcap Disc DIRC”. Dr. II. physikalisches Institut, 2017, 195 p. URL: [http://geb.uni-giessen.de/geb/volltexte/2017/12820/pdf/EtzelmueellerErik\\_2017\\_04\\_24.pdf](http://geb.uni-giessen.de/geb/volltexte/2017/12820/pdf/EtzelmueellerErik_2017_04_24.pdf).
- [114] J. Schwiening et al. “The PANDA Barrel DIRC”. In: *JINST* 13.03 (2018), p. C03004. DOI: 10.1088/1748-0221/13/03/C03004. arXiv: 1803.10642 [physics.ins-det].
- [115] Jürgen Engelfried. “Cherenkov light imaging—Fundamentals and recent developments”. In: *Nuclear Instruments and Methods in Physics Research Section A: Accelerators, Spectrometers, Detectors and Associated Equipment* 639.1 (2011). Proceedings of the Seventh International Workshop on Ring Imaging Cherenkov Detectors, pp. 1–6. ISSN: 0168-9002. DOI: <https://doi.org/10.1016/j.nima.2010.10.023>. URL: <http://www.sciencedirect.com/science/article/pii/S0168900210022576>.
- [116] D.M. Websdale. “Review of Cherenkov imaging devices in particle and nuclear physics experiments”. In: *Nuclear Instruments and Methods in Physics Research Section A: Accelerators, Spectrometers, Detectors and Associated Equipment* 595.1 (2008). RICH 2007, pp. 12–18. ISSN: 0168-9002. DOI: <https://doi.org/10.1016/j.nima.2008.07.040>. URL: <http://www.sciencedirect.com/science/article/pii/S0168900208009303>.
- [117] Volker Friese and Christian Sturm, eds. *CBM Progress Report 2014*. Darmstadt: GSI, 2015, 159 S. ISBN: 978-3-9815227-1-6. URL: <http://repository.gsi.de/record/97909>.
- [118] J. Adamczewski-Musch et al. “The CBM RICH project”. In: *Nuclear Instruments and Methods in Physics Research Section A: Accelerators, Spectrometers, Detectors and Associated Equipment* 766 (2014). RICH2013 Proceedings of the Eighth International Workshop on Ring Imaging Cherenkov Detectors Shonan, Kanagawa, Japan, December 2-6, 2013, pp. 101–106. ISSN: 0168-9002. DOI: <https://doi.org/10.1016/j.nima.2014.05.071>. URL: <http://www.sciencedirect.com/science/article/pii/S0168900214006111>.
- [119] J. Adamczewski-Musch et al. “The CBM RICH project”. In: *Nuclear Instruments and Methods in Physics Research Section A: Accelerators, Spectrometers, Detectors and Associated Equipment* 845 (2017). Proceedings of the Vienna Conference on Instrumentation 2016, pp. 434–438. ISSN: 0168-9002. DOI: <https://doi.org/10.1016/j.nima.2016.05.102>. URL: <http://www.sciencedirect.com/science/article/pii/S0168900216304958>.

- [120] Y. Riabov. “Talk given at the 31<sup>st</sup> CBM collaboration meeting”. In: (2018).
- [121] Volker Friese and Christian Sturm, eds. *CBM Progress Report 2012*. Darmstadt: GSI, 2013, 120p. ISBN: 978-3-9815227-0-9. URL: <http://repository.gsi.de/record/54078>.
- [122] S. Dalla Torre et al. “Remote alignment of large mirror array for RICH detectors”. In: *Nuclear Instruments and Methods in Physics Research Section A: Accelerators, Spectrometers, Detectors and Associated Equipment* 595.1 (2008). RICH 2007, pp. 220 –223. ISSN: 0168-9002. DOI: <https://doi.org/10.1016/j.nima.2008.07.067>. URL: <http://www.sciencedirect.com/science/article/pii/S0168900208009819>.
- [123] M. Alexeev et al. “Mirror alignment control for COMPASS RICH-1 detector”. In: *Nuclear Instruments and Methods in Physics Research Section A: Accelerators, Spectrometers, Detectors and Associated Equipment* 639.1 (2011). Proceedings of the Seventh International Workshop on Ring Imaging Cherenkov Detectors, pp. 219 –221. ISSN: 0168-9002. DOI: <https://doi.org/10.1016/j.nima.2010.10.149>. URL: <http://www.sciencedirect.com/science/article/pii/S0168900210024381>.
- [124] J. Adamczewski-Musch et al. “Determination of tolerances of mirror displacement and radiator gas impurity for the CBM RICH detector”. In: *Nuclear Instruments and Methods in Physics Research Section A: Accelerators, Spectrometers, Detectors and Associated Equipment* 766 (2014). RICH2013 Proceedings of the Eighth International Workshop on Ring Imaging Cherenkov Detectors Shonan, Kanagawa, Japan, December 2-6, 2013, pp. 221 –224. ISSN: 0168-9002. DOI: <https://doi.org/10.1016/j.nima.2014.04.074>. URL: <http://www.sciencedirect.com/science/article/pii/S0168900214004872>.
- [125] J.-C. Gayde B. Beauquis and N. L’Olivier. “CERN EDMS Report 837912”. In: (2007). COMPASS – RICH 1: Control of the orientation of 8 top sphere and 15 bottom sphere mirrors, p. 18. URL: <https://edms.cern.ch/document/837912>.
- [126] M. Alexeev et al. “Mirror alignment control for COMPASS RICH-1 detector”. In: *Nuclear Instruments and Methods in Physics Research Section A: Accelerators, Spectrometers, Detectors and Associated Equipment* 639.1 (2011). Proceedings of the Seventh International Workshop on Ring Imaging Cherenkov Detectors, pp. 219 –221. ISSN: 0168-9002. DOI: <https://doi.org/10.1016/j.nima.2010.10.149>. URL: <http://www.sciencedirect.com/science/article/pii/S0168900210024381>.
- [127] S. Costa et al. “CLAM, a continuous line alignment and monitoring method for RICH mirrors”. In: *Nuclear Instruments and Methods in Physics Research Section A: Accelerators, Spectrometers, Detectors and Associated Equipment* 553.1 (2005). Proceedings of the fifth International Workshop on Ring Imaging Detectors, pp. 135 –139. ISSN: 0168-9002. DOI: <https://doi.org/10.1016/j.nima.2005.08.034>. URL: <http://www.sciencedirect.com/science/article/pii/S016890020501586X>.
- [128] A. Gorišek et al. “Alignment of the HERA-B RICH optical system with data”. In: *Nuclear Instruments and Methods in Physics Research Section A: Accelerators, Spectrometers, Detectors and Associated Equipment* 433.1 (1999), pp. 408 –412. ISSN: 0168-9002. URL: <http://www.sciencedirect.com/science/article/pii/S0168900299003277>.
- [129] Hamamatsu Photonics K. K., ed. *Photomultiplier tubes: basics and applications*. Edition 3a. 2007, 323p. URL: [https://www.hamamatsu.com/resources/pdf/etd/PMT\\_handbook\\_v3aE.pdf](https://www.hamamatsu.com/resources/pdf/etd/PMT_handbook_v3aE.pdf).
- [130] “Flat panel type multianode pmt assembly h127000 series”. In: (2018). Ed. by Hamamatsu Photonics K. K., p. 4. URL: [https://www.hamamatsu.com/resources/pdf/etd/H12700\\_TPMH1348E.pdf](https://www.hamamatsu.com/resources/pdf/etd/H12700_TPMH1348E.pdf).
- [131] Jan Kopfer. “Development of a prototype camera and Monte Carlo studies for the optimisation of the CBM-RICH detector”. Gutachter: Karl-Heinz Kampert, Claudia Höhne; Bergische Universitaet Wuppertal, Diss., 2014. Dr. Wuppertal: Bergische Universitaet Wuppertal, 2014, 192 p. URL: <https://repository.gsi.de/record/97528>.

- [132] J. Adamczewski-Musch et al. “Influence of wavelength-shifting films on multianode PMTs with UV-extended windows”. In: *Nuclear Instruments and Methods in Physics Research Section A: Accelerators, Spectrometers, Detectors and Associated Equipment* 783 (2015), pp. 43–50. ISSN: 0168-9002. DOI: <https://doi.org/10.1016/j.nima.2015.02.014>. URL: <http://www.sciencedirect.com/science/article/pii/S0168900215001953>.
- [133] J. Adamczewski-Musch et al. “Wavelength shifting films on multianode PMTs with UV-extended window for the CBM RICH detector”. In: *Nuclear Instruments and Methods in Physics Research Section A: Accelerators, Spectrometers, Detectors and Associated Equipment* 766 (2014). RICH2013 Proceedings of the Eighth International Workshop on Ring Imaging Cherenkov Detectors Shonan, Kanagawa, Japan, December 2-6, 2013, pp. 180–182. ISSN: 0168-9002. DOI: <https://doi.org/10.1016/j.nima.2014.05.011>. URL: <http://www.sciencedirect.com/science/article/pii/S0168900214005105>.
- [134] V. Patel. “Talk given during group meeting”. In: (2017). URL: <https://cbm-wiki.gsi.de/foswiki/bin/view/Rich/CbmRichMeeting171018>.
- [135] Volker Friese, Christian Sturm, and Alberica Toia, eds. *CBM Progress Report 2015*. Literaturang. Darmstadt: GSI, 2016, 155 S. : Ill., graf. Darst. ISBN: 978-3-9815227-3-0. URL: <http://repository.gsi.de/record/186952>.
- [136] J. Adamczewski-Musch et al. “Development of the CBM RICH readout electronics and DAQ”. In: *Nuclear Instruments and Methods in Physics Research Section A: Accelerators, Spectrometers, Detectors and Associated Equipment* 876 (2017). The 9th international workshop on Ring Imaging Cherenkov Detectors (RICH2016), pp. 246–248. ISSN: 0168-9002. DOI: <https://doi.org/10.1016/j.nima.2017.03.043>. URL: <http://www.sciencedirect.com/science/article/pii/S0168900217303960>.
- [137] C. Pauly et al. “Upgrade of the HADES RICH photon detector with H12700 MAPMTs”. In: *Nuclear Instruments and Methods in Physics Research Section A: Accelerators, Spectrometers, Detectors and Associated Equipment* 876 (2017). The 9th international workshop on Ring Imaging Cherenkov Detectors (RICH2016), pp. 164–167. ISSN: 0168-9002. DOI: <https://doi.org/10.1016/j.nima.2017.02.067>. URL: <http://www.sciencedirect.com/science/article/pii/S0168900217302632>.
- [138] *CBM Progress Report 2017*. Tech. rep. CBM Progress Report 2017. ccby 4.0. Darmstadt, 2018, 220 p. DOI: 10.15120/GSI-2018-00485. URL: <http://repository.gsi.de/record/209729>.
- [139] Egor Ovcharenko. “Development of simulation, readout and data acquisition methods for physical experimental setups and their application for the RICH detector of the CBM experiment”. Dr. Joint Institute for Nuclear Research, 2018, 137 p. URL: [http://wwwinfo.jinr.ru/dissertation/Dissertation\\_Ovcharenko.pdf](http://wwwinfo.jinr.ru/dissertation/Dissertation_Ovcharenko.pdf).
- [140] J. Adamczewski-Musch et al. “Event reconstruction for the CBM-RICH prototype beamtest data in 2014”. In: *Nuclear Instruments and Methods in Physics Research Section A: Accelerators, Spectrometers, Detectors and Associated Equipment* 876 (2017). The 9th international workshop on Ring Imaging Cherenkov Detectors (RICH2016), pp. 76–79. ISSN: 0168-9002. DOI: <https://doi.org/10.1016/j.nima.2017.01.066>. URL: <http://www.sciencedirect.com/science/article/pii/S0168900217301560>.
- [141] “mCBM@SIS18 proposal”. In: (2017), p. 58.
- [142] “Talk given at the 31<sup>st</sup> CBM collaboration meeting”. In: (2018), p. 12.
- [143] J Bendarouach. “Conception and design of a control and monitoring system for the mirror alignment of the CBM RICH detector”. In: *Journal of Physics: Conference Series* 742.1 (2016), p. 012007. URL: <http://stacks.iop.org/1742-6596/742/i=1/a=012007>.

- [144] J. Adamczewski-Musch et al. “Conception and design of a control and monitoring system for the mirror alignment of the CBM RICH detector”. In: *Nuclear Instruments and Methods in Physics Research Section A: Accelerators, Spectrometers, Detectors and Associated Equipment* 876 (2017). The 9th international workshop on Ring Imaging Cherenkov Detectors (RICH2016), pp. 119 – 122. ISSN: 0168-9002. DOI: <https://doi.org/10.1016/j.nima.2017.02.033>. URL: <http://www.sciencedirect.com/science/article/pii/S0168900217302176>.
- [145] E. Albrecht et al. “The mirror system of COMPASS RICH-1”. In: *Nuclear Instruments and Methods in Physics Research Section A: Accelerators, Spectrometers, Detectors and Associated Equipment* 502.1 (2003). Experimental Techniques of Cherenkov Light Imaging. Proceedings of the Fourth International Workshop on Ring Imaging Cherenkov Detectors, pp. 236 –240. ISSN: 0168-9002. DOI: [https://doi.org/10.1016/S0168-9002\(03\)00280-8](https://doi.org/10.1016/S0168-9002(03)00280-8). URL: <http://www.sciencedirect.com/science/article/pii/S0168900203002808>.
- [146] M. Alexeev et al. “On-line mirror alignment monitoring method for COMPASS RICH-1”. In: *Nuclear Instruments and Methods in Physics Research Section A: Accelerators, Spectrometers, Detectors and Associated Equipment* 595.1 (2008). RICH 2007, pp. 194 –196. ISSN: 0168-9002. DOI: <https://doi.org/10.1016/j.nima.2008.07.014>. URL: <http://www.sciencedirect.com/science/article/pii/S0168900208009741>.
- [147] Lukáš Steiger. *Mirror alignment control for COMPASS RICH-1 detector at CERN*. 2013, 126 p.
- [148] Thomas Luhmann et al. *Close Range Photogrammetry and 3D Imaging*. Nov. 2013. ISBN: 978-3110302691. URL: <https://www.degruyter.com/view/product/203264>.
- [149] Marko Starič and Peter Križan. “Calibration of the mirror system in the HERA-B RICH”. In: *Nuclear Instruments and Methods in Physics Research Section A: Accelerators, Spectrometers, Detectors and Associated Equipment* 586.2 (2008), pp. 174 –179. ISSN: 0168-9002. URL: <http://www.sciencedirect.com/science/article/pii/S0168900207024217>.



# Acknowledgements

First I would like to thank Frau Professor C. Höhne, for her invaluable guidance and advices on the technical aspects as well as for providing a stimulating, healthy and suitable working environment. She was always willing to give me precious insights into the physics and helped me hone my scientific mind and skills. Many thanks to my colleagues from the working group for their help in my integration to the project and for fruitful discussions on several technical challenges. In particular I want to thank T. Mahmoud for his supervision, C. Deveaux, S. Lebedev, E. Ovcharenko and K. Wolf for their support with simulation and other software related issues and A. Rühl for taking care of a lot of administrative matters. I also want to thank J-H Otto, C. Riesen and A. Weber for adding a touch of fun to the daily work.

I want to thank colleagues from the CBM experiment, the GSI centre and the CBM RICH detector group for sharing their knowledge and helping me put my work in a more global context. Thanks to J. Förtsch, I. Kres, C. Pauly and S. Reinecke from the University of Wuppertal for their cooperation and their cheerful atmosphere during business trips. I would like to express my gratitude to colleagues from the technical University of Liberec, L. Steiger and M. Šulc for sharing their experience and giving me several advices which spared me precious time while adapting the CLAM method to the CBM RICH detector.

I would like to thank the Helmholtz Graduate School for Hadron and Ion Research (HGS-HIRe), the Bundesministerium für Bildung und Forschung, the Justus Liebig University Gießen and the GSI for their financial supports, without which this thesis could not have been completed. In addition to its financial support, the graduate school program of HGS-HIRe gave me stimulating and challenging workshops throughout the course of this thesis to gain insights on physics as well as one's own personality.

Finally I want to express my deepest gratitude to my parents Florence and Jamal for their unconditional support and enthusiasm. I want to thank profoundly Linda for her constant encouragements, her devotion and love throughout all these years. And I want to thank my irreplaceable brother, Jérémy, for bringing me strength and honour over the course of this chapter of my life. I am eternally grateful to have you all.

